Universidade do Minho
Escola de Engenharia

Luís Manuel Machado de Amorim

Different strategies towards the mitigation of low velocity impact damages in advanced composites

outubro de 2020

Different strategies towards the mitigation of low velocity impact damages in advanced composites
Luís Manuel Machado de Amorim
UMinho | 2020

Universidade do Minho
Escola de Engenharia

Luís Manuel Machado de Amorim

Different strategies towards the mitigation of low velocity impact damages in advanced composites

Tese de Doutoramento
Programa Doutoral em Ciências e Engenharia de Polímeros e Compósitos

Trabalho efetuado sob a orientação de
Professor João Pedro Lourenço Gil Nunes
Professor Júlio César Machado Viana

outubro de 2020

ACKNOWLEDGMENTS

First of all, I'd like to express my gratitude to all those who somehow support me along these least years of hard work.

To the project "IAMAT—Introduction of advanced materials technologies into new product development for the mobility industries", with reference MITP-TB/PFM/0005/2013, under the MIT-Portugal program exclusively financed by FCT—Fundação para a Ciência e Tecnologia, for the finantial support.

A special acknowledgment to my supervisors, Professor João Pedro Nunes and Professor Júlio Viana, for the opportunity, continuous guidance, all support, sympathy, and scientific knowledge given to me. Without them this work would not have been possible.

I also would like to thank all team of Department of Polymers Engineering, Institute for Polymers and Composites and PIEP – Centre for Innovation in Polymers Engineering, for the friendship and cooperation.

I would like to thank all the support given to me by my friends in the good and bad moments. Thank you for the good people you really are.

I would like to express all my gratitude to my girlfriend Milene for all the love, support and encouragement along all this path and for always being by my side.

A very special acknowledgment to my parents, João e Maria Glória, and my brothers, Maria João e Francisco, for all the love, affection, understanding and strength given to me during all the journeys of my life and for always being by my side and believing in my capabilities. What I am today I own to you.

Thank you all!!

STATEMENT OF INTEGRITY

I hereby declare having conducted this academic work with integrity. I confirm that I have not used plagiarism or any form of undue use of information or falsification of results along the process leading to its elaboration.

I further declare that I have fully acknowledged the Code of Ethical Conduct of the University of Minho.

RESUMO

Os polímeros reforçados com fibras de carbono (CFRP) são hoje em dia utilizados numa vasta gama de aplicações avançadas, tais como, aeronáutica, aeroespacial e militar. No entanto, e apesar da sua baixa densidade e elevado desempenho mecânico, eles continuam ainda a apresentar algumas debilidades, como a fraca resistência interlaminar. Quando sujeitos a condições de carregamentos dinâmicos, de impacto e de corte, eles tendem a formar no seu interior micro-fissuras que podem propagar-se na região interlaminar, comprometendo desta forma o desempenho mecânico de peça. Numa tentativa de superar este problema, muitas estratégias têm sido estudadas, tais como o reforço através da espessura (por exemplo, preformas fibrosas 3D, Z-pinning e stitching), modificação da matriz e/ou reforço, e ainda reforço interlaminar.

Tendo isto em consideração, este trabalho de pesquisa visa estudar diferentes estratégias para melhoria da resistência e tolerância ao dano de compósitos avançados quando submetidos a impactos de baixa velocidade. Para esse fim, um conjunto de novos laminados carbono/epóxi serão produzidos por infusão por vácuo, com o objetivo de comparar e analisar as suas características morfológicas bem como o seu desempenho mecânico. Neste sentido, novas configurações bioinspiradas assim como diferentes estratégias, estruturas e materiais para reforço interlaminar serão consideradas como potenciais abordagens para mitigação do dano para uma nova geração de compósitos laminados.

A campanha de teste terá como especial foco testes de impacto de queda de dardo, a fim de avaliar e caracterizar a resistência e tolerância a danos de novos laminados, bem como a sua resposta mecânica. Posteriormente, a fim de avaliar os danos inferido, inspeções visuais e testes não destrutivos (NDT) serão realizados para medir e avaliar o dano dos provetes. Além disso, os compósitos serão caracterizados quanto à sua espessura e fração volúmica dos seus diferentes componentes. Visualizações em microscópicas serão realizadas de modo a instigar a adesão matriz/fibras, morfologia dos laminados e conteúdo de vazios. Também serão realizados ensaios mecânicos quasi-estaticos para avaliar e comparar o desempenho e os modos de falha dos novos compósitos.

Palavras chave: Compósitos avançados; Compósitos bioinspirados; Resistência ao dano; Reforço interlaminar; Impacto de baixa velocidade.

ABSTRACT

Carbon fibres reinforced polymers (CFRP) are nowadays widely used in advanced applications, such as aeronautic, aerospace and army. Even though these materials possess light weight and high mechanical performance, they are still presenting some critical weaknesses, namely low interlaminar resistance. When submitted to dynamic, impact and shear loading conditions, they usually tend to develop internal micro-cracks that may propagate throughout the interlaminar region, compromising the whole composite part performance. In order to overcome this problem many strategies have been studied, such as through-thickness reinforcements (e.g., 3D-wovens, Z-pinning and stitching), matrix and/or reinforcement modifications, and interlaminar toughening.

With this in mind, this research work aims to study different strategies to improve low velocity impact (LVI) damage resistance and tolerance, of advanced laminated composites. To this end, several novel vacuum bag infused carbon/epoxy laminates were manufactured, and their morphologic characteristics and mechanical performances were compared and analysed. Therefore, new bioinspired configurations and different strategies, structures and materials to interleaf conventional laminates were adopted as potential damage mitigation approaches for a new composite laminate generation.

Test campaign had specially focus in drop weight impact tests in order to evaluate and characterise new laminates damage resistance and tolerance, as well as their mechanic response. In order to evaluate impact damages, visual inspections and non-destructive testing (NDT) were carried out to measure and evaluate specimens' damage. Besides this, composites were characterised according their thickness and components volume fraction. Microscopy visualisations were performed to instigate matrix/fibres adhesion, laminates morphology and voids content. In-plane mechanical tests were also performed to evaluate and compare the performances and failure modes of the new composites.

Keywords: Advanced composites; Bioinspired composites; Damage resistance; Interlaminar reinforcement; Low velocity impact.

CONTENTS

LIST OF FIGURES

LIST OF TABLES

PUBLICATIONS AND CONFERENCES

Publications:

- **L. Amorim**, A. Santos, J.P. Nunes, L.A. Rocha, A.F. Silva and J.C. Viana, "A NEW APPROACH TO ATTENUATE LOW VELOCITY IMPACT DAMAGES ON CFRP STRUCTURES", Materiales Compuestos Vol 4, no 1, pág. 60-66, 2020;
- A. Santos, **L. Amorim**, J.P. Nunes, L.A. Rocha, A.F. Silva and J.C. Viana, "ALIGNED CARBON NANOTUBE BASED SENSORS FOR STRAIN SENSING APPLICATIONS", Sensors & Actuators: A. Physical 289 (2019), 157-164, https://doi.org/10.1016/j.sna.2019.02.026;
- A. Santos, **L. Amorim**, J.P. Nunes, L.A. Rocha, A.F. Silva and J.C. Viana, "A COMPARATIVE STUDY BETWEEN KNOCKED-DOWN ALIGNED CARBON NANOTUBES AND BUCKYPAPER-BASED STRAIN SENSORS", Materials 12 (2019), 2013, doi:10.3390/ma12122013;
- **L. Amorim**, A. Santos, J. P. Nunes and J. C. Viana, "BIOINSPIRED ARCHITECTURES TOWARD IMPROVING DAMAGE RESISTANCE ON CFRP LAMINATES", 22nd International Conference on Composite Materials – ICCM 22, Melbourne, Australia, 2019;
- **L. Amorim**, A. Santos, M. Branco, V. Infante, J. P. Nunes and J. C. Viana, "IMPACT DAMAGE MITIGATION USING BIOINSPIRED CFRP LAMINATE ARCHITECTURES", 18th European Conference on Composite Materials – ECCM 18, Athens, Greece, 2018;
- L. Oliveira, R. Fazenda, I. Santos, M. Vasconcelos, B. Barros, **L. Amorim**, J. P. Nunes and J. F. Silva, "PRODUCING FILAMENT WOUND COMPOSITE PRESSURE VESSELS FOR COMMERCIAL APPLICATIONS", 16th European Conference on Composite Materials – ECCM 16, Seville, Spain, 2014;
- L. Oliveira, J. P. Nunes, J. F. Silva, B. Barros, **L. Amorim** and M. Vasconcelos, "COMPOSITE PRESSURE VESSELS FOR COMMERCIAL APPLICATIONS", 19th International Conference on composite materials – ICCM 19, Montreal, Canada, 2013;
- J. P. Nunes, **L. Amorim**, J. C. Velosa and J. F. Silva, "OPTIMIZING THE CONTINUOUS DRY IMPREGNATION OF THERMOPLASTIC MATRIX FIBER REINFORCED MATERIALS", 14th European Conference on Composite Materials – ECCM 14, Budapest, Hungary, 2010;

Attended Conferences:

- **L. Amorim**, A. Santos, J. P. Nunes and J. C. Viana, "TWO DIFFERENT INTERLEAVING APPROACHES TO MITIGATE IMPACT DAMAGE PROPAGATION ON CARBON/EPOXY

LAMINATES", *oral presentation*, FiBreMoD Conference 11th and 12th December 2019, Leuven, Belgium;

- **L. Amorim**, A. Santos, J. P. Nunes and J. C. Viana, "BIOINSPIRED ARCHITECTURES TOWARD IMPROVING DAMAGE RESISTANCE ON CFRP LAMINATES", *oral presentation*, 22nd International Conference on Composite Materials, 11th – 16th August 2019, Melbourne, Australia;
- **L. Amorim**, A. Santos, J. P. Nunes and J. C. Viana, "DAMAGE RESISTANCE IMPROVEMENT ON CFRP LAMINATES BY THE USAGE OF THIN VEILS STRATEGICALLY INTERLEAVED", *poster*, Polímeros2019, 15th July 2019, Centro Cultural Vilaflor, Guimarães, Portugal;
- **L. Amorim**, A. Santos, J. P. Nunes and J. C. Viana, "A NEW APPROACH TO ATTENUATE LOW VELOCITY IMPACT DAMAGES ON CFRP STRUCTURES", *oral presentation*, MATCOMP'19 – XIII Congreso Nacional de Materiales Compuestos, Vigo, Spain;
- **L. Amorim**, A. Santos, J. P. Nunes and J. C. Viana "THIN VEILS STRATEGICALLY INTERLEAVED TO REDUCE LOW VELOCITY DAMAGES ON CFRP", *oral presentation*, 12th International Conference on Composite Science and Technology, 8th – 10th May 2019, Sorrento, Italy;
- **L. Amorim**, A. Santos, V. Infante, J. P. Nunes and J. C. Viana "BIOINSPIRED CFRP STRUCTURES TO IMPROVE IMPACT DAMAGE TOLERANCE", *oral presentation*, Materiais 2019, 14th – 17th April 2019, Reitoria da Univercidade Nova, Lisboa, Portugal;
- **L. Amorim**, A. Santos, M. Branco, V. Infante, J. P. Nunes and J. C. Viana, "DAMAGE MITIGATION ON CFRP LAMINATES BY BIOINSPIRED ARCHITECTURES APPROACH", *poster*, Polímeros2018, 29th June 2018, Centro Cultural Vilaflor, Guimarães, Portugal;
- **L. Amorim**, A. Santos, M. Branco, V. Infante, J. P. Nunes and J. C. Viana, "IMPACT DAMAGE MITIGATION USING BIOINSPIRED CFRP LAMINATE ARCHITECTURES", *poster*, 18th European Conference on Composite Materials ECCM18, 24th - 28th June 2018, Megaron Athens International Conference Centre (MAICC), Athens, Greece;
- **L. Amorim**, A. Santos, M. Branco, V. Infante, F. Vaz, J. P. Nunes, L. R. Rocha and J. C. Viana, "IMPACT RESISTANCE IMPROVEMENT AND SELF-SENSING IN BIO-INSPIRED CFRP", *poster*, Polímeros2017, 30th June and 1st July 2017, Centro Cultural Vilaflor, Guimarães, Portugal;
- **L. Amorim**, A. Santos, M. Branco, V. Infante, F. Vaz, J. P. Nunes, L. R. Rocha and J. C. Viana, "CFRP BIOINSPIRADOS PARA MELHORIA DA RESISTÊNCIA AO IMPACTO E AUTOSSENSORIZAÇÃO", *oral presentation* and *poster*, I Reunião do Grupo do Carbono (I RGC), 12th and 13th June 2017, Biblioteca Municipal Almeida Garret, Porto, Portugal.

Conferences (participation):

- A. Santos, **L. Amorim**, J.P. Nunes, L.A. Rocha, A.F. Silva and J.C. Viana, "STRAIN SENSORS BASED ON KNOCKED DOWN CARBON NANOTUBES AND BUCKY PAPERS THIN FILMS", ***oral presentation***, 8th Annual World Congress of Advanced Materials-2019, 22nd – 24th July 2019, Osaka, Japan;
- M.M. Silva, **L. Amorim**, D. Moura, R.J. Young, M.C. Paiva, "EPOXY COMPOSITES WITH FUNCTIONALIZED AND METAL DECORATED SINGLE WALL CARBON NANOTUBES", ***poster***, CNPComp2019 - 8th International Conference on Carbon NanoParticle based Composites, 17th-19th July 2019, London, UK;
- M.M. Silva, **L. Amorim**, D. Moura, R.J. Young, M.C. Paiva, "EPOXY COMPOSITES WITH FUNCTIONALIZED AND METAL DECORATED SWCNT", ***poster***, Polímeros2019, 15th July 2019, Centro Cultural Vilaflor, Guimarães, Portugal;
- A. Santos, **L. Amorim**, J.P. Nunes, L.A. Rocha, A.F. Silva and J.C. Viana. "A COMPARATIVE STUDY BETWEEN KNOCKED-DOWN ALIGNED CARBON NANOTUBES AND BUCKYPAPER-BASED STRAIN SENSORS", ***poster***, Polímeros2019, 15th July 2019, Centro Cultural Vilaflor, Guimarães, Portugal;
- A. Santos, **L. Amorim**, J.P. Nunes, L.A. Rocha, A.F. Silva and J.C. Viana, "ALIGNED CARBON NANOTUBE FOR STRAIN MONITORING" ***oral presentation***, Materiais 2019, 14th – 17th April 2019, Reitoria da Univercidade Nova, Lisboa, Portugal;
- A. Santos, **L. Amorim**, J.P. Nunes, L.A. Rocha, A.F. Silva and J.C. Viana "ACNT-BASED SENSORS FOR STRAIN MONITORING/SENSING APPLICATIONS", ***poster***, Polímeros2018, 29th June 2018, Centro Cultural Vilaflor, Guimarães, Portugal;
- A. Santos, **L. Amorim**, J.P. Nunes, L.A. Rocha, A.F. Silva and J.C. Viana, "CNT-BASED SENSORS FOR STRAIN MONITORING/SENSING APPLICATIONS", ***oral presentation***, NANOSTRUC 2018 - The 4th International Conference on Structural Nano Composites, 23rd an 24th May 2018, Berlin, Germany;
- L. Oliveira, R. Fazenda, I. Santos, M. Vasconcelos, B. Barros, **L. Amorim**, J. P. Nunes and J. F. Silva, "PRODUCING FILAMENT WOUND COMPOSITE PRESSURE VESSELS FOR COMMERCIAL APPLICATIONS", ***oral presentation***, 16th European Conference on Composite Materials – ECCM 16, 2014, Seville, Spain;

- L. Oliveira, J. P. Nunes, J. F. Silva, B. Barros, **L. Amorim** and M. Vasconcelos, "COMPOSITE PRESSURE VESSELS FOR COMMERCIAL APPLICATIONS", ***oral presentation***, 19th International Conference on composite materials – ICCM 19, 28th July – 2nd August 2013, Montreal, Canada;
- J. P. Nunes, **L. Amorim**, J. C. Velosa and J. F. Silva, "OPTIMIZING THE CONTINUOUS DRY IMPREGNATION OF THERMOPLASTIC MATRIX FIBER REINFORCED MATERIALS", ***oral presentation***, 14th European Conference on Composite Materials – ECCM 14, 7th – 10th June 2010, Budapest, Hungary.

Awards:

2018 **Best Poster Award ECCM18** - **L. Amorim**, A. Santos, M. Branco, V. Infante and J. P. Nunes, J. C. Viana, "IMPACT DAMAGE MITIGATION USING BIOINSPIRED CFRP LAMINATE ARCHITECTURES", poster, 18th European Conference on Composite Materials ECCM18, 24th - 28th June 2018, Megaron Athens International Conference Centre (MAICC), Athens, Greece.

Chapter 1
Introduction

In this chapter will be presented a brief advanced composite materials background, thesis motivation, methodology used, main objectives as well as thesis outline.

1.1 Background

Composite materials are usually defined as a combination of, at least, two materials, usually denominated as matrix and filler (or dispersed phase) macroscopically distinguishable, in order to optimize properties of a final product. While matrix is responsible for giving the shape and homogenise the characteristics all over the composite part, filler provides or optimizes new performing properties (e.g. electrical, thermal, mechanical, etc.) [1][2]. Composite materials can be classified according to their matrix (e.g. metallic, ceramic or polymeric) or dispersed phase (e.g. particles, short or continuous fibres) [2].

In the second half of the XX century, fibre reinforced polymers (FRP) have gained popularity, especially, because they were easy to process, yielding low density and superior mechanical properties final parts [3][4]. A subclass of FRPs are the advanced composites, characterised by their unique mechanical properties, they are made of layers of high performance continuous fibrous reinforcements, such as carbon, aramid or boron fibres, in form of unidirectional tissues, waiving fabrics or roving, and thermosetting polymeric matrices as epoxy or vinylester [1][2][5].

The possibility to optimize laminate mechanical characteristics according the specific solicitation field, turn polymeric advanced composite materials very attractive to perform in high demanding environments in alternative to the traditional ones (e.g. metal alloys). In the last decades, industries specialised in advanced applications, such as aeronautic, aerospace, sports and defence, have been taking advantage of the high mechanical properties and low-density combination that these materials present to enhance better performances [1][3][4]. However, despite of their extraordinary in-plane mechanical properties and low density, when exposed to out-of-plane loading conditions, they tend to develop internal damages that may propagate during the component service lifetime [1][2][4][6][7]. This misbehaviour arises, essentially, from the high brittleness and layer-by-layer architecture of these materials, which turn them quite vulnerable to solicitations dominated by shear and dynamic stresses [8].

In order to overcome this problem, some techniques have been already proposed which include, the fibres surface modification to improving the adhesion between phases [9], the matrix modification to reduce its brittleness [10][11], the inclusion of macro-mechanic through-thickness reinforcements (e.g., 3D-wovens, Z-pinning and stitching) [12][13], or, the reinforcement of interlaminar region with energy dissipator materials or structures between [14][15]. Despite all of those strategies have revealed improvements on damage mitigation, several issues have been reported associated to their implementation, such loss on in-plane mechanical properties, incrementation of thickness and weight, among others. Therefore, improving the damage resistance of advanced composites remains a challenge for materials engineers.

1.2 Motivation

One of the most problematic and dangerous solicitations that advanced composites must face during their lifetime are low velocity impacts (LVI). Such unpredictable events are especially problematic in aeronautic industry, where may occur in the most various ways, for instance, during maintenance routines by tool dropping, or even during flight time by bird striking or hailstorms. These occurrences may lead to develop intralaminar subcritical damages that, when arrived to the interlaminar regions, tend to propagate throughout them, forming extensive delaminations, compromising the part mechanical behaviour or even, in the worst case scenario, lead to its catastrophic failure [1][2][4][6][7].

A schematic representation of different impact damages inside laminate composites may be seen in Figure 1.

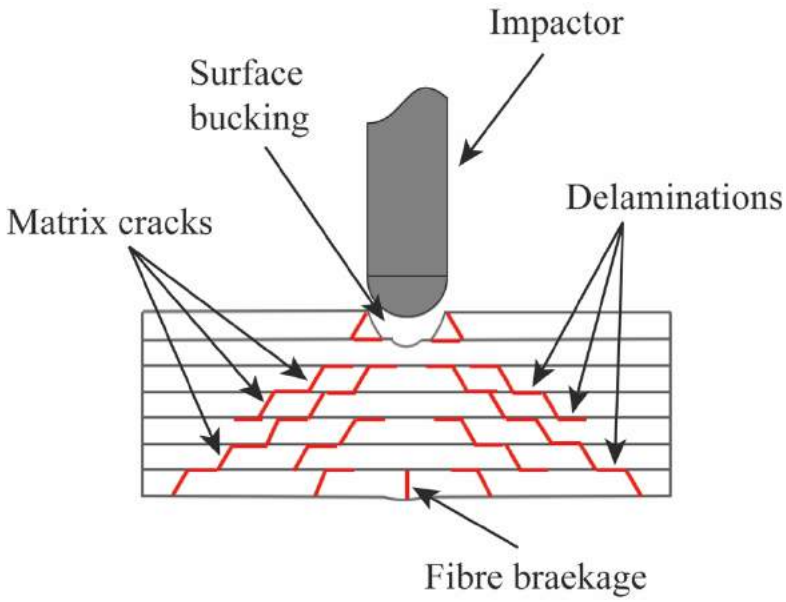

Figure 1: Schematic representation of different impact damages inside laminate composites.

Beside unpredictable, these happenings, typically do not leave any physical trace, which requires expensive and time-consuming constant inspections. This specificity low velocity impact damage on advanced composites is usually called Barely Visible Impact Damages (BVID) [16][17].

Therefore, several work have been carried out in order to understand the mechanisms behind impact damage resistance (damage caused be impact events) and tolerance (composite performance after impact damaged) of these materials [17]. Those studies have revealed that these properties are especially related to the high brittleness and layer-by-layer arrangement of advanced composites [1], [8], [18]–[21]. On the other hand, several other factors may play an important role on impact damage development, among them, impactor geometry, material properties, mass and velocity, laminate stack sequence,

geometry (shape, thickness,) material properties, boundary conditions and finally environmental conditions and impact angle [20]–[23].

Considering all those aspects, it is imperative find out new strategies that may mitigate low velocity impact damages in advanced composites. Therefore, this study is motivated by the need to propose new approaches capable to improve damage resistance and tolerance of these promising materials, enhance them to preform for longer, safely and with low residual costs.

1.3 Methodology

In the last decades, several works have been carried out regarding the improvement of impact damage resistance and tolerance in polymeric advanced composites, especially those composed by stacked layers of carbon and glass continuous fibres. Subsequentially, a large range of new "engineering" approaches have been proposed. The usage of thought-thickness reinforcements (e.g. Z-pinning or stitching) or reduce matrix brittleness by the meaner of rubbers or thermoplastics have shown to be very effective to improve interlaminar toughness and arrest crack propagation [17][24][25]. However, these benefits may affect in-plane mechanical properties or increase resin viscosity. Another common strategy to mitigate damage propagation consists in reinforce the interlaminar resin rich region using toughening materials or structures [26][27]. Acting only where the crack is more likely to propagate extensively, this approach has shown to reduce damage propagation without causing substantial losses on in-plane mechanical properties [16][27][28].

Other hypothetical approaches have been proposed based on biological structures. Observing the natural world, some other authors noted that a large range of living beings have developed their own strategies to better resist to impact. Particularly, a twisted fibrous plywood arrangement, known as Bouligand arrangement [29], has attracted lot of attention owing its similar structural architecture to the conventional laminated composites. Lately, inspired by those biological structures, several studies have been carried out in order to mimic them using synthetic advanced materials as carbon, aramid and even glass unidirectional fibre layers. The results have shown that those bioinspired laminates may delay extensive delaminations and increase load bearing capability under out-of-plane solicitations [30]–[34].

Aware of the importance of reducing production costs, considering this background on advanced laminated composites and strategies to improve damage resistance and tolerance on them, in this work, three vacuum bag infused new approaches are proposed and compared to a conventional carbon/epoxy aircraft laminate manufactured using the same manufacturing process.

Following the structure of this document, the three new approaches are briefly described below:

I. Bioinspired Bouligand-like architectures – Vacuum bag infused Bouligand-like laminates;
II. Strategically thin veils interleaving – Using a finite elements model, the most critical interfaces will be identified to interleaved with four different thin veils;
III. 3D-printed interlaminar interlocking structures – Two different materials and patterns will be directly printed over the unidirectional carbon fibres to create three-dimensional interlocking layers.

Should be noted that approaches II and III, share the same principal of reinforcing interlaminar laminates' region, which may be classified as an interleaving technique.

The comparison between the laminates will consist on: laminates morphological evaluation, mechanical performance (tensile, interlaminar shear strength (ILSS), three-point bending (3-PB) and low velocity impact tests), damage analysis (visual and ultra-sound inspection) and compression after impact (CAI) tests.

1.4 Main objectives

With the intension to meet the need to improve damage resistance of advanced composite, in this work it is proposed new and different approaches to optimise carbon fibres reinforced polymers (CFRP) advanced laminated composites, minimising or delaying low velocity impact damages. Therefore, the main objectives of this research study are:

- Improve low velocity impact damage resistance and tolerance of novel advanced composites applying bioinspired approaches, strategical interleaved thin veils and 3D printed interlaminar interlocking layers;
- Validate vacuum bag infusion process suitability to manufacture the new proposed advanced composites with high damage resistance and tolerance;
- Validate the performance of the different novel approaches by the manner of mechanical tests and damage analyse techniques;
- Compare and discuss the performance of the novel advanced composites proposed to a conventional aircraft laminate.

The specific objectives of this research work are:

- Propose a conventional laminate to work as a comparative baseline;
- Propose new strategies to improve damage resistance on advanced composite laminates;
- Analyse physic and morphologic characteristics of all materials and micro-structures selected produce and optimise laminates;

- Produce conventional and proposed composite laminates vacuum bag infusion manufacturing process;
- Produce unidirectional laminates in order to characterise lamina engineering constants;
- Optimise vacuum bag infusion manufacturing process;
- Evaluate composites processing quality;
- Analyse laminates morphology and determine volume fractions of their different components;
- Evaluate and compare some quasi-static mechanical properties of different layups;
- Conduct low velocity impact tests at different energy levels in all laminates proposed;
- Evaluate and compare low velocity impact mechanical response of all configurations;
- Analyse and compare low velocity impact damage resistance and tolerance of all proposed composites;
- Discuss the results obtain from each configuration and understand different damage mechanisms based on failure modes observed.

1.5 Thesis layout

This thesis is organized into nine main chapters. In this chapter (**Chapter 1**) is presented a brief introduction to advanced composite materials and their main issues, thesis motivation, methodology used, main objectives and outline to provide the reader a clear overview about the aims and main concerned to be discussed as well as a structural organization of this thesis.

The general aspects related with advanced composite materials, their typical compounds and processing technologies are revised in **Chapter 2**. A special emphasis is also given to laminated composites damage resistance and tolerance as well as the main strategies already proposed in literature to mitigate this issue.

Chapter 3 is dedicated to describing main compounds and processing technology selected to manufacturing advanced composites in this work. A general description of experimental mechanical tests and impact damage evaluation procedures is also presented in the chapter.

Chapter 4 presents the experimental work carried out, methodology used and obtained results of lamina engineer constants assessment. Afterwards, the three following chapters will be dedicated to describing the different approaches proposed in this work to mitigate low velocity impact damage. All of them are structurally similar, in first place the conceptual idea is presented followed by the description of experimental testing campaign, results presentation, their discussion and main conclusions. Therefore, **Chapter 5** is dedicated to bioinspired Bouligand-like arrangements, **Chapter 6** to the strategical

interleaving of thin veils into a conventional aircraft laminate and, finally, **Chapter 7** to the usage of 3D printing novel technology to reinforced standard layups.

In **Chapter 8** is presented an objective comparison over damage resistance among the different approaches proposed in this work. Finally, in **Chapter 9** are summarised the overall conclusions of the different approaches proposed in this work to mitigate impact damage in advanced composite materials, together with ideas for a future work.

Chapter 2
Literature Review

In this chapter will be made a general literature review concerning advanced composite materials, their typical compounds and processing technologies. A special emphasis will be given to laminated composites damage resistance and tolerance as well as the main strategies proposed in literature to minimise this issue.

2.1 Composite materials

Since the beginning of civilization, the man used natural composite structures as construction materials, using straws from plants to reinforce mud bricks. The goal of any composite material is optimising the properties of final material, which can be tailored through manipulation of their components and interfaces. Typically, a filler, in less amount, that optimizes and/or provides new proprieties to the final material, and a matrix that is responsible to give shape to the final part and distributes uniformly new features over the whole material [1]. Enhanced mechanical performance is just one of purposes of composite materials. Typically for this purpose, the fillers, usually called reinforcements, are fibres. For other purposes, e.g., improvement of electrical or thermal properties, particles are the most common type of filler.

Composite materials can be divided in different groups depending on different aspects. They can be classified by reinforcement/filler dimensions, where the main groups are nanocomposites, short-fibres composites and continuous-fibres composites. Another possible classification is in order to its matrix, in this case they can be divided in metal, ceramic and polymeric matrices composites [2].

Fibre reinforced polymers (FRP) are now one of youngest and more interesting members of composite materials family. First developed during 1950s, FRP are nowadays wildly used, paving the way to advanced composite materials. With lightweight and outstanding mechanical performances when compared to traditional materials, a subfamily of FRP, commonly known as advanced composites, have attracted attention of advanced applications, such as aeronautics, aerospace, marine, automotive sports, etc. [1]–[3], [35]. The outstanding performance of this subclass is in particular due to high performance fibrous reinforcements, as carbon or aramid fibres, very well aligned in one or more directions, typically impregnated with a high demanding thermosetting polymeric resin, as epoxy or vinylester resin [1][2][5]. A representation of composites family is schematically depicted in Figure 2.

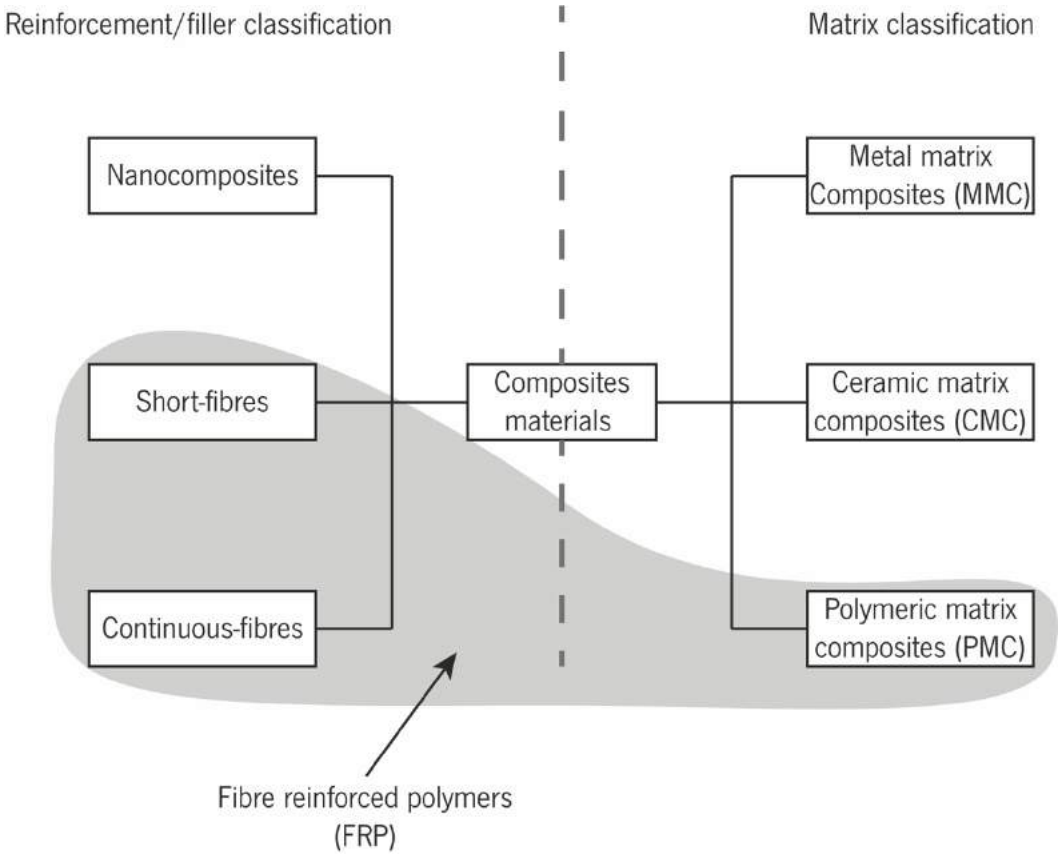

Figure 2: Composites family.

2.1.1 FRP component materials

Polymeric materials gained popularity essentially due to its low weight and easy processability in different shapes and sizes, despite their poor mechanical performance that limited their usage in advanced applications. On the other hand, fibrous materials exhibit remarkable mechanical properties when compared to the bulk material from which they are made of, but they can't be directly used in advanced applications due to their flexibility and brittleness [1], [2]. In FRP, the polymer matrix provides a solid shape to the part, protecting the fibres and, at the same time, transferring and distributing homogeneously loads to the fibrous reinforcements. Polymeric matrices are divided in two main groups: thermoplastics and thermosetting. Thermoplastic polymers are composed by individual long molecular chains weakly linked by weak forces (e.g., van der Waals forces and hydrogen bonds), allowing a higher mobility of macromolecules, and, consequently, a better mechanical properties (e.g., impact resistance), but long macromolecules result in higher viscosity making difficult impregnation in liquid resin processes of composites. Although, the ability to be recycled turn thermoplastic composite materials more attractive nowadays [2], [36]–[38].

Thermosetting polymers are the most common polymer matrices used in composite industries. They are characterized by a rigid three-dimensional linked molecular network. After solidification, this kind of polymers can't be reprocessed, unlike thermoplastic polymers. These resins are usually composed by two parts: resin and hardener. Once mixed, the polymerization (or cure) starts creating the three-dimensional molecular structure. A post-cure at high temperature is often required to promote intermolecular cross-links that were not created during the initial polymerization process [1], [39], [40]. Polyester, vinyl-ester and phenolic resins are widely used in non-structural or semi-structural applications, while epoxide, bis-maleimide and polyimide resins are often used as matrices in advanced composites due to its mechanical performance and high temperature resistance [1].

Fibrous reinforcements can be divided in natural or synthetic, although natural fibres are not commonly used as a reinforcement in composites due to its poor and high variable mechanical properties. On the other hand, synthetic fibres present high modulus and strength values, which make them preferential for structural applications. Glass fibres are widely used in non-structural and semi-structural polymeric composite materials, while carbon and boron, owing to its remarkable mechanical properties, are extensively used in advance applications, such aeronautic or aerospace industry [1], [2], [39].

2.1.2 Composite manufacturing technologies

Nowadays, FRP laminates are widely used in high performance and advanced applications, e.g., aeronautics, aerospace, marine, automotive sports etc., especially due to their exceptional balance between weight and mechanical properties [1], [3], [35]. To achieve the desired performances, it is important to select the appropriate reinforcements and ensure that their content and orientations remain according to those previewed in the design, after manufacturing. Thus, the composite manufacturing techniques being used must accomplish these objectives and, at the same time, ensure a homogenous impregnation over the entire part.

From the several processes used to manufacture advanced composite parts, some use liquid resin to impregnate fibres through the application of positive or negative pressures and other are dry consolidation techniques that use pre-impregnated fibres (prepregs) with a partially cured thermoset matrix (B-stage material) or thermoplastics (using films or other methods). Both present their own advantages, but cost remains has the main difference between them. Dry processes, using pre-impregnated fibres, tend to be more expensive when compared to liquid resin ones [40]. The scheme shown in Figure 3 presents a general view of the major available advanced composite manufacturing processes.

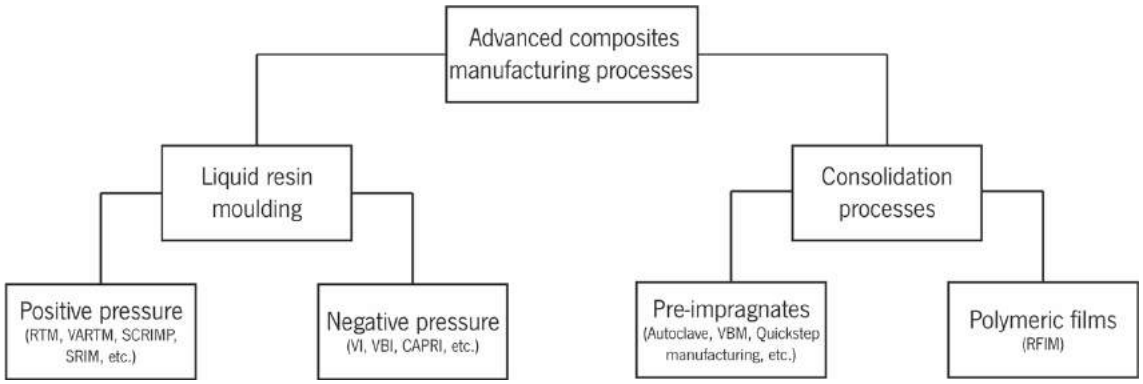

Figure 3: Advanced composites manufacturing processing methods general view.

Among liquid resin moulding processes, RTM is one of the most popular techniques used for producing laminate composite components with very good cost/volume of production ratio. The process uses a fully closed solid mould, where liquid pressurised resin is injected to impregnate reinforcement tissues previously placed inside it. RTM allows producing composite parts with smooth-finishing surfaces on both sides, good thickness control, high fibre contents and, consequentially, mechanical properties [1], [2], [39], [41]. The process presents several variants, being the mostly known ones the HPRTM (High-Pressure Resin Transfer Moulding) [42][43], VARTM (Vacuum-Assisted Resin Transfer Moulding), SCRIMP (Seemann Composite Resin Infusion Moulding Process) [1], [2], [39], [44] and SRIM (Structural Reaction Injection Moulding) [1], [39].

The VI process, very often also known as RTM light, presents many similitudes with RTM technology. Dry reinforcement tissues placed inside a sealed solid mould are impregnated by a liquid resin subjected to vacuum. The resin impregnates the reinforcements by being forced to replace air voids and flow throughout fibres due to the differential caused between the atmospheric and vacuum pressures. This technique allows produce large composite parts having low void content, good surface finishing and high mechanical properties [1], [2], [44]. The major differences between this technique and the traditional RTM rest in the use of vacuum instead of moderate pressure to force the resin to impregnate the dry fibres as well as in the employment of minimal and cheaper mould structures (namely, a semi-flexible material/structure is commonly used in the upper half part of the mould).

Based on the same principle and due to its lower tooling cost, Vacuum Bag Infusion (VBI) is one of the most successfully variations of VI. By using a flexible half part of the mould (usually, consisting in a thermoplastic film), VBI becomes much more cost-effective than VI. However, only one side of the final part presents good-surface finishing, because the surface contacting the plastic film always shows rougher surface than the one from the rigid mould side [2], [45]–[50]. The VI variation, so-called Controlled Atmospheric Pressure Resin Infusion (CAPRI), allows full control of the pressure differential throughout

the laminate, leading to minor thickness variations and much more accurately control of the fibre volume fraction on final parts [51], [52].

In all processes using fibre impregnation by liquid resins, the resin viscosity and tissues permeability are very important factors to be taken into account due to the risk of obtaining dry spots inside the composite part. Commonly, despite the additional costs that are usually associated to their use, dry manufacturing processes using pre-impregnated fibres (prepregs) are considered more reliable to avoid this problem and, in addition, they also allow obtaining higher fibre contents and control them with much better accuracy in the final composite parts.

Autoclave moulding is one of the processes mostly used to consolidate pre-impregnated fibre tapes and tissues, producing high performance composites for advanced markets. In this process an autoclave is used to consolidate the pre-impregnated reinforcements placed in a mould, simultaneously, maintained under pressure and/or vacuum and subjected to a carefully scheduled temperature cycle. Scheduled stages of temperature allow an accurately control of the curing reaction, while the pressure and/or vacuum ensures the inter-ply consolidation process and void removal. Despite the large initial investment required in equipment and the final part size limitations imposed by the autoclave internal dimensions, autoclave moulding enables good surface finishing on one side of the part and remarkable mechanical properties in final composites [1], [2], [35], [39], [40], [53].

Vacuum Bag Moulding (VBM) is another consolidation process using pre-impregnated reinforcements or hand-lay-up preforms. Using similar setup to the one of VBI, after vacuum-bagged, the resin cures inside an oven or at room temperature. This technique is very common on the aeronautic industry due to the high fibre volume fraction and low void contents that may be achieved and, as in vacuum bag infusion, the lower cost of process apparatus [1], [2], [40]. Recently, Quickstep Technologies Pty Ltd. developed a new out-of-autoclave (OOA) composite manufacturing process, where vacuum bag moulded pre-impregnates are warm up and pressurize inside a chamber containing a heat transfer fluid (HTF). The technique claims to enable obtaining composites presenting good mechanical properties with significant cost savings [53]–[55].

Another example of consolidation process is Resin Film Infusion Moulding (RFIM). In the process, dry reinforcement tissues are placed between or interleaved by thermoplastic films, and then the whole set is vacuum bagged and heated at high temperatures inside a woven. Due to the temperature, the films melt and impregnate the fibres. Beside outstanding mechanical properties and fibre content accuracy, the production costs can be minimized due to the unnecessity to use pre-impregnated reinforcements.

However, the process is time-consuming and requires the use of moulds and accessories able to resist to the high temperatures reached [39], [40], [44], [56].

2.2 Composites damage resistance and tolerance

In the last century the massive usage of plastics opened the door to the polymeric matrix composites that, combining different materials, took advantage of the low density and mouldability of polymers to perform in a large range of fields, from electrical, thermal, non-structural or structural applications [1]–[3], [35].

With lightweight and outstanding mechanical performances when compared to traditional materials, FRP produced using continuous fibres of carbon, aramid or boron, so called advanced composites, have attracted attention of advanced applications, such as aeronautics, aerospace, marine, automotive, sports, etc. [1]–[3], [35]. Usually produced from pre-impregnated materials or liquid thermosetting resin transfer processes, these materials may be used under extreme thermal and mechanical service conditions. However, when exposed to out of-plane, impact, shear and dynamic loading conditions, they tend to develop internal damages that may propagate during the lifetime of parts, compromising their performance in service. Issues related to the layer-by-layer nature, adhesion between different phases and intrinsic brittleness of these materials, were already identified as the most influent ones to the development of those damages [1], [8], [18], [19].

Therefore, along the last decades, advanced composite materials performance under out-of-plane loads and low velocity impact events have been studied massively in order to reduce or overcome their susceptibility to develop internal and almost imperceptible damages. Those studies usually are focus in two important and distinctive factors, damage resistance and damage tolerance. The first consists in evaluate the resistance of a given composite to develop damage during, or immediately after, the solicitation. Therefore, this damage resistance may be evaluated according to the maximum load or energy absorbed before damage onset and during the event, or damage severity, for instance, internal and external damage extension, type of damage (fibre breakage, matrix cracking and delaminations). On the other hand, the term damage tolerance is related to the performance of a damaged composite. The most popular experiment to evaluate damage tolerance is compression after impact (CAI) [22][57].

The following sections summarise the most common approaches proposed to improve damage resistance and tolerance in advanced composite materials.

2.2.1 Through-Thickness Properties Improvement Techniques

Delamination is one of the main causes of failure of advanced polymeric composite laminates. This phenomenon occurs more often in laminates submitted to impact and out-of-plane loadings, in which shear and dynamic stresses are developed. To overcome or mitigate those weaknesses, some attempts were already been made or are being pursued, such as, the use of three-dimensional (3D) woven fibre reinforcing structures or of interlaminar reinforcements with particular properties modification of matrices, optimisation of the adhesion and compatibility of fibre/matrix interface, etc. [24]. Next paragraphs will describe the most common methods to improve through-thickness properties of laminated FRP composites.

2.2.1.1 Mechanical through-thickness reinforcement

According to their manufacturing methods, three-dimensional fibre reinforcements are usually divided in: 3D fabrics, Z-pinning and stitching tissues (Figure 4 a) to c), respectively). Those methods consist basically in creating macro-mechanic bonds between layers improving thereby laminates through-thickness toughness.

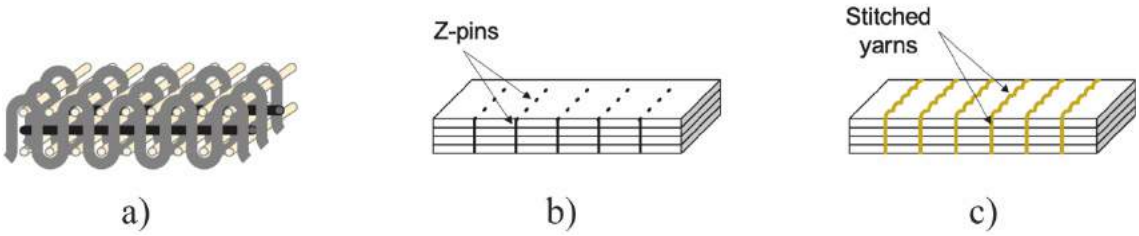

Figure 4: Scheme of mechanical through-thickness reinforcements approaches: a) 3D woven, b) Z-pining, c) stitching.

2.2.1.1.1 3D Woven

3D woven fibre structures, usually manufactured by weaving [12], are mainly used as preforms that are placed inside the mould in order to be impregnated by the resin. The use of preforms make their processing much cost effective by avoiding all manual cutting and stacking procedures that could be needed to place them properly in the mould. These reinforcements ensure an effective enhancement of though-thickness mechanical properties when compared to the traditional layer-by-layer manufactured ones [1], [12]–[14], [35].

It is well known that 3D woven reinforcing architectures ensure higher damage tolerance, delamination resistance and impact absorption of composite laminates [13], [58]–[60]. However, there is some

reluctance of composites industry using them due to the unpredictability of their in-plane properties [25], [61] and behaviour in service [13]. Accordingly to some authors [62], during the manufacturing process of those fabrics, several damages are infringed to a small part of fibre filaments such as, breakage, misalignment and bending. In fact, considering these factors, and also the different laminates and types of fibres used, becomes extremely hard to predict and know what can be expected from the behaviour of composites in working conditions. Misalignment and fibre breakage may compromise the in-plane mechanical properties of composites, whereas gaps close to fibres-crossing areas may create resin-rich zones where cracks may start [12], [13]. Regarding these problems and the lack of assessment to the mechanical response of 3D woven composites, it's easy to understand why they are not yet being widely used [13].

2.2.1.1.2 Z-pinning

The Z-pinning is another technique used to improve delamination resistance of composites, which basically consists on bonding (needling) groups of uncured prepreg laminae by inserting rods (reinforcing fibres) throughout their thickness. These inserting rods, so-called Z-pins or Z-fibres, can be made from fibrous cured composites or metals (titanium, for instance) and present diameters around 0,2-1,0 mm. Owing to their small dimensions, Z-pins generally represents a modest volume content (0,5 - 5 %) in the overall composite [24], [63], [64].

The Z-pinning method was, for the first time, used in the 1970's to improve though-thickness mechanical properties of composites and have proven to allow enhancing dramatically their damage and delamination resistances [236, 237] and the bonding [64] and adhesion properties between the prepreg layers [24], [67], [68].

To apply Z-pins on prepregs, the laminate stack sequence is first sandwiched between two foam brackets and the Z-pins, previously disposed and aligned perpendicularly over the top bracket, are then mechanically forced to overpass throughout the laminate. After z-pined, the foam brackets are removed and the fasteners that overrun the laminate are cut and, finally, the part is ready to be cured [63], [66].

Being easy to implement on existing composite processes, Z-pinning can be considered a promising technique to minimize through-thickness composites problems without relevant associated costs. However, some relevant variables should be taken into account to ensure the good final properties of composites. Some of those variables are: the laminate thickness, volume fraction of the z-pins, their areal density, their perpendicularity and also the material that they are made of [69].

Mouritz [24] evaluate the balance between through-thickness properties (Mode I) and in-plane missed performances (tension, compression, bending, inter-laminar shear, and fatigue properties) on Z-pinned carbon/epoxy laminates. The study revealed that, despite a decrease of in-plane mechanical properties, the Z-pinned laminates exhibit an increase of the interlaminar toughness of about 500% relatively to the unpinned ones. The reduction of in-plane properties observed seems to be related to the damage infringed by the needling process to the prepregs fibres and to the resin pockets formed around the fasteners. Other studies conducted by the same author [70][71] have also shown the usage of Z-pins may reduce the delamination area caused by low velocity impacts when the impact energy is higher than the threshold energy (in this case around 17 J for 4.3 mm thick samples). It was also demonstrated that the usage of Z-pins increases the damage resistance. However, this improvement was only observed for volume contents up to 2 %, after this amount they did not any additional improvement. Recently, Francesconi and Aymerich [72] studied performance of Z-pins on different laminates stack sequences under low velocity impact. In this work, they concluded that Z-reinforcements cannot delay interlaminar damage propagation, but they may reduce delamination size. The main reason for this behaviour was attributed to the activation of Z-pin bridging that reduces damage propagation. However, the same mechanism did not occur when delaminations were distributed across the laminate thickness in small sizes.

Despite the through-thickness properties improvement, this technique did not earn great acceptance by the industry due to the decrease of in-plane performance observed in the composite parts.

2.2.1.1.3 Stitching

Stitching is a process that uses yarns for bonding dry woven fibres and/or prepregs in order to give them extra though-thickness reinforcement. Some studies demonstrated that the use a small volume fraction of stitching yarns could improve the delamination resistance (in Mode I and II) [73]–[75], impact damage tolerance [76] and dynamic behaviour of structural joins between composite parts [12], [25], [77].

The technique consists in using needles to stitch yarns throughout the thickness of laminates in order to bond and tie by knots their constitutive layers before impregnation or curing. Aramid yarns are usually employed in the process due to the flexibility they present but, in some cases, carbon or glass fibres are used as well [78]. There are three main types of stitches generally used in the industry: lock stitches, modified lock stitches and chain stitches. Modified lock stitches are the most common, because they use knots made on the surface, which minimize damages caused by needle and avoid larges resin rich pockets inside the laminate. Besides these two aspects, other relevant factors that may also affect the in-plane performance of the laminate, are the yarn denier or stitch density [25], [77].

Some studies were already carried out in order to evaluate the through-thickness properties of stitched composites. Solaimurugan et al. [74] studied the Mode I interlaminar fracture toughness of stitched composites with carbon and aramid fibres. They found out that strain energy release, G_I, increased 5-23 times when aramid fibre stitches were used. On other hand, Jain et al. [75], studying mode II interlaminar toughness in CFRP laminates by using aramid fibre stitches, demonstrated that this property could increase up to 4 times in comparison to unstitched ones. Francesconi and Aymerich [79] studied the response to low velocity impact of carbon/epoxied laminates stitched by polyethylene threads. Their work revealed that stitched laminates could reduce damage propagation for impact energies above the threshold value (6 J in this case).

Despite the benefits of stitching on the through-thickness properties of laminate composites, studies made are not also fully conclusive about its effects on in-plane properties, although some of them reported a negative influence and in other cases no alterations or even some improvements were observed. The main reason for this divergence may be attributed to a lack of attention paid to some variables of the stitching process (e.g., stitches tightness) that may affect significantly the mechanical properties of final composites [25], [77].

In fact, three-dimensional physical reinforcements do improve the through-thickness properties of composites, giving them better interlaminar resistance, impact resistance and tolerance and performance. However, their influence on the in-plane properties are unpredictable and not completely well known, in some cases, studies revealed that they may even reduce them, compromising the performance of composites used in advanced applications.

2.2.2 Matrix modification

Matrix brittleness is another key factor that normally contributes to increase the risk of damage in advanced composite laminates, namely, delamination and facture propagation. Thus, improving matrix toughness and, therefore, its energy absorption capabilities, without compromising in-plane mechanical properties, seems to be a valid approach to increase damage resistance and tolerance of advanced composites. However, due to the extreme aggressive environments that usually advanced composited are exposed, they tend to be manufactured using thermosetting resins (e.g., epoxy resins) as matrices, which, typically are much more brittle than other polymers, namely thermoplastics and elastomers. The high brittleness of thermosetting polymers strongly depends on cross-links density present in their structures.

Adding plasticisers to thermosetting matrices and reduce the density of their cross-links are methods that were already used to improve their toughness. However, these modifications may cause an undesired increment of viscosity and/or reduce the resin mechanical, thermo-mechanical and chemical performances. Another way of increasing the matrix toughness is mixing it with particles (Figure 5), however it usually also imply an increment of viscosity and a disadvantageous poor dispersion and resin/particle interaction [10], [11], [17], [80], [81].

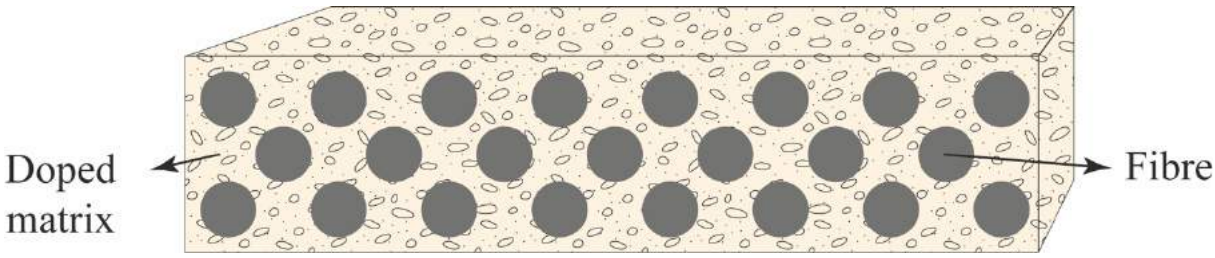

Figure 5: Scheme of matrix modification approach.

The inclusion of particles or liquid solutions of rubber in thermosetting resins has been studied in order to evaluate their effectiveness to improve toughness and through-thickness properties of advanced composite laminates. Scott et al. [82] employed epoxy resins modified with butadiene-acrylonitrile co-polymers (CTBN) as matrices of CFRP composites and verified that they contributed to increase considerably the toughness of laminates. The study revealed an improvement on mode I fracture release energy without compromising in-plane properties. Kim et al. [83] also confirmed a significant improvement in interlaminar fracture toughness (mode I) behaviour of CFRP composites using rubber-modified matrix resins, when compared to those produced with unmodified ones. However, under transversal impact test (Charpy impact test) at ambient temperature or above, CFRF laminates using rubber-modified resin present worse results, compared to unmodified ones. Subsequently, in a posterior study concerning the post-impact mechanical properties of CFRP laminates [57], the same research team concluded that the rubber-modified matrix composites presented improvement up to 80% on delamination fracture energy (mode I) and an increase of 25% of flexural strength and modulus, in comparison to the unmodified matrix ones.

Despite the small decrease of pristine resin modulus, the incorporation of reactive thermoplastic modifiers into epoxy resins also has shown to lead to an increase on their fracture toughness. Typically, the thermoplastic modifiers previously incorporated into the epoxy resin generate a second phase separation during the curing process. He at el. [84] studied the micro-cracking behaviour on epoxy resins modified with poly(ether imide) (PEI), polycarbonate (PC), and poly(butylene terephthalate) (PBT) to produce CFRP composites for cryogenic applications. Using dynamic mechanical analysis (DMA), they found out that all

modified resins had proved to present an increasing in their storage module and a decreasing on the coefficient of thermal expansion, when compared to the unmodified ones. Optical microscopy also revealed that PEI and PC are more effective to improve micro-crack behaviour owing to their low coefficient of thermal expansion and high impact strength.

A better thermoplastic/thermosetting interfacial bonding conjugated with the decrease of the crosslinked of the thermosetting resin leads to a higher toughness [85]. However, despite an increment of thermosetting resin viscosity promoted by the modifiers, during the impregnation process, reinforcement fibres may act as a filter, inducing a pure toughing distribution across the composite part.

The inclusion of polymers with spherical molecular structures was already considered as an alternative to increase the thermosetting resin toughness due to their much moderate viscosity increment. The spherical structure of dendritic hyperbranched polymers (HBP) have shown to cause much less viscosity increase, for almost the same molecular weight increment, when compared to linear polymers. Moreover, being their structural morphology being core-shell type, a large variety of chemical arrangements may be promoted on the shell, enhancing a better bonding to thermosetting resins [10], [80]. Several works [10], [80], [86], [87] revealed significant improvements on toughness of thermosetting resins modified with HBP, with only a slight loss of stiffness. The lower increment of viscosity, in comparison to other matrix modifiers, have shown that HBP are also better suitable to produce advanced composites parts using liquid resin impregnation processing techniques.

The use of thermoplastic homopolymers to modify epoxy resins, depending on the percentage of incorporation, usually leads to undesired increments upon the viscosity due to higher molecular weight of the added polymer [17]. To overcome the problem, some research works have been carried out on the incorporation of copolymers in epoxy resins. Denneulin et al. [88] studied the behaviour under low velocity impact tests of aramid reinforced composite laminates produced from epoxy resins incorporating acrylate based block copolymer additives. It was found that the produced laminates from the modified epoxy resins presented better performance under impact loads due to nanostructures created by the block copolymers.

Recently, the interest from the use of nanoparticles to modify the polymeric matrices, such as exfoliated graphite, metals, silica, carbon black, carbon nanofibers (CNF) and carbon nanotubes (CNT), have also grown due to the improvements (with only a small content) that they could bring to the mechanical, thermal and electrical properties of polymers. However, those improvements are strongly dependent on the interfacial relationship between matrix and filler and degree of dispersion of it [89], [90]. Another benefit that may result from the use of nanoparticles is the low increment on viscosity that they cause on

the matrix in comparison to other microparticles and this advantage makes them more suitable for production of advanced materials by liquid processing techniques [90], [91]. However, it is not already clear if the fibre reinforcements bed acts as a filter for nanoparticles during resin flow [91], [92].

Since their discovery in the 1990s, CNT have been exhaustively studied due to their remarkable mechanical, thermal and electric properties. Godara et al. [93] studied the effect of incorporation of different types of functionalized and non-functionalized CNT in epoxy resins used in the production of prepregs for CFRP composites. They reported a reduction in coefficient of thermal expansion for resins modified by using thin-multi-wall (TMWCNT) and double-wall CNT (DWCNT), and a substantial improvement in ILSS and mode I crack initiation energy of MWCNT–epoxy system with a compatibilizer. Ashrafi et al. [94] also produced prepregs made from an epoxy resin modified by functionalised single-wall CNT (SWCNT). Composites manufactured from those prepregs revealed that the use of only 0,1 wt% of SWCNT enabled the reduction of impact damage area (5 %), higher compression-after impact (CAI) strength (3.5 %) and the increase in mode I and II interlaminar fracture toughness (13 % and 28 %, respectively).

2.2.3 Reinforcements modification

The majority of failures observed in advanced composite materials occur in interface between fibres and matrix. One strategy to improve bonding between these two phases is to apply surface treatments to the fibre surfaces, in order to promote physical or chemical adhesion between them and the matrix. Some examples of surface treatments applied on carbon fibres to improve adhesion to matrix are oxidation treatment, coating and plasma processing methods [9].

Plasma treatment of carbon fibres is an effective method used to improve the bonding characteristics of the surface of fibres to the matrix. It usually brings roughness to the fibre surface and generates polar functions, both contributing to improve the interfacial adhesion and fibre/matrix loading transfer. Studying the effect of oxygen plasma treatment and isobutylene plasma polymerization on carbon fibres, Pittman et al. [95] concluded that the oxygen plasma treatment had increased the interfacial adhesion and interlaminar shear strength of composites without any significant effects on the tensile strength of fibres. The application of electrolyte solutions on the carbon fibres was investigated by Ma et al. [9] as electrochemical surface treatment. Using sulphuric and phosphoric acids, sodium sulphate, sodium phosphate, ammonium bicarbonate as electrolyte solutions, they found out that all of them promoted the physical bonding of the carbon fibres to the matrix.

Recently, the use of the so-called multi-scale composites has been seen as a promising method to improve toughness of composite parts. Incorporation of CNT on reinforcements surface (Figure 6) appeared as an effective technique to overcome problems caused by stress concentration, voids and in-plane misalignments of fibres, that may result from other techniques such 3D woven fabrics, stitching and Z-pinning manufacturing [96]. Using electrophoretic deposition, An et al. coated successfully glass [97] and carbon [98] fibres with CNT. The coated fibres, used to produce composites plates by vacuum assisted resin transfer moulding, have shown an effectively improvement on shear strength and fracture toughness of final laminates. Xu et al. [99] proposed a new method to deposit directly CNT on carbon fibres surface. By using a floating device and the catalyst chemical vapour deposition (FCCVD) method, CNT aerogel is blown out directly from the FCCVD oven to the carbon fibres. Composite plates using those carbon fibres were then produced by hot-pressure moulding, and have shown higher flexural strength (16,04 %) and interlaminate shear strength (21,51 %) than composites produced by uncoated fibres.

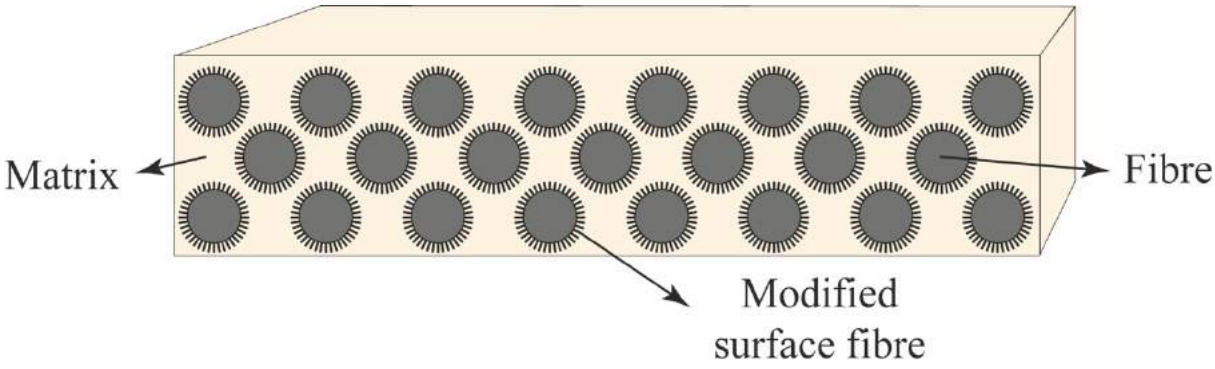

Figure 6: Scheme of reinforcement modification approach.

The coating of carbon nanotubes forests grown direct on carbon fibres surface, using the chemical vapour deposition (CVD), shows up as an effective method to improve the loading transfer mechanisms and avoid problems, such as, agglomerations or uneven dispersion of CNT on the composites [100]. Single fibre testing showed that the presence of vertical aligned carbon nanotubes (VA-CNT) on the carbon fibres surface enhances the interfacial shear strength of composites and that such improvement results, essentially, from the higher interphase adhesion and strength between matrix and fibres promoted by the presence of VA-CNT [101], [102].

In a work carried out by Veedu et al. [100], CNT have been grown by CVD on SiC fibre fabrics that were, then, impregnated with epoxy and cured in autoclave to produce composite laminates. The final 3D hybrid composites produced presented 348 % and 54 % higher values of interlaminar fracture toughness in mode I and II, respectively, than those without CNT. Moreover, in-plane mechanical tests revealed improvements in strength, modulus and toughness, which means that these properties were not affected

by the increasing of the through-thickness properties. Kepple and his co-workers [103] reported as well an increase of 50 % in fracture toughness (Mode I) in composites made from carbon fibres grafted with VA-CNT impregnated by an epoxy resin. Wardle [104] carried out a work to evaluate the performance of hybrid composite architectures using VA-CNT grown by CVD on the surface of microfibers. These hybrid architectures had shown to provide to composites more multifunctionalities and higher interlaminar shear strength. In another work, Wardle reported that the same architectures presented improvements in both initiation and steady-state toughness when submitted to mode I interlaminar fracture tests and, an increase in bearing stiffness, critical and ultimate strengths when submitted to tension-bearing test [105]. He evaluated, also, how the length of VA-CNT grown on carbon fibres surface could influence in mode I fracture toughness by using two different epoxy resins as matrices. The study revealed that the steady-state mode I fracture toughness increases in composites using longer VA-CNT grafted on microfibers, because they create tortuous fracture growing paths, which maximise the crack propagation surface areas, showing more relevance in toughness properties than resin type used in composite production [106].

2.2.4 Interleaf method

It is well know that interlaminar regions of composite laminates play an important role on their mechanical performance, often showing up as common failure place due to their intrinsic brittleness resin-rich zone [107]. The interleaf (or interlayer) technique was introduced and studied as an attempt to improve the response to damage and increase the energy dissipation in these regions of laminates.

The interleaf technique consists in inserting, for instance, films, nonwoven tissues, self-same resin films or other kind of materials or structures, between composite laminate layers (Figure 7) to increase the plastic behaviour and provide higher damage resistance to those regions [14].

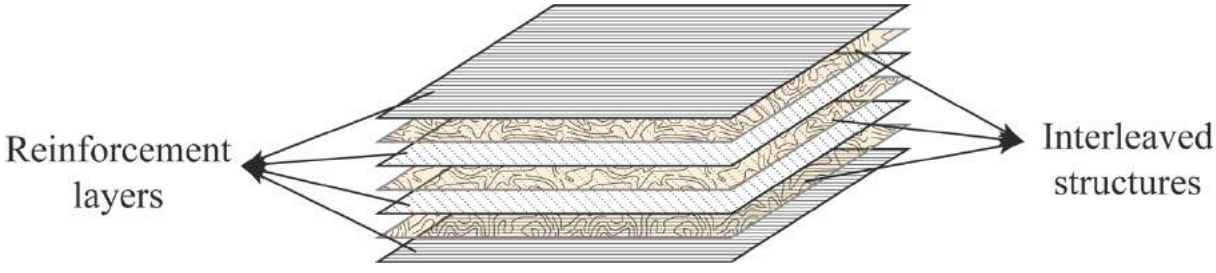

Figure 7: Scheme of interleaving approach.

The use of more ductile resins in interlaminar layers to increase the composite laminates toughness has been used for a long time. In the 1980's a "high-strain resin" employed between the laminate layers had proven to improve the composite compression strength after impact. After this, many types of materials

and structures have been tested as a possible solution to improve damage resistance and tolerance of advanced composite materials [108].

Singh et al. [108] studied carbon-fibres modified-thermosetting matrix prepregs interleaved with self-same resin films in order to study crack mechanisms and toughness in unidirectional composite laminates. Films made of prepregs self-same resin (cyanate ester/epoxy) were placed into the central resin-rich region where the crack would start on mode I and II interlaminar fracture tests. The study revealed an impressive enhancement on composites delamination resistance of 50% and 200% in mode I and mode II, respectively, in comparison to non-interleaved ones. Toughness enhancement observed in both loading configurations was considered related to the constant reorientation of the crack front though the isotropic resin-rich layer.

Interleaved carboxil-terminated butadiene acrylonitrile (CTBN) and polyurethane (PU) modified epoxy resins were used by Jang and Chen [109] for studying the fracture behaviour of carbon/epoxy laminates. By spraying a thin layer of the modified resin on the surface of prepregs, they observed an increase of 40-50 % and 200-300 % in mode I and II fracture toughness, respectively, and an improvement in damage resistance of laminates. They also concluded that as higher was the thickness of the interleaved layer, as higher was the laminate fracture toughness obtained. Cheng et al. [26] studied the application of a polyetherketone with a phenolphthalein side group (amorphous thermoplastic) (PEK-C) to tough carbon fibre laminates. They compared neat bismaleimide resin (BMI) matrix laminates with the following ones: BMI modified by PEK-C matrix (in-situ toughening), BMI interleaved by PEK-C films (ex-situ toughening) and BMI interleaved by BMI/PEK-C blend films with different concentrations (ex-situ toughening). The work revealed that interleaved laminates, when compared to that produced with neat BMI and BMI modified by PEK-C (in-situ) as matrix, had better performance regarding damage resistance and higher compression after impact (CAI) strength, particularly those ones that were interleaved by films composed by PEK-C and BMI.

Yasaee et al. [110] inserted thermoplastic film rings between layers to confine the damage area in low velocity impact and compression after impact (CAI) tests. Using different stack dispositions of polyimide film rings in glass-fibre/epoxy laminates, they restricted and reduced the impact damage area up to 38 % and increased the CAI strength up to 18 %. However, they also observed that some laminates presented worse behaviour due to the important role that fibre orientation plays in impact damage.

CNT were also used as interleaved structures for providing interlaminar toughness to composite laminates. Chen et al. [111] inserted between layers of a carbon/bismaleimide (BMI) composite, polyetherketone with a phenolphthalein side group (PEK-C) neat films and modified with MWCNT, to study

how they work as interleaf tougher structures. Results obtained shown that the interleaved laminates, specially MWCNT modified films, reduced damage area in low velocity impact tests and improve CAI strength up to 33 % when compared to non-interleaved laminates. In other study, Liu et al. [112] incorporated CNT Buckypapers (BP – thin layer of CNT with random orientation) directly into interlaminar region of unidirectional prepreg composites. To investigate interlaminar fracture toughness in mode I and II, they used two different types of BP to interleaf carbon/epoxy laminates: as-prepared CNT BP and cross-linked CNT BP. Cross-linked CNT BP interleaved laminates provided an enhancement in interlaminar fracture toughness of 74 % and 82 %, in mode I and mode II tests, respectively. These improvements in toughening were attributed to the better interfacial bonding between CNT, to bridging mechanisms through a higher fracture surface area and to the extra force needed to pull out CNT from the resin.

Carbon nanofibers (CNF) BP were also studied by Khan et al. [113] to be used as interleaved tougher system in composite laminates. After impregnating CNF BP by epoxy resin, they were pre-cured and interleaved between unidirectional prepreg layers to produce CFRP laminates. Interleaved CNF BP shown to be an efficient tougher structure in interlaminar shear strength (ILSS) tests, improving 31 % shear strength, and 104 % in mode II interlaminar fracture toughness. ILSS improvements were attributed to the increasing of matrix shear properties resulting from the inclusion of CNF and better interfacial CNF/epoxy adhesion. On the other hand, the mode II improvement was associated to the better bridging mechanism, the higher CNF pull out force and the crack deflection.

The incorporation of VA-CNT in the interlaminar region of CFRP laminates was also investigate by Wardle et al. in [96] and [114], [115]. By transplanting VA-CNT grown by CVD to prepregs surface, they create a kind of “nanostitching”. Interlaminar fracture toughness in mode I and II [114], bolt pull out critical strength, open-hole compression ultimate strengths and L-shape laminate energy [96] properties were investigate. VA-CNT provided to the composite specimens an improvement of 150-250 % and 300 % in mode I and mode II fracture toughness, respectively, being also reported improvements of 30 % in bolt pull out critical strength, 14 % in open-hole compression ultimate strength and about 25 % in L-shape laminate energy. The main tougher mechanisms responsible for those improvements were attributed to interleaved layer toughness, plastic deformation and crack bridging.

Recently, Stahl et al. [116] improved 2-3 times the interlaminar fracture toughness in mode I of carbon fibre composites, by interleaving arrays of horizontal aligned CNTs. Forests of multi wall carbon nanotubes grown by CVD were knocked down by a shear mechanical process. The horizontally aligned CNT obtained were then pre-infused by a low viscosity epoxy resin and interleaved between unidirectional carbon fibres

prepregs. The results obtained have shown an increase of interlaminar fracture toughness is, probably, caused by the complex delamination tortuous path created through interlaminar films, crack deflexion to adjacent composite plies and a combination of both effects.

Thin nonwoven tissues, so-called veils, were also used as an interleaf structure to tough composite laminates. Their high permeability allow manufacturing hybrid interleaved composites using liquid resin processing techniques, such as, RTM, vacuum bag infusion, among others [14]. Incorporation of nonwoven carbon fibres between carbon prepregs to produce composite laminates, was first studied by Noguchi et al. [117]. Their initial studies demonstrated that these structures could improve in-plane shear behaviour, although a reduction on static tensile strength was reported. In-plane shear properties improvement was found to be related to the delay of matrix cracking and delamination promoted by nonwoven carbon tissues. Improvements in interlaminar fracture toughness were also reported by the usage of the same interlaminar tougher. In Mode I, interlaminar fracture toughness, an improvement of 28 % was reported in interleaved laminates when compared to non-interleaved ones. The mechanism responsible for these improvement was attributed to the breakage out-of-plane of the short fibres present into interleaved layer [118]. Subsequently, Kuwata et al. studied the effect of using different types of veils in interlaminar fracture toughness Mode I [119] and mode II [120]. In Mode I tests, thermoplastic veils (polyester and polyamide) shown to be more efficient as a tougher system. Debonding between nonwoven fibres and the resin, in addition to the ability of plastic deformation of nonwoven fibres in themselves, shown up as the main tougher mechanisms. However, the adhesion between fibres and resin and the areal density of the fibre reinforcement seem to be important aspects to be considered. Results from interlaminar fracture toughness tests made in mode II were not so conclusive due to complex mechanisms associated to the application of loads, while seems to be more likely that nonwoven tissues architecture and shear resin properties played a much more important role in this case than in Mode I tests. Recently, Sampson et al. [121] studied the effect of nonwoven thermoplastic tissue architectures, namely, polyphenylenesulfide (PPS) and polyetheretherketone (PEEK), in the interlaminar fracture toughness behaviour. No significant differences were observed between PPS and PEEK veils for the same areal density. Although, the study revealed that in Mode I the nonwoven tissues with higher areal density increase interlaminar fracture toughness, moreover, outperform was obtained when veils formed by fibres with low linear density were used. In Mode II, the same dependence of veils areal density and improvement of interlaminar fracture toughness was observed, while no strong relation with linear density of fibres was observed. They reported also, that Mode I and II interlaminar fracture toughness do not

depend from fibres linear density in comparison to veil coverage, so they concluded that both mechanisms depend upon the fraction of crack propagation in the veil uncovered surface.

Interleaving thin veils between plies have already shown to increase interlaminar fracture toughness in Mode I and II, however, there are not yet many studies carried out to demonstrate that their usage may improve damage tolerance caused by impact events. Walker et al. [122] interleaved short fibres of different materials in to each interlaminar region of a CFRP and reported a reduction of the global and local damage of these composites when compared to the non-interleaved ones. Hogg [123] has shown that interleave carbon-polyester veils, increase the impact tolerance of laminates by compression after impact (CAI). Stanley et al. [16] found out that the use of polyamide (PA) veils reduced damage area and increase CAI resistance, although some void spots remained into carbon layers because the high permeability of the veil plies prevented the resin impregnation of less permeable areas. Tanoglo et al. [124], also interleaved PA veils into a CFRP laminate and has shown that those interlaminar structures improved the Charpy impact strength, despite a reduction of in-plane mechanical properties have been reported. García-Rodríguez et al. [27] introduced a low melt temperature 4 g/m^2 weight coPA between all plys and found out that, in some cases, this allowed to increase the CAI strength and reduce low velocity impact damage area in more than 100 %.

Electrospinning technology allows to produce nonwoven thermoplastic nanofibers tissues. Nonwoven nanofibers tissues produced by this process have higher surface bonding area to the matrix and, besides, they allow higher coverage without increase significantly weight and thickness [15]. Several studies of electrospun nonwoven tissues applied in structural composites can be found in literature, many of them have reported the effective enhancement of composite interlaminar toughness. Beckermann and Pickering [125] studied the effect of a range of different polymeric electrospun nonwoven tissues with various areal weight and fibre diameters in mode I and II interlaminar fracture toughness. The study showed that 4,5 g/m2 polyamide 6'6 (PA66) nonwoven tissue seemed to be the best option, when comparted to the others polymeric nonwoven tissues tested, presenting an improvement of 156 % and 69 % of interlaminar fracture toughness in mode I and II, respectively. According to the authors, areal weight has influence in mode I interlaminar fracture toughness, increasing this property until a maximum of 4,5 g/m2 and G_{Ic} tends to stabilise above this value of areal weight. In mode II, the influence of areal weight seems to be similar as in mode I at the beginning, but G_{IIc} presented a slight decrease after the 4,5 g/m2 areal weight. However, they didn't find any influence of fibre diameter in studied properties. Van der Heijden et al. [126], interleaved electrospun polycaprolactone (PCL) nanofibers on glass fibre/epoxy composites produced by VARTM. The study showed that the number of nanofibers and the

way they are placed between layers can influence mode I interlaminar fracture toughness. Composites containing 20 g/m2 of PCL nanofibers directly electrospun over the both sides of glass fibre tissue surfaces before impregnation, improve almost 100 % mode I fracture toughness. Moreover, PCL nanofibers seemed to not influence the impregnation process, and neither tensile nor dynamic composite mechanical properties.

Only a few studies may be found in literature regarding low velocity impact response of composites laminates interleaved with electropun nonwoven tissues, however, some of them have reported a suitability of these interlaminar reinforcement structures by the reduction of damage area, delay of damage initiation, increment of peak load and energy absorption, when compared to their non-interleaved peers [127]–[129].

Lately, the usage of emergent technologies, as additive manufacturing, more than a trend, have been seen as a powerful alternative to improve interlaminar properties in composite materials. Taking advantage of the degree of freedom to create new designs and the wide range of different materials that additive manufacturing (3D-printing) allows, such interlaminar toughening structures may be optimized depending on adjacent plies orientation, aiming a better damage resistance and tolerance.

Only few works may be found in literature exploring the potential of 3D-printing to improve interlaminar damage resistance. Islam and Prabhakar [130] have shown that 3D-printed polylactic acid (PLA) line over the prepreg surface may improve multidirectional composite laminates interlaminar shear strength (ILSS) up to 28 %. Szebényi et al [131] have printed a poly(ε-caprolactone) (PCL) pattern over dry carbon before being hand ley-up impregnated by an epoxied resin. The final composite has shown a higher ductility under flexural tests, however no relevant improvements were observed regarding the absorbed energy under Charpy impact tests. Recently, Damodaran et al [132], demonstrated that the spacing between PLA lines directly printed over carbon/epoxy prepregs, plays an important role on the interlaminar Mode-II fracture toughness. The experimental tests revealed, the smaller the spacing between 3D-printed lines, the higher the energy release rate. An improvement of 76 % was achieved in Mode-II fracture toughness due to the wavelike crack path formed between carbon layers.

2.2.5 Bioinspired Composite Structures

In the last decades, biological structures have been seen as a potential inspiration to mitigate impact damage on synthetic advanced composites. A close insight on shells [133][134] , bones [135][136] and crustacean exoskeletons [137]–[139] microstructures have revealed several physical and morphological aspects that strongly influence their outstanding damage resistance.

Owing to its structural similarity with conventional synthetic laminate composites, a periodic micro-scale fibrous twisted arrangement, so called Bouligand arrangement [29], that may be found in a large range of animal species as beetles [140], fishes [141] and crustaceous [137][138], has shown an impressive fracture resistance under impact conditions. These laminate structures are composed by unidirectional chitin-fibrous layers stacked each other with a small rotation angle between them completing a 180° helical rotation over the staking plane perpendicular axis (Figure 8). In the particular case of mantis shrimps (Odontodactylus *Scyllarus*, Figure 8), this Bouligand-like structure can be found in their dactyl club that they use as a hammer to strike and smash their shelled preys [137][142]. Despite the high energy and stresses generated in each dactyl club during the impact, they are able to dissipate them without develop catastrophic damages. Regarding this impressive structural behaviour, studies by Weaver et al. [142] and Yaraghi et al. [139] identify on dactyl club two main regions composed by Bouligand-like structures, namely, the periodic and the impact region (Figure 8). The first is composed by several planar Bouligand unites staked each other across its thickness [142], whereas, in the impact region, those structures are stacked in a herringbone way (waveform), creating also a though-the-thickness fibrous reinforcement [139]. The transition between both regions has shown to be smooth and progressive, from a flat stacking architecture (periodic region) to a well-defined herringbone pattern where the amplitude to wavelength ratio increase gradually throughout impact region thickness up to the surface. This soft transition is accompanied by a gradual variation in Young's modulus, avowing a drastic change of material mechanical properties and a hypothetical catastrophic failure between both regions [139].

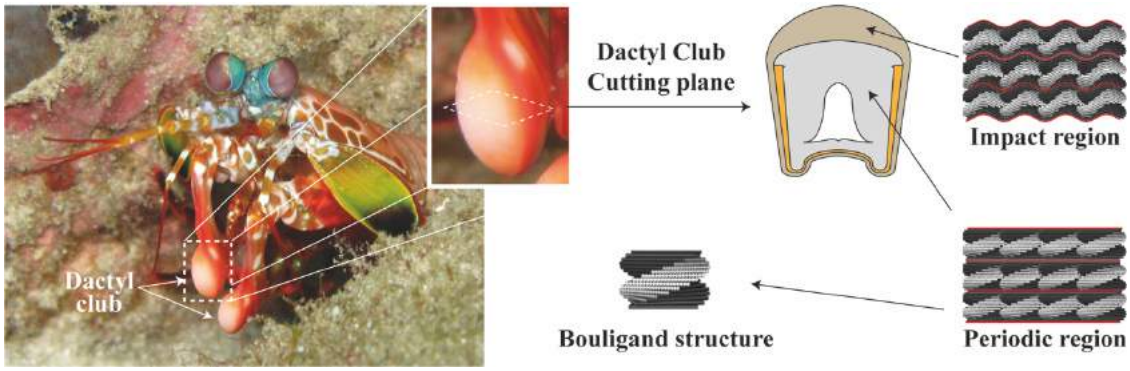

Figure 8: Picture of Odontodactylus Scyllarus [143] and a schematic representation of: dactyl club cutting plane, impact and periodic region and Bouligand-like structure.

Inspired by this outstanding performance under out-of-plane loading conditions, several authors have been mimicked Bouligand laminated structures to evaluate their suitability on carbon, aramid and glass laminate composites [30]–[34], [144]–[153]. Most of those studies compared conventional laminate composites with Bouligand-like arrangements and revealed that helical composite layups may improve fracture and delamination resistance, reduce fibre failure and increase load bearing capability peak load

under out-of-plane solicitations. Liu and his co-workers carried out several plate bending experiments over Bouligand-like layups with different arrangements and materials [30][31][150][151]. Besides demonstrate that in most of the cases, those structures were able to perform better than their quasi-isotropic and cross-ply correspondents under out-of-plane quasi-static loading conditions, they also conclude that optimal inter-ply angle depends on play thickness [150] and matrix/fibre properties [151]. Despite these promising outcomes, only few studies evaluated the suitability of those bioinspired arrangements under low velocity impact (LVI) conditions. Pinto et al. [148] used standard carbon/epoxy prepregs to manufacture 15° inter-ply Bouligand-like laminates and compare its LVI performance to a similar quasi-isotropic (QI) layup. Under 30 J impact energy, those bioinspired composites have shown higher load bearing capability, however a slight reduction on absorbed energy has been reported. Mencattelli and Pinho [32] explored the influence of Bouligand-layup pitch angle under 12 J LVI solicitations. Using ultra-thin carbon/epoxy prepregs they were able to investigate a large range of different configurations between 2.5° and 45° inter-ply angles. The results have demonstrated that small pitch angles (2.5°) led to higher load bearing capability and small internal damage areas, despite presenting less energy absorption ability when compared to those with larger inter-ply angle laminates.

Even though these studies have revealed some promising insights about these bioinspired structures under LVI conditions, some others have reported large delaminations of those Bouligand-like layup arrangements comparatively to their conventional peers [146][149]. This indicates that, contrary to what would be expected, sometimes, crack prefers to spread throughout the interlaminar region rather than across the thickness. Therefore, it seems that the interlaminar medium plays an important rule on the expected structural response of those architectures under LVI conditions.

Recently, Mencattelli and Pinho [34] carried out a study about synthetic (carbon/epoxy) Herringbone-Bouligand laminates under quasi-static plate bending conditions. The results have demonstrated that this three-dimensional Bouligand-like arrangement can reduce internal damages (fibre breakage, delaminations and matrix cracking), improve load bearing capability and total dissipated energy, when compared to a classical Bouligand-like laminate with the same interlaminar pitch angle.

Chapter 3
Procedures

In this chapter will be described the main raw materials, manufacturing process and the major experimental techniques used to characterise laminates and their constituents.

3.1 Materials

The baseline materials used to manufacture advanced composites are: an epoxy resin and unidirectional carbon fibres. In this section, a general description of those materials will be made, and a brief introduced of selected grades will be presented.

3.1.1 Epoxide Resin

Epoxy resins are the most common matrix system of advanced composite materials. The epoxide group, composed by a ring of three atoms, one oxygen and two carbon, is usually modified in order to improve crosslinking reaction. This modified neat resin (epichlorohydrin) is then mixed with hardeners, usually aliphatic and aromatic amines or polyamides, to make most of the epoxies. Depending on the hardener used, a large range of epoxies may be obtained with different viscosities and final characteristics. Typically, these resins are characterised by their outstanding chemical, wear and mechanical resistance, no volatile release during cure process, low shrinkage and moisture absorption and also high adhesion to fibres [2][39].

In this work, a low viscosity (610 mPa.s) bicomponent epoxy was used as a matrix system in all manufactured composites. Specifically designed from Sika® for infusion process, Biresin® CR83, allows a good impregnation, especially of carbon fibre reinforced composites. Three different hardeners offer a large range of processing times, in this case we use CH83-6, with allows a processing window of approximately 2.5 hours. Both components were mixed in a proportion of 70 % of CR83 neat resin and 30 % of CH83-6 hardener.

A photography of both component containers, neat resin CR83 and hardener CH83-6, is presented in Figure 9 a) and b), respectively.

Figure 9: Containers of a) neat resin CR83 and b) hardener CH83-6.

Additional information of CR83 neat resin and CH83-6 hardener may be consulted in material datasheets in Appendix A.

3.1.2 Carbon Fibres

Carbon fibres are high performance fibres composed by sheets of hexagonal rings of carbon (graphite) orientated on fibre direction. They may be made from three main types of precursors (raw materials), cellulose, pitch or polyacrylonitrile (PAN). However, pitch and PAN are the most commons [39]. Pitch carbon fibres own lower mechanical properties than the ones produced from PAN, however they claim economic advantages. PAN carbon fibre possesses both high tensile strength vs weight and high tensile modulus vs weight ratios, low linear thermal expansion coefficient and high thermal and electrical conductivity. All those features make them extremely attractive in high demanding application fields, as aeronautic and aerospace [39][40].

In this work, all laminates were produced using as a main reinforcement a 150 g/m^2 unidirectional carbon fibre (UDCF) fabric (Dynanotex HS 24/150 DLN2) from G. ANGELONI s.r.l.. According to the provider, Dynanotex are unidirectional carbon fibres tissues manufacturing system that consists of two layers of PAN carbon fibres (Grafil 24K 1600 dtex) from Mitsubishi, perfectly aligned and bonded together by a central polyester fibre weft thread with resin compatible adhesive. Therefore, the final UDCF tissue is composed by 98 % of carbon fibres and only 2 % of weft threads, which combined represent 93 % of the tissue nominal mass and the remaining 7 % of adhesive.

A schematic representation of Dynanotex HS 24/150 DLN2 UDCF tissue may be observed in Figure 10.

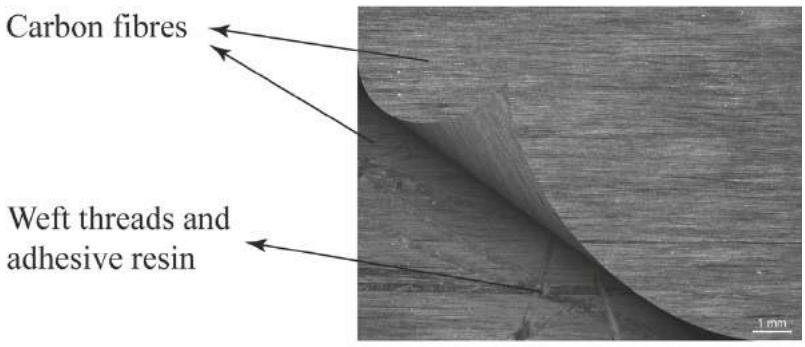

Figure 10: Schematic representation of Dynanotex HS 24/150 DLN2 UDCF tissue.

Additional information of Dynanotex HS 24/150 DLN2 UDCF tissue and Grafil 24K 1600 dtex PAN carbon fibre may be consulted in material datasheets in Appendix A.

3.2 Composites Manufacturing

The manufacturing process selected to produce advanced composites was vacuum bag infusion. In this section this manufacturing process will be introduced, and the implementation procedures described.

3.2.1 Vacuum Bag Infusion

Vacuum bag infusion is a liquid resin process using only a half rigid side of the mould (made of metal, FRP material or glass). The other side is flexible and usually consists in a polymeric film. This particularity makes the process cheaper than RTM. Parts processed by vacuum bag infusion usually present very good mechanical properties and low manufacturing cost, making this process attractive to high performance applications [2][45]–[48].

The setup preparation starts by covering the surface of rigid mould part with a thin layer of a release agent, afterwards a removal fabric layer (peel-ply) may be necessary to facilitate demoulding and improve resin flow. The fibre reinforcements are laid down sequentially and according the desired orientation over those tow releasing layers and the covered by two more removal layers, namely peel-ply and flow-mesh. The first one, peel ply, is placed just over all dry reinforcements to ensure roughness on the surface in order to improve future bonding of the part [47][49][50], whereas the second one, flow-mesh, is placed over the top peel-ply layer to work as an easier path for the resin flow and ensure better and faster impregnation. Afterwards, a resin flow pipe system, equipped with an inlet and outlet valves, is strategically installed in order to ensure a balanced impregnation. The whole set is then bagged by a thermoplastic film and sealed using a sealant tape. The resin inlet is connected to a chamber containing catalysed resin, and the outlets are linked to a resin trap that has direct connection to the vacuum pump. The resin is forced to flow throughout the pipe system and then the reinforcements by pressure differential [2]. The flexible mould side forces resin through-the-thickness of reinforcements, yielding a three-dimensional flow, improving the impregnation [47][46]. When the resin starts to drop into resin trap the mould is fulfilled and the inlet valve is closed. Catalysed resin should be able to keep its low viscosity during the impregnation process to fulfil the part and promote good bonding between fibres and matrix, avoiding dry spots or voids [2]. To avoid reproducibility problems, the vacuum infusion process must be, as much as possible, efficiently automated and, whenever possible, jigs should be also employed to ensure the accurately cutting and assembling of the fibre reinforcing preform layers to be used. To ensure an adequate mould filling (resin flow), required thickness and uniform compaction pressure on the preform inside the bag, it is strongly recommended to use an available processing simulation software

(e.g., PAM-RTM, Polyworx, etc.) before manufacture the final composite to help optimising overall processing parameters.

In comparison to autoclave processing, which still is one of the mostly used moulding techniques employed to manufacture advanced composite parts, vacuum infusion presents, at least, the following major advantages: much lower cost of raw-materials, tools, equipment and infrastructure, much larger possibility of raw-materials choice (almost all types of thermosetting resins, reinforcing fibres and their numerous fabrics, i.e. woven, stitched, knitted, braided or random) and much higher ability for the production much larger composite parts. However, in respect to the previous processing method the following major drawbacks are also usually appointed to vacuum infusion: need of using low viscosity resins, more difficulty in ensuring so low void content levels, impossibility of using honeycomb cores in laminates, minor accuracy in ensuring the right orientation and content of fibre reinforcements when compared to the use of high precision prepregs and the requirement of subjecting many manufactured parts to post-cure procedures.

Anyway, it may be claimed that vacuum bag infusion, despite its low production rate, allows producing advanced structural composite parts of almost any size presenting low void content and release of volatiles and also high fibre volume contents and mechanical properties [45]–[48].

In this work, all laminates were manufactured by vacuum bag infusion at room temperature. A schematic illustration of manufacturing setup may be seen in Figure 11.

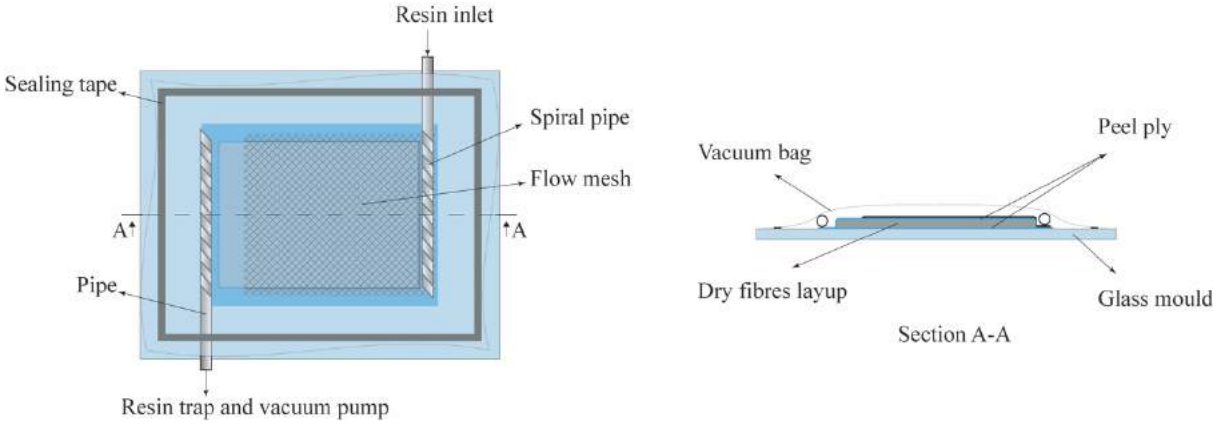

Figure 11: Vacuum bag infusion schematic representation.

All reinforcement layers were first cut according to the desired orientation in a laser cutting machine and then carefully stack up manually over a flat glass mould. The whole setup was then vacuum bagged at approximately -995 mbar (relative to room air pressure) and dry tissues allowed to compact during 1 hour before being impregnated with the epoxy resin. After weight, both components of epoxy resin were

manually mixed and degassed in a vacuum chamber during approximately 20 minutes before impregnation. Once the resin starts to drop into resin trap, setup pressure was increased to -400 mbar in order to stabilise thickness and avoid over degassing that could lead to voids formation inside the composite. Finally, the resin was allowed to cure for 48 hours and then submitted to a post-cure into an oven at 70 °C for 8 hours.

Photographs of the main manufacturing steps are presented in Figure 12.

The final composite plate was then cut using a circular cutting table and carefully polished to ensure the dimensions required from each standard test preformed.

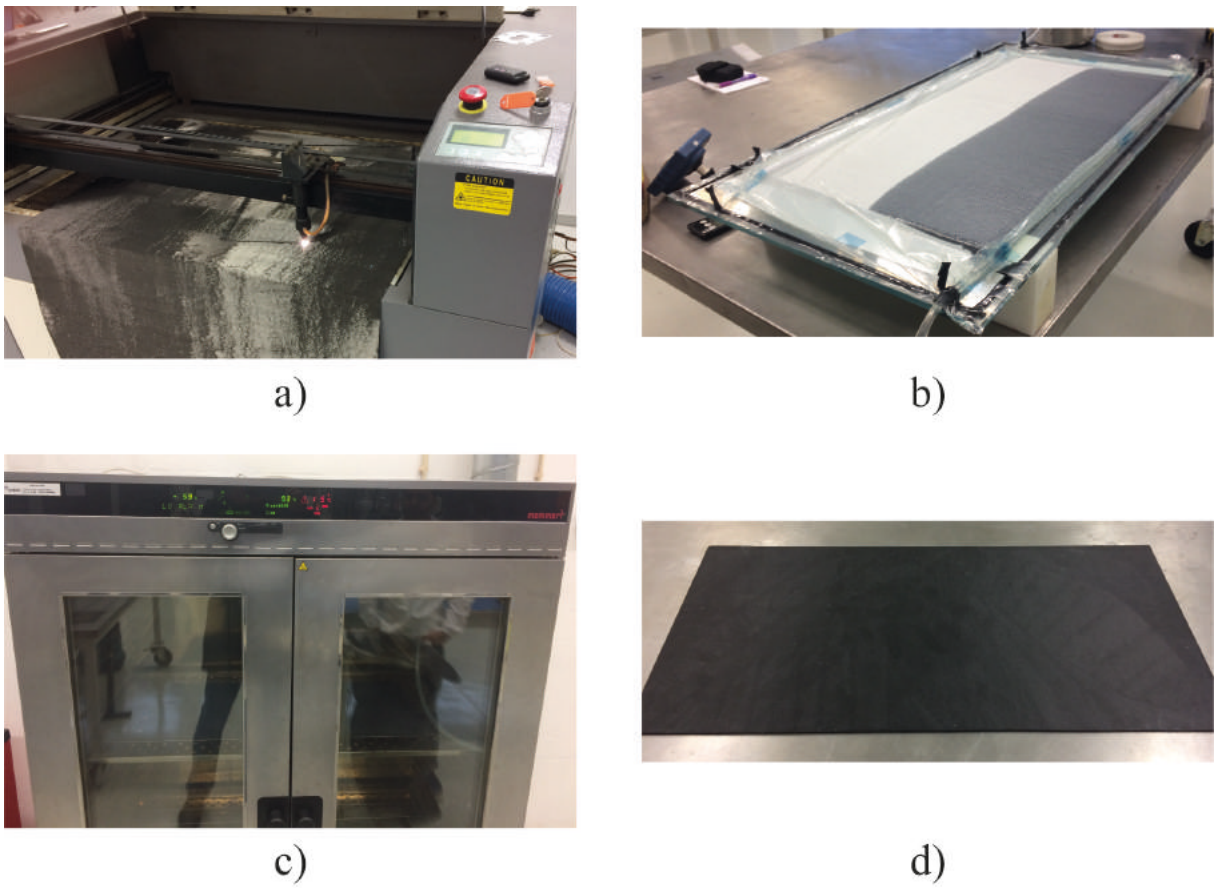

Figure 12: Photographs of the main manufacturing steps, namely a) fibres laser cutting, b) ongoing vacuum bag infusion fibres impregnation, c) composite laminate post-cure and d) final composite laminate plate.

3.3 Characterization Techniques

Depending on the approach studied during this work, different characterization techniques of materials and laminates were used. Therefore, for the sake of clarity, materials physical properties, as specific mass, areal weight and micro structural analyses, as well as laminates' fibre volume fraction and morphology, will be described in more in chapters where they come along.

3.4 Mechanical Tests

Since the focus of this work is to propose, to evaluate and to compare different approaches and strategies to mitigate damage in advanced composite materials, special attention was given to mechanical experimental tests. In this section are described the five different standard tests performed along this work, namely tensile, tree-point bending (3-PB), interlaminar shear strength (ILSS), low velocity impact (LVI) and compression after impact (CAI) tests.

3.4.1 Tensile test

Tensile tests are, certainly, one of the most important mechanical experiments in structural composites, as is the case of advanced composites. This experimental procedure consists in apply a longitudinal controlled loading to a rectangular material specimen. The main objective of this tests is determinate several important properties of a given materials, such as stiffness, or Young's modulus (E), ultimate stress (σ) and Poisson's ratio (ν), so-called engineering constants. The experiment is usually conducted in a universal testing machine equipped with two grips, where the specimen is fixed and pulled, and an acquisition data system which records the force and displacement applied to the grips [1].

Considering the high stiffness and intrinsic anisotropy of advanced composites, it is recommended the usage of strain-gauges or extensometers in order to avoid undesired measurements related to specimen slippage on the testing machine grips. Moreover, the usage of tabs on the specimen is also encouraged, they allow to avoid damages and stress concentrations caused by the grips [1].

For logistic, timing and economic reasons, tensile tests were only performed in two circumstances along this work, namely, to assess lamina engineering constants (Chapter 4) and compare bioinspired laminates to conventional reference one (Chapter 5).

All tensile tests were performed according to ASTM D3039 standard procedures. Depending on the laminate, two different testing machines were used, however, strain gauges or clip-on extensometers, and glass/epoxy tabs were used in all performed experiments. All specimens were cut from the respective laminate plate using a circular cutting machine and tabs were attached to them using a high performance two-parts adhesive (EA 9394 AERO), from Loctite®, following datasheet procedures that may be seen in Appendix A. End tabs were placed in both specimen surfaces using jigs to ensure their correct location (Figure 13).

Details about testing machine and apparatus, and engineering constants determination will be given as tensile tests come along in the following chapters.

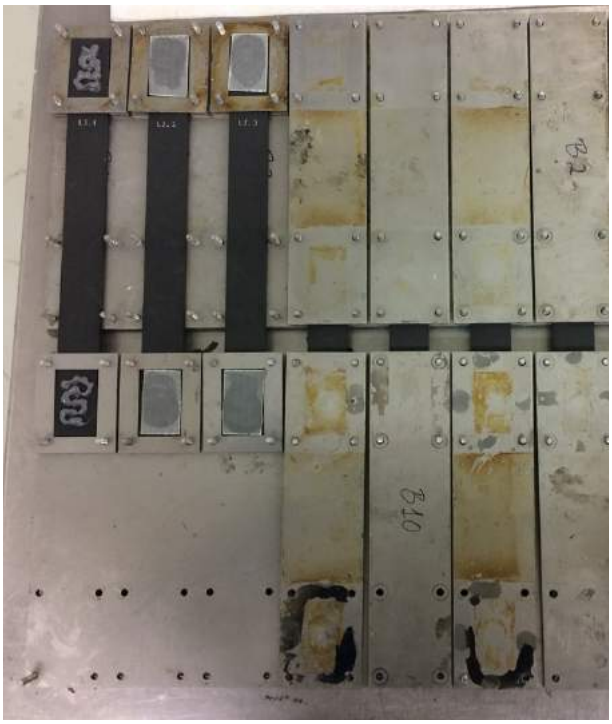

Figure 13: Tabs attachment on tensile specimens.

3.4.2 Three-point bending (3-PB) test

Flexural tests are very common in composite materials due to their simplicity and no instrumentation requirements, however they are only useful for comparison ends and quality control, since non engineering constant may obtain by them for design proposals. Those tests are usually conducted in a universal testing machine equipped by acquisition data system, two cylindric supports and one or two loading noses, depending if the test is a three- or four-point bending test, respectively. A rectangular shape specimen is placed on the supports separated with a span that depends on specimen's thickness to ensure pure bending, while an out-of-plane loading is applied by the nose(s). From the measurements recorded by the acquisition data system of nose force and displacement, may be obtain the flexural modulus ($E_{flex.}$) and outer face maximum stress ($\sigma_{out.surf.}$) of the material [1].

In this work, three-point bending tests were conducted to all studied configurations in accordance with ASTM D7264 standard, procedure A. Tests were conducted on a SHIMADZU® AG-X universal testing machine (Figure 14 a)) with a loading cell of 50 kN at a testing speed of 1 mm/min.

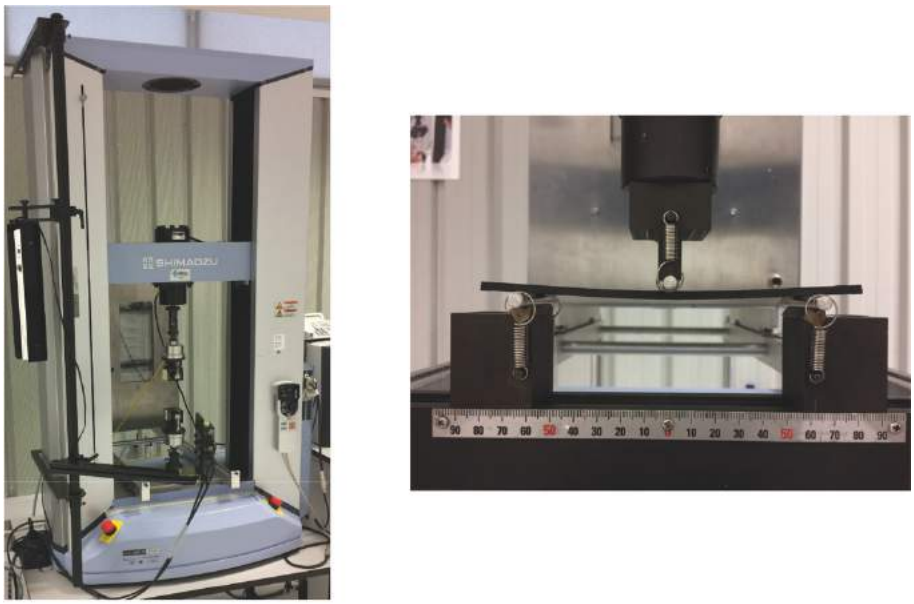

Figure 14: Photographs of a) Universal testing machine SHIMADZU® AG-X with a loading cell of 50 kN and b) 3-PB apparatus.

A set of five 170 x 13 (mm) specimens of each configuration were cut from the composite plate using a circular cutting machine and tested. Specimens were placed on the supports with the 0° plies oriented perpendicularly to loading nose, and a support span of 32 times specimen's thickness (Figure 14 b)). From the force and displacement results obtained by the acquisition data system, outer surface stress ($\sigma_{out.surf.}$) in (MPa) and strain (ε) were calculated for each specimen, according equation (1 and 2) respectively.

$$\sigma_{out.surf.} = \frac{3PL}{2bh^2} \quad (1)$$

Where P is the force (N), L the support span (mm) and b and h are the specimen width and thickness (mm), respectively.

$$\varepsilon = \frac{6\delta h}{L^2} \quad (2)$$

Where δ is the mid-plane deflection in (mm).

Subsequentially, flexural modulus ($E_{flex.}$), in GPa, was calculated between 0.001 and 0.003 strain range following equation (3).

$$E_{flex.} = \frac{L^3 m}{4bh^3} \quad (3)$$

Finally, laminates failure mode was analysed and compared each other using a digital magnifier Leica DMS1000 (Figure 15).

Figure 15: Digital magnifier Leica DMS1000.

3.4.3 Interlaminar shear strength (ILSS) test

The laminar structure of advanced composite materials is one of the most important failure factures on these materials, therefore, the evaluation of interlaminar resistance may give an insight of laminate's global resistance to delamination. Similar to 3-PB tests, interlaminar shear strength (ILSS) experiments do not provide any engineering constants for composite designers, however, may be useful to compare different laminates.

The most common method to evaluate ILSS composite response is short-beam shear test. This experimental procedure become popular due to its simplicity. Test requirements and apparatus is very similar to 3-PB described in section 3.4.2.. A short rectangular composite beam is supported by two supports, and an out-of-plane load is applied by a loading nose. The distance between supports should be appropriated to ensure a specimen response dominated by shear stresses [154].

Interlaminar shear strength of all composites proposed in this work were performed using the short-beam shear test, in accordance with ISO 14130 standard. The results allow to evaluate and compare strength and failure mode among different laminates. All experiments were performed using a 50 kN SHIMADZU®AG-X universal testing machine (Figure 14 a)) at a loading speed of 1 mm/min. Specimens

directly cut from the laminate plate by a circular cutting machine, with dimensions of 40 × 20 (mm), oriented with the 0° plies perpendicularly to the loading nose, were used in this tests according to the standard recommendations, with a support span of 5 times the specimen's thickness.

The apparent interlaminar shear strength (τ_{13}) in MPa of each specimen was calculated from the obtained data, as:

$$\tau_{13} = \frac{3}{4} \times \frac{P}{bh} \tag{4}$$

where, P, b, and h are the maximum applied force (N) and the specimen width and thickness in mm, respectively.

Furthermore, the failure mode of each configuration was analysed under a Leica DMS1000 digital magnifier (Figure 15), and then compared each other.

3.4.4 Drop weight impact test

Advanced composites are very sensitive to out-of-plane loading conditions. A particular case of this kind of solicitations is an impact event. Generically, impacts may be classified in two main categories, low and high velocity impacts. Both may lead to a catastrophic failure of a composite part, however, while high velocity impacts, usually, left behind well visible damages, low velocity impacts are typically barely visible, especially, on the impact surface. According several authors [155]–[157], low velocity impacts are those loadings that occur up to 10 m/s. Such events are unpredictable and normally are related to tool-dropping during maintenance routines or finishing processes, or even in service, for instance bird-strikes in aeronautic industry.

Advanced composites are typically brittle and composed by a laminar structure. Under an impact event, they tend to dissipate the input energy elastically and in damage mechanisms, such matrix cracking, delamination and fibre breakage. Therefore, it is important evaluate how they can resist to damage caused by low velocity impacts.

Attending to these aspects, drop weight impact test is the most common experimental procedure to evaluate low velocity impact resistance in advanced composites. The test is performed in a drop weight tour machine connected to a high-speed acquisition data system. The specimen is attached to a fixture base, under an impactor instrumented with a piezoelectric sensor. Adjusting the impactor mass and its distance to the specimen, the impact energy may be properly set. During the impact, time and impactor force are recorded by the acquisition data system.

In this work, a drop weight impact testing machine "Fractovis Plus", connected to an DAS 1600 acquisition data system (Figure 16 a) and b), respectively), both from Ceast, and equipped with an anti-rebounding system, was used to perform the LVI tests in all laminates. A 20 mm diameter hemispherical steel sticker impactor with a total drop mass of 5.045 kg was used in the impact tests made at the energy levels of 13.5, 25 and 40 (J).

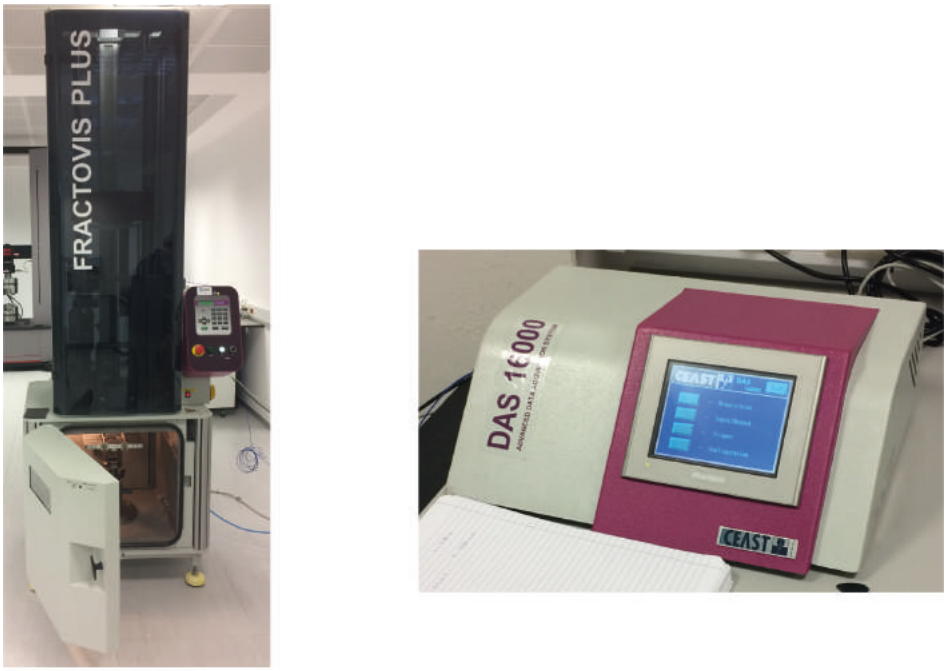

a) b)

Figure 16: Photography of a) "Fractovis Plus" drop weight impact testing machine and b) DAS 1600 acquisition data used to preform LVI tests.

Different energy levels (E_{impact}) were obtained by carefully adjusting the impactor height to the specimen upper impact surface, which was determined using the following equation:

$$h = \frac{E_{impact}}{mg} \tag{5}$$

where m, g and h are the impactor mass (kg), the gravity acceleration (9.807 m/s^2) and the impactor height (m), respectively.

Specimens previously cut from the composite plate by a circular cutting machine, with 150 mm of length and 100 mm of width, in accordance with ASTM D7136/D7136M standards, were held to a support steel plate by the means of four clamps with rubber tips. This supporting plate exhibits a 125x75 (mm) cut-out at its centre, which by staying below the specimen allows exposing it to the impact.

The three LVI test conditions are resumed in Table 1.

Table 1: LVI test conditions resume.

Impact Energy level	Impactor		
	Velocity at the impact instant	Height	Weight
	m/s	m	kg
13.5	2.314	0.273	5.045
25	3.147	0.505	5.045
40	3.986	0.810	5.045

The load and time were recorded by the equipment software during each impact test. Admitting a perfect contact between the impactor and the specimen, the support plate and the specimen, the specimen and clamps and by considering that kinetic energy (*KE*) equals the previously selected impact energy test level, the initial velocity of the impactor at the moment of impact (v_i) can be calculated at moment of impact from the following equation:

$$KE = \frac{1}{2} \times m{v_i}^2 \tag{6}$$

where m is the total drop mass (kg) and v_i is the initial impactor velocity (m/s).

Furthermore, during the impact, impactor velocity can be calculated at any time t (s) by using the numerical integration of the force versus time stated by the equation:

$$v(t) = v_i + gt - \int_o^t \frac{F(t)}{m} dt \tag{7}$$

where $v(t)$ is the impactor velocity (m/s) at time t (s), g the gravitational acceleration (m/s^2) and $F(t)$ the load (N) measured at the same instant t.

The impactor displacement at a given instant ($\delta(t)$), in m, may be calculated by:

$$\delta(t) = \delta_i + v_i t + \frac{gt^2}{2} - \int_0^t \left(\int_0^t \frac{F(t)}{m} dt \right) dt \tag{8}$$

where δ_i corresponds to the initial displacement in m.

Finally, the energy absorbed ($E_a(t)$) in J, by the specimen at each instant, is determined by:

$$E_a(t) = E_{a\,i-1} + \frac{m(v_i^2 - v(t)^2)}{2} \quad (9)$$

It's well-known that the impact response depends on many factors, such as, the laminate architecture, specimen dimensions and material, impactor geometry and impact energy, being just only expected that identical specimens present similar behaviour when submitted to the same impact testing conditions. Therefore, a typical response of a given laminate during an LVI event, begins to present a roughly linear increase of the contact load, which suggests that along this stage only subcritical damages, as matrix cracking and small delaminations, occurred inside the laminate and the impact energy was absorbed, mostly, from the specimen elastic deformation. After this stage, if there is enough energy on the impactor, it may be observed a severe load drop, which indicates a loss of stiffness by the specimen, usually related with severe damage, as extensive delaminations and fibre breakage inside or even on its back-side surface. Those critical damages work as energy release mechanisms, since the specimen elastic bending capability was exceeded. From now on, this point will be denominated by the critical point, and the contact load and absorbed energy up to it, as critical load (P_{cr}) and critical energy (E_{cr}), respectively. After this critical point, load may increase, typically, pointed by several severe oscillations and may reach a new maximum. This characteristic behaviour, designated by propagation stage, is related to new severe damages formation and last until all the impactor energy is dissipated, which coincides with the maximum displacement (δ_{max}). Finally, once dissipated all impactor energy, a rebounding stage takes place which is characterised by a progressive load reduction up to zero accompanied by a smooth displacement reduction. It is assumed that during this stage no new damages are formed and, all the energy restored to the impactor is result of the potential elastic energy stored on the specimen.

Therefore, the typical mechanical response to a LVI test may be graphically analysed in two different forms, according the simultaneous interpretation of the contact load and energy absorption history, as it is schematised in Figure 17 a), and by the contact load vs displacement curve, as may be seen in Figure 17 b).

From Figure 17 a) it can be more explicit to analyse contact load and energy absorption evolution along the test and directly obtain their values in a specific instant of time, namely, peak and critical (P_{cr}) load and maximum (E_{max}) and final (E_{abs}) energy absorption. Additionally, by the simultaneous analyse of contact load and energy absorption histories, it is possible to determine the critical energy E_{cr}, since it is the energy absorbed by the specimen at same instant, when P_{cr} occurs (graphically illustrated in Figure 17 a) by a dotted vertical over contact load and energy absorption history curves). Moreover, energy absorption history may be also useful to obtain the characteristic rebounding and propagation energy, by the

difference between E_{max} and E_{abs}, in the first case, and the difference between E_{max} and E_{cr} in the second one.

In Figure 17 b) is depicted the same previous example in form of contact load vs displacement. From this graphic representation it is also possible to obtain the characteristic load bearing capability (peak load) and critical load (P_{cr}) and the displacement where they occur, δ_{max} and δ_{cr}, respectively. However, despite it is known that the dark and light grey areas are the final absorbed (E_{abs}) and the rebounding ($E_{rebound}$) energy, respectively, and, consequently, the sum of both is the maximum absorbed energy (E_{max}), is not that explicit to obtain from the graph their exact values. On the other hand, this data representation may give us a direct analyses of specimen mechanic response in terms of stiffness.

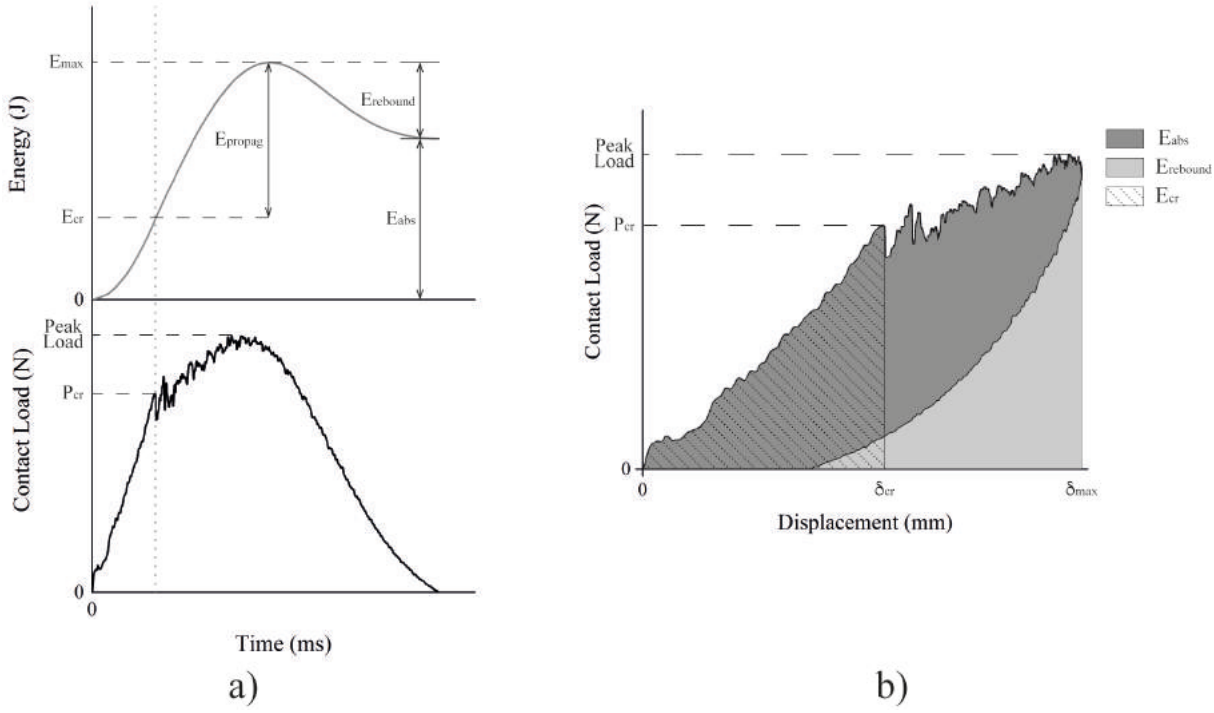

Figure 17: Typical LVI a) contact load and energy absorption history and b) contact load vs displacement curve.

3.4.5 Compression after impact (CAI) tests

Advanced composites impact damage resistance evaluation is a very important aspect to understand how much damaged a laminate may be when submitted to a given impact. However, as it well known, under low velocity impact events, damage on these materials are often barely visible, therefore, it is imperative evaluate how much such damage may affect the composite performance, in other words, how tolerant it is to damage. Compressive strength is, perhaps, the most dangerous solicitation on a damaged laminate. The structural instability caused by delaminations can easily lead to its catastrophic failure [22].

Therefore, the most common experimental test to evaluate composites impact damage tolerance is compression after impact (CAI).

This test consists in a compressing a pot-impact specimen that is placed in a fixture of a universal testing machine, and the compressing force and displacement are recorded by an acquisition data system.

In this work, due to logistic issues, impact damage tolerance was only evaluated in some proposed laminate configurations, namely, bioinspired (Chapter 5) and some strategically interleaved laminates (Chapter 6).

All CAI tests were conducted at INEGI – Instituto de Ciência e Inovação em Engenharia Mecânica, Porto, using an electromechanical universal testing machine Instron®, Model 5900R, with a 200 kN load cell at a loading speed of 1 mm/min, following ASTM D7137 standard procedures.

A photography of test apparatus may be seen in Figure 18.

Figure 18: CAI test apparatus.

Tested specimens were previously measured and their ultimate strength F_{CAI} (MPa) was computed from the following equation.

$$F_{CAI} = \frac{P_{max}}{h \cdot b} \tag{10}$$

Where P_{max}, h and b, are maximum force (N), specimen thickness (mm) and width (mm), respectively.

3.5 Impact damage evaluation

In this section will be introduced the two main impact damage analysis carried out along this work, namely, visual inspection and non-destructive impact damage evaluation.

3.5.1 Visual inspection

An intuitive idea about damage severity may be first given by a careful visual inspection of the specimen after impact. Therefore, damage resistance of a given composite may be qualitatively evaluated according specimen back-face damage severity. Aspects as back-face damage extent and its typology (i.e. matrix splitting or fibre breakage) are usually related to damage propagation inside the laminate.

With regard to this, in this work, using a caliper rule, back-face damage extent, λ (mm), and its characteristics were evaluated in all low velocity impacted specimens.

3.5.2 Non-destructive impact damage evaluation

As it been mentioned earlier, advanced composites, under low velocity impact events tend to develop internal damages that are almost imperceptible at naked eye, so-called, barely visible impact damages (BVID). An easy way to evaluate impact internal damages, could be, cut or de-ply the composite part and dirtily measure the damage, however, this is inconceivable for composite parts in service, and, in laboratory, becomes impossible to evaluate laminate damage tolerance. Therefore, several techniques have arisen to evaluate composite part internal damages avoiding its destruction, so-called non-destructive damage tests. Nowadays, the most common technique is the ultrasonic impaction. It consists on the emission of an ultrasonic frequency and according to the echo received damage may be localised and measured [158].

In this work, two ultrasonic damage inspection devices were used to evaluate impact internal damages. More details of them will be given as they come along in the following chapters.

Chapter 4
Lamina Characterization

Engineering constants are the key properties for composites design and modelling. In this work, lamina engineering constants, as normal E_{11} and E_{22} moduli, shear modulus G_{12}, and υ_{12} and υ_{23} Poisson's ratios, were useful to perform finite elements models to understand some mechanical behaviours of proposed laminates. Therefore, in this section will be described the experimental work conducted to evaluate those characteristic lamina properties.

4.1 Unidirectional laminate composites

In order to evaluate lamina engineering constants, three unidirectional laminates, namely, 0°, 90° and 45°, were manufactured.

The 0° unidirectional laminate is composed by 8 layers of UDCF tissues (Dynanotex HS 24/150 DLN2), whereas, 90° and 45° laminates, possess 16 layers of the same unidirectional carbon fibre reinforcement. All configurations were manufactured by vacuum bag infusion process, according to description present in Section 3.2.1, Chapter 3, using the CR83 epoxy resin as matrix.

After production, each unidirectional laminate was characterised in terms of fibre volume fraction and its engineering constants determined by instrumented (strain gauges) tensile tests. Both procedures are detailed described in the follow two sections, while results are presented in Section 4.2.

4.1.1 Lamina fibre volume fraction

In order to assess laminates fibre volume fraction, the specific mass was first determined on their individual compounds and the fibre content then evaluated on each unidirectional layup by thermogravimetric analysis (TGA).

The specific mass was determined on each laminate compound by the immersion method, following ISO 1183 standard procedures. Using a digital balance with an accuracy of 1×10^{-4} g, five samples of each raw material were first weighted, in air and then immersed in 2-propanol. Then, the specific mass of laminate components was determined from equation 11:

$$\rho = \frac{W_d \times \rho_l}{W_d - W_w} \tag{11}$$

Where, ρ is the sample specific mass (g/cm^3), W_d and W_w the sample mass weighted in air and immersed in 2-propanol (g), respectively, and ρ_l is 2-propanol specific mass (0.785 g/cm^3). A photography of experimental apparatus may be seen in Figure 19.

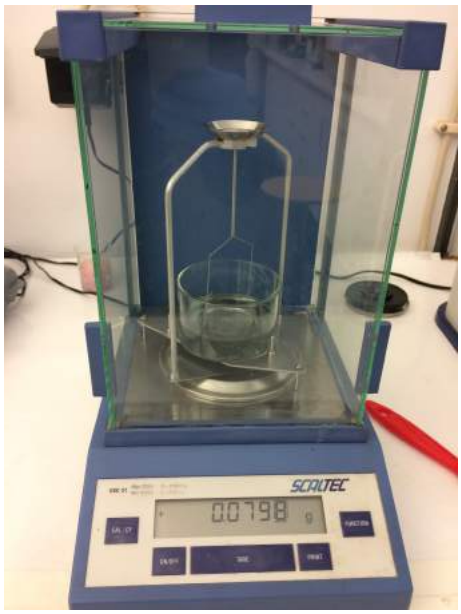

Figure 19: Apparatus used to determine experimentally the density.

It is well known that, in presence of oxygen, carbonisation tests are inadequate to determine the fibre content of CFRPs due to the degradation they may cause on carbon fibres. Therefore, in the present work, the laminates fibre mass content was determined by submitting, individually, them and their raw materials to TGA tests using a Q500 TA Instruments gravimetric balance (Figure 20), under a nitrogen atmosphere to minimize carbon fibres degradation.

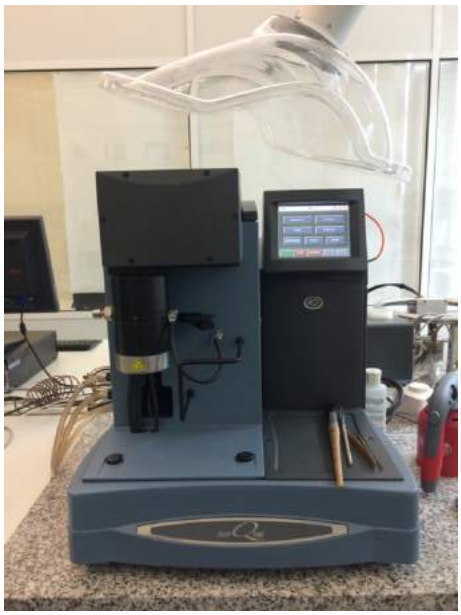

Figure 20: TGA Q500 gravimetric balance.

Three samples of each laminate and five from UDCF tissues (Dynanotex HS 24/150 DLN2) and cured epoxy matrix (Biresin CR83), were subjected to the TGA tests. After heating them from room temperature up to 800 °C, at a heating rate of 10 °C/min, the final content of UDCF tissue and matrix remaining

residues in the TGA balance were determined and recorded as, w_{cf}^{res} and w_{m}^{res}, respectively. Three specimens randomly picked from each unidirectional laminate, manufactured as described in section 3.2.1 of Chapter 3, were also tested in the same conditions to assess and record their remaining residual contents, as $\mathrm{w}_{\mathrm{lam}}^{\mathrm{res}}$.

Assuming that the initial composite only contains carbon fibres and epoxy matrix, the total weight of the remaining laminate residue was determined from the total initial weight of the composite laminate (W_{lam}^{i}) and respective carbon fibre present on it (W_{cf}^{i}), using the following equation:

$$w_{lam}^{res} \cdot W_{lam}^{i} = w_{cf}^{res} \cdot W_{cf}^{i} + w_{m}^{res} \cdot (W_{lam}^{i} - W_{cf}^{i}) \tag{11}$$

which may be simplified as:

$$w_{lam}^{res} = w_{cf}^{res} \cdot w_{cf}^{true} + w_{m}^{res} \cdot (1 - w_{cf}^{true}) \tag{13}$$

which allow determining the true carbon fibre mass content in the initial laminate, w_{cf}^{true}, as:

$$w_{cf}^{true} = \frac{w_{lam}^{res} - w_{m}^{res}}{w_{cf}^{res} - w_{m}^{res}} \tag{14}$$

and its carbon fibre volume content, v_{cf}, as:

$$v_{cf} = \frac{w_{cf}^{true}/\rho_f}{w_{cf}^{true}/\rho_f + (1 - w_{cf}^{true})/\rho_m} \tag{15}$$

where, ρ_f and ρ_m are the carbon fibre and resin matrix densities, respectively.

4.1.2 Tensile test

The mechanical properties of each unidirectional configuration were assessed by tensile testing. A set of five tabbed 250 × 15 (mm) specimens were tested in the fibres direction (0°) and three other ones of 175 × 25 mm in the cross-fibre (90°) and 45° fibre directions, according to the ASTM D3039 standard procedures, in a 50 kN loading cell SHIMADZU® AG-X universal testing machine (Figure 14 a)), using a testing speed of 2 mm/min. Before testing, all specimens were measured by a caliper rule and instrumented with strain gauges, connected to the testing machine acquisition data system, in order to

record transverse and longitudinal strain, ε_t and ε_l, respectively. Strains in a range of 0.001 and 0.003 were used to calculate the longitudinal Young's moduli and Poisson's ratios of samples. Tests were stopped when a catastrophic fail occurred.

Figure 21 shows a photography of the failure mode of an instrumented 45° laminate specimen immediately after being tensile tested.

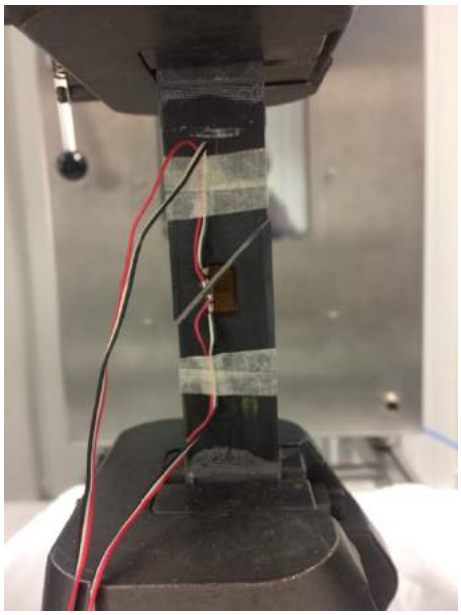

Figure 21: Photography of 45° unidirectional laminate specimen immediately after being tensile tested.

From the recorded load data was possible to calculate the longitudinal stress, σ (MPa), at each instant of the tests using the following equation:

$$\sigma = \frac{P}{h \cdot b} \tag{16}$$

where, *P*, *h* and *b*, are the force (N) and the specimen width and thickness (mm), respectively.

Since strain, ε, was directly obtained from the displacements measured by strain gauges, the longitudinal Young's modulus, E (GPa), may be calculated from:

$$E = \left(\frac{\Delta\sigma}{\Delta\varepsilon}\right)/1000 \tag{17}$$

where, $\Delta\sigma$ and $\Delta\varepsilon$, are the longitudinal stress and strain variation from the strain range between 0.001 and 0.003. Using the same strain range, Poisson's ratios υ_{12} and υ_{23} may be determined from strain values from the 0° and 90° fibre direction tests, respectively, from the generic follow equation:

$$\upsilon = -\frac{\Delta\varepsilon_t}{\Delta\varepsilon_l} \tag{18}$$

where, $\Delta\varepsilon_t$ and $\Delta\varepsilon_l$, are the transverse and longitudinal strain variation measured by strain gauges, respectively.

Knowing the Young's moduli at 0° (E_{11}), 90° (E_{22}) and 45° (E_{45}) laminate fibre directions, and Poisson's ratios υ_{12}, determined from equations 17 and 18, respectively, the lamina shear moduli (G_{12}) may by computed using the follow equation [7][159]:

$$G_{12} = \frac{1}{\frac{4}{E_{45}} - \frac{1}{E_{11}} - \frac{1}{E_{22}} + \frac{2\upsilon_{12}}{E_{11}}} \tag{19}$$

Equation 19 comes from the theory of mechanical analysis of a lamina. More details may be consulted in the following literature [7][6].

4.2 Results

Table 2 presents the densities determined (equation 11) by immersion method in each of the compounds used to produce unidirectional laminates. The results obtained were very similar to those ones given by the epoxy resin supplier (1.14 g/cm³) and expected for carbon fibres.

Table 2: Materials specific mass.

Material	Specific mass g/cm³
Biresin CR83	1.137 ± 0.001
Dynanotex HS 24/150 DLN2	1.658 ± 0.014

In Table 3 are presented the mass content of residues obtained from the TGA tests of epoxy resin (Biresin CR83), UDCF tissues (Dynanotex HS 24/150 DLN2) and laminates 0°, 90° and 45°.

Table 3: Average mass content of residues obtained in the TGA tests.

Materials	N° of samples	Content of residues %
Biresin CR83	5	4.98 ± 0.45
Dynanotex HS 24/150 DLN2	5	86.34 ± 4.20
Laminate 0°	3	59.10 ± 2.43
Laminate 90°	3	64.91 ± 0.58
Laminate 45°	3	65.28 ± 1.34

As may be seen from the results in Table 3, a slight variation of mass content of residues was obtained among the unidirectional laminates. While this difference is especially visible on laminate tested at 0° fibre direction, the 90° and 45° layups have shown similar values. This suggests that the number of UDCF layers used in laminates induced variations of the carbon fibres content obtained by vacuum bag infusion process, resulting in the higher fibre volume fractions experimentally determined in the layups with more UDCF layers, as it may be confirmed by data shown in Table 4.

The results obtained from the tensile tests, as well as the fibre volume fractions determined on the different laminates are presented in Table 4.

Table 4: Laminates thicknesses, fibre volume fractions (v_{cf}), Young's moduli (E) and Poisson's ratios (υ).

Laminate	N° of spec.	N° of layers	Thickness	v_{cf}	E	υ
			mm	%	GPa	
0°	5	8	1.11 ± 0.02	57.72 ± 3.24	99.78 ± 9.38	0.315 ± 0.036
90°	3	16	2.04 ± 0.01	65.73 ± 0.83	6.45 ± 0.09	0.017 ± 0.001
45°	3	16	2.09 ± 0.03	66.28 ± 1.93	8.06 ± 0.10	0.312 ± 0.034

From unidirectional laminates tensile properties, the lamina engineering constants were determined as described in section 4.1.2.

For the purpose of this work it was considered that all unidirectional laminates had a similar fibre volume fraction, transversal Young's moduli E_{22} and Poisson's ratio υ_{13} (both directly obtained from 90° laminate tensile tests) is equal to E_{33} (across the thickness lamina Young's moduli), and υ_{23}, respectively. Similarly, shear moduli G_{12} was considered the same as G_{13} and G_{23}. Therefore, lamina engineering constants considered in this work for finite elements modelling proposals, are presented in Table 5.

Table 5: Average and (±) standard deviation of experimental results of lamina engineering constants.

E_{11}	$E_{22}=E_{33}$	$G_{12}=G_{13}=G_{23}$	υ_{12}	$\upsilon_{13}=\upsilon_{23}$
GPa	GPa	GPa		
99.78 ± 9.38	6.45 ± 0.09	2.96 ± 0.05	0.32 ± 0.04	0.017 ± 0.001

Chapter 5
Bioinspired Bouligand-like Architectures

Nowadays, biologic material structures have been a stimulus to inspirer new highly demanding impact resistance composites. Therefore, owing to their similarities to advanced composites, several Bouligand structures have being mimicked in composites materials to evaluate their performance under impact loading.

Despite all efforts made to optimize the suitability of those bioinspired structural arrangements in advanced composites, all experimental works that may be found in literature were carried out using prepreg systems to manufacture those laminar structures by autoclave. This leaves behind other manufacturing technologies, such as liquid (LCM) and out of autoclave (OOA) composites moulding, neglecting the different morphologic and physical characteristics and also mechanical performance that these latter processing techniques may introduce in final parts.

In this context, in this work and for the first time, three different Bouligand-like laminates and a conventional aircraft one, were manufactured by vacuum bag infusion to allow comparing their morphologic and physical properties. Furthermore, experimental tensile, three-point bending (3-PB) and short-beam interlaminar shear strength (ILSS) tests were performed for all laminates. Additionally, low velocity impact (LVI), at three different energy levels, and compression after impact (CAI) tests were also conducted in order to evaluate their impact damage resistance and tolerance, respectively. Results, failure modes and mechanical response were then investigated and discussed exhaustively.

5.1 Approach

In this work, three new bioinspired laminates, named helical (HL), helical-symmetric (HL_S) and hybrid (HYB), were produced by vacuum bag infusion and their physical and morphology characteristics, mechanical response and failures modes were compared to those of a conventional aeronautic layup (LS), which has been produced and tested in a similar way.

In order to mimic the Bouligand structure, the HL laminate was produced with a constant inter-ply angle of 13,3°. Since this HL laminate presents an anti-symmetric arrangement, which leads to a physical twist after cure, a second laminate HL_S was built using a helical-symmetric structure with exactly the same pitch angle (13,3°) between plies to overcome the problem.

Based on the idea of generating a smooth transition angle between plies may improve the damage laminate resistance, the HYB laminate was designed using three thinner plies orientated in a way that ensured a soft transition between main layer orientation of the conventional LS laminate $[0/45/90/-45/45/-45/0]_{2S}$.

Figure 22 shows a schematic representation of this proposal approach.

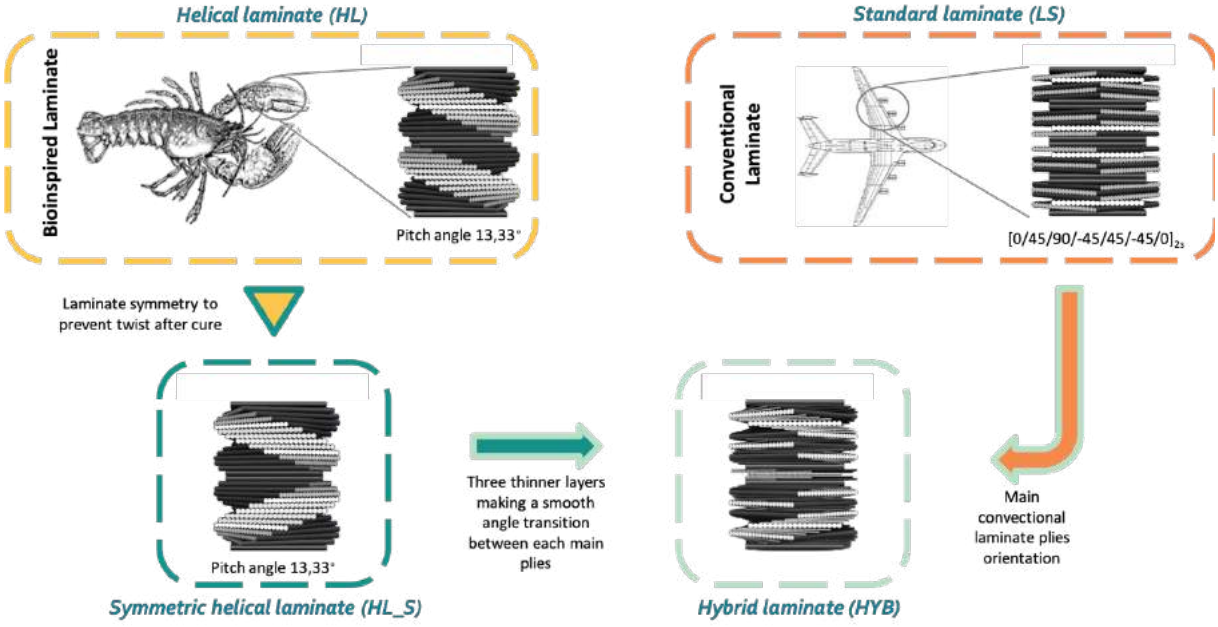

Figure 22: Bioinspired proposal schematic approach.

5.2 Laminates layup

Four different CFRP layup arrangements were manufactured in this work: a standard aircraft (LS) and the three bioinspired laminates (HL, HL_S and HYB). Similar to LS laminate, both Bouligand-like layup arrangements consist in 28 layers of a 150 g/m² unidirectional carbon fibre (UDCF) fabric (Dynanotex

HS 24/150 DLN2 from G. ANGELONI s.r.l.). On the other hand, the HYB configuration has 14 main layers of the same fabric (150 g/m^2 UDCF) interleaved by sub-laminates (α_1) of three thinner dry UDCF layers of 50 g/m^2 (Dynanotex HS 15/50 SLN2 also from G. ANGELONI s.r.l.).

According to the provider, the 50 g/m^2 Dynanotex HS 15/50 SLN2 fabrics are manufactured by using the same technology of Dynanotex HS 24/150 DLN2, which was described in section 3.1.2, Chapter 3. However, only a single carbon fibre layer is used in this case, which means that weft threads are visible in one of the fabric sides. An image of the Dynanotex HS 15/50 SLN2 UDCF fabrics is presented in Figure 23.

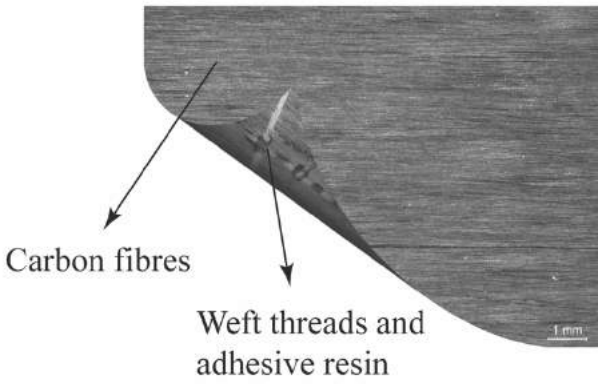

Figure 23: Image of Dynanotex HS 15/50 SLN2 UDCF tissue.

Dynanotex HS 15/50 SLN2 UDCF fabrics are composed by 95 % of carbon fibres (Grafil 15K 1000 dtex) and 5 % of weft threads, which when combined represents a 90 % real mass fraction of fabric and 10 % of adhesive. Additional information may be consulted on materials datasheet in Appendix A.

All configurations were manufactured in the same conditions according the procedure described in section 3.2.1 (Chapter 3).

In both Bouligand-like configurations (HL and HL_S) was used an inter-ply angle of 13.3°. However, while HL presents an antisymmetric arrangement ([B]≠0), HL_S was designed with a midplane symmetric architecture ([B]=0) to avoid physical in-plane twisting of the laminate. Following the idea behind Bouligand structures, HYB layup consists in a mixture of LS and Bouligand-like configurations. Its midplane symmetrical layup contains 14 main layers (150 g/m^2) orientated similarly to LS laminate interleaved by 3 thinner layers (50 g/m^2) strategically orientated to ensure a smooth angle transition.

In addition to the schematic representation of laminates depicted in Figure 24 and their main characteristics may be seen in Table 6.

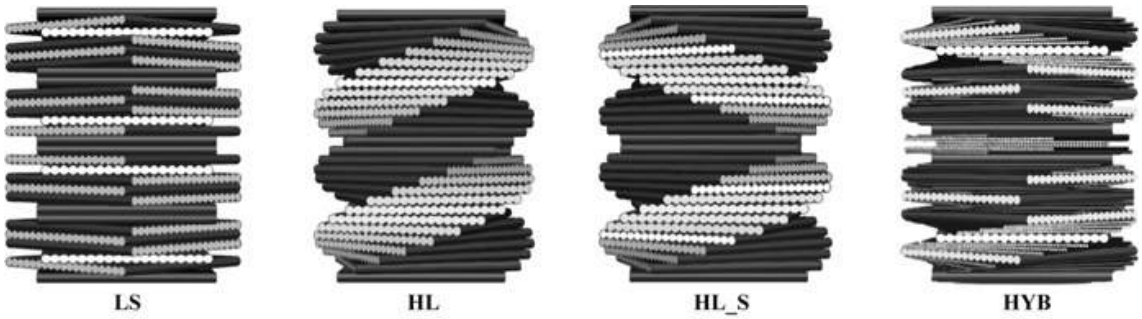

Figure 24: Laminates schematic representation.

Table 6: Laminates characteristics. ν_{cf} is their fibre volume fractions (ν_{cf}) and sub-laminates αi are composed by 50 g/m2 UDCF layers, where: $\alpha 1$ = [11.25/22.5/33.75]; $\alpha 2$ = [56.25/67.5/78.75]; $\alpha 3$ = [-78.75/-67.5/-56.25]; $\alpha 4$ = [-22.5/0/22.5]; $\alpha 5$ = -$\alpha 4$; $\alpha 6$ = [-33.75/-22.5/-11.25] and $\alpha 7$ = [30/60/90].

Laminate	N° of layers	Thickness	ν_{cf}	Stacking Sequence
		mm	%	
LS	28	3.83 ± 0.05	63.3 ± 1.2	$[0/45/90/-45/45/-45/0]_{2S}$
HL	28	3.77 ± 0.08	65.1 ± 0.8	[0/13.3/26.6/.../360]
HL_S	28	3.79 ± 0.08	63.1 ± 0.4	$[0/13.3/26.6/.../173.3]_S$
HYB	56	4.20 ± 0.17	55.3 ± 1.1	$[0/\alpha^1/45/\alpha^2/90/\alpha^3/-45/\alpha^4/45/\alpha^5/-45/\alpha^6/0/\alpha^7]_S$

5.3 Characterization and testing campaign

The testing campaign presented in the present chapter was divided in three main topics: i) laminates physical and morphological characterisation, ii) quasi-static mechanical performance and iii) impact damage resistance and tolerance.

5.3.1 Physical and morphological characterisation

Physical and morphological characterisation aims to compare manufacturing process quality aspects, as laminates' thickness, fibre volume fraction and void content and evaluating the different layups in terms of fibre/matrix adhesion and interlaminar region morphology. Such analysis was conducted following the next steps:

1. To assess the laminates thickness, all impact specimens were measured in four different locations using a caliper rule;
2. Laminates fibre volume fraction was determined according the procedure described for unidirectional laminates in section 4.1.1, Chapter 4
3. For the morphological analysis, three samples of each laminate were first carefully polished, covered with a thin layer of gold–palladium and then observed under scanning electron microscope

(SEM) Nova NanoSEM 200, to evaluate matrix/fibres adhesion, presence void spots and interlaminar region appearance.

5.3.2 Quasi-static mechanical performance

Three different tests were selected to evaluate laminates quasi-static mechanical performance, namely, tensile, three-point bending (3-PB) and sort-beam shear (ILSS) tests.

5.3.2.1 Tensile tests

A set of five tabbed 250 × 25 (mm) specimens of each laminate, where the 0° plies are orientated with the loading direction, were tested following procedures described in section 3.4.1 (Chapter 3), using a 100 kN loading cell SHIMADZU® AG-X universal testing equipment and exatly all other conditions described in section 4.1.2 (Chapter 4) for testing the unidirectional composites. An axial clip-on extensometer was also used to measure the specimen longitudinal deformation up to 0.004, then the test was stopped, to remove the extensometer, and restarted again until the specimen fails. Strains and all tensile properties of laminates were also measured and calculated according to the procedure and equations (16 and 17) decribed in section 4.1.2 of Chapter 4.

5.3.2.2 Three-Point Bending (3-PB) tests

Five 170 × 13 (mm) specimens of each laminate, with the 0° plies oriented perpendicularly to the loading nose, were tested according to the procedure described in section 3.4.2 to determine their maximum flexural surfacial stress ($\sigma_{out.surf.}$) and modulus ($E_{flex.}$) from equations 1 and 3. The slope of the linear force vs deflection curve was used to calculate the flexural modulus in the deflection range between 0.001 and 0.003 flexural strain. All tests were concluded when a significant load drop followed by a visible failure occurred.

5.3.2.3 Interlaminar Shear Strength (ILSS) test

Short-beam shear tests were performed in accordance to the procedure described in section 3.4.3 (Chapter 3) to evaluate and compare the interlaminar shear strength of different laminates. In order to evaluate the first failure mode of each configuration, tests were stopped when load started to fall on the load/displacement curve depicted on the testing machine screen.

Specimens failure mode under each quasi-static mechanical test were then visualised using a Leica DMS1000 digital magnifier (Figure 15).

5.3.3 Low Velocity Impact (LVI) tests

Low velocity impact tests were performed according the procedure described in section 3.4.4 (Chapter 3) under three different impact energy levels: 13.5, 25 and 40 (J). Four specimens of each laminate, with dimensions of 150 x 100 (mm), were tested for each energy level condition. The mechanical response of each specimen was analysed according its peak load, final energy absorption (E_{abs}), and critical load (P_{cr}) and energy (E_{cr}).

After impacted, all samples were first visual inspected to observe their characteristic back-face damage and its extent was measured by a caliper rule. Ultrasonic inspections were carried out in all impacted specimens by an industrial partner, Ria Blades.SA, using a 1 MHz Olympus - Omni Scan Sx C-scan equipment (Figure 25).

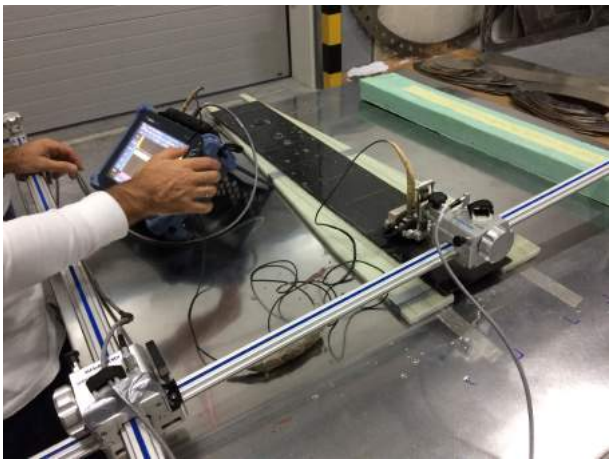

Figure 25: C-scan inspection of specimens.

Before inspection, all specimens were properly placed in a support and their impacted surface was covered with a thin layer of a water and soup liquid mixture, in order to reduce scanner/specimen surface friction and promote the ultra-sonic signal. Afterwards, C-scan data were converted into grey scale images before using the image analysis software Leica Application Suite from Leica (LAS v4.4.) to measure the impact damage areas into samples.

5.3.4 Compression after impact (CAI) tests

Three impacted specimens of each condition (laminate and impact energy level) were submitted to compression after impact tests in order to evaluate laminates damage tolerance. CAI tests were performed according to the procedure and using the equipment already described in section 3.4.5 (Chapter 3).

5.4 Results

This section aims to present and briefly comment all results obtained in experimental testing campaign carried out on bioinspired laminates.

5.4.1 Laminate morphologic characterization analysis

Laminates fibre volume fraction was assessed following the same procedure used to characterise unidirectional laminates in section 4.1.1 (Chapter 4). Therefore, since unidirectional laminates were composed by the same reinforcement and matrix, results obtained for CR83 cured resin and 150 g/cm^3 UDCF tissue densities and TGA residue mass contents, were used to calculate fibre volume fraction of bioinspired laminates (see Tables 2 and 3 in section 4.2). However, as carbon fibre fabrics "Dynanotex HS 15/50 SLN2" were also used in the interply-angle transition layers of the HYB laminate in addition to the UDCF Dynanotex HS 24/150 DLN2 fabrics of its main layers, it was necessary also determine the density on the first type of above mentioned reinforcement. Therefore, five Dynanotex HS 15/50 SLN2 samples were randomly picked from fabric roll to determine their specific mass. The average obtained result is presented in Table 7.

Table 7: Specific mass determined on the UDCF Dynanotex HS 15/50 SLN2 fabric

Material	Specific mass
	g/cm^3
Dynanotex HS 15/50 SLN2	1.641 ± 0.039

Five samples of each laminate were randomly picked from each laminate in order to determine the mass content of residues after TGA calcination. The results are presented in Table 8.

Table 8: Mass content of residues obtained from the TGA tests.

Laminate	Content of residues
	%
LS	63.2 ± 0.86
HL	64.4 ± 0.58
HL_S	63.0 ± 0.30
HYB	57.4 ± 0.81

Table 6 presents the thickness and fibre volume fractions in terms of average determined for each laminate. As may be seen the LS, HL and HL_S laminates presented very similar thicknesses and fibre volume fractions with values around 3.8 mm and 64 %, respectively, while HYB laminate has shown to

be thicker and with lower fibre volume content, +11 % and -14 %, when compared to the other laminates, respectively.

Figure 26 (a) presents a 300 times magnified SEM microphotography where is possible to observe the main different material phases detected in all laminates. By the image may be identified clearly UD carbon fibre, Biresin® CR83 matrix system used to impregnate those fibres by vacuum bag infusion, weft thread and the adhesive resin used during UDCF tissue manufacturing process to keep carbon fibre bonded to weft thread and aligned in the same direction. Red doted area identifies interlaminar regions. Figure 26 (b) shows a representative image magnified 5000 times of the good adhesion observed in all laminates between fibre/matrix. Finally, only a no significative number of small voids were found inside HL laminate, an example may be seen in Figure 26 (c).

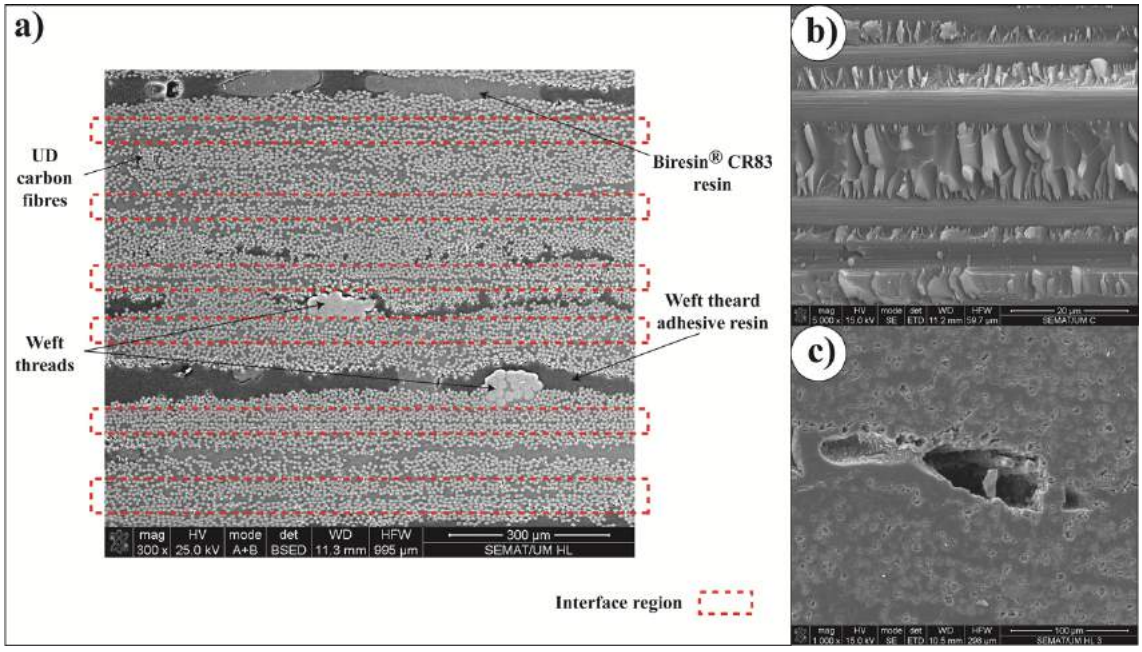

Figure 26: Morphologic analysis under SEM, where (a) shows interlaminar regions (red dotted) and the different phases of the laminate (e.g. UD carbon fibres, Biresin CR83 resin, UD carbon tissues weft threads and their adhesive resin), (b) the good adhesion between carbon fibres and matrix and (c) a void spot in HL laminate, magnified 300, 5000 and 1000 times respectively.

5.4.2 Quasi-static mechanical test results: Tensile, 3-PB and ILSS

Table 9 summarises the average results obtained from three different quasi-static mechanical tests performed: tensile modulus (E) and failure stress (σ), long beam 3-PB flexural modulus ($E_{flex.}$) and maximum outer surface stress ($\sigma_{out.surf.}$) and maximum short-beam interlaminar shear stress (τ_{13}).

Table 9: Average results obtained from the quasi-static mechanical tests.

Laminate	Tensile		3-PB		ILSS
	E	σ	$E_{flex.}$	$\sigma_{out.surf.}$	τ_{13}
	GPa	MPa	GPa	MPa	MPa
LS	43.8 ± 3.0	539.8 ± 64.0	38.2 ± 1.3	461.6 ± 25.3	18.8 ± 0.9
HL	39.8 ± 0.8	399.4 ± 41.5	42.5 ± 0.5	362.0 ± 20.0	19.2 ± 0.9
HL_S	40.8 ± 2.6	339.0 ± 28.4	44.9 ± 0.8	371.7 ± 16.6	16,9 ± 1.1
HYB	39.9 ± 1.8	> 408.9	36.7 ± 1.6	427.6 ± 17.1	25.1 ± 1.0

Figure 27 to Figure 30 show a magnified image of a representative specimen of the LS, HL, HL_S and HYB laminates after tested, respectively. Figure 27, Figure 28 and Figure 29 (a, b and c) show tensile, 3-PB and ILSS tested specimens, respectively, while images in Figure 30, (a and b) correspond to 3-PB and ILLS samples. The colour bar on each image identify the ply orientation angles across laminate thickness. Significant damages observed are pointed by white arrows and red arrows indicate damages around weft threads, while yellow dotted lines show the failure trend. Moreover, the bending load should always be considered applied on specimen top surface in mages showing 3-PB and ILSS tested specimens.

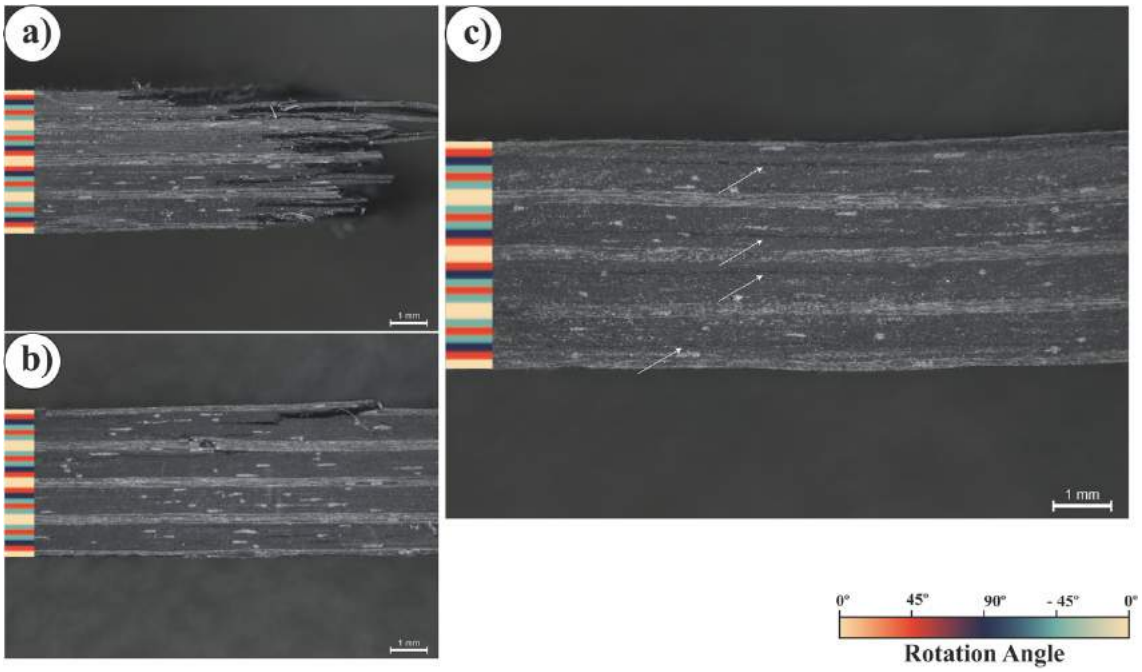

Figure 27: LS laminate failure modes: (a) tensile, (b) 3-PB and (c) ILSS tests.

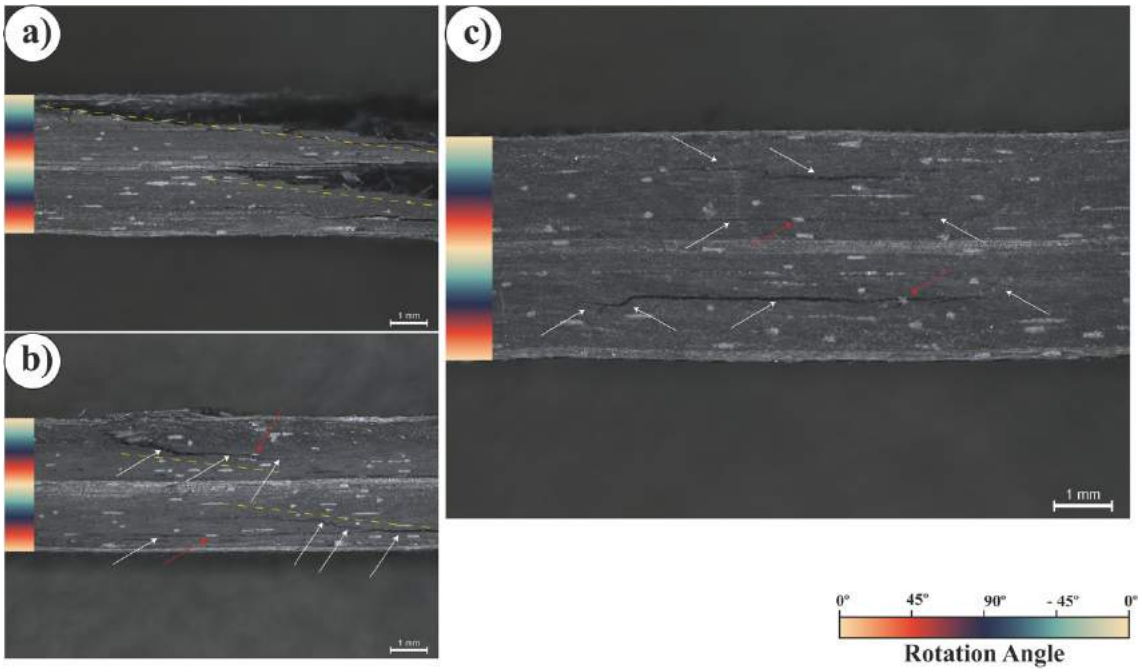

Figure 28: HL laminate failure modes: (a) tensile, (b) 3-PB and (c) ILSS tests.

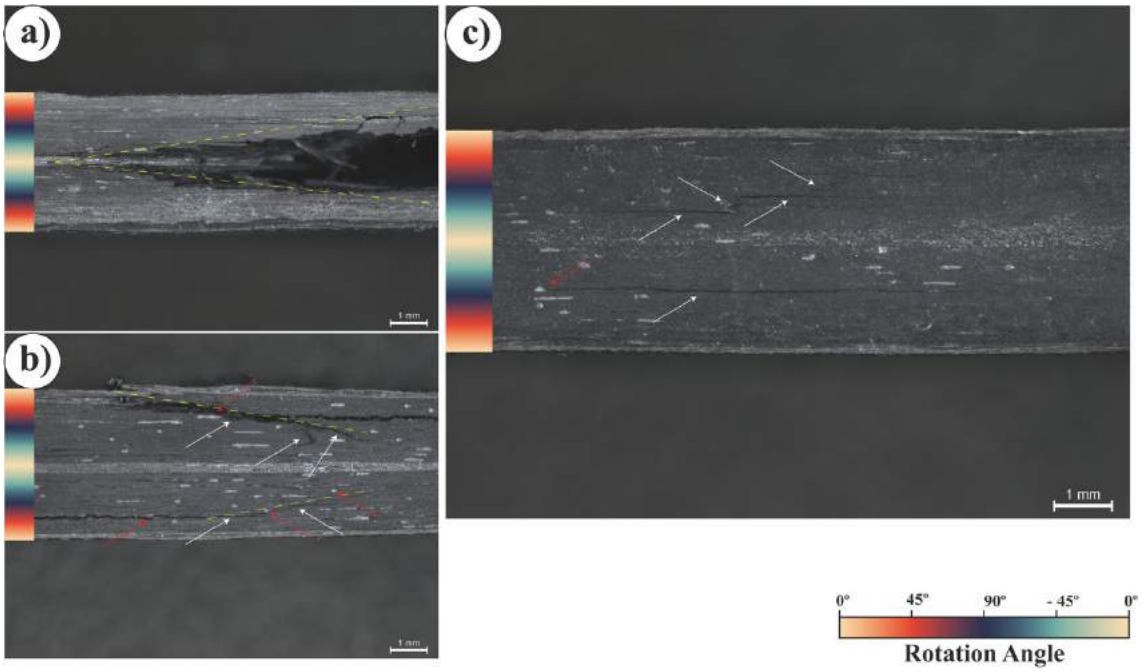

Figure 29: HL_S laminate failure modes: (a) tensile, (b) 3-PB and (c) ILSS tests.

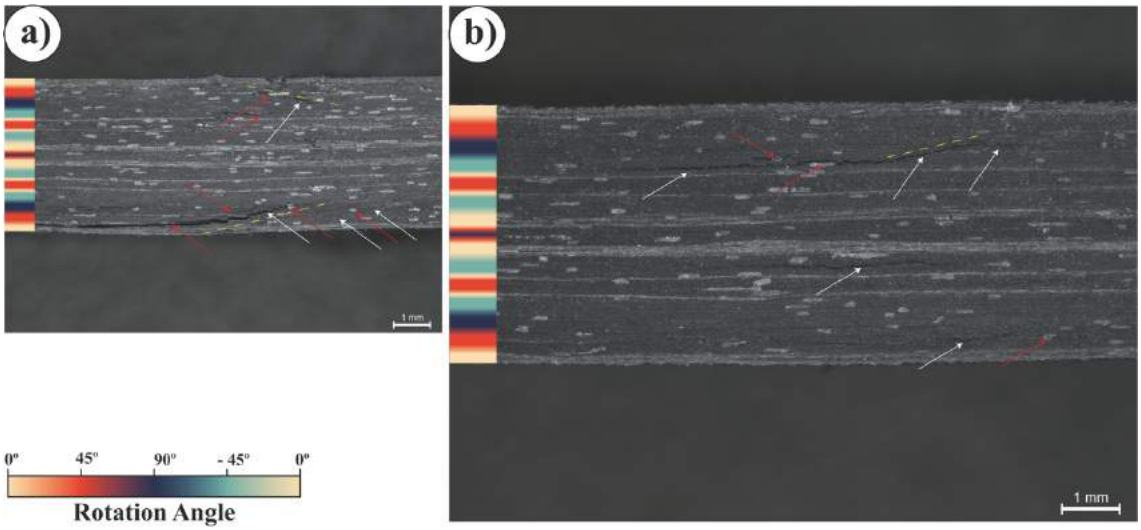

Figure 30: HYB laminate failure modes under (a) 3-PB and (b) ILSS tests.

5.4.2.1 Tensile tests

In tensile tests (see Table 9), only whole HL experimental set presented valid failure, while one specimen of HL_S, two of LS and all of HYB configuration failed on tab's region. The clip-on extensometer used in all experiments made possible determine the elastic modulus (E) in all tests. However, only tests considered valid were used to determine failure stresses (σ).

Tensile tests did not reveal a significant difference between the Young's modulus (E) of laminates, with all of them presenting values around 40 GPa. However, HL and HL_S configurations have shown smaller tensile failure stresses, around 26 % and 37 % lower values than those of LS laminate, respectively. Moreover, despite have failed in tab's regions, HYB tensile failure stress has shown to be at least slightly higher than HL and HL_S configurations.

5.4.2.2 Three-Point Bending (3-PB) tests

The results obtained under 3_PB tests (Table 9) show that HL and HL_S configurations present superior flexural moduli ($E_{flex.}$), around 11 % and 18 % higher than the standard LS laminate, respectively, while HYB layup has a flexural modulus approximately 4 % lower than reference configuration. On the other hand, results revealed that LS layup withstood larger flexural stress (on tensile side) than any of the other configurations, which presented 22 %, 19 % and 7 % lower failure stress values in case of the laminates HL, HL_S and HYB, respectively.

Figure 31 shows the load vs displacement curves obtained from the 3-PB tests made in all laminates.

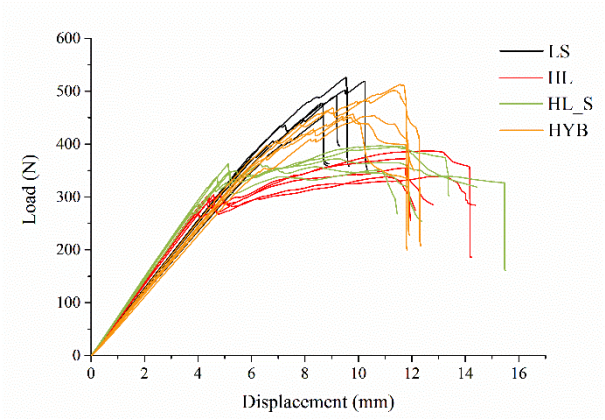

Figure 31: All load vs displacement curves obtained from the 3-PB tests.

5.4.2.3 Interlaminar Shear Strength (ILSS) tests

In ILSS tests (see Table 9), HYB laminate presented the highest maximum apparent interlaminar shear stress (τ_{13}) before first failure, 34 % higher than LS laminate, while HL configuration only has shown an improvement of 2 %, when compared to the same reference (LS). On the other hand, HL_S laminates has shown the lowest interlaminar global resistance, around -11 % when compared to LS layup arrangement.

5.4.3 Low Velocity Impact (LVI) results

Figure 32 shows load vs displacement curves obtained for each laminate specimen at 13.5 J, 25 J and 40 J of impact energy. As may be seen, at 40 J all specimens presented a roughly linear "elastic" behaviour up to a critical load value (P_{cr}) where suddenly it drops to a reset point. This drastic reduction in stiffness indicates that severe damages (e.g. fibre breakage and/or delaminations) have occurred on the laminate. At the impact energy of 25 J, similar performance was observed in all LS and HYB specimens and only in one specimen of HL_S. However, at 13.5 J only two LS specimens presented such critical damage indicator.

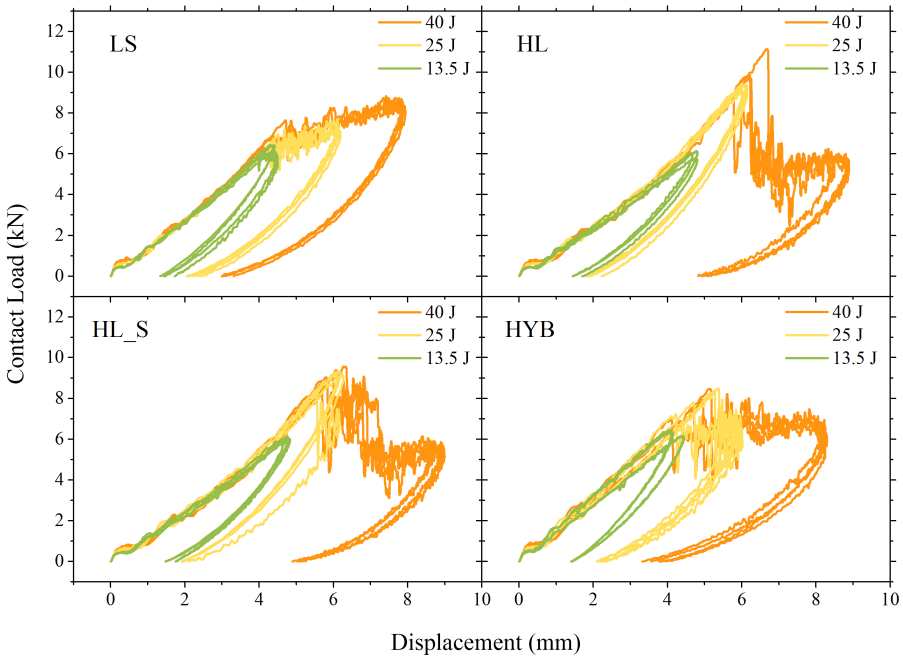

Figure 32: Load vs displacement curves obtained for 13.5, 25 and 40 (J) impact energy.

Table 10 presents LVI results obtained for the peak load, critical load (P_{cr}), maximum impact energy (E_{max}), energy absorbed by the specimens up to the critical loading point (E_{cr}) and total absorbed energy (E_{abs}) of each laminate for the three different impact energy levels.

Table 10: Results obtained from the LVI tests performed at three different impact energy levels.

Energy level (J)	Laminate	Peak Load	Pcr	Emax	Ecr	Eabs
		kN	kN	J	J	J
13.5	LS	6.28 ± 0.16	5.97 ± 0.20	13.73 ± 0.00	12.11 ± 1.12	6.87 ± 0.63
	HL	6.02 ± 0.14	-	13.74 ± 0.00	-	6.40 ± 0.39
	HL_S	6.01 ± 0.01	-	13.74 ± 0.00	-	6.64 ± 0.46
	HYB	6.30 ± 0.15	-	13.72 ± 0.01	-	6.84 ± 0.23
25	LS	7.48 ± 0.19	6.60 ± 0.28	25.29 ± 0.00	13.57 ± 0.53	15.33 ± 0.50
	HL	9.31 ± 0.13	-	25.29 ± 0.00	-	11.65 ± 0.63
	HL_S	9.04 ± 0.37	8.42	25.29 ± 0.00	23.03	12.42 ± 1.78
	HYB	7.97 ± 0.49	7.96 ± 0.50	25.28 ± 0.00	18.66 ± 2.51	16.65 ± 0.53
40	LS	8.71 ± 0.11	6.88 ± 0.51	40.47 ± 0.00	14.08 ± 1.79	27.73 ± 0.25
	HL	9.90 ± 0.80	9.90 ± 0.80	40.51 ± 0.01	26.56 ± 2.96	34.16 ± 0.11
	HL_S	9.16 ± 0.26	9.07 ± 0.38	40.51 ± 0.01	23.52 ± 1.98	34.11 ± 0.11
	HYB	7.81 ± 0.45	7.73 ± 0.56	40.48 ± 0.00	17.53 ± 2.12	31.64 ± 1.09

As may be seen from Table 10, despite the drop weigh impact testing machine had been set to ensure impact energy levels of 13.5, 25 and 40 J, a slightly higher energy than the previously estimated was

absorbed by samples during impact tests. Nevertheless, from the results obtained it may be concluded that:

At 13.5 J of impact energy:

- LS and HYB layups presented similar peak load and slightly higher load-bearing capability (4 %) than the other two helical arrangements;
- Only two LS laminate specimens presented a critical load-drop (P_{cr}) while all others did not seem suffer, apparently, any kind of damage at this energy impact level;
- Laminates LS and HYB absorbed a similar final energy, presenting a value 7 % and 3 % above to HL and HL_S layups, respectively.

At 25 J of impact energy:

- HL and HL_S laminates showed similar and 12 % higher peak loads than LS and HYB layups, that presented roughly the same load-bearing capability;
- Only HL specimens presented an "elastic" response for this impact energy level (without P_{cr}) and only in one of HL_S specimens was observed an abrupt load-drop (P_{cr}). In average, HL_S configuration, has shown to withstand elastically 22% and 5 % higher loads (up to P_{cr}) than LS and HYB layups, respectively. This enhance its elastic energy dissipation (E_{cr}) capability by 41% and 19 % compared to that of the LS and HYB laminates, respectively;
- Total absorbed energy has shown to be similar in the case of both helical laminates that presented a value 22% and 28% less than that of LS and HYB layups, respectively. However, the only one HL_S specimen that presented P_{cr}, was able to absorb an energyof 15.50 J, which is a value similar to that of LS samples (15.33 J) and 7 % less than that of HYB laminate.

At 40 J of impact energy:

- Helical laminates presented higher peak load than any other layup. Especially, HL layup has shown to withstand 12 %, 7 % and 21 % higher load than LS, HL_S and HYB laminates, respectively;
- HL configuration has presented a P_{cr} load 31 %, 8 % and 22 % higher than LS, HL_S and HYB laminates, respectively. This corresponds to an enhancement of E_{cr} of 47 %, 11 % and 34 % comparatively to LS, HL_S and HYB layups, respectively;
- Helical configurations (HL and HL_S) have also shown to be able to absorb more impact energy than all the other laminates, namely 19 % and 7 % more than LS and HYB ones, respectively.

5.4.3.1 Visual inspections

Figure 33 presents the characteristic failure mode observed on the back-face of each laminate for the three different impact energy levels. Photographs show a progressive increment on damage severity and extent as the impact energy increased.

Visible damage was verified at all impact energy levels on LS layups. At 13.5 J, two LS specimen and one of HYB presented visible damage, while all other laminates seem to be undamaged after impact. At 25 J energy impact level, all specimens of LS and HYB laminate and three of HL and HL_S presented visible damage, while at 40 J of impact energy, visible damage was observed in all specimens.

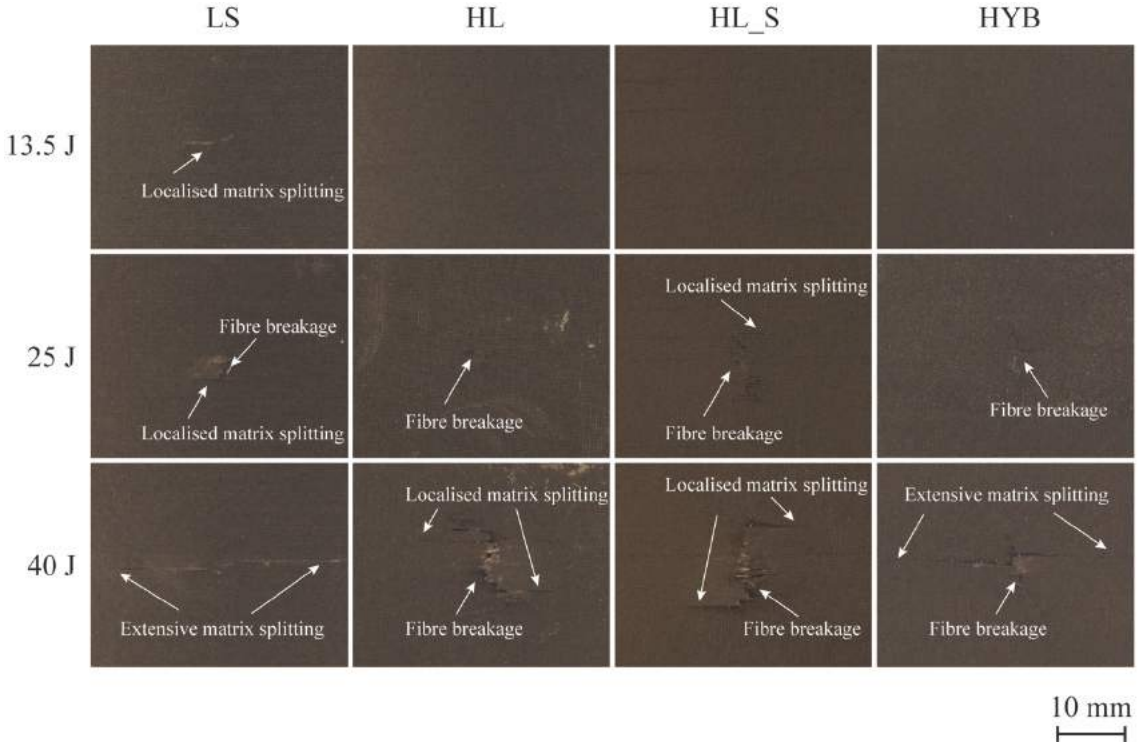

Figure 33: Characteristic back-face damage developed on each laminate for the three different impact energy levels.

Figure 34 presents the average back-face damage extent (λ) measured in all specimens for each impact energy level. As may be seen, up to 25 J of impact energy, all bio inspired layups presented less damage extent than the LS one. However, HYB has shown to develop larger damages than all the other laminates at 40 J of impact energy. On the other hand, both helical architectures demonstrated less propensity for developing larger damages than LS laminate. In fact, at 13.5 J of impact energy, none of those two helical laminates have presented any damage on their back face.

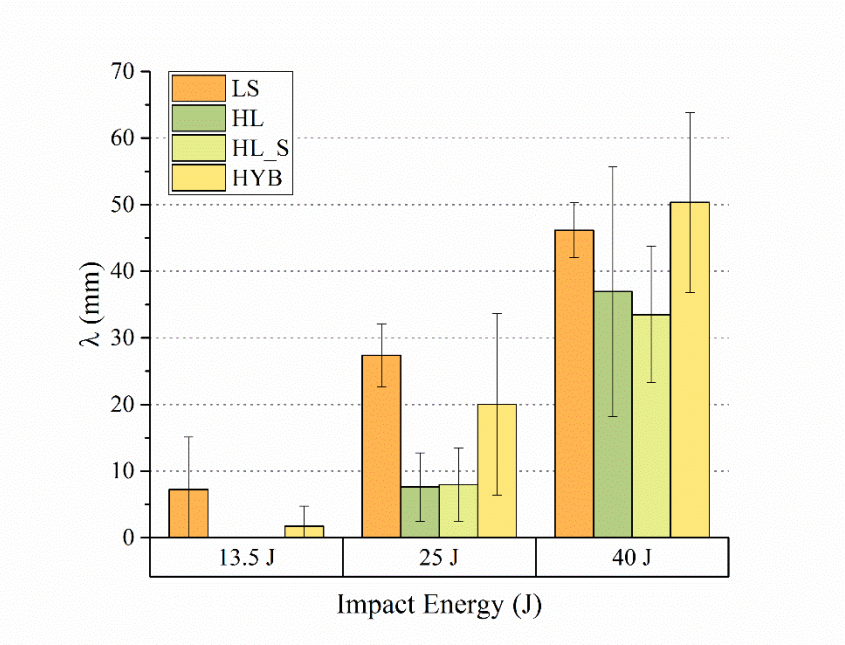

Figure 34: Average back-face damage extent (λ).

5.4.3.2 Impact damage area

The C-scan visualization made possible to observe the shape of damage developed inside each laminate. Despite the low image resolution, Figure 35 shows that both helical laminates (HL and HL_S) tended to develop circular-shape damages independently of the impact energy level, whereas LS ones developed oval-shape damages above 13.5 J impacts.

Circular-shape damage seems to be the mostly common one in HYB layup up to 25 J of impact energy. However, for impact energy levels above it, the oval-shape damages became predominant. This suggests that as the impact energy increased, LS and HYB laminates developed more extensive delamination areas, whereas the grow of translaminar matrix cracks, were the preferential damage mechanism in the HL and HL_S configurations.

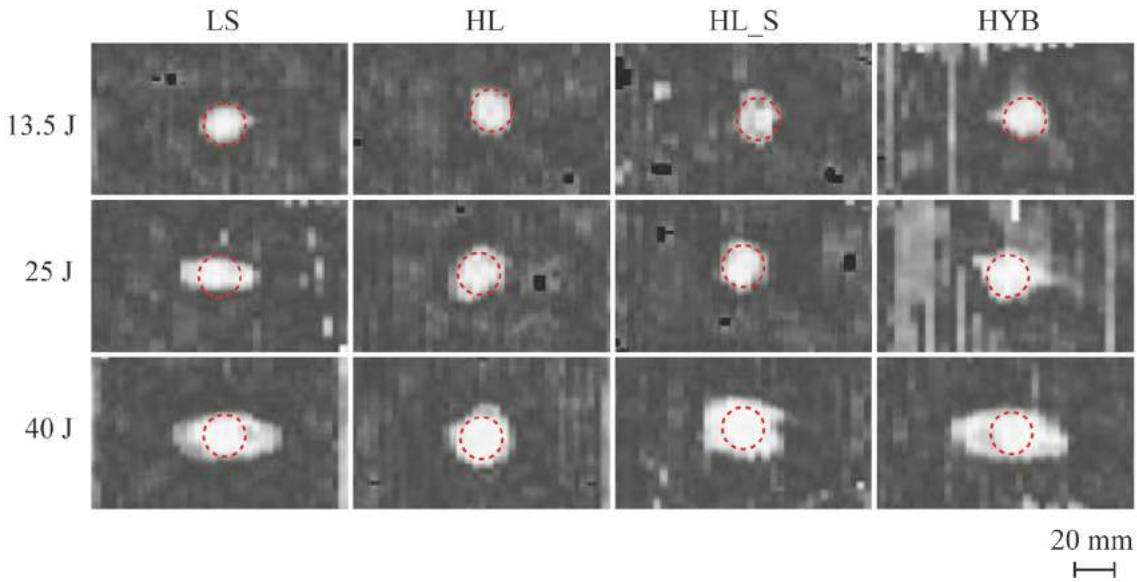

Figure 35: Typical greyscale C-scan images from each layup after the LVI tests at the three different impact energy levels. The red-doted circle corresponds to the impactor projection area.

Figure 36's chart presents laminates impact damage projection area measured by C-scan (Figure 35). At any impact energy level, both Bouligand-like configurations (HL and HL_S) have shown to be less prone to develop larger damages than LS layup. This is particularly evident at the impact energy of 40 J and, in HL_S laminate at 13.5 J of impact energy. At 25 J, no significant differences were observed between the helical and LS laminates, on the other hand, HYB layup presented larger damages than all other configurations.

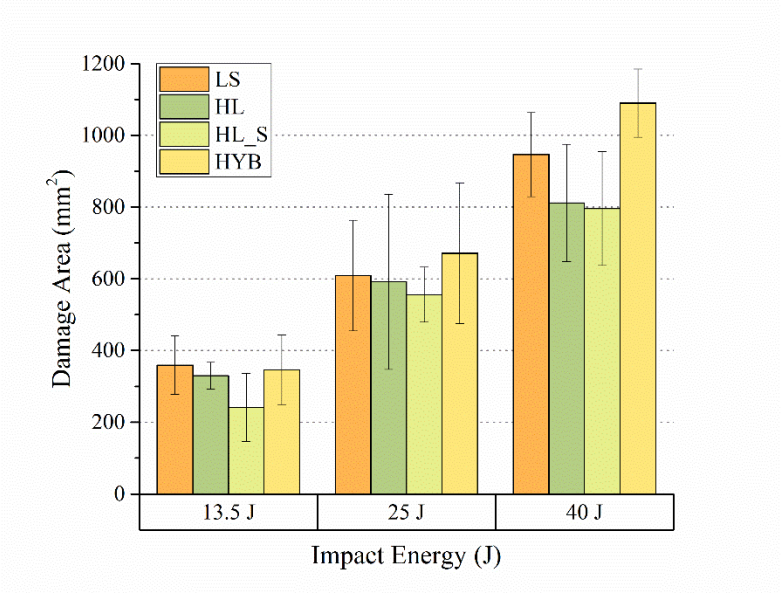

Figure 36: Laminates damage projected area of each impact energy level.

5.4.3.3 Compression After Impact (CAI) results

Impact damage tolerance of each laminate was evaluated by compression after impact (CAI) tests. Figure 37 presents the ultimate strength results obtained from the CAI tests made on laminates previously submitted to LVI tests at the three different energy levels selected. As may be seen, the CAI ultimate strength generically decreased with the impact energy level increasing, moreover, the LS reference laminate presented higher tolerance to damage at all impact levels.

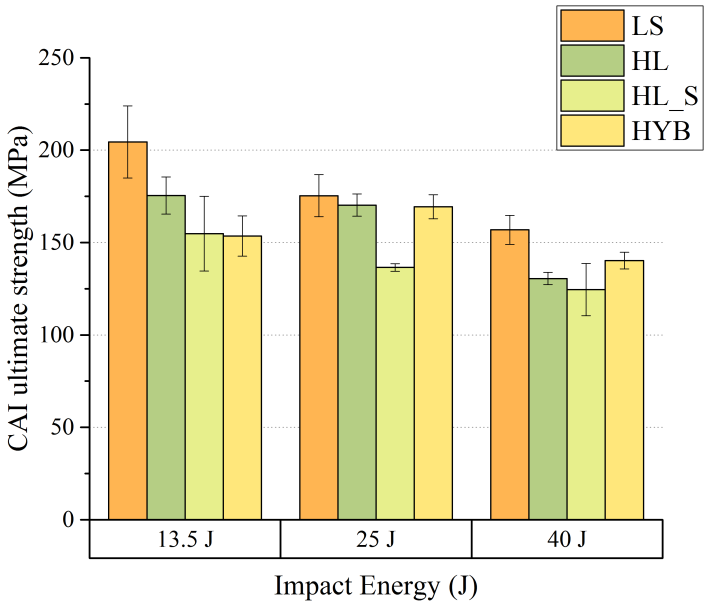

Figure 37: CAI ultimate strength results obtained on laminates after impact at the three different energy levels.

5.5 Discussion

This section will be dedicated to discussing, comparing and evaluating the results presented in the previous section.

5.5.1 Bouligand-like structures produced by vacuum bag infusion process

Figure 38 shows representative cross-section SEM images of each laminate magnified 300 times.

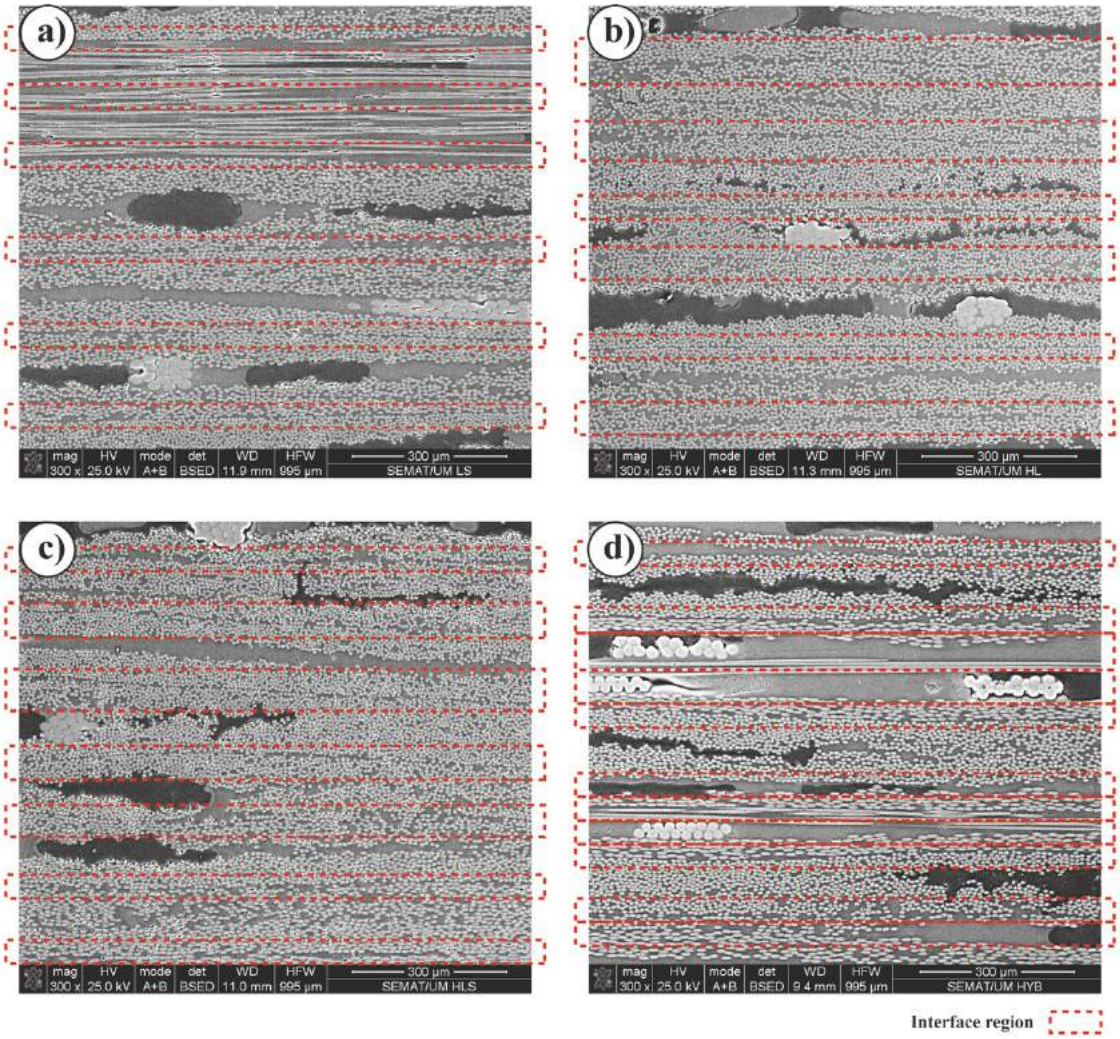

Figure 38: Typical cross-section morphology of (a) LS, (b) HL, (c) HL_S and (d) HYB laminates magnified 300 times observed under SEM.

The observations revealed that a substantial number of resin pockets was formed in laminates during their manufacturing. As Figure 38 shows, these rich resin spots apparently were mostly localised in the gaps created by the weft threads responsible for keeping carbon fibres correctly aligned. From images is also possible to see a darker phase present on theses resin pockets that corresponds to the adhesive used in the fabric manufacturing process to keep the UD carbon fibre and weft thread together, while the grey region corresponds to Biresin® CR83 epoxy resin used as matrix. It is also important to note that weft thread fibres have a much higher diameter in comparison to carbon fibres and that they appear in more amount in the HYB laminate (Figure 38 d)) due to the higher number of layers that this layup possesses (14 + 42· layers, see Table 6). This may also justify the higher amount of resin pockets present in this laminate relatively to the others (Figure 38 d)).

Figure 38 b) and c) also shows the rough and often poorly defined interlaminar region (red dotted area) typically observed on helical laminates (HL and HL_S). However, despite presenting some roughness, a

better defined interlaminar region was observed in LS laminate (Figure 38 a)). On the other hand, the HYB layup showed (Figure 38 d)) to have more thicker and well-defined ply interfaces due to the resin pockets that were formed around weft threads.

The rough and disperse interlaminar region detected in the cross-section of laminates contrasts with the microscopy observations made by other researchers using CRFP prepreg manufacturing techniques [160]–[162]. This seems to be related to the compaction and rearrangement suffered by dry fibre plies during the vacuum bag infusion process before resin impregnation. As Figure 38 (b and c) shows, the phenomenon became more evident when smaller mismatch angle between layers were used because fibres tend to fill partially the gaps between each other, whereas in cases where the angle between layers are larger (i.e. LS laminate, in Figure 38 d)) less interlaminar roughness was observed. Moreover, the rough interlaminar interface observed in both helical-like laminates (i.e. HL and HL_S ones) may improve interlaminar toughness and crack propagation resistance, as revealed by Yaraghi et al. [139] and Mencattelli et al. [34]. Nevertheless, this high interlaminar compaction can also difficult resin flow during manufacturing process and may justify the insignificant number of small voids found in HL laminate (see Figure 26 c).

5.5.2 Quasi-static tests discussion

5.5.2.1 Plies orientation rule on the failure mode

Figure 27, Figure 28 and Figure 29 a) show images of the typical tensile failure modes observed on LS, HL and HL_S layups, respectively. As all HYB specimens failed in the tabs, none of them were considered valid for this analyse.

As may be seen in Figure 27 a), LS tensile specimens presented an abrupt and catastrophic failure, without signs of a pattern or a progressive crack propagation. On the other hand, in both helical laminates, HL and HL_S, the failure seemed to be progressive an along fibres direction as may be seen, highlighted by yellow dotted lines, in Figure 28 and Figure 29 a). Moreover, while the double Bouligand arrangement led to a clear antisymmetric twisting crack propagation in HL layup (Figure 28 a)), HL_S specimens presented a symmetric failure about their mid-plane along the fibres direction.

Under 3-PB experiments, LS laminate (Figure 27 b)) presented clear catastrophic compression failures surrounded by several delaminations on sample compression side, while only a small number of delaminations was observed on tensile side. As the same figure shows, some of those delaminations were generated near weft thread regions (pointed by red arrows), which suggests that the larger polyester fibres diameter and resin pockets may induce crack initiation.

Figure 28 and Figure 29 b) show the typical 3-PB failure mode of HL and HL_S configurations, correspondingly. Both laminates presented twist failure mode, along fibres direction, in both specimen's compression and tensile sides. As happened for tensile tests, while the double helical Bouligand HL layup led to an antisymmetric twisted crack propagation across specimen's thickness (Figure 28 b)), HL_S laminate presented a symmetrical failure following its fibrous laminar arrangement (Figure 29 b)). Besides those main failure mode trends (highlighted by yellow dotted lines on images), some crack branching were also observed in both laminates leading to extensive delamination in some cases. As happened for LS laminate, weft threads and resin pockets formed around them seem to have induced crack branches and delaminations as well in these cases.

The inclusion of thinner layers to smooth pitch angle transition in the HYB layup led to a apparent twist failure mode during 3-PB tests (Figure 30 a)). Apart from two main symmetric helical failures in the compression and tensile sides, several delaminations (sometimes extensive) were observed, most of them near weft thread fibres and throughout resin rich pockets formed by them.

The ILSS tests carried out (see Figure 27 c)) caused delaminations on specimen's compression and tensile sides, between the ±45° and 90° plies of the LS laminate. As may be seen from Figure 28 and Figure 29 c), both Bouligand-like laminates have shown as main fail two extensive cracks between the 90° and -45° plies that at some point jump to other plies in branching or single translaminar manner. Small delaminations were also often observed on the compression side, near the specimen mid-plane, especially in HL configuration (Figure 28 c)).

A more diffuse failure mode was observed in HYB configuration (Figure 30 b)). On the compression side, a twist translaminar failure was often observed, while on the tensile side, several delaminations were observed mostly near to -45° main layer closer to the mid-plane and in the bottommost 45° main layer. However, cracks close to weft threads and throughout their resin pockets have shown to happen more often in this configuration.

The failure modes observed on different quasi-static tests for each laminate suggest that, the smooth angle transition between plies on both Bouligand-like and HYB layup configurations induce a progressive twisted failure mode, which contrasts with a catastrophic failure observed in LS laminate. This much smooth and progressive failure observed in all bioinspired laminates seems not only be induced by the soft reduction of stiffness from layer to layer, but mostly by fibres orientation which drives crack front across interplay region, as it was already suggested by the work of Suksangpanya et al. [163] and [153].

5.5.2.2 ILSS finite elements elastic model

Regarding the complex shear stresses field (τ_{13}) developed under the loading nose specimen's cross-section during ILSS experiments and to better understanding the failure mode of laminates under these conditions, four finite elements elastic models representing the four configurations used in this study were built using a commercial ABAQUS® software. The material engineering constrants assigned to the lamina were those experimentally estimated in section 4.2 (Chapter 4), presented in Table 5.

Both supports and loading nose components were modelled as discrete rigid parts, using the geometry stated by the ISO 14130 standard. Each laminate 40 x 20 x 4 (mm) coupon was built as a solid elastic part and, after mesh convergence study to ensure a realistic representation of the experimental elastic stage, 0.1 mm standard linear cubic C3D8R elements were used in the loading region. Laminate specimens were simply supported over the supports and the loading nose has made to suffer a 0.5 mm displacement.

5.5.2.2.1 ILSS finite elements elastic model results and discussion

Figure 39 shows the three-dimensional distribution of τ_{13}, while the projection of its intensity on specimen's cross-section under the loading nose is depicted in Figure 40. Width dimension of each model was considered between 0 and 1 and τ_{13} intensity was normalized to its maximum and minimum of each layup. The top-right colour bar classifies the level stress intensity in both figures, while the bottom-right one identifies the orientation of plies across laminate's thickness.

From the Figure 39, may be seen a soft τ_{13} transition along the width of each ply, reaching its maximum and minimum close to specimen´s edges. However, from ply to ply, this transition has shown to be highly dependent on plies orientation and more abrupt at larger mismatch angles. This is particularly evident in Figure 39 a) due to the larger difference between orientation of plies that LS layup has. On the other hand, in bio-inspired layups this transition tends to be softer, following through the thickness plies orientation (Figure 39 b) to d)). Although, when plies are orientated close to certain angles, abrupt changes in stress intensity were observed followed by a reset of new helical τ_{13} distribution trends.

From the τ_{13} projection field presented in Figure 40 it is possible to see that stresses are more intense in specimen compression side than in tensile side for all laminates. This figure also shows that the higher stresses are more prevalent at the specimen's edges than in the middle of cross-section and, roughly symmetrical about the middle-width.

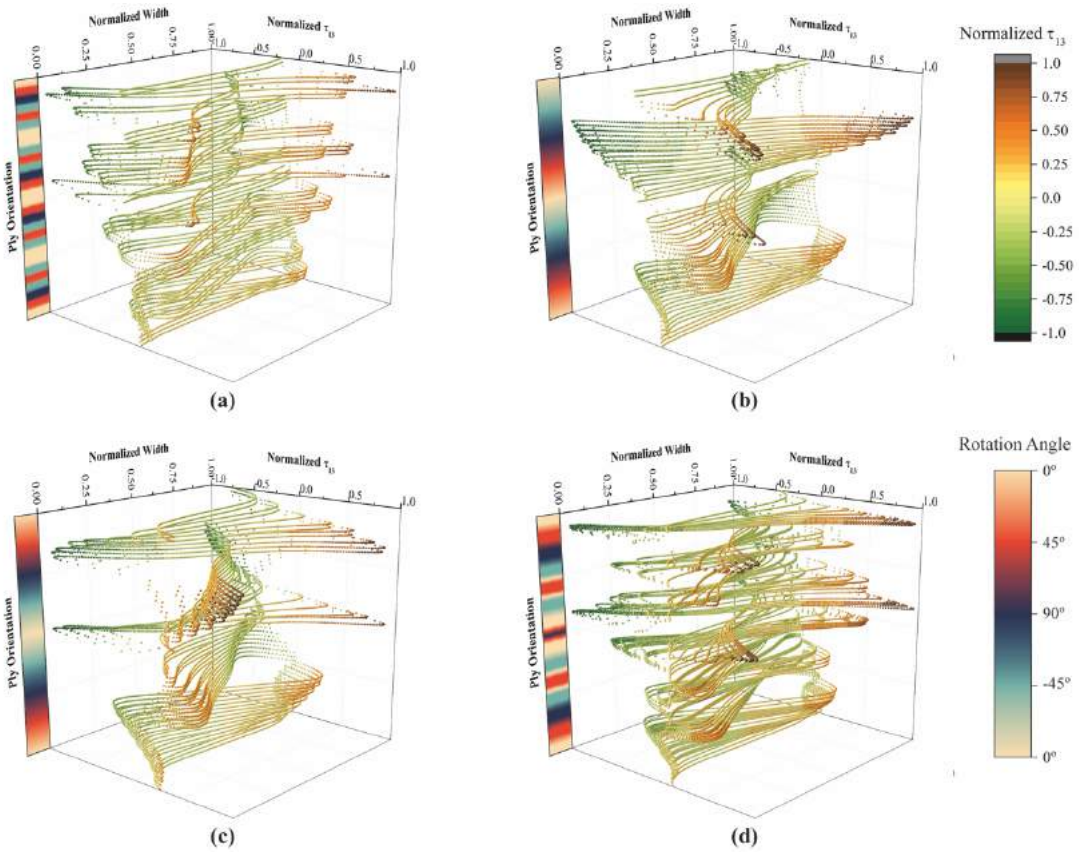

Figure 39: Three-dimensional τ_{13} distribution along (a) LS, (b) HL, (c) HL_S and (d) HYB cross-sections.

The projection of τ_{13} results on LS layup cross-section (Figure 40 a)) shows severe changes of stress intensity in several interlaminar regions, although a field of larger and similar stresses appears nearby 90° plies followed by a smaller drastic chance in stress intensity. This is in agreement with the location of delamination observed after the ILSS experiments (Figure 27 c)). On the other hand, results for bioinspired layups (Figure 40 b) to d)) demonstrate a much smoothest transition in stress intensities than the LS ones. This is particularly evident for HL and HL_S, in Figure 40 b) and c), respectively, which exhibt a constant pitch angle between plies. However, two particular severe changes in stress intensities may be seen in specimen compression and tensile side of both these laminates. Once again results are in good agreement with the location of the main failures observed in Figure 28 and Figure 29 c), moreover the translaminar crack propagation also observed seem to follow the stress distribution observe in Figure 39 b) and c).

Despite the smoothest transition in stresses between plies observed in HYB results (Figure 40 d)) when compared to LS ones, several abrupt changes were also detected. In this case, despite the translaminar crack propagation experimentally observed (Figure 30 b)), may be related to the smooth helical stress distribution obtained from model simulations (Figure 39 d)), no significant correlation can be done

between interlaminar abrupt transitions that have been from results of Figure 40 d) and the main failure modes observed in ILSS tests. As it was before mentioned in section 5.5.2.1, the high number of weft threads seem to induce cracks initiation that then may propagate following the stress fields or connecting other weft threads throughout resin pockets.

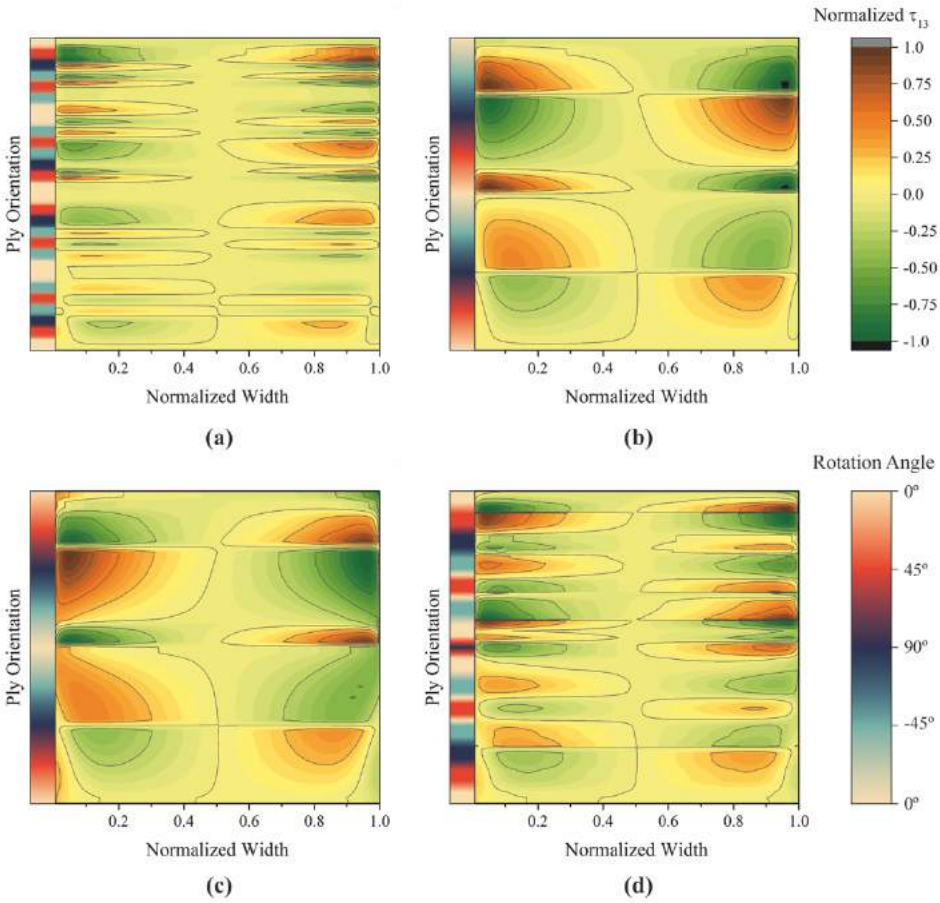

Figure 40: Projection of τ_{13} intensity on (a) LS, (b) HL, (c) HL_S and (d) HYB cross-section.

5.5.2.3 Plies orientation rule on laminates mechanical response

On previous chapter we discuss how fibre orientation could lead to such damages or failure mode mechanisms observed in studied laminates, now we are going to take a look at fibres orientation rule on mechanical response of each layup.

Under unidirectional tensile loading conditions, by taken into account standard deviation, all laminates seemed to present very similar Young's moduli (Table 9). However, both Bouligand-like layups (HL and HL_S ones) have shown significant reduction of maximum tensile stresses. It seems that at lower deformations, the small rotation angle between the plies of those laminates allowed to withstand similar loads as the conventional LS configuration but, the lower number of fibres orientated on loading direction

(Table 6) and progressive failure mechanism observed in both helical configurations (Figure 28 and Figure 29 a)) resulted in a reduction of their load bearing capability.

Under 3-PB experiments, despite all specimens to have the outer layers orientated with the span direction (layers at 0°), both Bouligand-like laminates have presented higher flexural moduli than LS and HYB configurations. This superior through thickness stiffness may be justified by a higher amount of fibres orientated close to 0° direction in the outer layers when compared to LS layup. On the other hand, the lowest flexural modulus obtained in the HYB layup is certainly related to its lower fibre volume fraction (Table 6).

From the curves depicted in Figure 31 (above section 5.4.2.2), it is possible to conclude that LS specimens presented the highest load bearing capability in the 3-PB tests, followed by HYB and then HL and HL_S samples, these last two with similar behaviour. Such load/displament curves also revealed a similar and superior flexural modulus (elastic response in the first stage of curves) of the HL and HL_S laminates, followed by LS and HBY ones, with similar $E_{flex.}$ values between them (Table 9 in section 5.4.2). Despite its ability to withstand higher loads, LS configuration has shown an earlier severe loss of stiffness, while bioinspired laminates presented a progressive stiffness reduction before fail catastrophically. As Figure 28 and Figure 29 b) (section 5.4.2) showed, HL and HL_S laminates presented a twist failure mode on the compression and tensile side that, under 3-PB loading conditions and in agreement with Suksangpanya et al [153] and Mencattelli et al. [33], typically onsets on 90° layers and grows throughout thickness as result of matrix cracking. Whereas LS configuration, as may be seen in Figure 27 b), some layers failed catastrophically on compression side while on the tensile side, where plies kept their integrity, only some delaminations occurred. The higher number of undamaged plies orientated in 0° direction on the tensile side, conferred a superior load bearing capability to this laminate than to the HL and HL_S ones.

Despite of also presenting a partial twist failure mode and a lower fibre volume fraction, HYB layup has shown a higher load bending capability under 3-PB solicitations than both Bouligand-like structures. This may be explained by higher number of plies orientated in 0° direction in HYB layup tensile side.

ILSS results have shown that LS and HL layups have similar apparent resistance to delamination and HL_S laminate does not present any significant reduction of this property. On the other hand, HYB layup presented the highest value of τ_{13} (see Table 9 in section 5.4.2). The higher interlaminar shear stresses resistance of HYB layup may be attributed to the lower fibre volume fraction observed during laminates characterization (Table 6 in section 5.2). This may be explained by the much greater presence of interlaminar resin-richer regions in this laminate than in all other ones, as may be seen in Figure 38 a),

b) and c) (section 5.5.1), which seems to be responsible to improve the resistance between adjacent plies. This is in good agreement with other experimental works, where it was observed a reduction of ILSS resistance with the increase of fibre volume fraction [164][165].

5.5.3 Low Velocity Impact (LVI) tests discussion

5.5.3.1 Impact damage analysis

Analysing the C-scan images in Figure 35 (section 5.4.3.2) it is perceptible that, at the impact energy level of 13.5 J, damage tends to be more localized under the impactor region in all laminates, which indicates that the vast majority of damages were mostly caused by the matrix cracking generated by shear stresses. When the impact energy was increased (see Figure 35 and Figure 36's graphs), LS and HYB laminates tended to develop more extensive damage areas, whereas HL and HL_S layups, despite the increase in their diameters, kept essencially the same circular-shape damages. This suggests that LS and HYB laminates tended to develop extensive delaminations at impact energies higher than 13.5 J, while the translaminar matrix cracking was the preferential damage mechanism generated in both Bouligand-like structures.

The analysis of back-face damages (see Figure 33 in section 5.4.3.1), demonstrated a progressive increment of global damage extent on laminates with the increasing of impact energy. Despite presenting more severe damages on the back-face for impact energies higher than 13.5 J, such as, fibre breakage, both Bouligand-like laminates have shown to be less prone to develop extensive damages than the LS and HYB ones, which developed extensive matrix splitting. This confirmed the C-scan observations on both Bouligand-like layups, where damage has propagated mostly across the laminates thickness, whereas LS and HYB have developed extensive delaminations and, consequently, larger back-face damages due to the larger stiffness mismatch between layers they present.

It is interesting to notice that the HYB structure seems to be more sensitive to the incrementation of impact energy than the other layups. For the lower impact energy (13.5 J), back-face damage has shown to be similar on both helical-like structures, in terms of average extent. However, at 40 J of impact energy, extensive matrix splitting and fibre breakage were observed. This suggests that the lower stiffness, due to the higher matrix volume fraction, and extra thickness of this laminate can delay larger damages for low impact energies. However, at 40 J, the interleaved thin-layers sub-laminates led to a greater fibre breakage and the higher number of weft threads promoted extensive interlaminar debonding and matrix splitting on the back-face.

Summarising, in comparison to all other layups, the two Bouligand-like laminates have shown to reduce impact damages both in terms of internal area and extension on the back-face. On the other hand, the inclusion of thin UDCF tissues between plies of HYB layup has shown to reduce back-face damage extent up to 25 J but, in comparison to LS laminate, the large amount of weft threads induced larger internal damages for impact energies above 13.5 J.

5.5.3.2 Impact resistance (LVI tests)

Generically, LVI events in CFRP is characterized by two main stages: i) loading and ii) recovering. In the first instants of the LVI event, loading stage, the mechanical behaviour of the laminate is dominated by an elastic response that is translated as a roughly linear increase of the load/displacement curve. Along this sub-stage, subcritical damages, mainly matrix cracks, may be developed inside the specimen but most of the energy is transformed in potential elastic energy. If the specimen's capability to transform impact energy into "elastic" energy is exceeded, severe damages (e.g. delaminations and/or fibre breakage) will take place, working as energy release mechanism. The overcome of this critical or threshold energy (E_{cr}) may be clearly identified in load vs displacement curve when load reaches a critical load (P_{cr}) and sudden drops to a reset value, indicating a loss of specimen's stiffness and consequently severe damages formation on it. After this point, depending on the sample's residual stiffness, load may increase, or not, up to a new peak load until the remanding impact energy is totally dissipated, meanly by severe damage formation. Finally, the recovering stage is characterized by a progressive unloading process down to zero load, theoretically, without damage formation. Therefore, the final absorbed energy (E_{abs}) is result of energy dissipated during the subcritical and severe damage formation along the loading stage.

Overall, by analysis of the characteristic load vs displacement curve, four main factors can describe the global damage resistance of a given laminate to impact: i) peak load – maximum load bearing capability; ii) critical load (P_{cr}) – if exists, indicates the load bearing capability without severe damage formation; iii) critical absorbed energy (E_{cr}) – if exists, indicates the absorbed energy up to P_{cr}, or the energy transformed during the "elastic" response; and iv) final absorbed energy (E_{abs}) – global absorbed energy at the end of impact solicitation.

Figure 41 a) to d) graphically shows the evolution of those four main factors at the three different impact energy levels for all studied layups.

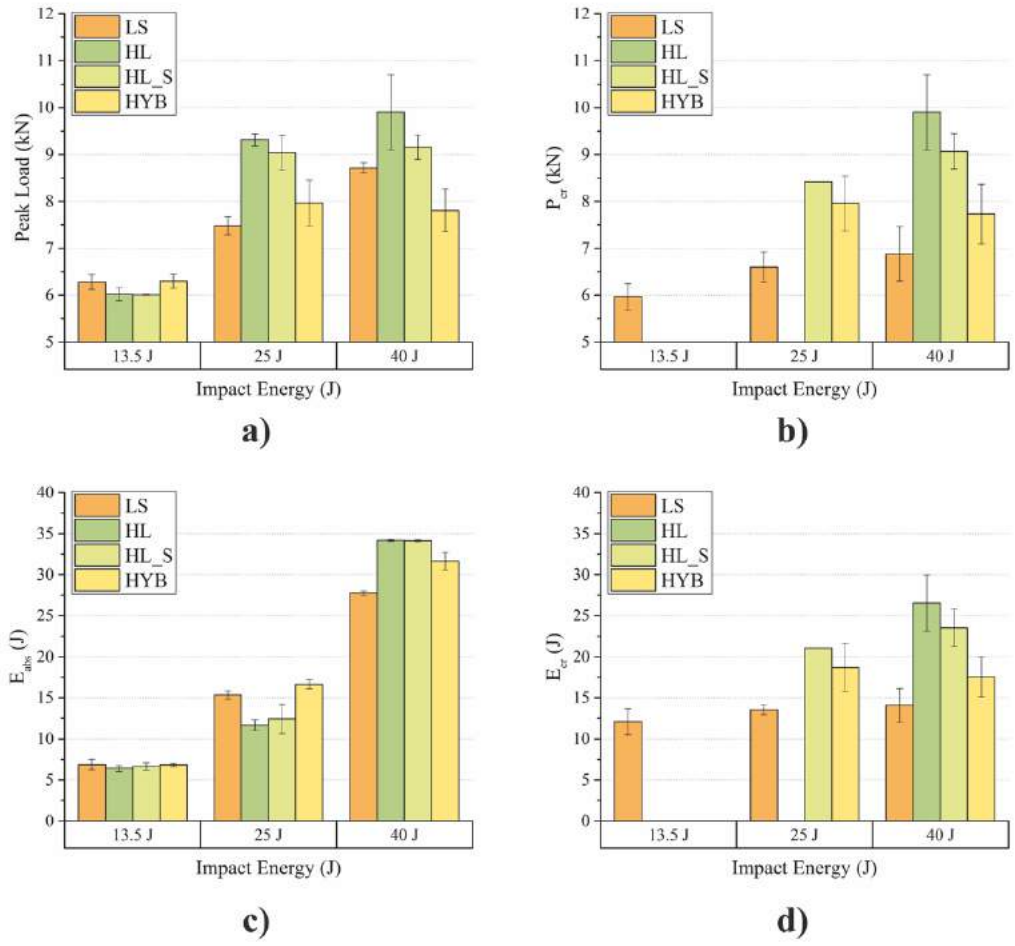

Figure 41: Evolution of a) peak load, b) critical load (P_{cr}), c) final absorbed energy (E_{abs}) and c) critical energy (E_{cr}) in all layups with impact energy incrementation.

5.5.3.3 Load vs displacement curves considerations

Analysing the load vs displacement curves in Figure 32 (section 5.4.3), it may be concluded that all specimens of each laminate presented very similar response to the same impact input, which confers representativity to the tests made. However, HYB layup was the one showing greater variability, especially during the "elastic" phase of the event. The uneven distribution and extensive resin pockets observed inside this laminate, which may lead to different through thickness stiffnesses, seems to be the main reason for this uncertain response at the initial impact stage.

The progressive incrementation of impact energy, from 13.5 J to 40 J, leads to higher peak loads at larger displacements and consequent increment of final absorbed energy (E_{abs}). In terms of peak load (see Figure 41 a)), this corresponded to an increment of 28 % for LS configuration, 39 % for HL, 34 % for HL_S and 19 % for HYB. With respect to E_{abs} (Figure 41 c)), the increment has been of 75 % for LS, 81 % for HL and HL_S and 78 % for HYB.

It is also important notice the distinctive mechanical response of laminates under similar conditions. In fact, curves depicted in Figure 32 (section 5.4.3) also show, that P_{cr} and peak load coincided for HL, HL_S laminates in most of the cases and for some of HYB specimens, while in LS laminate, P_{cr} occurred always before the maximum load is reached. Furthermore, P_{cr} occurred always at higher displacement and load on HL and HL_S laminates than in LS and HYB ones.

Should be also referred that LS and both Bouligang-like (HL and HL_S) laminates presented progressive increment in stiffness during the "elastic" response to impact (see Figure 32 in section 5.4.3). This behaviour is particularly evident at the highest levels of impact energy (40 J for LS and, 25 J and 40 J for both Bouligand-like layups) when displacement exceeded ~3 mm. Similar behaviour was also observed by Mencattelli et al. [34] in CFRP Herringbone-Bouligand structures submitted to bending. According to them, the interlaminar wave pattern of those bioinspired structures leads to a mechanical interlock between two adjacent plies, which reduces the delamination area, promotes subcritical matrix crack formation and, consequently, yields a stiffer mechanical response.

Considering the rough interlaminar region observed in LS, HL and HL_S laminates, even poorly defined in the last two cases, may suggest that such increase in stiffness is related to the delay on delaminations formation. In addition, the successive formation of subcritical translaminar matrix cracking, and consequent progressive loading transfer to the stiffer carbon fibres, in both Bouligand-like configurations, may intensify this phenomenon. Moreover, the formation of translaminar matrix cracking by Bouligand-like laminates, led to larger displacement and energy dissipation before severe damage take place (P_{cr}), on the other hand, in LS layup this subcritical damage mechanism is limited, with led to an early load drops (P_{cr}) and consequent formation of severe damages, such as, the extensive delaminations confirmed by the C-scan observations in Figure 35 (section 5.4.3.2). This my justify why the increment in stiffness is more visible in HL and HL_S specimens than in LS ones.

5.5.3.4 At 13.5 J of impact energy

Figure 41 a) (previous section 5.5.3.2) shows that HL and HL_S layups presented similar and slight lower average peak load than LS and HYB ones, which also have shown similar load bearing capability. However, despite the presence of severe initial damages (much lower P_{cr}) in LS layup (Figure 41 b)), all laminates have shown similar energy absorption (E_{abs}) (Figure 41 c)). This suggests that in the bioinspired laminates the whole 13.5 J impact energy was spent in "elastic" deformation and in formation of subcritical damages while, in the case of LS layup, must of it was also transformed into "elastic energy"

before severe damage formation (specifically the 12.11 J that may be seen in Figure 41 d)) and only a small part of this energy was spent during sever damaging.

5.5.3.5 At 25 J of impact energy

At 25 J of impact energy all bioinspired configurations have shown higher load bearing capability when compared to LS laminate (Figure 41 a)). However, LS and HYB laminates demonstrated to absorb more energy than both Bouligand-like layups (Figure 41 c)). This may be explained by the energy dissipated by severe damages. As mentioned before, none of HL has presented P_{cr}, which means that all of the 25 J of impact energy was transformed into "elastic" energy without severe damage formation. On the other hand, HL_S and HYB structures presented higher P_{cr} values then LS one, as Figure 41 b) shows. This suggests that for the same amount of energy (25 J), HL_S and HYB laminates were able to transform more impact energy into "elastic" energy (E_{cr} in Figure 41 d), while a larger amount of impact energy was released by severe damage mechanisms in LS layup. Nevertheless, LS and HYB layups have shown similar E_{abs} values, despite the last one presented higher values of E_{cr}. In comparison to LS laminate, HYB layup presents higher ductility (due to the higher matrix volume content) and thickness (Table 6 in section 5.2), which confers to it, at this impact energy level, higher load bearing capability (peak load Figure 41 a)), load and energy before severe damage formation (Figure 41 b) and c), respectively), dissipate more energy by subcritical matrix cracking and matrix plastic deformation, and increase the final absorbed energy E_{abs} (Figure 41 d).

5.5.3.6 At 40 J of impact energy

At 40 J of impact energy level, both HL and HL_S laminates presented higher load bearing capability when compared to LS layup, contrary to HYB which has shown the lowest peak load (Figure 41 a)). Despite presenting higher values of P_{cr} and, consequently, better ability to absorve impact energy before severe damages formation (E_{cr}) (see Figure 41 b) and d)), all bioinspired structures have shown to absorb more energy during the whole impact event than LS configuration (see Figure 41 c)). This indicat that all bioinspired laminates are able to withstand higher load and impact energy keeping their structural integrity and, at the same time, dissipate more impact energy. Which also demonstrates that tranlaminar matrix cracking and fibre breakage observed in for HL and HL_S specimen's back-face (see Figure 33, section 5.4.3.1) was much more effective in terms of energy releasing mechanisms than extensive matrix splitting and large delaminations developed and observed by C-scan (see Figure 35, section 5.4.3.2) in LS and HYB layups.

Nevertheless, despite being thicker than LS, HYB layup presented lower load bearing capability due to its higher matrix volume fraction (Table 6, section 5.2), which contributed to the development of more subcritical damages formation and delay of severe damage mechanisms at higher loading and energy levels (see Figure 41 b) and d)). Additionally, HYB laminate has also demonstrated to combine large delaminations (Figure 35, section 5.4.3.2) with extensive matrix splitting and fibre breakage (Figure 33, section 5.4.3.2), which conferred it higher energy absorption than LS laminate (Figure 41 c)).

5.5.3.7 Impact energy vs damage indicators

As it was mentioned before, during an impact event, energy may be absorbed by two main mechanisms: i) first, most of the energy is dissipated by sample's elastic deformation and subcritical matrix cracking damages and, ii) second, once sample's elastic deformation capability is exceeded, by much severe damage, as massive delaminations and/or fibre breakage. The boundary between those two mechanisms may be clearly identified by the first load-drop (P_{cr}) in load vs displacement curve, being the phenomenon, before P_{cr}, characterised essentially by the formation of subcritical damages and after it by the occurrence much severe damages. If P_{cr} does not happen, it may be assumed that no severe damages have been occurred and laminate structural integrity was mostly preserved.

Figure 42 presents the percentage of input energy absorved by laminates in subcritical and severe damage formation for the three different impact energy levels, according to the aboved mentioned criterium.

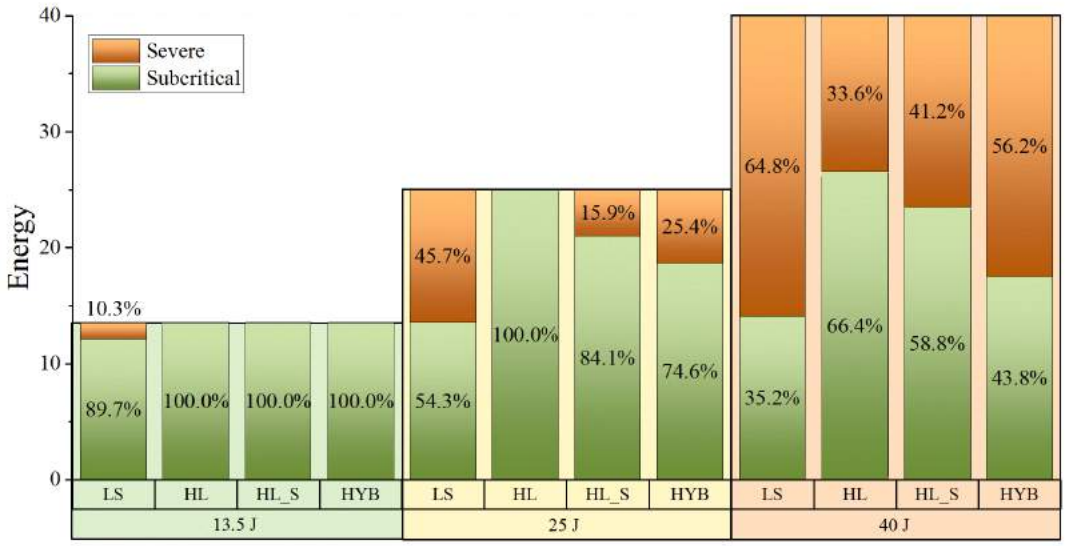

Figure 42: Energy spent in subcritical and severe damages formation for each configuration at different impact energy levels.

As may be seen, the whole 13.5 J of impact energy was totally absorved by elastic and subcritical damage phenomena in all bioinspired laminates, while two LS specimens of have dissipate 10.3 % of this energy through severe damages. At 25 J impact energy, all LS and HYB specimens dissipated most of the energy by severe damages, 45.7 % and 25.4 %, respectively, whereas only one of HL_S specimens spent 15.9 % of impact energy in such catastrophic damages. On the other hand, all HL specimens spent the whole energy in subcritical damages.

Finally, all specimens of all configurations developed severe damages at 40 J. Figure 42 shows that LS and HYB layups dissipated 64.8 % and 56.2 % of this amount of energy in catastrophic failures, respectively, while HL and HL_S only 33.6 % and 41.2 %, respectively.

Overall, results have shown that LS layup is more susceptible to develop severe damages than all the other bioinspired laminates. Moreover, all LS and HYB specimens have dissipated, at least, 25.4 % of energy in catastrophic failures for impacts above 13.5 J, whereas both Bouligand-like layups only revealed severe damage indicators at 40 J energy impact level, where they dissipate, at least, more than 33.6 % of energy in such damage mechanisms. Once again, this confirms the better impact resistance of those last two structures (HL and HL_S) when compared to the other layups. This allows to conclude that both Bouligand-like layups are able to keep their structural integrity for longer by dissipating energy by subcritical damages.

5.5.3.8 Critical load and energy thresholds

Results from the load vs displacement curves (Figure 32, section 5.4.3) and critical load (P_{cr}) and energies (E_{cr}) (Figure 41 b) and d), section 5.5.3.2), allow concluding that, for a given laminate, since the severe damage indicator shows up at a given impact energy level, it becomes a constant presence for higher impact energy levels. Therefore, the first load-drop (P_{cr}) on load vs displacement curves of a given laminate may be defined as the load, and consequent critical energy (E_{cr}), threshold for severe damage initiation. Based on this assumption, Figure 43 a) depicts the critical energy (E_{cr}) recorded for each laminate at each impact energy level (top-left colour bar) as function of its respective critical load (P_{cr}). Whereas, Figure 43 b) presents the energy and load thresholds (minimum values of E_{cr} and P_{cr}) of each laminate and their enhancement with respect to LS layup. For better interpretation, both charts are linked by a dotted line.

As may be seen from above mentioned figures, independently of the impact energy, critical load and energy may be arranged in clusters corresponding to each configuration and disposed from the following lowest to the highest values: LS, HYB, HL_S and HL. This cluster arrangement confirms that each laminate has a characteristic load and energy threshold to trigger severe damage mechanisms. Moreover,

Figure 43 b) also shows that HL configuration presents the highest thresholds, with an remarkable enhancement of 66 % and 120 % in terms of load and energy in respect to LS layup, respectively. Not less impressive were the results for the HL_S and HYB laminates, which revealed critical load thresholds 41 % and 33 % higher than LS layup, respectively, which corresponds to an enhancement of the critical energy (E_{cr}), with respect to the same laminate, of reference of 74 % and 54 %.

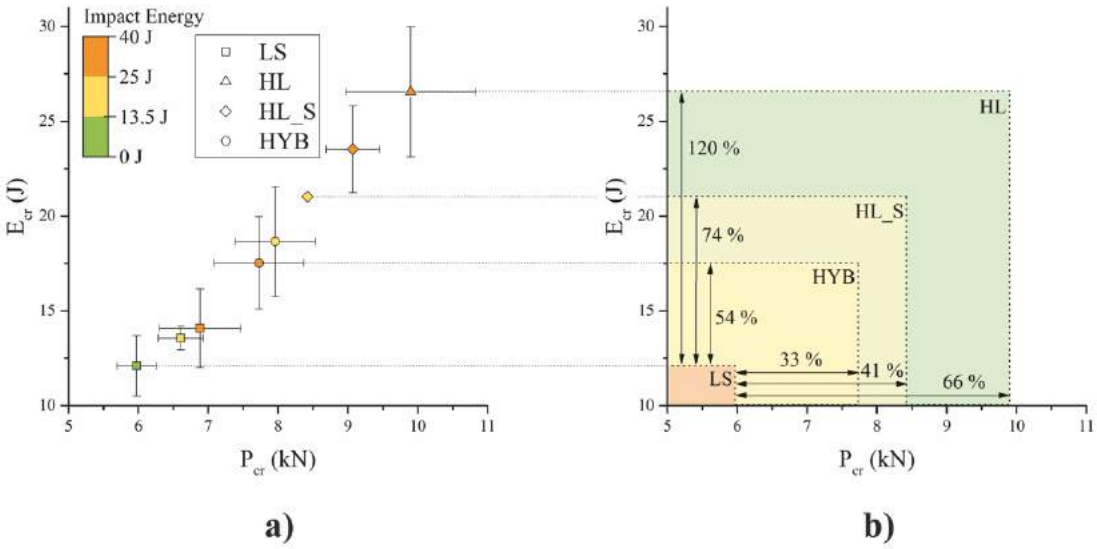

Figure 43: a) critical energy (E_{cr}) and load (P_{cr}) necessary to trigger severe damages on laminates at a given impact energy level and b) their thresholds and enhancements relatively to LS configuration.

Overall, results demonstrated that the bioinspired layups were able to delay severe damage trigger to much higher values of load and energy when compared to reference laminate (LS).

This outstanding behaviour is result from those configurations be able to redirect subcritical matrix cracking across laminate's thickness, contrarily to configurations that exhibit larger pitch angles between plies, as LS layup. This latter tends to develop extensive delamination due to the large mismatch in interlaminar shear stresses values τ_{13}, as also demonstrated by Mencattelli and Pinho [32][33]. Additionally, the rough and poorly defined interlaminar region particularly observed in HL and HL_S configurations, due to the use of dry fibre fabrics in the vacuum bag infusion process, delays extensive delaminations and promote the subcritical matrix cracking, as the same authors found in Herringbone structures [34].

5.5.3.9 Impact tolerance (CAI tests)

As Figure 37 (section 5.4.3.3) shows, all bioinspired laminates have demonstrated lower impact tolerance when compared to the LS reference one. Being well-known that the compressive strength after impact varies proportionally with the number of fibres oriented in load direction [166], this was somehow

expected, since the LS laminate had higher amount of fibres aligned on compression load direction (eight plies oriented in 0°) than all other ones.

Figure 44 a) to d) present the ultimate strengths obtained from the CAI tests in all studied laminates, after have been impact tested at the three energy levels.

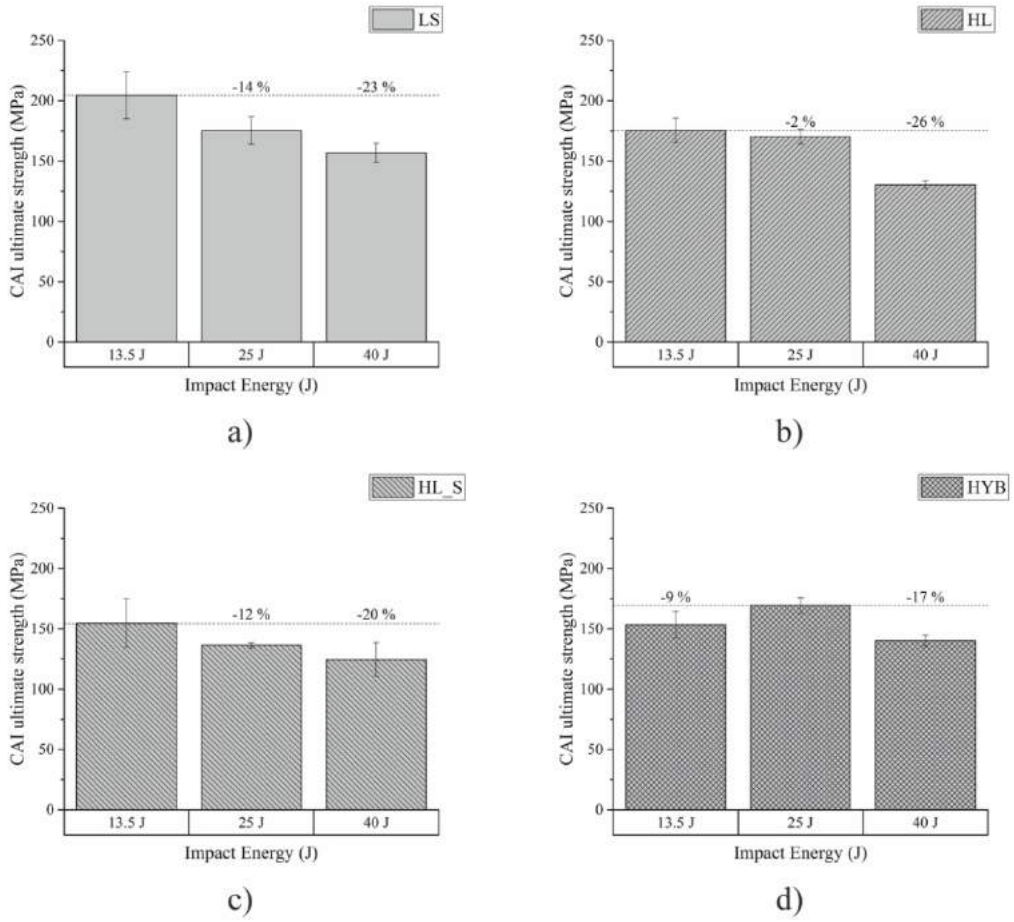

Figure 44: CAI ultimate strength of a) LS, b) HL, c) HL_S and d) HYB laminates tested at the three impact energy levels.

As may be seen, as expected, the LS, HL and HL_S layouts have shown a decreasing on their residual strength as the impact energy increases. However, HYB specimens after impact at 25 J have demonstrated better CAI performance than those previously impacted at 13.5 J and 40 J. The higher resin volume fraction of HYB laminate seems to have made its CAI performance to be much more steady and almost independent on the impact energy. In fact, the HYB laminate presented only a variation between maximum and minimum CAI ultimate strength of 17 %, whereas all other layups have shown variations above 20 %, and clear residual strength stepdown as impact energy increases.

5.6 Conclusion

In this chapter, three new bioinspired carbon/epoxy laminates were proposed and manufactured by vacuum bag infusion. Additionally, in order to evaluate and compared the different mechanical response and damage resistance and tolerance of those new configurations, a standard aircraft configuration (LS) produced by the same processing method was taken as reference.

From laminates characterisation, no significant differences in terms of thickness and fibre volume fraction were found between the reference (LS) and both Bouligand-like layups (HL and HL_S). However, the larger amount of weft threads in the HYB laminate has led to a high presence of resin pockets, which reduced its fibre volume fraction and slightly increased its thickness. Moreover, no significant number of voids were found inside laminates, which confirms the suitability of vacuum bag infusion to produce these kinds of composite layups.

Quasi-static mechanical response of laminates was evaluated by tensile, three-point bending (3-PB) and interlaminar shear strength (ILSS) tests. From the experimental results and tested specimens' observations, it was concluded that:

- Under tensile conditions, all laminates have shown roughly the same Young's modulus (E) (40 GPa). However, all bioinspired configurations have revealed to fail at lower tensile stresses. On the other hand, while LS configuration has failed catastrophically, both Bouligand-like layups have shown a much progressive failure mode;
- When compared to LS reference layup, both Bouligand-like laminates have revealed higher flexural moduli in the 3-PB tests, whereas HYB layup has demonstrated a slightly reduction on this property. Moreover, all bioinspired structures have developed translaminar failure mode, which lead to a lower load bearing capability, while LS layup has shown a catastrophic failure in one of the 0° layers inside the laminate;
- Both Bouligand-like laminates have shown similar interlaminar shear strength (ILSS) to that of LS reference, while the larger resin volume fraction brought superior performance to the HYB layup. It has been also found good corelation between finite element models and the failure mode of the reference and both Bouligand-like arrangements. The large amount of weft threads in the HYB layup has shown to play an important role on its failure mode.

Low velocity impact (LVI) mechanical response of laminates was evaluated at the following three different energy levels: 13.5, 25 and 40 (J). Independently on impact energy level, all new bioinspired layups have delayed damage onset for higher loads (P_{cr}) and energies (E_{cr}), when compared to the reference LS one. At 13.5 J, all laminates revealed to have similar load bearing capability but, for the higher impact energy

level of 25 and 40 (J), both Bouligand-like structures demonstrated to withstand larger impact loadings. Moreover, the higher elastic response of bioinspired laminates, especially HL and HL_S arrangements, up to 25 J impact energy level, has shown to reduce final absorbed energy (E_{abs}) but, at the impact energy of 40 J, the formation of through-thickness matrix cracking has led to higher energy absorption.

Visual damage inspection has revealed that both Bouligand-like laminates have less propensity to develop back-face damage extent than all other layups, independently of the impact energy. Similar trend was observed on C-scan internal damage area evaluation, especially at 40 J of impact energy.

Results from compression after impact (CAI) tests demonstrate residual strength reduction with the increase of impact energy, for most of laminates. Moreover, due to the lower number of fibres oriented in the loading direction, comparatively to LS reference laminate, all bioinspired layups revealed to have lower residual strength after impact.

Chapter 6
Strategical Thin Veils Interleaving

When exposed to low velocity impact (LVI) solicitations, composite laminates tend to develop internal damages that may be barely visible at naked eye. The high complex field of internal stresses developed during impact, usually, causes small cracks, which may propagate throughout the interlaminar region due to the low toughness that this region exhibits. Interleaf toughening structures/materials between layers have shown to be very effective to crack propagation without seriously affect in-plane mechanical properties, however, this method, usually, introduce an extra thickness and weight to the final part.

Even though only few studies focused on low velocity impact response of composite laminates interleaved by thin veils may be found in literature, a leak of strategy is evident about the position they should be placed in the layup. Therefore, in this chapter, a finite elements model was previously built to identify the most critical interfacial stresses in a bended laminate, in order to select the best interleaving positions. This strategy intended to minimise impact damage propagation without introducing excessive thickness and weight on the laminate.

The new carbon/epoxy laminates win thin veils strategically interleaved were produced by vacuum bag infusion and their mechanical responses compared with those obtained on a non-interleaved one, produced in similar conditions. A previous experimental study over veils microstructural network was carried out and, then, all configurations were characterised physically and morphologically according their thickness, fibre/resin/veils volume fraction and voids content. Interlaminar shear strength (ILSS), three-point bending (3-PB), low velocity impact (LVI) and compression after impact (CAI) tests were performed in order to evaluate their mechanical response and damage resistance and tolerance.

6.1 Approach

The major drawback regarding interleaving toughening structures between composite plies is the increase of thickness of the final part. Therefore, in order to minimise the number of interleaved thin veils into the laminate, in this work a finite element (FE) model has first carried out using a commercial ABAQUS® software to evaluate the level of interlaminar stresses developed across the laminate thickness in bending conditions. Then, the thin veils were placed only between layers where higher discrepancies between stresses occurred.

According to Choi and Chang [20], impact damage mechanisms tend to start in the intralaminar region due to the occurrence of matrix cracks caused by shear stresses, then, initiated from those subcritical damages, delaminations tend to propagate throughout the interlaminar region induced by the presence of bending stresses. Based in this idea and being aware that interleaving approach mainly prevents damage propagation in composites interlaminar region, an elastic model was built to identify the locations where maxima interlaminar normal (σ_{11} and σ_{22}) and shear (τ_{12}) stresses occur, which theoretically should correspond to the most critical places for damage propagation. Afterwards, the six most critical interlaminar regions were interleaved with thin veils made from four different materials, namely glass, carbon, aramid and polyester fibres.

The mechanical behaviour of the interleaved CFRP laminates manufactured in this work were also compared with a non-interleaved layup, that is the same conventional CFRP aircraft laminate (LS) (see Table 11) used as reference in the previous chapter.

6.2 Laminates

6.2.1 Materials

All CFRP laminates were produced using the 150 g/m^2 UDCF fabrics (Dynanotex HS 24/150 DLN2) and epoxy resin from Sika® (Biresin® CR83 resin and Biresin® CH83-6 hardener), also used in Chapters 4 and 5 (see sections 3.1.1 and 3.1.2, Chapter 3).

In order to mitigate LVI impact damages, four non-woven thin veils made of glass (17 g/m^2), carbon (17 g/m^2), aramid (14 g/m^2) and polyester (17 g/m^2) fibres, provided from ACP Composites, USA, were used as interlaminar tougher. Figure 45 shows the selected interleaved veils and data sheets provided by their supplier may be found in Appendix A.

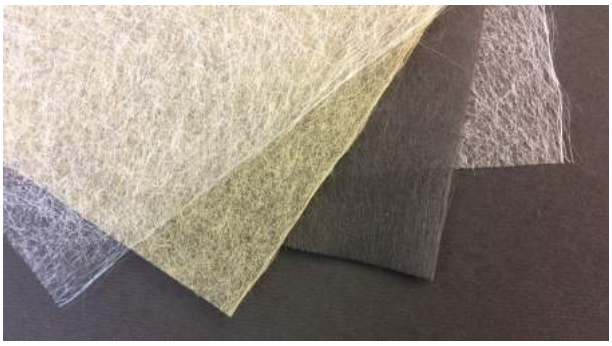

Figure 45: Photography of the selected interleaved veils.

6.2.2 Laminate manufacturing

All laminates were manufactured by vacuum bag infusion according to the procedure described in section 3.2.1, Chapter 3. The new interleaved laminates were built by introducing the selected veils in six interfaces of the standard aircraft laminate (LS) that was taken as a reference. Only 6 in 27 interfaces were chosen to be interleaved in order to avoid thickness and weight overage in the final composite. Previously, a finite element model analysis was made to select the two sets of six distinctive interfaces to be strategically interleaved, which corresponded to the locations where maximum normal and shear stresses were expected occur. The four different types of thin fibre reinforced non-woven veils (glass, carbon, aramid and polyester) were cut by a laser cutting machine before being interleaved into both previously identified locations. The three stacking arrangements used in this work, a non-interleaved and two interleaved configurations, are presented in Table 11.

Table 11: Laminates stacking sequence.

Laminate	Interleaving location	N° layers		Stacking Sequence
		UDCF tissue	Veil	
LS	-	28	-	$[0/45/90/-45/45/-45/0]_{2s}$
Interleaved laminates	Normal stresses	28	6	$[0/\mathbf{V}/45/\mathbf{V}/90/\mathbf{V}/-45/45/-45/0/0/-45/45/-45/90/45/0]_{s}$
	Shear stresses	28	6	$[0/\mathbf{V}/45/90/-45/\mathbf{V}/45/\mathbf{V}/-45/0/0/-45/45/-45/90/45/0]_{s}$

V interleaf veil

6.3 FE model

The interlaminar location of thin veils was strategically selected from a preliminary study over the normal and shear bending stresses distribution across the LS laminate thickness. For this end, a quasi-static element elastic model was built using ABAQUS® FEM software in order to identify the six most critical

interfaces (those which presented larger interlaminar bending stresses) and interleaved them with four different fibre type thin veils.

Regarding the similarity between LVI and quasi-static plate bending (QSPB) tests reported in some studies [167][168], a quasi-static elastic FE model was built to evaluate the stresses distribution across the thickness of a specimen submitted to flexure under the LVI indentation area. For that purpose, both, LS impact specimen and indenter have the very same geometry as the ones used in LVI impact tests. The indenter was modelled as a discrete rigid part, whereas the specimen was set as a solid elastic using conventional linear cubic C3D8R elements. A mesh study was carried out to ensure the realistic representation of the experimental LVI test during the elastic stage for a maximum displacement of 2.5 mm. The normal ($|\sigma_{11}|$ and $|\sigma_{22}|$) and shear ($|\tau_{12}|$) stress field of each ply was evaluated on the 20 mm square area just under the indenter, as represented in Figure 46 a), with a mesh in plane (xy) square element size of 0.1 mm. The material properties assigned to each lamina were obtained experimentally and may be consulted in Table 5 (section 4.2, Chapter 4).

The interlaminar bending stresses between two generic plies *k* were obtained by the difference between the stress in the top of the ply *k* (bottom ply) and its correspondent in the bottom of the ply *k+1* (ply above). This calculation was done for each adjacent integration points corresponding to the stresses on the top of the ply *k* and bottom of the ply *k+1* inside the impact area, and may be mathematically represented by the equation (20) for the normal stresses $|\sigma_{11}|$ and $|\sigma_{22}|$ and for the shear stresses $|\tau_{12}|$ by the equation (21).

$$|\sigma_{ij}^{k}|_{interface} = |\sigma_{ij}^{k}|_{top} - |\sigma_{ij}^{k+1}|_{bottom} \quad (20)$$

Where $/\sigma/$ is the absolute normal stress value, $k = 1$ to 27 and $i = j = 1, 2$.

$$|\tau_{ij}^{k}|_{interface} = |\tau_{ij}^{k}|_{top} - |\tau_{ij}^{k+1}|_{bottom} \quad (21)$$

Where $/\tau/$ is the absolute shear stress value, $i = 1$ and j = 2.

The maximum normal and shear interlaminar results obtained from equation 20 and 21, respectively, are presented in Table 12.

Table 12: Absolute maxima interlaminar normal ($|\sigma_{11}|$ and $|\sigma_{22}|$) and shear ($|\tau_{12}|$) stresses at each interface computed from the finite element model results. The most critical (maximum) are highlighted in bold.

Stacking order	Interface	Maximum Interlaminar Stresses		
		$\|\sigma_{11}\|$ MPa	$\|\sigma_{22}\|$ MPa	$\|\tau_{12}\|$ MPa
Bottom	1	**452,87**	**20,34**	**30,23**
|	2	**456,30**	**20,49**	24,75
	3	**368,65**	16,55	24,76
	4	336,74	15,12	**34,89**
	5	299,59	13,45	**30,38**
	6	298,19	**18,59**	30,37
	7	0	0	0
	8	182,88	8,21	9,47
|	9	150,68	6,77	12,25
|	10	113,54	5,10	7,70
|	11	66,30	2,98	3,34
|	12	47,91	2,15	3,44
|	13	85,81	3,85	4,81
↓				
Mid-plane	14	0	0	0
|	15	163,13	7,33	9,66
	16	201,86	9,06	12,23
	17	242,99	10,91	14,68
	18	179,70	10,22	14,71
	19	281,49	12,64	34,03
	20	376,30	16,90	21,94
|	21	0	0	0
|	22	470,19	21,11	27,12
|	23	437,66	19,65	**52,69**
|	24	476,78	21,41	**57,39**
|	25	**581,03**	**26,09**	36,88
↓	26	**659,61**	**29,62**	37,66
Top	27	**668,90**	**30,04**	**42,62**

It was considered most critical interfaces those which present larger interlaminar stresses, and consequently where delaminations are theoretically most prone to occur.

However, despite almost insignificant, veils tend to present in-plane anisotropic mechanical and thermal properties induced during their manufacturing process. Therefore, a symmetrical placement of those interlaminar reinforcements has been ensured to minimize potential physical twist arising from the thermal expansion during the cure and post-cure manufacturing stages.

Regarding those two above assumptions, we first identified the three most critical interfaces in each side (bottom and top side) of the laminate and then evaluated and selected the better solution in order to ensure a symmetric architecture about the mid plane.

Highlighted in bold in Table 12 are the interfaces where the normal ($|\sigma_{11}|$ and $|\sigma_{22}|$) and shear ($|\tau_{12}|$) stresses are larger, they may be also visualized graphically in Figure 46 b), c) and d), respectively.

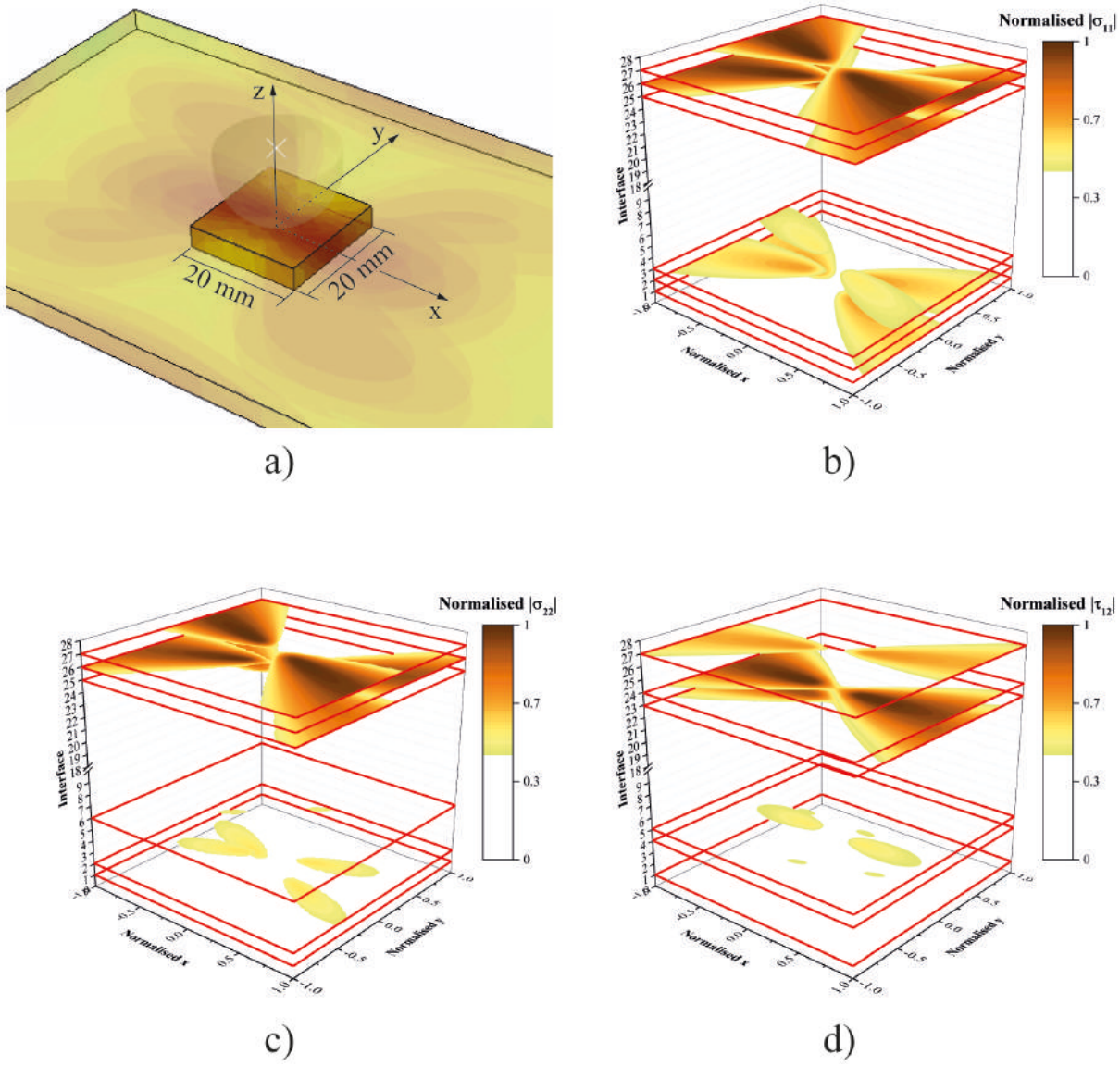

Figure 46: a) Schematic representation of the finite elements model region, b), c) and d) The six most critical (maximum) interlaminar normal ($|\sigma_{11}|$ and $|\sigma_{22}|$) and shear ($|\tau_{12}|$) stresses, respectively.

According to the results in Table 12, the most critical (maxima) interlaminar stresses are mainly located on the compression side and closer to the top of the laminate, moreover, from Figure 46 b) to d) may be seen there are two maxima interlaminar stresses per interface.

Must be noted that the six most critical normal $|\sigma_{11}|$ and shear $|\tau_{12}|$ stresses in both sides of the laminate are already symmetric regarding the laminate arrangement. On the other hand, despite to share

5 in 6 critical interfaces with $|\sigma_{11}|$, maximum $|\sigma_{22}|$ stresses present an anti-symmetric configuration. Therefore, in order to ensure a symmetric configuration and supported by the similarity of critical interfaces between maximums normal stresses $|\sigma_{11}|$ and $|\sigma_{22}|$, in this work we have considered as critical interfaces regarding the normal stresses those obtained for $|\sigma_{11}|$.

To summarise, according to the criteria described previously: i) the six most critical interfaces identified considering the normal stresses were 1st, 2nd, 3rd, 25th, 26th and 27th, whereas, ii) regarding shear stresses, the most critical interfaces were 1st, 4th, 5th, 23rd, 24th and 27th.

The two layup arrangements selected to manufacture the interleaved laminates may be seen in Table 11.

6.4 Characterization and testing

In this chapter will be presented the characterization methods and mechanical tests undertaken to evaluate and compare the different laminate performances.

6.4.1 Raw materials characterisation

All veils were first analysed under scanning electron microscope (SEM) in order to measure and morphologically evaluate the fibres used in each one. Afterwards, veils micro-structural network was analysed to assess the surface area that fibres can cover of the back-support surface. Ten samples of each veil were observed using an Olympus SZ-PT transmission magnifier (Figure 47) and then, using an image analysis software, Leica Application Suite (LAS v4.4.) from Leica, the percentage of surface covered by the fibres (darker area) was determined (Figure 48).

Figure 47: Olympus SZ-PT transmission magnifier

Figure 48 shows a schematic representation of the analysis made to determine the veil surface area covered by fibres.

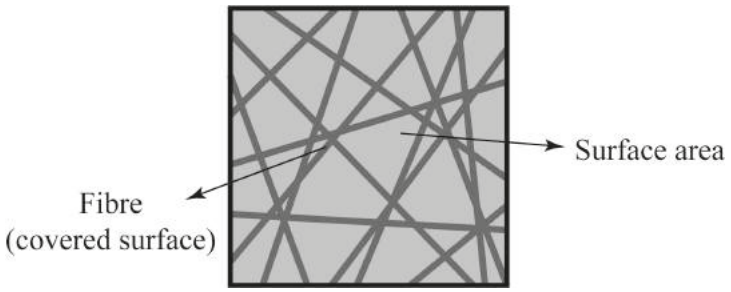

Figure 48: Schematic representation of the surface covered area by the veils.

The density was determined in all veils using the procedure described in section 4.1.1 (Chapter 4). Five samples of each material were used in these experiments.

The areal weight (g/m^2) was also experimentally assessed in all fibrous materials. Samples of each fibrous materials, namely UDCF tissues and all different veils, were first cut in a laser cutting machine in order to ensure a rigorous dimensional area. Therefore, ten 220 x 220 (mm) UDCF and 500 x 140 (mm) veils samples were individually weighted on a digital balance with accuracy of ±1x10^{-4} g. Finally, the areal weight (w_v), in g/mm^2, was calculated by the following equation (4):

$$w_v = \frac{W}{l \times b} \tag{22}$$

where, W, l and b are the sample's weight (g), length and width (mm), respectively.

In order to calculate the fibres/matrix contact area per unit of veil area, S_f, the following assumptions were taken into account:

i) Fibres cross-section is circular and uniform along their length;

ii) By neglecting the fibre cross-section, the area of the fibre in contact with the matrix A_f (mm^2) may be determined as:

$$A_f \approx 2\pi r_f l_f \tag{23}$$

where r_f and l_f are the fibre radius and length in mm, respectively;

Then, if veils are considered only made by fibres (all binding materias are disregarding), their weight W_v (g) is given by:

$$W_v = \pi r_f^2 l_f \cdot \rho_f \tag{24}$$

where ρ_f (g/mm^3) is fibre specific mass.

Being the veil areal weight, w_v (g/mm^2):

$$w_v = \frac{W_v}{A_v} = \frac{\pi r_f^2 l_f}{A_v} \cdot \rho_f \tag{25}$$

where A_V is the veil's area in mm^2;

On the other hand, by considering Eq (23) it is also possible define the fibres/matrix contact area per unit of veil area, S_f (mm^2/mm^2) as:

$$S_f = \frac{2\pi r_f l_f}{A_v} \tag{26}$$

and rewriting equation 25, as:

$$2w_v = \frac{2 \cdot \pi\, r_f \cdot r_f l_f}{A_v} \cdot \rho_f \tag{27}$$

which, by using Eq. 26, may be simplified as:

$$2w_v = S_f \cdot r_f \cdot \rho_f \tag{28}$$

Being, finnally, the fibres/matrix contact area per unit of veil area, S_f, (mm^2/mm^2) given by:

$$S_f = \frac{2 \cdot w_v}{r_f \cdot \rho_f} \tag{29}$$

or,

$$S_f = \frac{4 \cdot w_v}{d_f \cdot \rho_f} \tag{30}$$

where d_f is the fibre diameter in mm.

6.4.2 Laminates characterisation

A caliper rule was used to measure the thickness of each laminate and determine its increment caused by the incorporation of veils. The cross-section and void content of each laminate were analysed and evaluated under SEM on four carefully polished samples randomly picked up from them.

In order to assess carbon fibres and veils volume fractions in laminates, the density and areal weigh of each laminate were determined. Five samples were randomly cut from each tested composite and their own specific mass was determine by using the same methodology described for raw materials in the previous section. Then, length, width and weight were carefully measured on six impact specimens of each layup by using a calliper rule and a digital balance with an accuracy of $\pm 1\times10^{-4}$ g, respectively. Finally, laminates areal weight (w_L), in g/mm^2, was determined according equation 31.

$$w_L = \frac{W}{l \times b} \tag{31}$$

where W is the specimen mass and l and b its length and width, respectively.

Considering that w_L is the sum of UDCF (w_{cf}), veils (w_v) and matrix (w_m) areal weights, determined in according the previous section;

$$w_l = n_{cf} w_{cf} + n_v w_v + w_m \tag{32}$$

where n_{cf} and n_v are the number of UDCF and veils layers, respectively.

Since each laminate and its components have the same area, we may say that:

$$W_l = n_{cf} W_{cf} + n_v W_v + W_m \tag{33}$$

where W_c, W_{cf}, W_v and W_m, are the weight of laminate, UDCF, veils and matrix, in g, respectively.

Dividing every member of Eq. 33 by the respective specific mass:

$$W_l/\rho_l = {}^{n_{cf} W_{cf}}/_{\rho_{cf}} + {}^{n_v W_v}/_{\rho_v} + W_m/\rho_m \tag{34}$$

where ρ_l, ρ_{cf}, ρ_v and ρ_m, are the specific mass of the laminate, UDCF, matrix and veils in g/cm^3, respectively.

We may rewrite Eq. 34 in terms of volume, as:

$$V_l = V_{cf} + V_v + V_m \tag{35}$$

where V_l, V_{cf}, V_v and V_m, are the volume of the composite, UDCF, veils and matrix in cm^3, respectively.

Then, dividing both sides of Eq. 35 by the total laminate volume we obtain:

$$1 = v_{cf} + v_v + v_m \tag{36}$$

where v_{cf}, v_v and v_m, are the UDCF, veils and matrix volume fractions, respectively.

Therefore, the UDCF volume fraction is given by;

$$v_{cf} = \frac{n_{cf} W_{cf} / \rho_{cf}}{W_l / \rho_l} \times 100 \quad (37)$$

The veil volume fraction by;

$$v_v = \frac{n_v W_v / \rho_v}{W_l / \rho_l} \times 100 \quad (38)$$

and the matrix volume fraction by;

$$v_m = \frac{W_m / \rho_m}{W_l / \rho_l} \times 100 \quad (39)$$

or,

$$v_m = 1 - v_v - v_{cf} \quad (40)$$

6.4.3 Quasi-static mechanical tests

6.4.3.1 Three-Point Bending (3-PB) tests

Regarding laminates flexural properties, three-point-bending tests were performed according with procedure and equipment described in section 3.4.2 (Chapter 3). Tests were carried out on five 170 x13 (mm) specimens of each laminate and under similar conditions to that ones already described in section 5.3.2.2 (chapter 5) for the tests made on the bioinspired layups.

Finally, the laminates failure modes were analysed and compared to each other using a digital magnifier Leica DMS1000 (Figure 15, section 3.4.2).

6.4.3.2 Interlaminar Shear Strength (ILSS) tests

Interlaminar shear strength tests were performed in accordance with ISO 14130 standard, described previously in section 3.4.3, Chapter 3. All experiments were performed using the same equipment, similar 40mm × 20 (mm) specimens and under equal conditions to that ones already described before in section 5.3.2.3 for the tests made on the bioinspired laminates.

Furthermore, the failure mode of each configuration was also analysed under the Leica DMS1000 digital magnifier (Figure 15, section 3.4.2) and compared to each other.

6.4.4 Low Velocity Impact (LVI) tests

The LVI tests were performed by using the equipment and procedure described in section 3.4.4 (Chapter 3). Such as happened in the case of the bioinspired Bouligand-like layups (see section 5.3.3, Chapter 5), three specimens of each interleaved laminate were submitted to three different impact energy levels (13.5 J, 25 J and 40 J).and the results obtained compared to those ones found in the four tested specimens of the reference LS one (non-interleaved), already presented in previous bioinspired Bouligand-like architectures chapter.

Table 13 summarises the LVI testing conditions used.

Table 13: LVI test conditions resume.

Impact Energy level	Number of specimens		Impactor	
			Height	Weight
	Non-interleaved (LS)	Interleaved	m	kg
13.5	4	3	0.273	5.045
25	4	3	0.505	5.045
40	4	3	0.810	5.045

Impact external damage of all specimens were carefully visually inspected and, when existing, back-face damage was measured using a caliper rule.

Internal damages were also evaluated by ultra-sounds using the equipment of the industrial partner, Ria Blades.SA, already described in section 5.3.3 and shown in Figure 25 (Chaper 5), after samples have been also properly prepared in the same conditions also described in the same section.

6.4.5 Compression after impact (CAI) tests

Regarding the large number impact tested specimens (3 specimens x 9 condition x 3 energy levels = 81 impacted specimens), for logistic and economic reasons, only those submitted at 25 J of impact energy

were considered to CAI tests. All experiments were conducted in INEGI – Instituto de Ciência e Inovação em Engenharia Mecânica, Porto, in accordance with the procedure described in section 3.4.5 (Chapter 3).

6.5 Results

This section presents the main results and observations obtained from the following tests: i) veils / laminates physical and morphologic characterization, ii) quasi-static mechanical tests, namely, the three-point bending (3-PB) and interlaminar shear strength (ILSS) tests, iii) low velocity impact (LVI) tests and iv) Compression after impact (CAI).

6.5.1 Raw materials characterisation

Before laminates manufacturing, UDCF tissue (Dynanotex HS 24/150 DLN2) areal weight was determined, since resin Biresin CR83 and UDCF Dynanotex HS 24/150 DLN2 fabric densities were already determined in section 4.1.1 (Chapter 4), and values obtained may be consulted in Table 2 (section 4.2, Chapter 4).

Table 14 presents the experimental result obtained.

Table 14: UDCF tissue average (± standard deviation) areal weight.

Material	Areal weight
	g/m²
UDCF tissue Dynanotex HS 24/150 DLN2	136.47 ± 1.66

Four different low-weight veils were used to strategically interleaf the baseline LS laminate. In order to characterise their micro-structures, several experiments and observations were undertaken. Some of the main experimentaly determined characteristics of veils are presented in Table 15.

From SEM observations (Figure 49), it was possible to conclude that, contrary to the other veils, the polyester fibre veil was composed by trilobal cross-section fibres (Figure 49 d)), while glass, carbon and aramid fibres (Figure 49 a) to c), respectively) presented almost circular cross-section. Moreover, those images showed that glass, aramid and polyester fibres presented an apparent smooth surface, whereas the carbon ones had a rough interface.

Table 15: Fibres diameter and perimeter and veils thickness†, specific mass, areal weight, specific fibre surface area, and covered surface

		Glass	Carbon	Aramid	Polyester
Fibre	Diameter (μm)	13.35 ± 0.82	7.11 ± 0.71	15.72 ± 1.30	35.17 ± 1.97‡
	Perimeter (μm)	41.94 ± 2.59§	22.32 ± 2.23§	49.39 ± 4.07§	110.51 ± 6.18
Veil	Thickness (μm)	127.0†	139.7†	132.1†	119.4†
	Specific Mass (g/cm^3)	2.19 ± 0.08	1.88 ± 0.07	1.47 ± 0.06	1.40 ± 0.03
	Areal Weight (g/m^2)	18.7 ± 0.3	22.2 ± 1.1	15.3 ± 0.3	17.2 ± 0.3
	Spec. Fibr Surf. Cont. A. (mm^2/mm^2)	2.56	6.64	2.65	1.40
	Covered Surface (%)	46.6 ± 2.0	70.8 ± 3.1	57.0 ± 4.2	56.0 ± 6.1

† Data from datasheet (Appendix A)
‡ Equivalent diameter was computed from $d=p/\pi$, where d and p are the equivalent diameter and measured perimeter in μm, respectively.
§ Perimeter computed from $p=d\pi$.

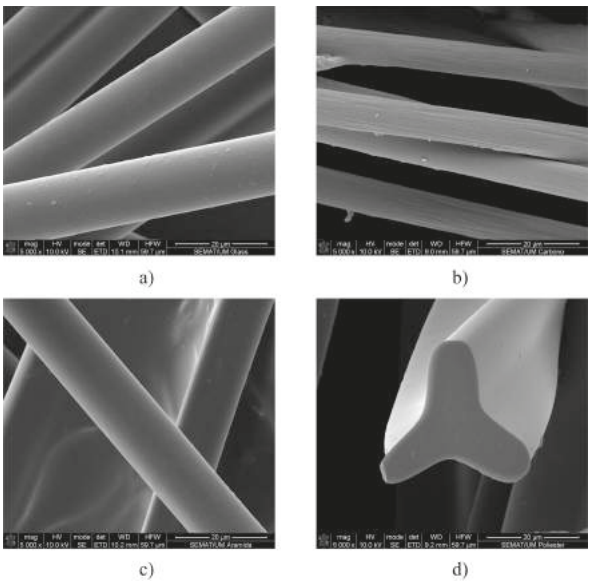

Figure 49: SEM images of veils fibres magnified 5000 times, where a) is the glass, b) carbon, c) aramid and d) polyesters fibre veils.

In order to determine veils fibre diameter and perimeter, ten SEM images of each veil were analysed and measured using the commercial graphic design software Illustrator 2020 v24.0.0 from Adobe. Diameters of glass, carbon and aramid fibres were directly assessed from SEM images and then their perimeter was calculated. However, in the case of polyester fibres their perimeter was first measured and, only posteriorly, the equivalent diameter was computed. The measurements have shown that polyester fibres presented the larger perimeter, followed by aramid, glass and carbon, respectively.

Veils were also analysed regarding their micro-structural fibrous network. Under transmission magnification, their permeable surface was observed in order to determine the back-surface area that they are able to cover. Results from treated images revealed that carbon fibre veil is the one whose covered more area of the support surface (71 %), followed by aramid (57 %), polyester (56 %) and glass fibre ones (47 %).

Figure 50 shows a black and white image representative of each veil from whose black areas (covered surface) were measured.

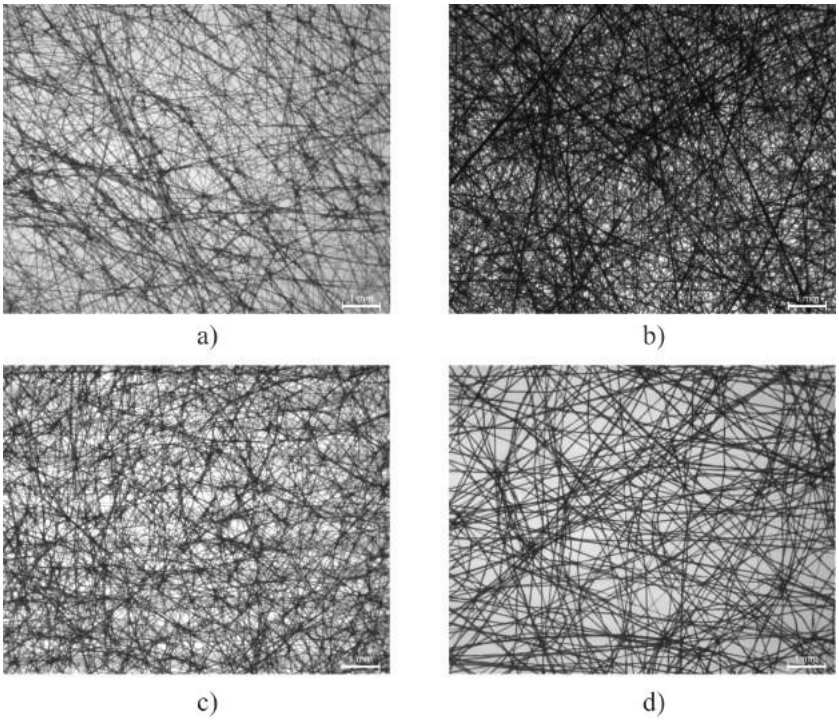

Figure 50: Black and white images of a) glass, b) carbon, c) aramid and d) polyester fibre veils observed under the transmission magnifier.

In most of the cases, the experimental veil analysis have shown different areal weigths than those ones claimed for the provider on material datasheets. With the exception of polyester fibre veil, which have presented a similar areal unit weight of its respective datasheet (17 g/m^2), all the other veils presented higher values, namely, carbon (the highest one, with 22 g/m^2), followed by glass, with 19 g/m^2, and aramid veil, with an areal unit weigth of 15 g/m^2.

Finally, the results of fibre surface contact area per unit of veil area (S_f) revealed that, in spite of being composed of fibres with the smallest perimeter, carbon fibre veil was the one whose dispose of higher contact area with matrix, which corresponds to 3.7, 2.2 and 1.7 times more than polyester, glass and aramid veils, respectively.

6.5.2 Laminate characteristics

Several tests were carried out regarding laminates characterisation, namely, thickness and density determination, cross-section and voids analysis, and UDCF and veils volume fraction content.

Table 16 presents the results obtained from those tests.

Table 16: Laminates average (± standard deviation) thickness, specific mass and volume fraction of UDCF and veils.

Laminate	Interleaving location	Thickness	Specific mass	Volume fraction	
				UDCF	Veils
		mm	g/cm³	%	%
LS	Non-interleaved	3.83 ± 0.05	1.48 ± 0.01	62.0	-
Glass veil interleaved	Normal stresses	4.32 ± 0.07	1.44 ± 0.00	54.2	1.2
	Shear stresses	4.22 ± 0.03	1.43 ± 0.00	54.5	1.2
Carbon veil interleaved	Normal stresses	4.77 ± 0.21	1.41 ± 0.00	49.7	1.4
	Shear stresses	4.22 ± 0.04	1.43 ± 0.00	53.8	1.5
Aramid veil interleaved	Normal stresses	4.55 ± 0.05	1.42 ± 0.00	51.8	1.4
	Shear stresses	4.23 ± 0.03	1.42 ± 0.01	53.0	1.4
Polyester veil interleaved	Normal stresses	4.42 ± 0.03	1.43 ± 0.00	53.3	1.7
	Shear stresses	4.15 ± 0.03	1.43 ± 0.00	54.8	1.8

As may be seen, veils inclusion increased the thickness and reduced specific mass of interleaved laminates.

Figure 51 shows the interleaved laminates stratigraphy observed under SEM. In those images it is possible to observe interleaved layers pointed by an arrow on the left side of each laminate. As may be seen, due to the high porosity of the veils fibrous network, interleaved regions presented higher volume of resin than the zones occupied by UDCF. This characteristic morphology increased laminate's thickness, at least 8 % (polyester veils interleaved in critical shear stresses location) and reduced up to 12 % UDCF volume fraction in the case of carbon veils interleaved into the most critical normal stresses interlaminar regions.

SEM observations were also used to inspect the presence of voids into the laminates after processing. Figure 52 presents a representative image of each interleaved laminates. From images may be seen that laminates interleaved in critical normal stresses interlaminar regions tended to present more and larger voids than those interleaved in critical shear stresses interplies. In most of the cases voids tend to be formed into or close to interleaved layers, with the exception of the polyester interleaved structure, where they seem to appear mostly in inner regions.

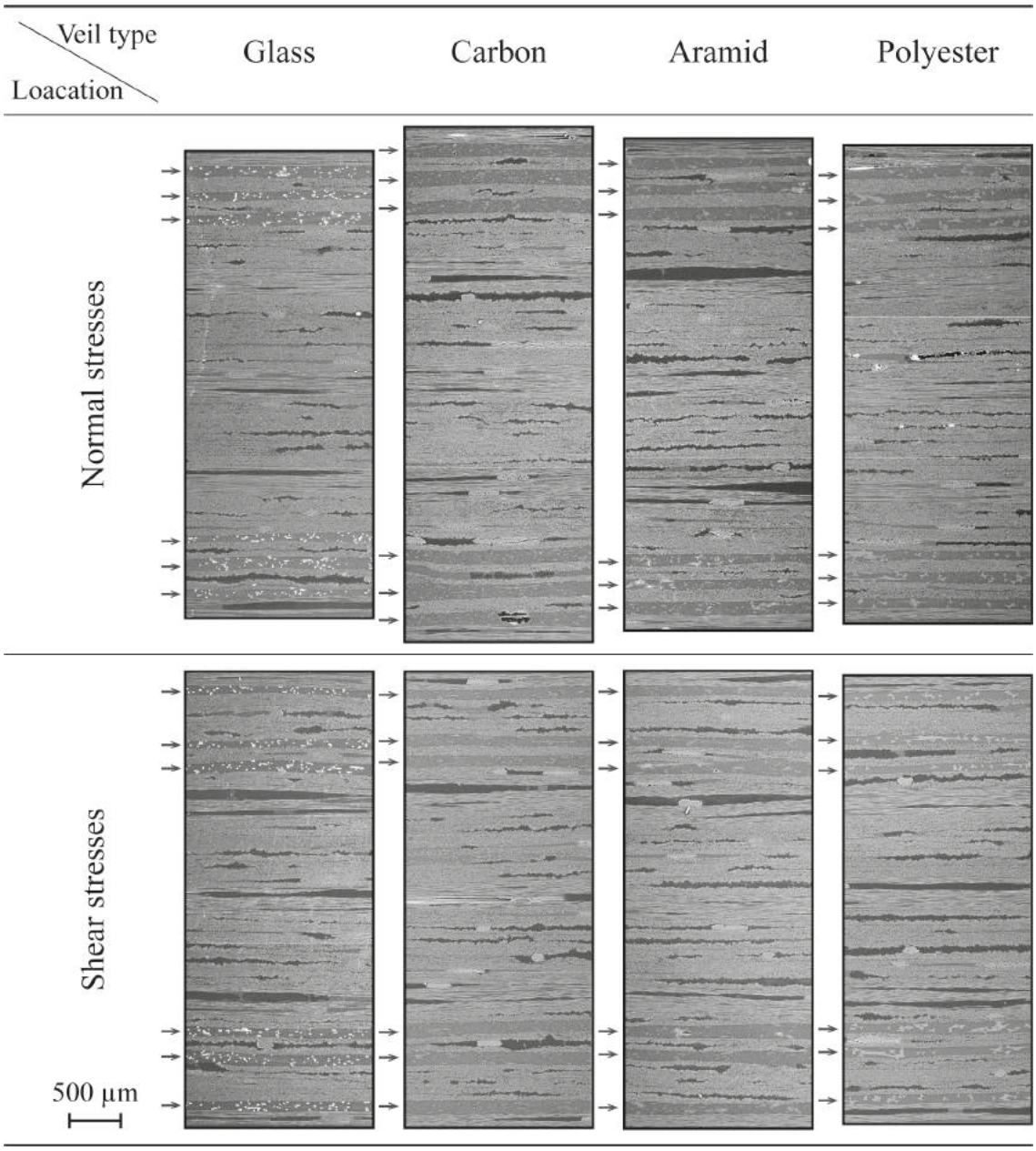

Figure 51: SEM observation of interleaved laminates stratigraphy.

Furthermore, SEM visualisations did not reveal a significant presence of voids into the laminate interleaved with polyester veils on the most critical shear stresses positions. Non-interleaved LS laminate, inspected in a previous section 5.4.1.4.1 (Chapter 5), didn't show also any presence of voids.

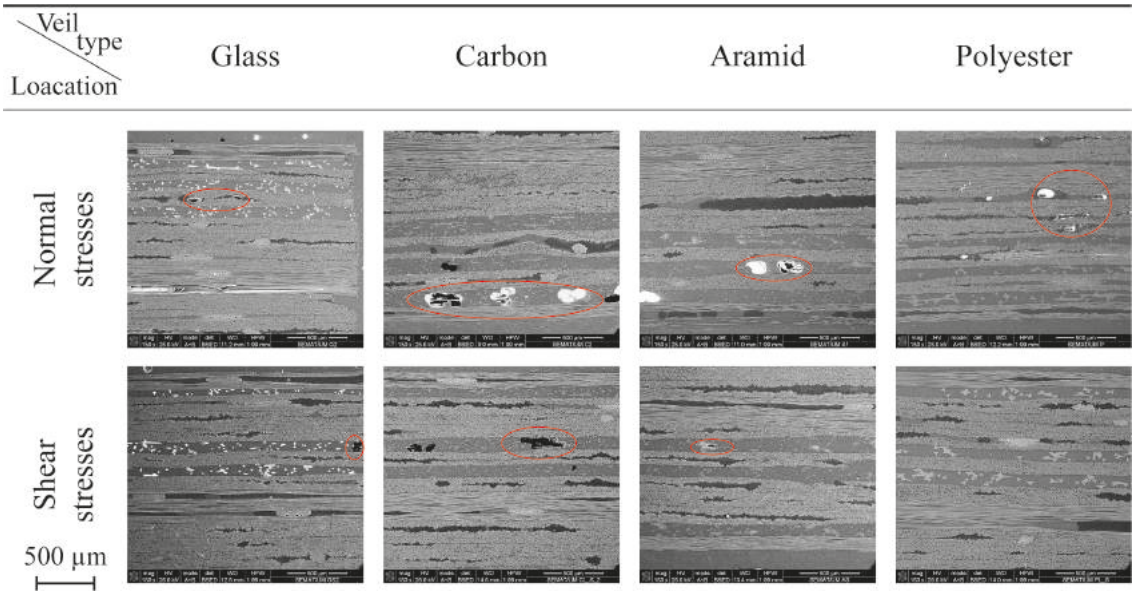

Figure 52: Voids images of observed by SEM magnified 150 times.

6.5.3 Quasi static mechanical test results: 3-PB and ILSS

Non-interleaved and interleaved composites were experimentally submitted to three-point bending (3-PB) and interlaminar shear strength (ILSS) tests in order to evaluate and compare their mechanical performance.

Table 17 presents the main results obtain from those tests, namely, 3-PB flexural modulus ($E_{flex.}$) and maximum outer surface stresses ($\sigma_{out.surf.}$), and ILSS maximum interlaminar shear stresses (τ_{13}) of each laminate.

Table 17: Average and (±) standard deviation of 3-PB flexural modulus ($E_{flex.}$) and maximum outer surface stresses ($\sigma_{out.surf.}$); and ILSS maximum shear stresses (τ_{13}).

Laminate	Interleaving location	3-PB		ILSS
		$E_{flex.}$	$\sigma_{out.surf.}$	τ_{13}
		GPa	MPa	MPa
LS	Non-interleaved	38.2 ± 1.3	461.6 ± 25.3	18.8 ± 0.9
Glass veil interleaved	Normal stresses	33.4 ± 1.8	441.1 ±18.8	23.6 ± 1.0
	Shear stresses	33.7 ± 0.5	438.5 ± 17.2	24.5 ± 0.7
Carbon veil interleaved	Normal stresses	31.7 ± 0.9	415.5 ± 6.5	23.1 ± 0.3
	Shear stresses	33.8 ± 0.9	425.3 ± 16.2	22.7 ± 1.0
Aramid veil interleaved	Normal stresses	31.7 ± 0.6	418.1 ± 13.4	23.0 ± 0.3
	Shear stresses	33.3 ± 0.8	426.0 ± 16.2	24.6 ± 0.3
Polyester veil interleaved	Normal stresses	32.9 ± 0.8	443.2 ± 19.2	23.7 ± 0.5
	Shear stresses	34.5 ± 0.7	444.6 ± 35.1	23.4 ± 0.5

6.5.3.1 3-PB test

In Figure 53 may be seen load vs displacement curves obtained from 3-PB tests of each laminate. The analysis of those curves revealed that non-interleaved LS laminate was able to withstand similar loads as the interleaved ones, but it tends also to fail at lower displacements than the latter ones. Results have also shown that the interleaved laminates, where shear stresses are more critical, tended more to fail earlier and at lower loading conditions than those interleaved in the normal stresses critical interplies.

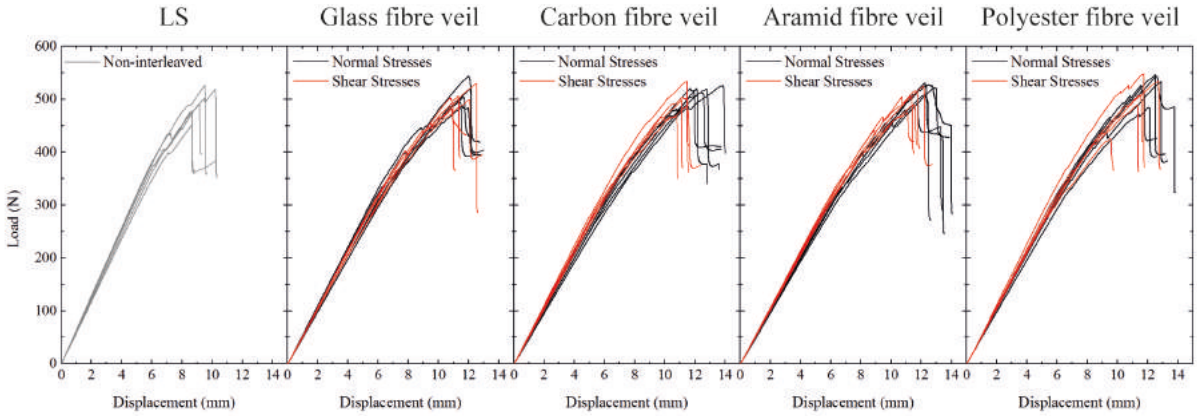

Figure 53: 3-PB load vs. displacement curves obtained from non-interleaved and interleaved laminates.

Figure 54 a) and b) present a graphical representation of maximum bending stresses on the bottom outer surface ($\sigma_{out.surf.}$) and flexural elastic modulus ($E_{flex.}$) obtained from the 3-PB tests in each laminate structure, respectively. In both cases it is possible to observe a reduction of these characteristic properties in all interleaved laminates when compared to the refence non-interleaved LS one. However, in most of the cases, the laminates reinforced in the critical shear stresses intralayers seem to present slight better performances than those interleaved in other strategical positions (critical normal stresses intralayers).

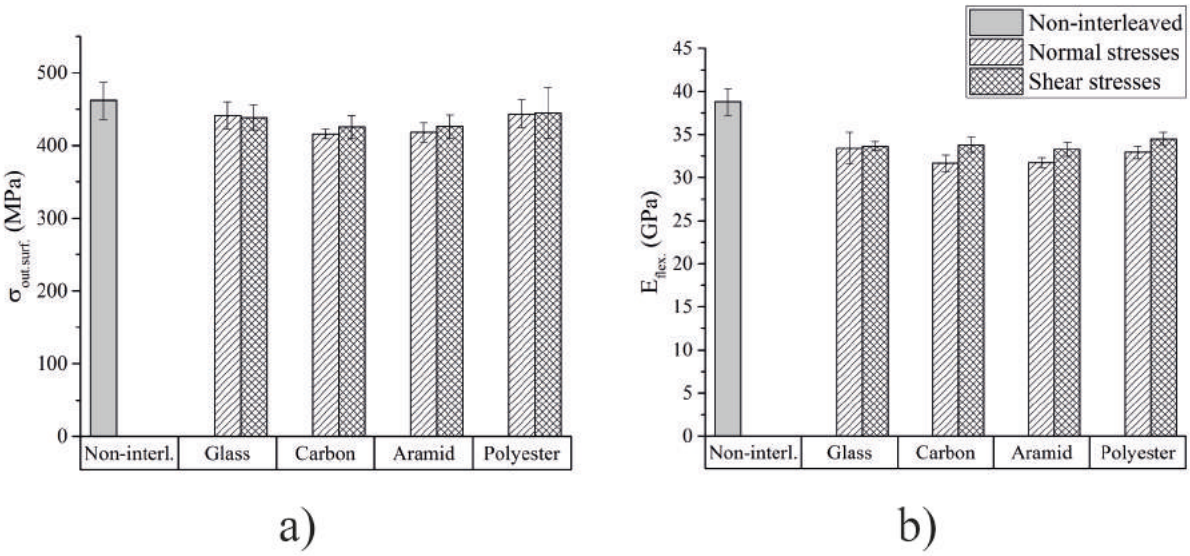

Figure 54: 3-PB results of a) maximum outer surface stresses and b) flexural modulus of non and interleaved laminates.

According to the results, no significant difference in terms of maximum outer surface stresses were found between interleaved laminates (considering standard deviation) and, on the other hand, regarding the flexural modulus, it seems that interleaving location play a more important role on its magnitude than the veil fibre material.

Figure 55 depicts the characteristic failure modes developed in each interleaved laminate. The digital magnifier photographs showed that independently of interleaved veil and position, all laminates tended to present larger failures on specimen's compression side (upper side on photographs). However, it is interesting to notice that, contrary to laminates interleaved in the critical normal stresses' interfaces, the critical interlaminar shear stresses reinforced structures seemed to resist better to tensile failures, especially those where polymeric and aramid based veils were used.

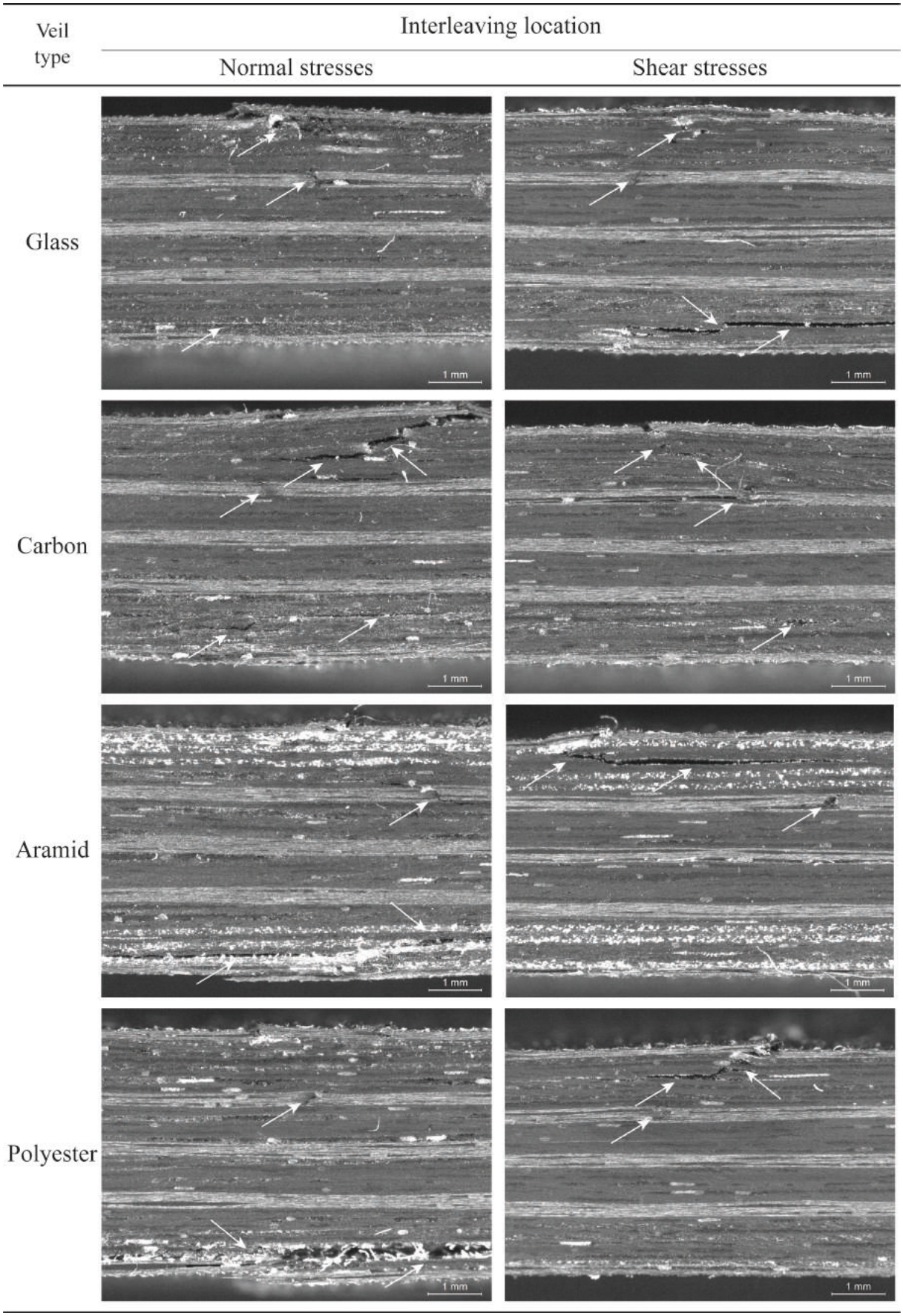

Figure 55: Characteristic 3-PB failure mode of different interleaved laminates.

6.5.3.2 ILSS test

Figure 56 shows a graphically representation of the maximum shear stresses (τ_{13}) obtained from ILSS results in both non-interleaved and interleaved laminates.

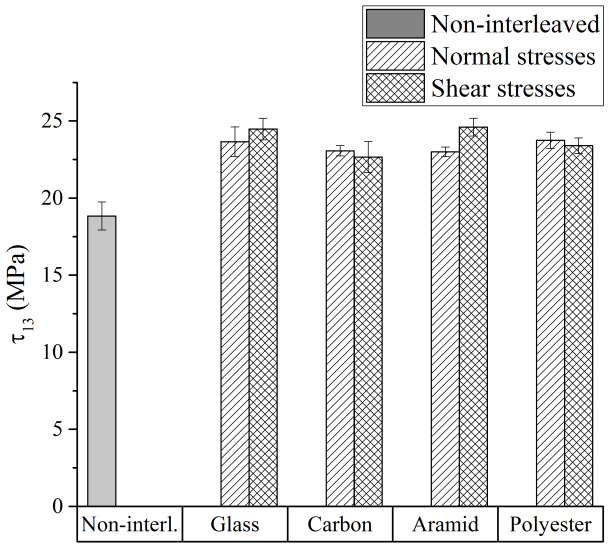

Figure 56: ILSS maximum shear stresses (τ_{13}) obtained for non-interleaved and interleaved laminates.

As may be seen from chart, independently on the location or interleaved veil, all modified laminates revealed an improvement of their global interlaminar shear resistance. Apparently, when placed into the most critical shear stresses interfaces, glass and aramid fibre veils seem to contribute more to increase the interlaminar shear strengths, independently of the location they were used. However, no significative differences in terms of interlaminar shear strengths were found between the different veils or position where they were used.

In Figure 57 may be seen photographs of the characteristic failure mode observed under digital magnifier in each interleaved laminate.

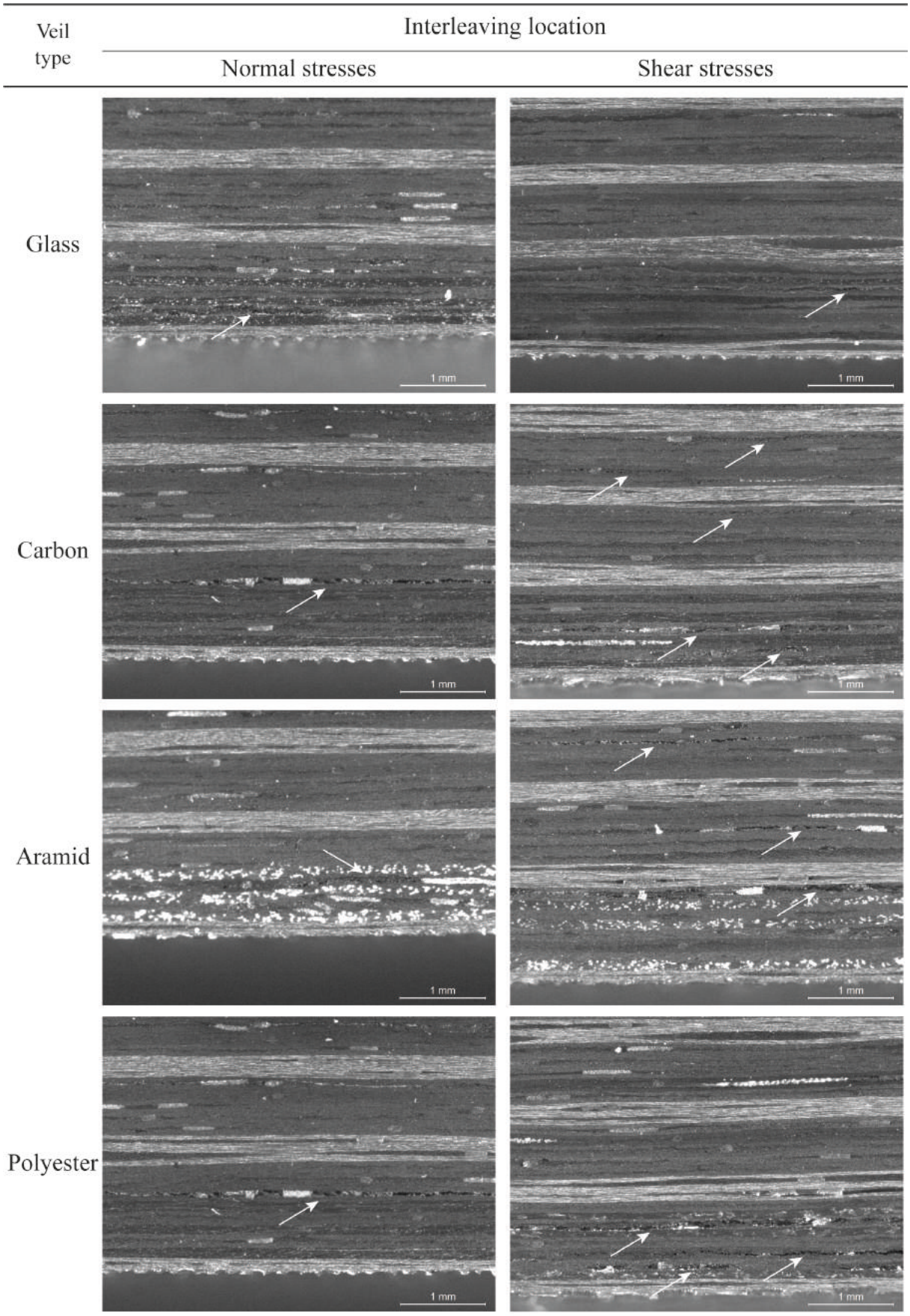

Figure 57: Photographs of the typical failure mode of different interleaved laminates.

6.5.4 Low Velocity Impact (LVI) tests results

In order to evaluate laminates impact resistance, all of them were submitted to three different levels of impact energy LVI tests, namely 13.5 J, 25 J and 40 J. Regarding the large amount of different laminates (total of nine distinctive structures) and since LVI tests are expensive and time-consuming, four non-interleaved and three specimens of each interleaved laminate were submitted to each impact energy level.

In Figure 58 shows typical load vs displacement curves obtained in all layups from the tests at the three impact energy levels. The reliability of the tests may be confirmed by the overlapping of curves that occurred in each laminate submitted to the same impact conditions.

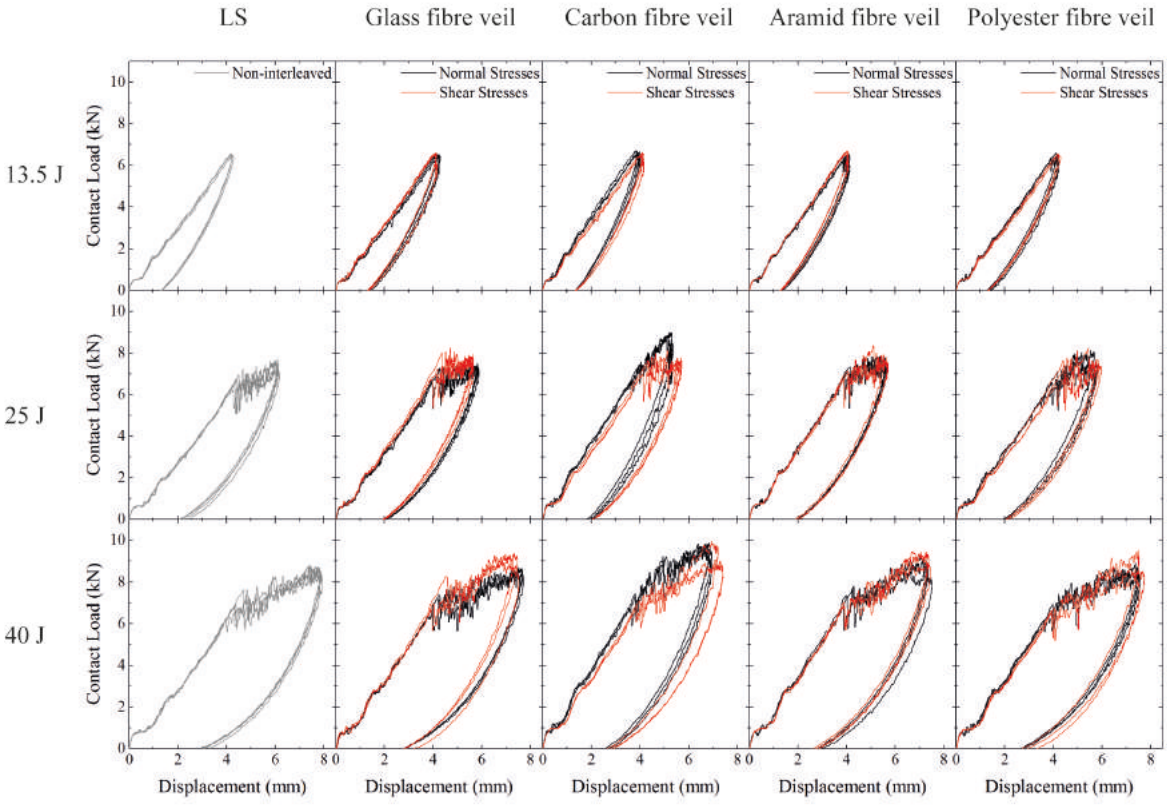

Figure 58: Load vs displacement curves of each layup arrangement (columns) for the three different impact energy levels (rows)

The LVI mechanical response of each structure was analysed according four characteristic values accessed from experimental data, namely peak and critical load (P_{cr}), and critical (E_{cr}) and final absorbed (E_{abs}) energy. Those values, calculated to each laminate for the three different impact energy levels, may be seen in Table 18. In this table it is also possible to access the maximum impact energy (E_{max}) recorded for each impact energy level and to verify that it has shown to be slightly superior than that the previously selected one for testing.

Table 18: Results from the LVI tests made in each laminate at the three different impact energy levels.

Imp. level	Interl. veil	Int. location	Peak Load	P_{cr}	E_{max}	E_{cr}	E_{abs}
			kN	kN	J	J	J
13.5	Non-int.	-	6.28 ± 0.16	5.97 ± 0.20	13.73 ± 0.00	12.11 ± 1.12	6.87 ± 0.63
	Glass	Normal	6.52 ± 0.04	6.39	13.72 ± 0.00	13.63	6.61 ± 0.37
		Shear	6.57 ± 0.04	6.40	13.71 ± 0.00	13.22	6.71 ± 0.46
	Carbon	Normal	6.66 ± 0.03	6.52	13.70 ± 0.00	12.63	6.97 ± 0.21
		Shear	6.59 ± 0.02	6.48	13.71 ± 0.00	13.05	6.83 ± 0.31
	Aramid	Normal	6.50 ±0.05	6.42 ± 0.01	13.71 ± 0.00	12.32 ± 0.08	7.06 ± 0.40
		Shear	6.67 ± 0.02	6.50	13.71 ± 0.00	13.24	6.62 ± 0.38
	Polyester	Normal	6.51 ± 0.07	6.37 ± 0.03	13.71 ± 0.00	12.53 ± 0.60	6.77 ± 0.40
		Shear	6.50 ± 0.05	-	13.72 ± 0.00	-	6.30 ± 0.11
25	Non-int.	-	7.48 ± 0.19	6.60 ± 0.28	25.29 ± 0.00	13.57 ± 0.53	15.33 ± 0.50
	Glass	Normal	7.44 ± 0.09	7.07± 0.25	25.27 ± 0.00	13.90 ± 0.98	15.61 ± 0.08
		Shear	7.99 ± 0.20	7.31 ± 0.53	25.26 ± 0.00	14.74 ± 1.36	15.37 ± 0.25
	Carbon	Normal	8.87 ± 0.09	6.90 ± 0.39	25.25 ± 0.00	12.82 ± 1.16	15.03 ± 1.04
		Shear	7.95 ±0.14	7.39 ± 0.32	25.27 ± 0.00	15.26 ± 1.00	15.72 ± 0.18
	Aramid	Normal	7.70 ± 0.17	7.12 ± 0.17	25.26 ± 0.00	14.04 ± 0.68	15.62 ± 0.09
		Shear	7.92 ± 0.33	6.98 ± 0.16	25.26 ± 0.00	13.63 ± 0.68	15.50 ± 0.15
	Polyester	Normal	7.88 ± 0.24	6.45 ± 0.57	25.27 ± 0.00	12.21 ± 1.94	15.39 ± 0.74
		Shear	7.92 ± 0.35	7.17 ± 0.52	25.28 ± 0.01	14.64 ± 1.33	15.52 ± 0.12
40	Non-int.	-	8.71 ± 0.11	6.88 ± 0.51	40.47 ± 0.00	14.08 ± 1.79	27.73 ± 0.25
	Glass	Normal	8.59 ± 0.11	7.10 ± 0.28	40.45 ± 0.00	14.15 ± 0.88	27.38 ± 0.31
		Shear	9.23 ± 0.18	7.30 ± 0.70	40.44 ± 0.01	14.53 ± 2.25	27.75 ± 1.18
	Carbon	Normal	9.84 ± 0.05	6.90 ± 0.26	40.42 ± 0.00	12.73 ± 0.78	27.02 ± 0.76
		Shear	9.31 ± 0.47	6.90 ± 0.18	40.44 ± 0.00	12.97 ± 0.49	27.05 ± 0.77
	Aramid	Normal	8.94 ± 0.33	7.29 ± 0.44	40.44 ± 0.00	14.33 ± 1.32	27.90 ± 0.52
		Shear	9.25 ± 0.27	6.91 ± 0.09	40.44 ± 0.00	13.04 ± 0.12	26.93 ± 0.75
	Polyester	Normal	8.72 ± 0.13	6.56 ± 0.31	40.45 ± 0.00	12.32 ± 0.97	27.32 ± 0.28
		Shear	8.97 ± 0.42	6.63 ± 0.10	40.45 ± 0.00	12.64 ± 0.25	27.76 ± 1.60

A graphical representation of LVI characteristic results, namely peak load, critical load (P_{cr}), final absorbed energy (E_{abs}) and critical energy (E_{cr}), may be seen in Figure 59 a) to d), respectively.

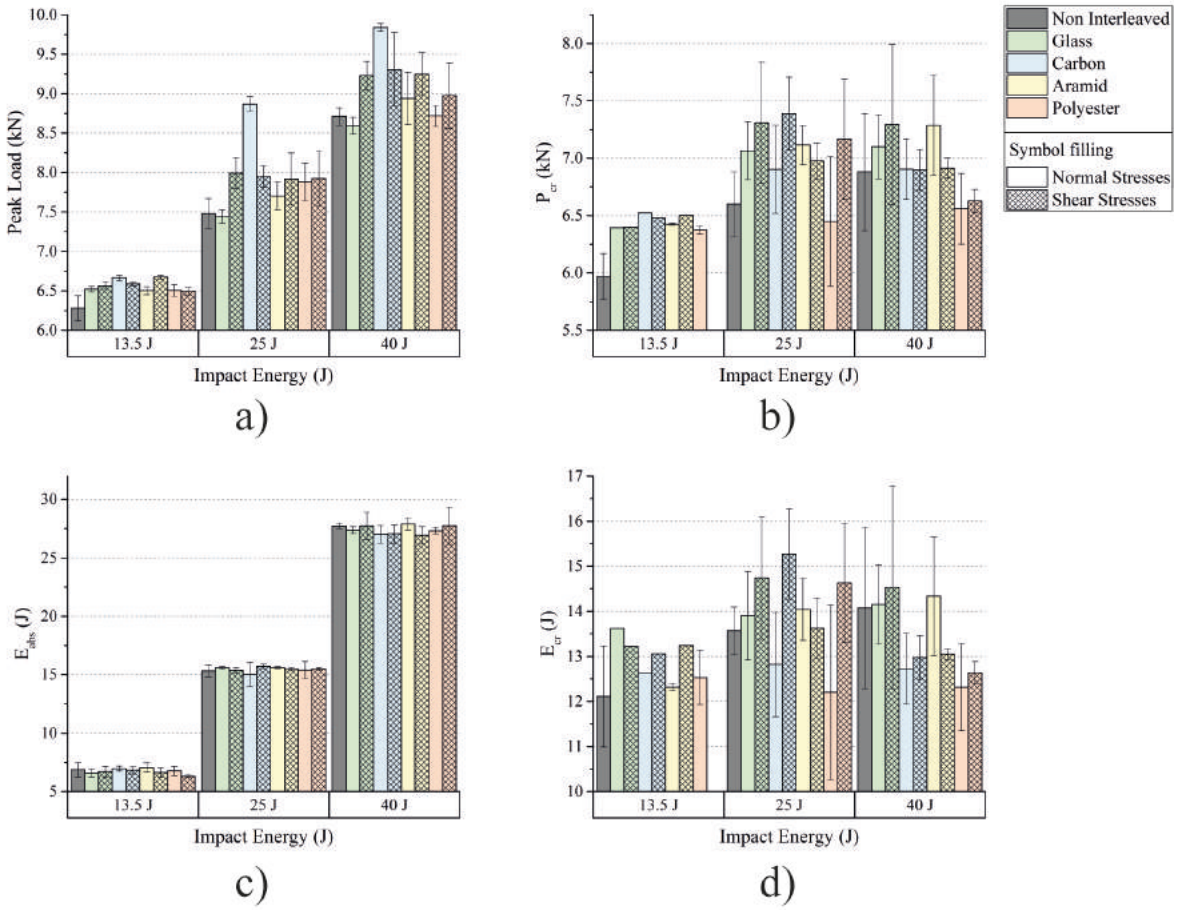

Figure 59: Graphical representation of a) peak load, b) critical load (P_{cr}), c) final absorbed energy (E_{abs}) and d) critical energy (E_{cr}) of each configuration for the three different impact energy levels.

The comparison between the experimental results obtained from the LVI tests in the interleaved laminates and those ones of the LS non-interleaved layup have shown:

At 13.5 J impact energy level;

- All interleaved laminates have presented higher peak load, however, between them, no significant differences were found (Figure 59 a));
- Not all specimens have presented P_{cr} at this impact energy level, as may be seen in the summary of results obtained in Table 19. However, in average, all interleaved laminates have presented higher load bearing capability before severe damages take place (higher P_{cr}, in Figure 59 b)), moreover, none of the specimens of interleaved laminate with polyester veils in the critical shear stresses have presented P_{cr};

Table 19: Number of specimens which presented Pcr during LVI tests at 13.5 J of impact energy.

Laminate	Interleaving location	N° specimens	N° of specimens with P_{cr}
LS	Non-interleaved	4	2
Glass veil interleaved	Normal stresses	3	1
	Shear stresses	3	1
Carbon veil interleaved	Normal stresses	3	1
	Shear stresses	3	1
Aramid veil interleaved	Normal stresses	3	2
	Shear stresses	3	1
Polyester veil interleaved	Normal stresses	3	2
	Shear stresses	3	0

- No significant differences were found between non-interleaved and interleaved laminates in terms of E_{abs},as may be seen in Figure 59 c). However, a slight lower energy absorption capability was observed on interleaved laminate with polyester veils in critical shear stresses;
- All interleaved laminates have demonstrated to absorb more energy before damage onset (E_{cr}), moreover, interleaved laminate with polyester veils in critical shear stresses has able to absorb all impact energy without any severe damage indicator;

At 25 J impact energy level;

- With the exception of interleaved laminate with glass veils in critical normal stresses, all the other interleaved laminates have shown higher peak load, especially interleaved laminate with carbon veils in critical normal stresses (Figure 59 a));
- All interleaved specimens have presented P_{cr}. With the exception of interleaved laminate with polyester veils in critical shear stresses, all configurations have shown higher load bearing capability before severe damages take place (higher P_{cr}, as may be seen in Figure 59 b));
- Once again, no significant differences were found between laminates in terms of final absorbed energy (E_{abs} in Figure 59 c));
- Interleaved laminates with carbon and polyester veils in critical normal stresses have shown lower Ecr, when compared to LS non-interleaved ones, whereas, all the other configurations presented higher elastic energy absorption before severe damage indicator. Among them, interleaved laminates with glass, carbon and polyester veils in critical shear stresses, seemed to be those whose presented better performances, with respect to this feature (Figure 59 d));

At 40 J impact energy level;

- In terms of peak load (Figure 59 a)), it was observed the same trend as at 25 J of impact energy level. However, this time all interleaved laminates in critical shear stresses seem to reveal higher

load capability when compared to those interleaved in critical normal stresses, with the exception of that which were interleaved with carbon fibres veils;

- All interleaved specimens have presented P_{cr}. Both laminates interleaved with polyester veils have shown to be more prone to develop severe damages at lower loads than non-interleaved and interleaved laminates. On the other hand, interleaved laminates with glass in both critical normal and shear stresses, and aramid in critical shear stresses, have presented higher load bearing capability before damage. All the other configurations did not present significant differences when compared to LS laminate (Figure 59 b));
- In terms of E_{abs}, once again no significant differences were found between interleaved and non-interleaved LS laminate (considering standard deviations), as may be seen in Figure 59 c).
- Figure 59 d) shows that, with the exception of interleaved laminates with glass veils in both critical stresses (normal and shear) positions and aramid veils in critical normal stresses location, all the other have demonstrate lower capability to dissipate energy without damage presence of damage indicators (E_{cr}).

6.5.4.1 Visual inspections

After impact, all specimens were carefully inspected visually and any damage on them was measured and analysed. For 25 J and 40 J of impact energy level, all specimens presented visible damage on their back-face (opposite surface to impact). However, for the lowest impact energy level (13.5 J), only a small number of specimens exhibited external damages. Table 20 presents the number of specimens of each laminate that have shown visible damages on their back-faces at 13.5 J of impact energy.

Table 20: Number of specimens which presented back-face visible damage at 13.5 J of impact energy.

Laminate	Interleaving location	N° of tested specimens	Back-face visible damage
LS	Non-interleaved	4	2
Glass veil interleaved	Normal stresses	3	1
	Shear stresses	3	1
Carbon veil interleaved	Normal stresses	3	1
	Shear stresses	3	1
Aramid veil interleaved	Normal stresses	3	1
	Shear stresses	3	1
Polyester veil interleaved	Normal stresses	3	2
	Shear stresses	3	0

As may be seen in the above table, in most of the cases at least one specimen of each structure has developed external damages at 13.5 J, the only exception was those interleaved with polyester veils in

interfaces presenting the most critical shear stresses. It is interesting to observe that this last one has shown an antagonistic behaviour, depending on the interleaving location. When polyester veils were interleaved on the most critical normal stresses interfaces, 2/3 of specimens have developed external visible damages, on the contrary, when this veil was placed in the most critical shear stresses interfaces, none damage was observed visually.

Figure 60 shows photographs of typical damages on each laminate after impact at 13.5 J and 40J energy levels. At 13.5 J, with exception of the laminate interleaved with polyester veils on the most critical shear stresses interfaces that did not present any damage, no significant differences were observed between the interleaved laminates. All of them have developed, at least in one specimen, small fibre breakage in their back-faces under the impactor, although the non-interleaved laminate of reference has shown localised matrix splitting.

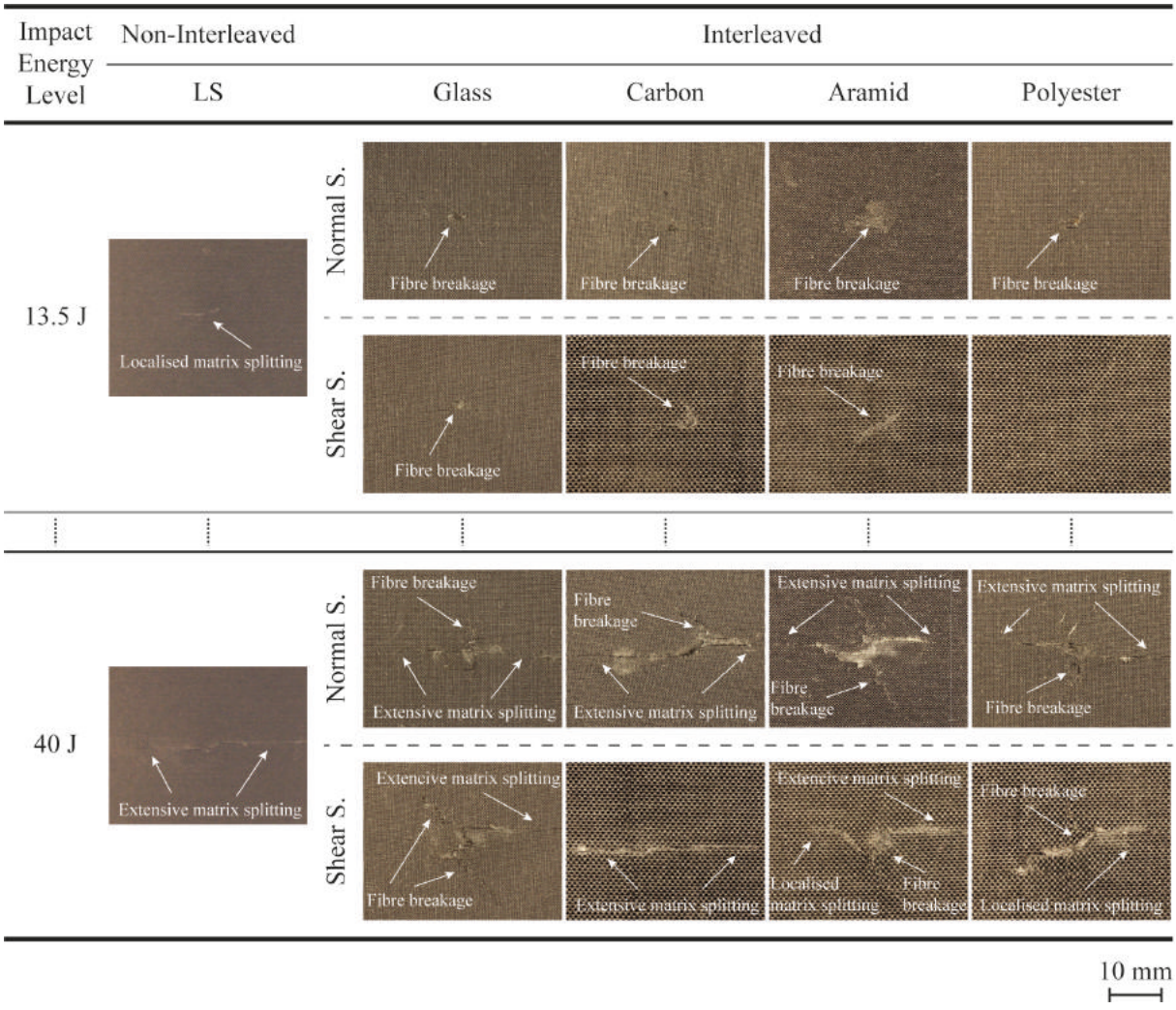

Figure 60: Photographs of characteristic back-face failure mode observed in each laminates after impact at 13.5 and 40 (J) of energy.

For the highest impact energy level, 40 J, much bigger damages were observed in all specimens. As may be seen in Figure 60, contrary to non-interleaved laminates that have developed extensive matrix splitting on specimens back-face, most of the other layups have shown a mix back-face failure mode, namely a combination between fibre breakage and extensive matrix splitting. Only the laminate interleaved with carbon veils on the most critical shear stresses interfaces has shown a back-face failure mode similar to that of the non-interleaved one.

Due to the similarity between back-face failure modes observed in all laminates at 25 J impact energy, their photographs were not presented in Figure 60. At this impact energy level, all laminates have shown fibre breakage on their back-face under the impact region, surrounded by small and localised matrix splitting.

As mentioned before, after inspection, back-face damage extent, λ, was measured on all laminates. The chart in Figure 61, presents the back-face damage extent measured on each laminate for the three impact energy levels.

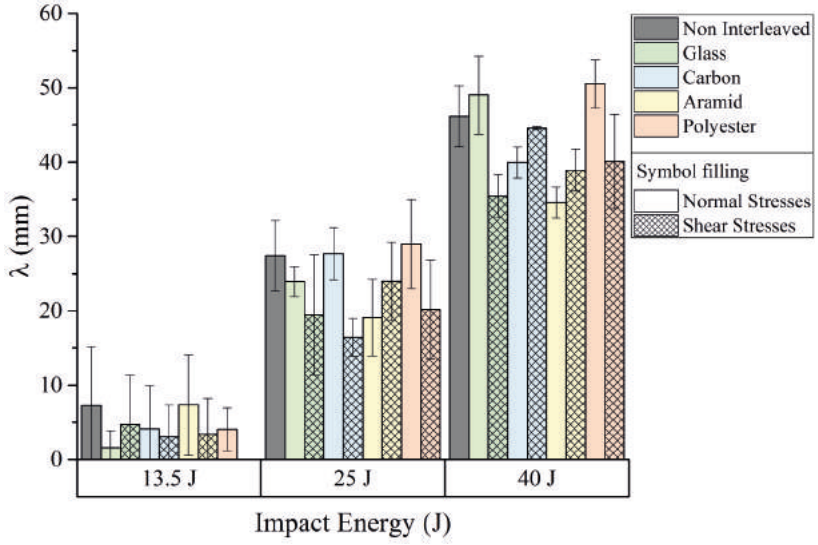

Figure 61: Back-face damage extent (λ) average of each laminate for the three different impact energy levels.

As results show, there was an increment of back-face damage extent with impact energy level increasing as it was somehow expected. However, no trend could be found between interleaved structures (veils) or their location into the laminate and the external damage extent. Even though the strategic interleaving has revealed, in most of the cases, a reduction of back-face damages extent, especially for those interleaved laminates on the most critical shear stresses interfaces, the new interleaved structures have always shown to be less propense to develop larger damages than the non-interleaved one.

6.5.4.2 Internal damage area after impact

After impact, the internal damage area and shape of all specimens submitted to the three different impact energy levels were investigated under C-scan. Figure 62 shows the typical grayscale C-scan images obtained from each laminate submitted to impact at 13.5 J and 40 J energy levels. Red dashed circle represents the impactor perimeter.

At 13.5 J of impact energy, images show that damage had circular shape in all laminates, typically smaller on interleaved laminates than on non-interleaved one. As the impact energy level increases, damage shape became oval, as may be well seen for 40 J impact energy level. Despite not represented in Figure 62, damages at 25 J have shown to have smaller dimensions but a similar shape to those observed at 40 J. From images it is also possible to observe, especially at 40 J, that laminates interleaved on the most critical shear stresses interfaces seem to present smaller damages than those interleaved on the most critical normal stresses interlaminar regions. The same trend was also observed at 25 J impact energy level.

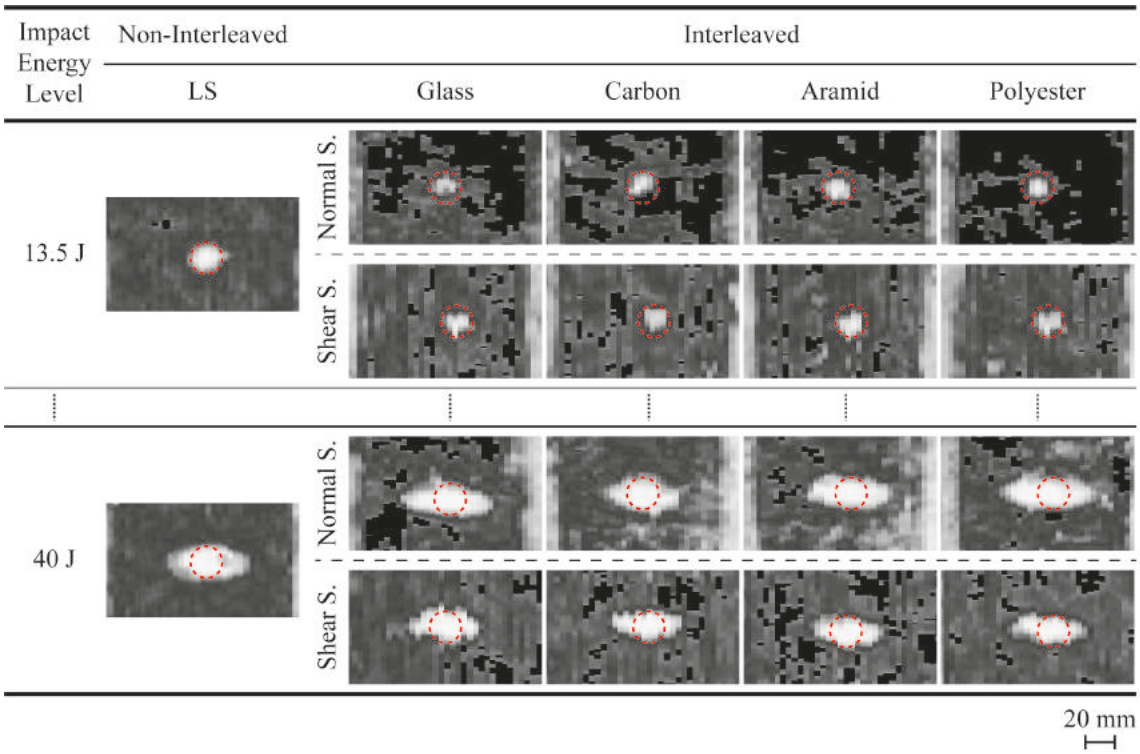

Figure 62: Grayscale representative images of each laminate impacted at 13.5 and 40 (J) of energy.

The areal dimension of damages was measured from C-scan images and results obtained at each impact energy level are presented in Figure 63.

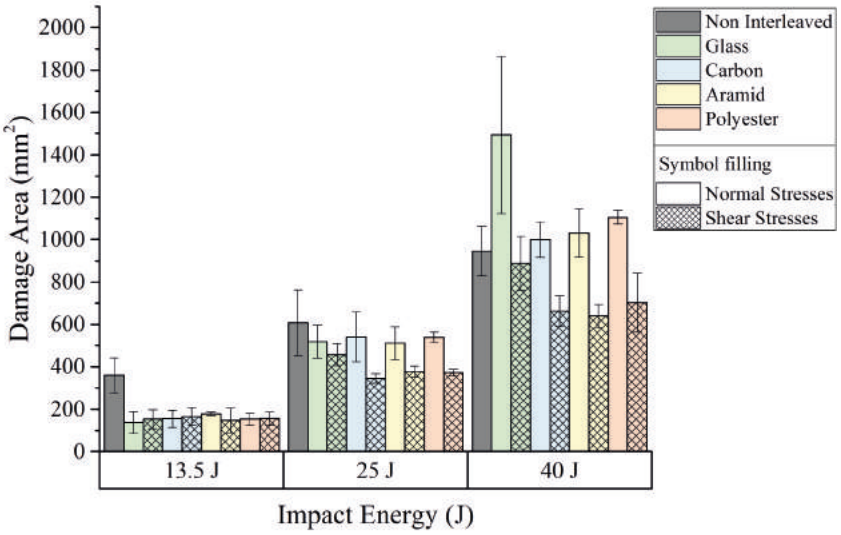

Figure 63: Impact damage area of laminates at each impact energy level.

The results show that, at 13.5 J and 25 J energy levels, all interleaved laminates had less propensity to develop larger damages than the non-interleaved one. On the other hand, at 40 J impact energy, laminates interleaved on the most critical normal stresses interfaces have developed larger damages than non-interleaved laminate, while laminates interleaved on the most critical shear stresses interlaminar regions have kept the same trend and developed internal damages with smaller areas than the same layup of reference.

Regarding the impact damaged area of interleaved laminates on the most critical shear stresses interlaminar regions at 25 J and 40 J, despite the expected increase of damage area, it may be seen that they maintained similar trends for both impact energy levels. This suggests that location where the veils are placed inside the laminate play an important role in terms of composites resistance to damage.

6.5.5 Compression After Impact (CAI) tests results

The laminates impact tolerance was evaluated by CIA tests. Due to problems associated to the experimental setup during testing campaign, two specimens, one from the configuration interleaved with glass veils in critical normal stresses interfaces and other from the laminate interleaved with polyester veils in critical shear stresses interlaminar regions, were not considered valid.

Figure 64 are graphically depicts the experimental results of all non- and interleaved laminates after impacted at 25 J of energy. As may be observed, if standard deviatin is considered, no significant differences were found among the different laminates.

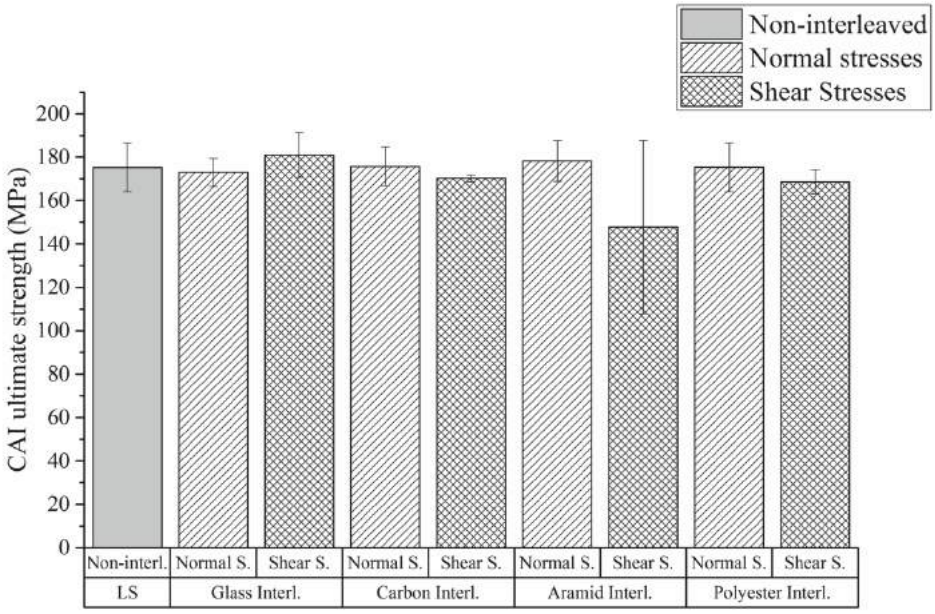

Figure 64: CAI ultimate strength of each configuration after impacted at 25 J of energy.

6.6 Discussion

The main results obtained from the veil and laminates characterisation, quasi-static mechanical tests, LVI and CAI tests were presented in the previous section. In this section, those results will be discussed regarding the micro-structure of veils, their materials and location inside the composite laminate.

6.6.1 Laminates characterisation

It was expected that the inclusion of veils to reinforce interlaminar regions would contribute to obtaining a thicker laminate. Despite a previous FE study undertaken to evaluate the most critical interfaces to be interleaved (see section 6.3) and reduce the number of interlaminar reinforcements by that way and, consequently, the expected laminate's thickness overage, it was observed, in fact, an increment in thickness of interleaved laminates when compared to the reference non-interleaved one. On the other hand, it was also observed a reduction on the specific mass of all interleaved configurations, comparatively to the same reference laminate. The variation of those two, apparently, dissonant characteristic results are graphically depicted in Figure 65. Labels on top of each bar which represents interleaved configurations, indicates the percentual variation when compared to the reference non-interleaved laminate.

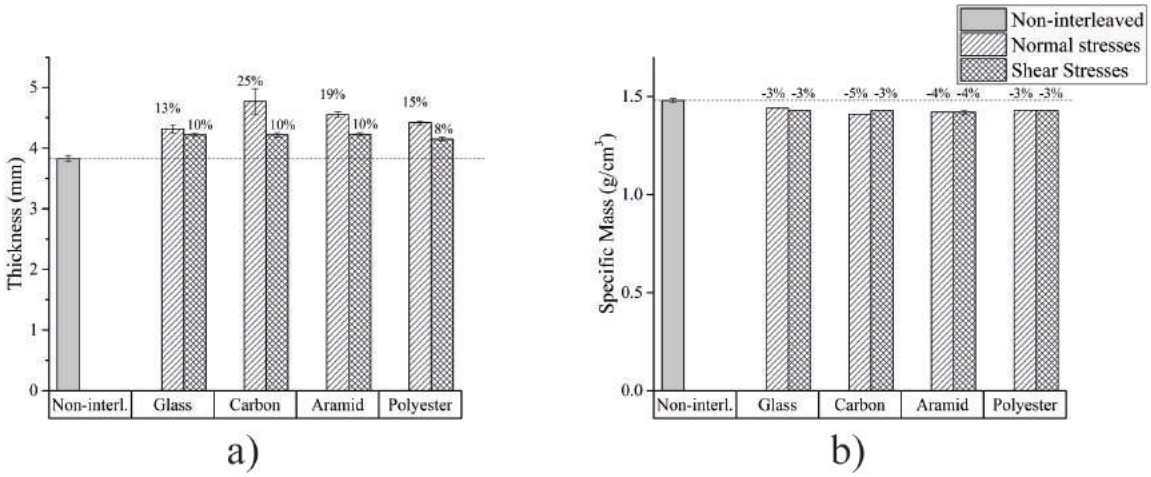

Figure 65: Comparison between non-interleaved and interleaved a) thickness and b) specific mass variation

As may be seen in Figure 65 a), the inclusion of six veils to reinforce critical interfaces introduced an increment in thickness up to 25 % when compared to non-interleaved one, however, the specific mass of those laminates decreased around -5 % to -3 % (Figure 65 b)). These apparent antagonise variations may be explained by the higher matrix volume fractions of interleaved laminates.

The high porosity veils medium, when compared to UDCF tissue, led to the formation of resin rich regions in the interfaces where they were placed, as may be seen in Figure 51, and a consequent increment in laminate's volume. Since matrix possesses a lower specific mass when compared to all the other composite laminate components (see Table 14 and Table 15), whose kept the same volume in all configurations, laminates with higher matrix volume fraction present a lower specific mass. Laminates components volume fraction of each configuration are presented in Figure 66.

Another interesting observation was the less increment of thickness for laminates interleaved on the most critical shear stresses interfaces, when compared to those interleaved on critical normal stresses (Figure 65 a)). This suggests that veils completion and relaxation during vacuum bag infusion process, behave differently depending on their position inside the laminate. However, further studies must be done in order to understand this peculiar phenomenon.

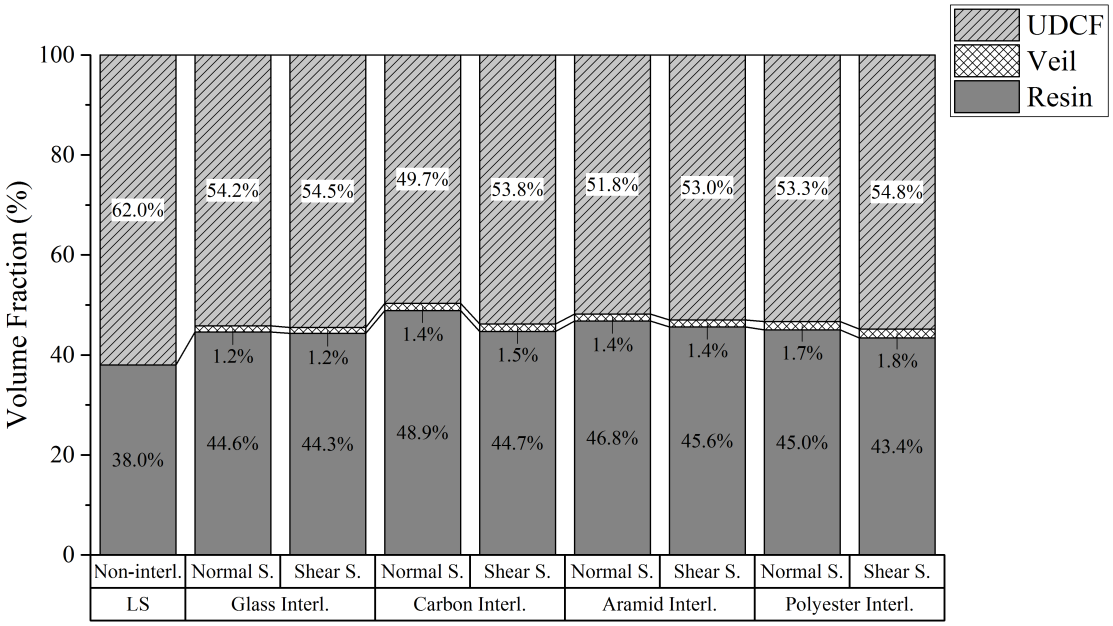

Figure 66: Laminates UDCF, veils and matrix volume fraction.

The laminates cross-section observations under SEM, also revealed several voids inside most of interleaved configurations, in contrast with non-interleaved one where no voids were found. As may be seen in Figure 52, most of the voids are typically in the interleaved layer or in the gaps formed from the weft threads, moreover, laminates interleaved on most critical shear stresses interfaces have shown less propensity to voids formation than the other interleaved configurations.

It is well known that voids formations in liquid composite moulding, e.g. vacuum bag infusion, is dominated by resin flow and the fibrous medium to be impregnated [169]. Since the resin flow in vacuum bag infusion is relatively slow, capillary flows tend to prevail over the hydrodynamic ones and, therefore, dry UDCF will be impregnated first, due to the small gaps between fibres and consequent higher superficial tension, than more porous mediums as veils and gaps inside the laminates, which leads to air entrapments on these last ones.

This explain why voids were mostly found into veil layers and gaps formed by the weft threads. On other hand, considering the higher volume fraction and lower thickness of UDCF layers (higher fibres compaction) in laminates interleaved in critical shear interfaces may also justify the smaller number of voids found on these structures.

6.6.2 Quasi-static mechanical tests discussion

6.6.2.1 3-PB laminates performances

As Figure 54 shows (section 6.5.3.1), despite to be lower than non-interleaved laminate, no significant differences were found between the values of maximum stresses and flexural modulus obtained from the 3-PB tests made on the strategically interleaved layups. The type of veils used to reinforce laminates interlaminar regions did not appear also to have any influence on the bending properties of these layups, however, their seem to be more affected by laminates' resin volume fraction, as shows Figure 67.

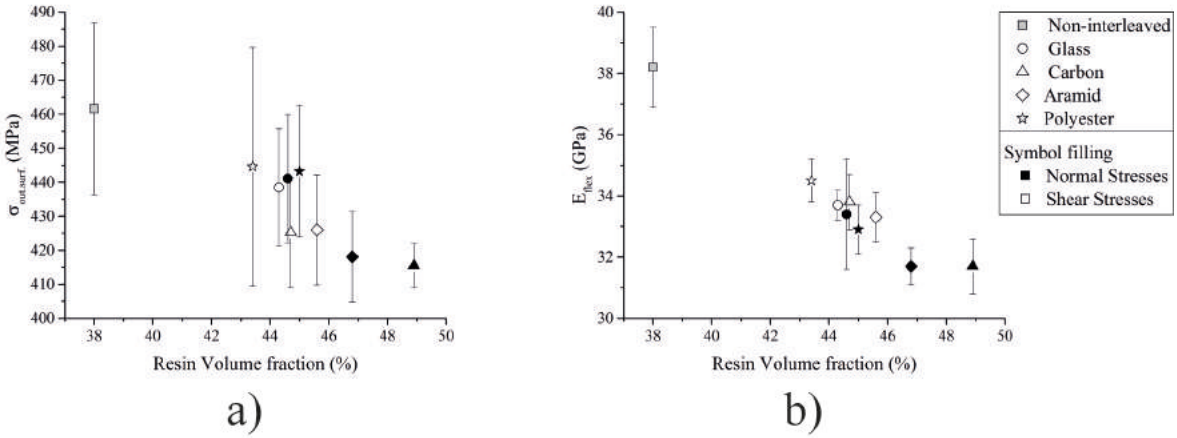

Figure 67: 3-PB a) maximum outer surface stresses ($\sigma_{out.suf.}$) and b) flexural modulus ($E_{flex.}$) vs resin volume fraction.

In fact, despite the large standard deviation obtained in the maximum stress values obtained from the 3-PB tests performed on most of the laminates, Figure 67 a) shows that the average values of those stresses seem to have been directly influenced by the resin volume fraction of each of those structures. The chart suggests that, the lower the laminate resin fraction is, the higher its maximum outer surface stress.

As Figure 67 b) shows, the same trend was observed for flexural modulus. However, contrary to maximum outer surface stresses of interleaved laminates, flexural modulus seems to have been more sensitive to veils position into the laminate, the further away the veils were from laminate surfaces, the higher was stiffness obtained on flexure. This characteristic may be clearly observed in Figure 67 b) chart, where laminates interleaved on the most critical shear stresses interfaces (the 1st, 4th and 5th interlaminar regions) showed to have higher flexural modulus than those interleaved on the most critical normal stresses interfaces (1st, 2nd and 3rd interfaces).

The higher flexural stiffness obtained in those interleaved laminates is essentially due to the higher amount of layers with superior stiffness (UDCF layers) that were located close to the surfaces, contrary

to laminates interleaved on the most critical normal stresses interfaces, where veil layers (with higher resin volume fraction and lower stiffness) were mostly located close to outer surfaces.

Regarding the characteristic failure mode of interleaved laminates under 3-PB conditions, it does no differs much from the non-interleaved layup. Comparing both, interleaved laminates (Figure 55, section 6.5.3.1) and non-interleaved one (Figure 27 b) in section 5.4.2, Chapter 5), it is possible to conclude that all of them tend to fail catastrophically on specimen's compression side and that, on the tensile side, laminates interleaved at interfaces with most critical normal stresses are more susceptible to develop catastrophic failures than, both the non-interleaved and any of the other interleaved ones.

The presence of veil layers close to the outer surfaces on laminates interleaved at the most critical normal stresses interfaces seem to have induced the formation of cracks due to their lower stiffness, leading to more severe failures on adjacent UDCF plies. On the other hand, when veils were located far away from surfaces (laminates interleaved on shear stresses interfaces), crack propagation was delayed, driving to small delaminations (for glass and carbon interleaved laminates), or even (up to the applied deformation during tests) no damage formation on aramid and polyester reinforced layups.

6.6.2.2 ILSS laminates performance

According the ILSS testing results, despite the voids observed inside interleaved laminates, all of them have presented improvements on their global interlaminar shear stresses resistance when compared to the non-interleaved one (Figure 56, section 6.5.3.2). Similar to 3-PB results, no correlations were found between the different type veils used to interleave laminates, since only a small difference in the values of interlaminar shear stresses (τ_{13}) (between 23 and 25 MPa) was observed among them. Nevertheless, laminates interleaved with glass and aramid veils at the most critical shear stresses interfaces demonstrated to have better performance than those peers interleaved on critical normal stresses interlaminar regions. While for the other configurations interleaved with carbon and polyester veils, similar values were achieved for both interleaving positions.

As other studies [164][165][170] demonstrated that laminate's resin volume fraction could influence its ILSS resistance, the interlaminar shear strength of laminates was, therefore, plotted against their resin volume contents in Figure 68.

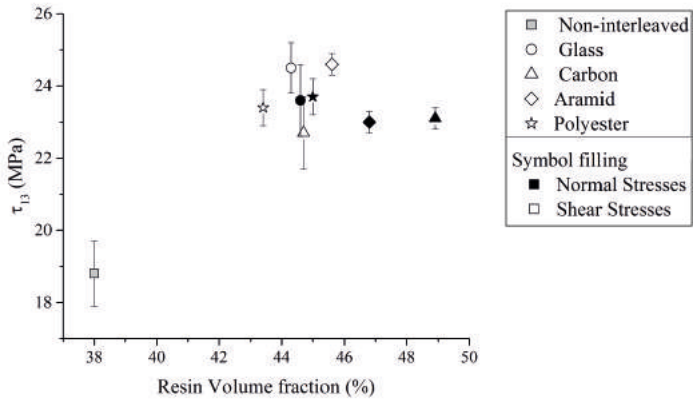

Figure 68: Interlaminar shear strength of laminates vs resin volume fraction.

As may be seen in Figure 68's chart, the higher was the resin volume fraction of interleaved laminates the better was their ILSS performance. Results suggest that laminates apparently improve this mechanical property until a resin volume fraction close to approximately 45 % was reached, suffered a slightly decrease after that value. The resin rich interfaces caused by inclusion of veils seems to lead, up to a certain point, to a more uniform distribution of shear stresses, redirecting the loading to UDCF layers and increasing by that way the interlaminar shear strength.

Despite their undeniable improvements on interlaminar shear strength that interleaved laminates presented, no significant differences were found in terms of failure mode between them, as may be also observed in Figure 57 (section 6.5.3.2). On the other hand, comparatively to non-interleaved LS laminate, previously observed in Figure 27 c) (section 5.4.2, Chapter 5), in most of the cases the strategicaly interleaving structures failed between or close to reinforced interfaces that were typically localised near the opposite surface of the loading nose (bottom surface on photographs), while non-interleaved laminate typically failed throughout all thickness and close to 90° plies.

Should be noted that laminates interleaved by carbon and aramid veils in critical shear stress positions also presented some interlaminar failures across thickness. However, as may be observed from photographs, those cracks were typically close to UDCF layers weft threads, suggesting that those structures may induce crack initiation and propagation, as observed in the previous study on bioinspired laminates.

6.6.3 Low Velocity Impact (LVI) tests mechanical response

It is well known that composites impact response depends on many factors, among them, and perhaps one of the most important their thicknesses [171]. Therefore, considering the significative increment in thickness revealed from some interleaved configurations relatively to the non-interleaved one, the row

results presented in Table 18 and Figure 59 (section 6.5.4), may lead to an incorrect data analysis. In order to reduce thickness's influence in this discussion, Figure 69 presents the characteristic mechanical response, namely, peak load, critical load (P_{cr}) and energy (E_{cr}), and final absorbed energy (E_{abs}), of each laminate for the three different impact energy levels per unit of thickness.

Figure 69 clearly shows that in most of the cases, interleaved laminates have shown a lower performance when compared to non-interleaved one. However, between them, laminates interleaved on the most critical shear stress interfaces have demonstrated better mechanical responses when compared to other ones interleaved in normal stress critical interlaminar regions. This trend is particularly visible in Figure 69 a) and c), where those interleaved laminates have shown equal or superior (in most of cases) peak load and final absorbed energy, respectively, at any impact energy level. Moreover, configurations interleaved on the most critical shear stress interfaces have shown similar response in terms of peak load and absorbed energy at any impact energy level applied.

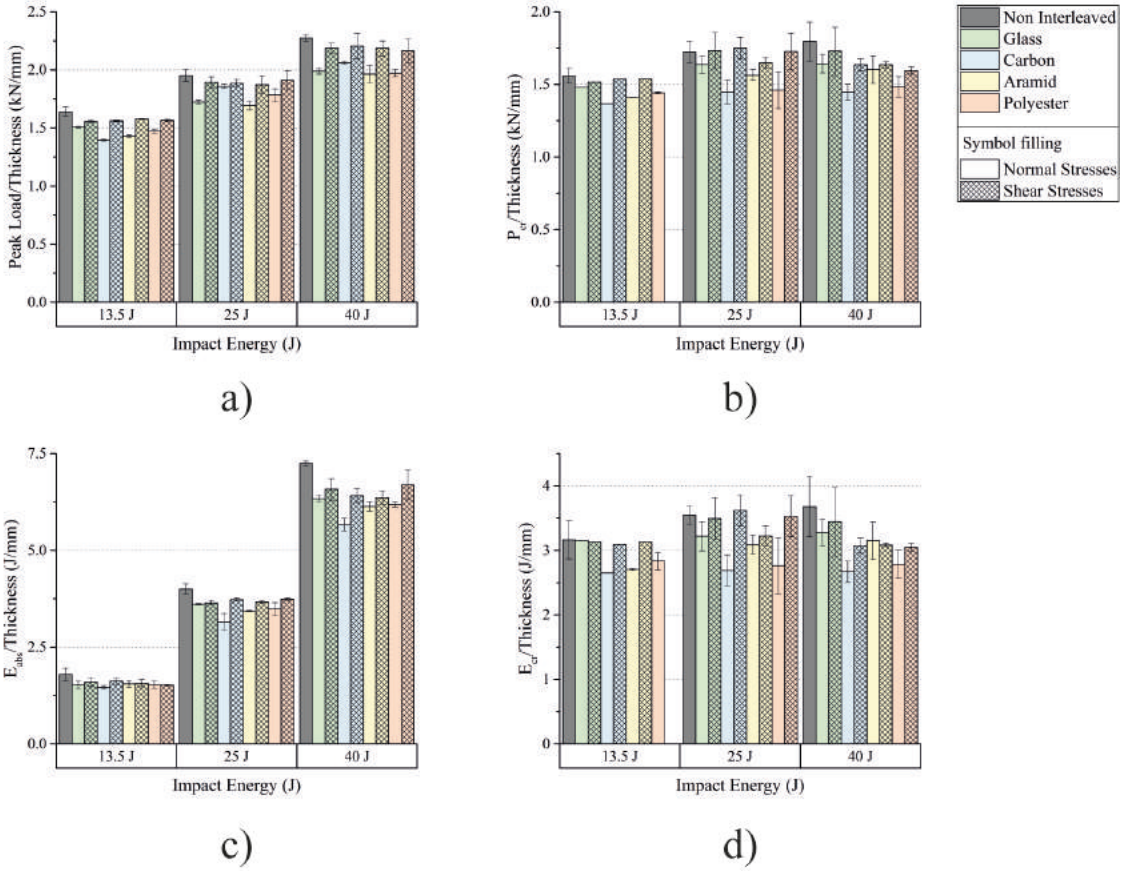

Figure 69: Graphical representation of a) peak load, b) critical load (P_{cr}), c) final absorbed energy (E_{abs}) and d) critical energy (E_{cr}) of each laminate per unit of thickness at the three different impact energy levels.

On the other hand, laminates interleaved in normal stress critical interlaminar regions seem to depend on the veil used in the layup, despite no trend may be identified for the different impact energy levels. For

instance, up to 13.5 J impact energy level, the interleaved laminates having carbon fibre veils in critical normal stresses interfaces have shown lower load bearing capability (peak load) and final absorbed energy, while, at higher impact energy levels, the same layup presented the highest peak load while the final absorbed energy remains the lowest when compared to the other laminates interleaved in the same location with other veils, which roughly kept the same trend between them. This lack of tendency may be related with the large number of voids found in these laminates in comparison to those interleaved on the most critical shear stress interfaces.

Regarding the critical point (indicator of first severe damage), results revealed that at 13.5 J, laminates interleaved on critical shear stress interfaces, with the exception of the polyester veils reinforced structures which outperform all the others, have shown similar critical load (P_{cr}) and energy (E_{cr}) per unit of thickness than the non-interleaved layup, as it is shown in Figure 69 b) and d), respectively. On the other hand, those ones interleaved in the most critical normal stress interlaminar regions, have shown higher propension to develop severe damages at lower loads and energy levels.

At 25 J impact energy level, laminates interleaved with glass, carbon and polyester veils on the critical shear stress interfaces, have shown similar results in terms loads (P_{cr}) and energy (E_{cr}) per unit of thickness than the non-interleaved reference one, whereas all the other interleaved configurations have demonstrated worse performances. Finally, at 40 J, all interleaved laminates presented severe damage indicator at lower loads (P_{cr}) and energies (E_{cr}) than the reference one.

According to the above results, is clearly visible that the laminates interleaved on the critical shear stress interfaces, once again, outperform those interleaved on normal stresses critical regions in terms of the critical load (P_{cr}) and energy (E_{cr}) per unit of thickness needed to trigger the first severe damage. Nevertheless, no correlation was possible to stablish among the types of veil nor their micro network structures concerning their propensity to onset severe damage formation.

To summarise, it was undeniably observed a better mechanical response from laminates interleaved on the most critical shear stresses interfaces and, it was possible to conclude, that such mechanical response was much more sensitive to the location where laminates are interleaved than the type (fibrous material) or micro-structure of the veils used.

6.6.4 Low velocity impact damage evaluation

In the previous section, the mechanical response of new strategically interleaved laminates was discussed and compared to non-interleaved LS configuration. Now, the damages caused by the LVI tests performed

on laminates will be discussed in relation to the interleaved strategy adopted and selected veils characteristic micro-structure.

6.6.4.1 Role of interleaving location on impact damage

Back-face damage extent is considered a first indicator of damage severity caused by an impact event, however, it depends from the impact energy level and laminate morphology. Figure 70 shows the comparison between back-face damage extent (λ) measured on each interleaved laminate and LS non-interleaved reference one after impact at each energy level. Label above each patterned bar indicates the variation with respect to baseline non-interleaved laminate.

From the depicted charts it is possible to observe that, independently of the energy level, laminates strategically interleaved on critical shear stress interfaces have always reduced back-face damage comparatively to non-interleaved laminate of reference. On the other hand, all those interleaved on critical normal stress interlaminar regions have developed more extensive back-face damages than the laminate of reference, at least at one of the 3 different impact energy levels.

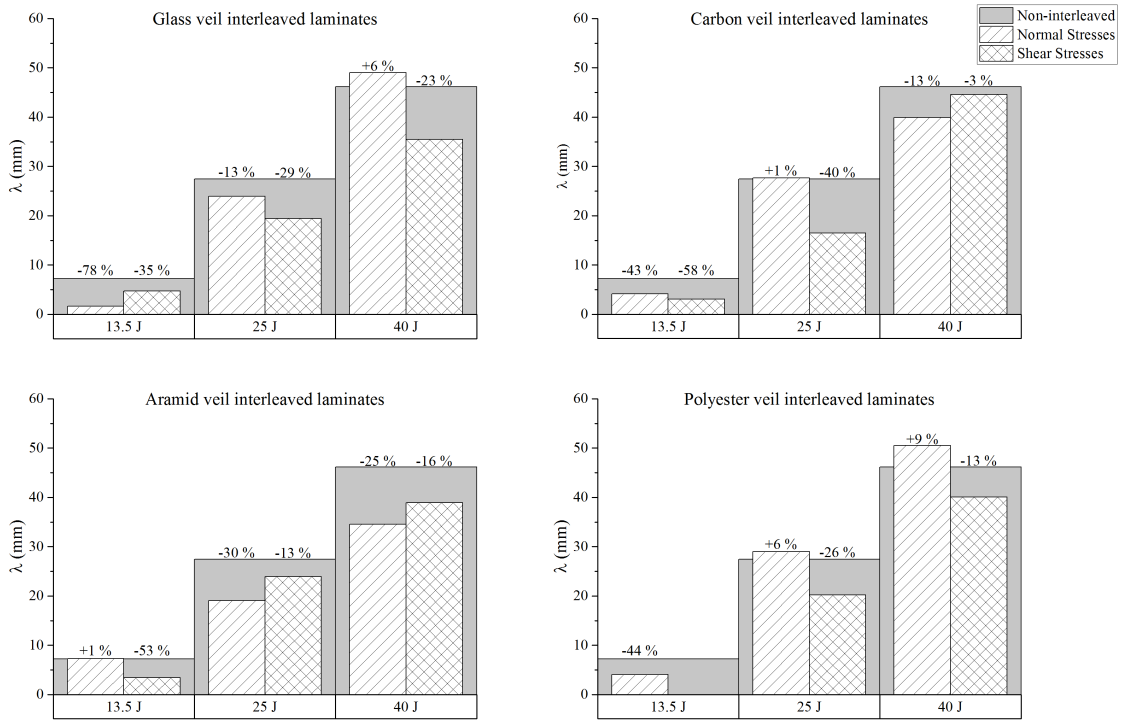

Figure 70: Comparison between back-face damage extent (λ) on each interleaved laminate and non-interleaved one at each impact level.

At 13.5 J, the best performance was achieved by the interleaved laminate with polyester veils on critical shear stress interfaces, whose did not show any damage in none of the tested specimens. However,

among those which have presented damage, the better performance was reached by the interleaved laminate with glass fibre veils placed on critical normal stress interfaces, with a extension of damage 78% smaller than the reference one. On the other hand, on same interleaving location, aramid veils reinforced structure has developed similar extensional damages (1 % larger) than the same layup of reference.

When the impact energy was increased to 25 J, similar to the lowest impact energy level (13.5 J), most of structures interleaved on critical shear stress interfaces have shown to be less prone to develop extensive external damages, being the only exception the layup interleaved with aramid veils on critical normal stress interfaces.

Curiously, the laminates reinforced with carbon and polyester veils have demonstrated antagonistic performances, just by changing the interleaving critical location from shear to normal stresses interfaces. In both cases, the laminates reinforced on critical shear stress interfaces have outperformed non-interleaved layup, having damage extensions lower than this last mentioned one in about 40 % and 26%, in the case of the structures reinforced with carbon and polyester veils, respectivel. Contrarly, when the same veils were placed on the most critical normal stress interfaces, both laminates presented slightly larger damages than the reference one, 1 % and 6 % larger in the case of the carbon and polyester veils reinforced layups, respectively.

At the higher impact energy level (40 J), the interleaved laminates with carbon and aramid veils have shown smaller external damages when compared to the reference, independently on the interleaving strategy used. Among them, the laminate interleaved with aramid veils on critical normal stress interfaces demonstrated better performance at this impact level, with back-face extensional damage 25 % lower than the non-interleaved one. On the other hand, laminates interleaved with glass and polyester veils revealed opposite behaviour, depending on the interleaving strategy implemented. Once again, when those veils were placed on critical shear stress interfaces, laminates have developed smaller damages than the one of reference, 23 % and 13 % lower in the case of structures using glass and polyester veils, respectively. When critical normal stresses interleaving strategy was implemented, both layups revealed lager damages than that one of reference, with damages about 6 % and 9 % larger in the case of glass and polyester veils were used, respectively.

Despite of the important impression given by the back-face damage about the severity of damge caused by impact events, it is well known that composites may develop internal damages under impact that may be almost imperceptible at naked eye, the so-called Barely Visible Impact Damage (BVID) [16][17].

Thus, Figure 71 presents the comparison between internal damage area of interleaved and non-interleaved configurations at each impact energy level.

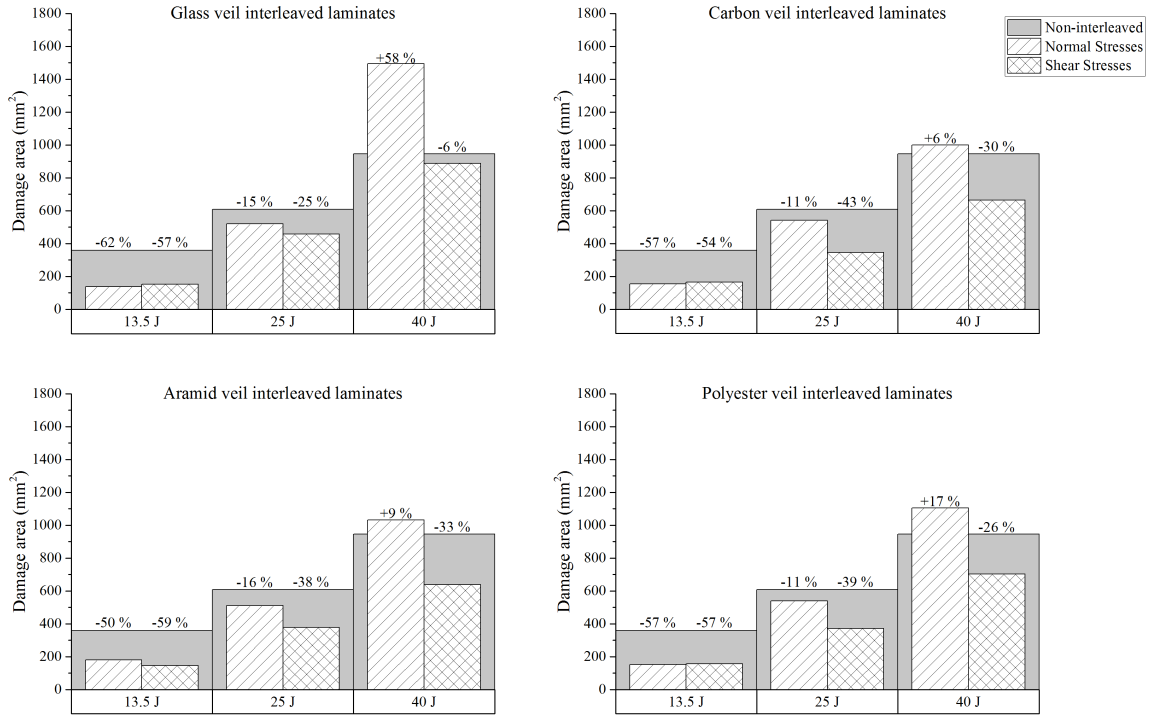

Figure 71: Comparison between internal damage area of each interleaved configuration and non-interleaved reference at each impact energy level.

From results depicted in Figure 71 it possible to say that up to 25 J impact energy level, independently on the strategy used, the interleaved laminates developed less damage area than the one of reference. Moreover, for any considered impact energy level, laminates interleaved on most critical shear stress interfaces have developed smaller damages than non-interleaved one. This interleaving strategy also demonstrated to be more effective in terms of damage sensivity when compared to the interleaving on critical normal stress interfaces, especially at the higher impact energy levels (25 J and 40 J), where it has reached up to 43 % lower damage area, whereas the interleaving strategy based on normal stresses presented 58 % larger damage area than the non-interleaved laminate of reference.

At 13.5 J, all interleaved laminates have demonstrate an impressive damage performance, with damage area reductions between 62 % and 50 % below the layup of reference, in the case of those that used glass and aramid veils on critical normal stress interfaces, respectively.

At 25 J, all interleaved layups have also outperformed non-interleaved one of reference. However, while critical normal stresses strategy demonstrated to reduce the damage area in 16 % to 11 %, shear stresses interleaving has exhibited reductions up to 43 %, in the case of carbon veils reinforced laminates.

This outstanding performance of critical shear stresses interleaved structures was somehow confirmed when impact energy was increased for 40 J, where all of them have demonstrated to be less prone to develop extensive damages when compared to laminates interleaved on critical normal stresses and the non-interleaved one. Moreover, while shear stresses interleaving strategy has shown to reduce impact damage area up to 33 %, when aramid veils were used, all normal stress interleaved laminates develop damages at least 6 % larger (carbon veil reinforcement) than that one of reference. The worse performance at this impact energy level (40 J) was reported for interleaved laminates reinforced with glass fibre veils on critical normal stress interfaces, which developed damages 58 % larger than non-interleaved one of reference.

To summarise, from the analysis on back-face and internal damages and for any impact energy level applied in this study, it is obvious to state the better undeniable performance against damage demonstrated by the laminates that used the critical shear stresses interleaving strategy in comparison, not just with layups that used the other interlaminar reinforcement approach (critical normal stresses interleaving), but also with the laminate non-interleaved of reference. This suggests that the selection of interlaminar strategy to be implemented will perform a very important role in regard to damage formation and propagation in composite materials.

6.6.4.2 Role of veils micro-structural network on impact damage

In the previous section, the role of interleaving strategy on damage development was discussed, but it was not clear how the different micro-structures of the reinforcement (veils) used may also influence damage. To this end, two distinctive micro-structural properties will be considered in this section in order to evaluate their effect on back-face and internal damage formation, namely, the veil surface area covered by fibres and the specific fibre/matrix contact area, (S_f).

Figure 72 shows the evolution of back-face damage extent (λ) against the fibre covered surface area (Figure 72 a)) and specific fibre/matrix contact area (S_f) (Figure 72 b)) of each interleaved laminate for the three different energy levels of impact.

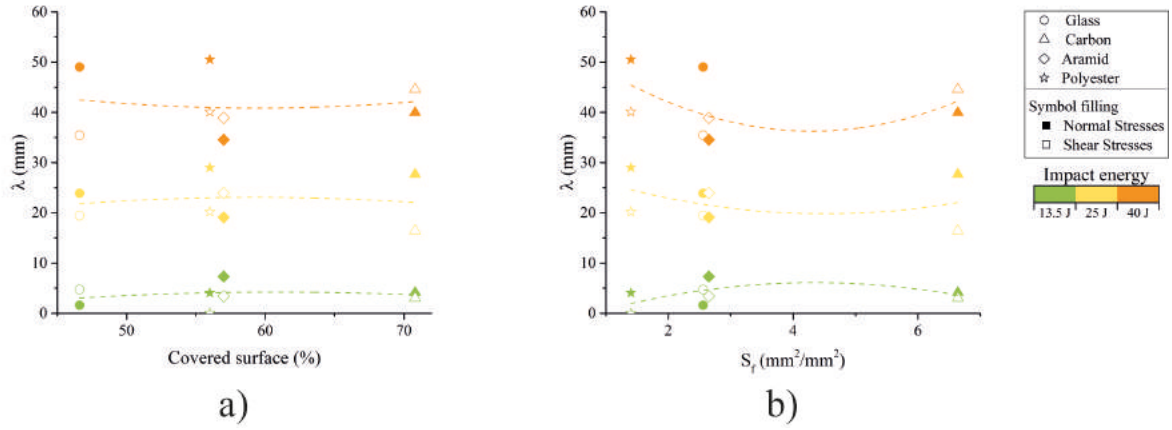

Figure 72: Back-face damage extent (λ) versus a) covered surface area and b) specific fibre/matrix contact area on interleaved laminates.

From the trendlines obtained for each impact energy level plotted in Figure 72 a), it may be concluded that the fibre covered surface area in veils did not play an important role on back-face damage extent. On the other hand, fibre/matrix contact area seems to have influenced much more this damage indicator (Figure 72 b)).

At 13.5 J, veils with an intermedium S_f (glass and aramid veils) have formed slightly extensive back-face damages than those with smaller and larger S_f, which are the polyester and carbon veils, respectively. Nevertheless, not all specimens have develop external damages at this lowest impact energy level, suggesting that the impact at the 13.5 J could be considered as the threshold for severe damage formation (see section 6.5.4.1, Chapter 6). Moreover, as only very small differences were observed between average damage extents among all the specimens at 13.5 J, it seems that no strong correlation may be done between results at this impact energy level.

On the other hand, for impact energies of 25 and 40 (J), yellow and orange trendlines, respectively, suggest a slightly higher tendency for laminates reinforced with lower and higher specific fibre/matrix contact area (polyester and carbon veils, respectively) develop more extensive damages.

Considering veils covered surface area , as it may be seen in Figure 73 a), up to 25 J impact energy level, this morphological veils characteristic did not seem to influence internal impact damage, however, a strong correlation may be observed for the highest impact energy level. At 40 J, laminates interleaved with glass fibre veils, which present lower fibre covered surface area of veil, have demonstrated to have the larger internal damages, whereas those reinforced with polyester, aramid and carbon veils have progressively smaller damages, respectively. This trend shows that, the lower was the fibre covered surface area of veil, the larger was the impact internal damage area.

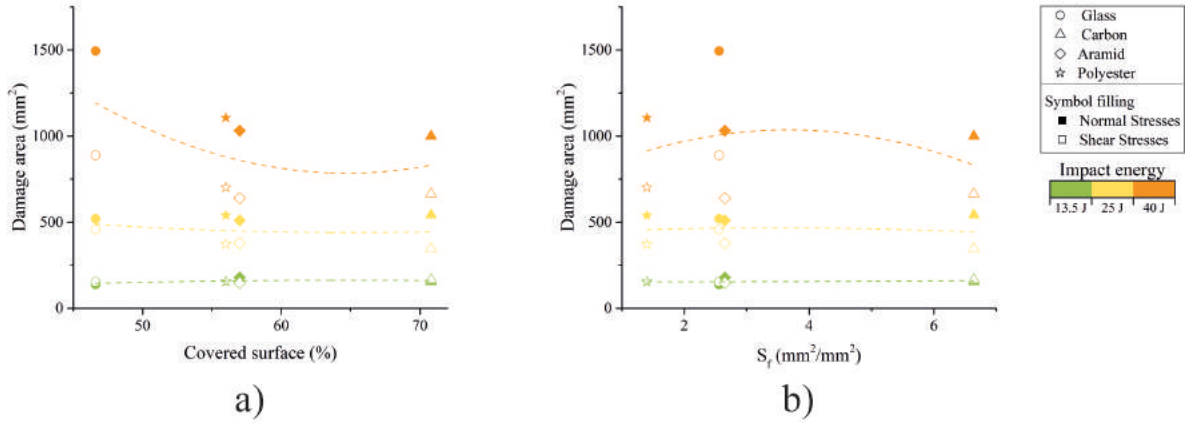

Figure 73: Influence on interleaved laminates internal damage area of a) covered surface area and b) specific fibre/matrix contact area.

In Figure 73 b), the internal impact damage area is plotted against veils specific fibre/matrix contact area (S_f). As may be observed, up to 25 J of impact energy, damage area seems to be independent of the veils S_f. However, for the highest impact energy level, 40 J, those laminates interleaved with veils which present intermedium specific fibre/matrix contact area, glass and aramid ones, have revealed larger internal damages than those with lower S_f.

Moreover, independently of fibre covered surface area of veils or specific fibre/matrix contact area, the laminates interleaved at critical shear stress interfaces have always outperformed those interleaved at critical normal stress interfaces.

To summarise, back-face damage extent seems to be more dependent on veils specific fibre/matrix area than on fibre covered surface area of veils. This suggests that damage propagation on, or close, laminate's surface may be more dependent with fibre bridging mechanisms than matrix cracking (crack propagation into the resin pockets inside veils). On the other hand, internal damage has demonstrated to be first affected by interleaving strategy used, and only for higher impact energy those two micro-structural parameters (fibre covered surface of veils and specific fibre/matrix contact area). At 40 J of impact energy, laminates reinforced with veils with lower fibre covered surface area have revealed larger damages, which indicates that crack, preferentially, grows faster throughout reinforced region with larger resin spots. Contraly, when those gaps between fibres are smaller, crack tend to be deflected constantly, leading to a smaller damaged area.

From Figure 73 a) it is also possible to observe that veils with large number of fibres in a tiny volume, which means a higher specific fibre/matrix contact area, crack is constantly deflected, dissipating more energy in a small area and delaying its propagation. This may justify the better performance obtained for laminates interleaved with carbon fibre veils. However, despite presenting the lowest specific fibre/matrix

contact area among all veils selected for this study, laminates interleaved with polyester veils seem to perform better than aramid and glass veils reinforced laminates. Our explanation is that the phenomenon may be caused by the fibres geometry. According to M. Herráez et al. study [172], trilobal cross-section fibres tend to develop higher residual stresses on their interfaces, comparatively to circular cross-section ones, resulting in an easier interfacial debonding between fibres and matrix. On the other hand, J. Mohan et al. [173] studied the interlaminar fracture toughness in mode I of composite joins using an adhesive epoxy film reinforced with trilobal cross-section polyester fibres. Under microscopic visualizations of the crack path, they observed a crack growing against direction of main crack propagation on adhesives. Based on those hipothesis, we may suppose that both mentioned subcritical damages occurred on laminates interleaved with polyester veils, acting as energy dissipator mechanisms and, consequently, leading to smaller severe damages (e.g. extensive delaminations).

6.6.5 Impact tolerance (CAI tests)

As it was been observed in Figure 64 (section 6.5.5), despite the large number of voids observed in some interleaved laminates (Figure 52, section 6.5.2), no significant difference was observed on the CAI strength results obtained among non- and most of interleaved laminates. Figure 74 presents the average CAI ultimate strength results of all interleaved configurations after impacted at 25 J of energy and its percentual variation to reference LS layup.

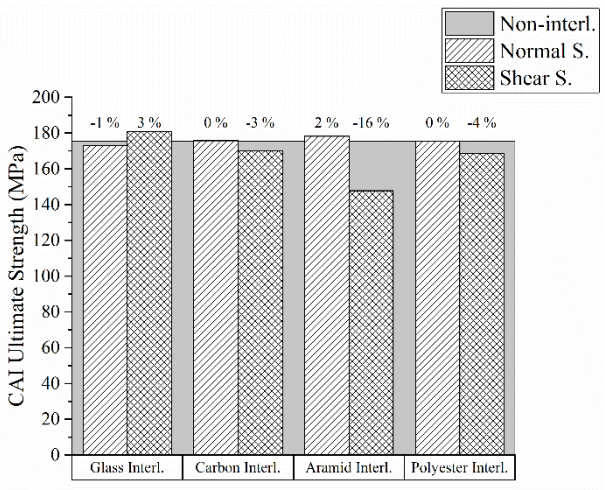

Figure 74: CAI ultimate strength results of all interleaved laminates after impacted at 25 J and its percentual variation against the LS of reference.

As may be seen from figure, most of interleaved configurations have shown only slight or, in some case, no differences in terms of residual strength after impact, when compared to non-interleaved reference layup. The only exception was the laminate interleaved with aramid veils in the most critical shear stresses

interfaces, which has presented a reduction of 16 % in CAI residual strength relatively to the standard layup of reference. However, should be noticed that this laminate interleaved with aramid veils also presented the largest variation of results in the experimental tests (see Figure 52, section 6.5.2).
Therefore, based in the experimental results, it may be concluded that residual strength after impact is not affected by the interleaving strategy neither by veils material.

6.7 Conclusions

In this chapter, a conventional aircraft laminate was strategically interleaved at six layers with four different thin veils in order to improve its resistance and tolerance to impact events. To minimise the number of interlaminar regions to be reinforced, a finite element model was built to evaluate interlaminar stresses across the laminate under plate banding conditions. Afterwards, the six most critical normal and shear stress interfaces where selected to be interleaved with four different veils.
All laminates were manufactured by vacuum bag infusion and characterized with respect to their thicknesses, components volume and voids contents. Their global interlaminar shear resistance (ILSS), three-point bending (3-PB) performance, low velocity impact (LVI) and compression after impact (CAI) response were also assessed by mechanical testing.
Interleaved laminates characterisation has revealed an increment in thickness and resin volume fraction when compared to reference non-interleaved layup. Moreover, those laminates interleaved at the most critical normal stress interfaces have shown to be thicker than those interleaved with the same veils in critical shear stress interfaces. SEM observations also have shown that interleaved laminates tend to have more voids than non-interleaved ones.
From the experimental three-point bending (3-PB) and interlaminar shear strength (ILSS) tests, no significant corelation was observed between the results and the interleaved position nor veil's material. However, they reveal a strong dependency on laminates resin volume fraction. It was found that 3-PB properties decrease as the laminate resin volume fraction increases and, on the other hand, despite the presence of voids inside some interleaved configurations, ILSS experimental results have shown to be improved as the resin volume fraction rises up to approximately 45 %.
When normalised to laminates' thicknesses, no drastic changes were observed between non- and interleaved configurations in terms of LVI mechanical response. However, independently on the impact energy level, laminates interleaved in the most critical shear stress interfaces have presented slightly better performance in terms of peak load, absorbed energy (E_{abs}) and critical load (P_{cr}) and energy (E_{cr}) than the other ones interleaved at critical normal stress interlaminar regions.

Regarding back-face damage extent, no corelation were observed among interleaving strategy nor veils material. Nevertheless, most of interleaved laminates have developed less extensive damages then non-interleaved one of reference. At 13.5 J of impact energy, laminates interleaved with polyester veils at critical shear stress interfaces did not present any external damage, whereas those ones interleaved with carbon veils at critical normal stress and with aramid veils at critical shear stress interfaces revealed to be the most effective in reducing damage at 25 J and 40 J impact energy levels, respectively, by minimising damage up to 40 % and 25 % in comparison to non-interleaved one, correspondingly. Moreover, veils with an intermedium specific fibre/matrix contact area, namely, glass and aramid veils, have shown less propensity to develop extensive back-face damages than those in which this property is smaller or larger, polyester and carbon veils, respectively.

In terms of internal damage area, a strong dependency was observed on the interleaving strategy adopted, since most of laminates interleaved in the most critical shear stress interfaces have shown to develop smaller damaged areas then those where critical normal stresses strategy was applied. Comparatively to non-interleaved layup, at the lowest impact energy level (13.5 J), the best performance was observed in the laminate interleaved with glass fibre veils interleaved in critical normal stresses interfaces, which presented a reduction in damaged area of 62 %. However, at this impact energy level all interleaved configurations have revealed an impressive damage reduction of at least 50 %. At 25 J and 40 J impact energy levels, where larger damages were observed, laminates interleaved with carbon and aramid veils at most critical shear stress interfaces have shown to be able to reduce damage area up to 43 % and 33 %, respectively. Moreover, for the highest impact energy level (40 J), a strong correlation was observed between the fibre covered surface area of veils and impact damage area. The larger the fibre covered surface area, the lowest was the impact damaged area obtained.

Compression after impact (CAI) tests conducted on specimens previously subject to an impact of 25 J did not reveal significate differences among non- and interleaved configurations, which suggests no influence of veils interleaving on residual strength after impact.

Those results allow us to conclude that impact damage depends, essentially, on interleaving strategy adopted, although, some microstructural characteristics of veils, as specific fibre/matrix contact area and fibre covered surface area of veils, may play an important role depending on the impact energy.

Chapter 7
3D Printed Interlaminar Interlocking Structures

Despite of their extraordinary in-plane mechanical properties and low density, advanced composite materials are quite susceptible to out-of-plane loading. This misbehaviour arises, essentially, from the high brittleness and layer-by-layer architecture of these materials. One of the most common and dangerous examples of those solicitations are low velocity impact (LVI). Under these conditions, several barely visible internal damages (BVID) may be formed and then propagate throughout the interlaminar region (delaminations), compromising its mechanical performance along its service lifetime.

In the attempt to mitigate this problem, some strategies have been already explored, one of the most promising one consists on reinforce the interlaminar resin rich region using toughening materials or structures. Acting only where the crack is more likely to propagate, this approach has shown to decrease damage propagation without causing substantial losses on in-plane mechanical properties. Taking advantage of the degree of freedom to create new designs and the wide range of different materials that additive manufacturing (3D-printing) allows, such interlaminar toughening structures may be optimized in order to create effective interlocking interfaces and improve composites impact damage resistance.

In this Chapter, two different interlocking structures were designed (pattern A and B) and printed using two thermoplastic materials, namely a polyether-polyurethane elastomer (TPU) and a polylactic acid thermoplastic (PLA), into six interplay regions of a standard aircraft laminates. Morphology, mechanical response and damage resistance of those new 3D printing reinforced configurations were compared to a reference no printed layup. The four distinctive structures (two patterns printed with two different materials) were directly printed over unidirectional carbon fibre (UDCF) tissues at selected interfaces and then impregnated with an epoxy resin by vacuum bag infusion. All the 3D printing modified laminates were characterized and compared to a non-modified according their thickness and voids content under scanning electron microscopes (SEM). A mechanical test campaign was also carried out to evaluate the composites performance under ILSS, three-point bending (3-PB) and LVI tests. Finally, all tested specimens were inspected under microscope to evaluate the main failure mode and the projected delamination area after impact was assessed by ultrasonic testing.

7.1 Approach

Incorporation of interlocking mechanisms is a common, and well reported in literature, strategy used to improve intra- and interlaminar properties of advanced composite materials. Matrix and surface fibres modification and through-thickness mechanical reinforcements, as 3D woven, stitching and z-pining, are well-known engineering attempts to promote fibre/matrix and layer by layer adhesion by mechanical interlocking systems [61][104][174].

Such interlocking mechanisms may be also found in several organic-inorganic nanocomposite biomaterials, as nacreous shells. Among them, abalone shell is one of the most studied. Its brick-mortar like structure, composed by 95 % of aragonite bricks, and the mechanical interaction between them ensures good stiffness and toughness to this bio-composite material [175]. The rough surface between platelets of the brick-mortar like structure, ensures a high energy dissipation of this nacreous shells as result of the constant crack deflection and, consequently, yields larger resistance to its propagation [175]–[177]. Figure 75 shows a schematic illustration of this nacreous shell asperities interlaminar interlocking mechanism.

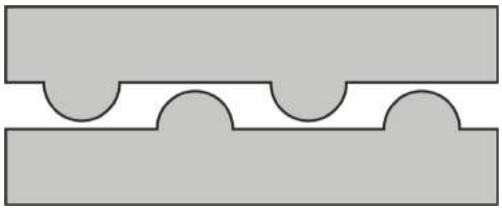

Figure 75: Nacreous shell asperities interlaminar interlocking mechanism.

Inspired by this interlaminar interlocking mechanism, in this work, two different 3D printed patterns were, for the first time, strategically printed into a conventional aeronautic carbon/epoxy laminate with 28 unidirectional carbon fibre layers (27 interfaces) to study its suitability and response to low velocity impact. Two different polymers, a thermoplastic polyether-polyurethane elastomer (TPU) and a polylactic acid thermoplastic (PLA), were used to print directly patterns over the laminate dry carbon fibres layers before resin impregnation by vacuum bag infusion. In order to avoid thickness and weight overage, and based by impact damage resistance results obtained in the previous chapter (Chapter 6), only six interfaces were selected to print interlaminar interlocking patterns.

7.2 Laminates

7.2.1 Materials

As happened in the three previous chapters, all CFRP laminates were manufactured using the 150 g/m^2 unidirectional carbon fibre (UDCF) fabrics (Dynanotex HS 24/150 DLN2) and a bi-component epoxy resin from Sika® (Biresin® CR83 epoxy resin and Biresin® CH83-6 hardener) already described in sections 3.1.1 and 3.1.2 (Chapter 3).

The two distinctive polymeric filaments selected to create six interlocking 3D printed interfaces into a standard aircraft laminate were: a polylactic acid thermoplastic (PLA) and a thermoplastic polyether-polyurethane elastomer (TPU), provided form BQ and Recreus Industries s.l. from Spain, respectively. Both filaments used, which a diameter of 1.75 mm, are shown in Figure 76.

Figure 76: PLA (green) and TPU (orange) 3D printing filaments.

More details about both polymeric filaments may be found in their respective datasheets in Appendix A.

7.2.2 Laminate manufacturing

All laminates were manufactured by vacuum bag infusion according to the procedure described in section 3.2.1 (Chapter 3).

The 28 UDCF layers standard aircraft laminate (LS) was, once again, taken as reference. Using the same unidirectional carbon fibre stack sequence, four new 3D printing reinforced laminates were also produced in order to be compared to the reference along the testing campaign.

To avoid thickness and weight overage in the final composite, only six interfaces were selected to print an interlocking system. Supported by the results regarding damage resistance achieved in the previous

chapter (Chapter 6), selected interfaces in this work were those where shear stresses have shown to be more critical, according to the FE model developed in section 6.3 (Chapter 6). Therefore, the new interlaminar interlock proposed system was incorporated in the 1st, 4th, 5th, 23rd, 24th and 27th interlaminar regions. Table 21 shows the reference and 3D printed interlaminar laminates studied in this Chapter

Table 21: Laminates stacking sequence

Laminate	N° layers		Stacking Sequence
	UDCF tissue	Printed interfaces	
Reference (LS no print)	28	-	$[0/45/90/-45/45/-45/0]_{2s}$
3D Printed reinforced laminates	28	6	$[0/\mathbf{P}/45/90/-45/\mathbf{P}/45/\mathbf{P}/-45/0/0/-45/45/-45/90/45/0]_{s}$

P Printed interfaces

In order to reduce damage propagation in composites laminates, two different interlocking systems are proposed in this work, namely, Patterns A and B. Using as reference the top and bottom carbon fibre layer oriented at 0° in LS laminate, both patterns were composed by several straight lines (printed filaments) printed at 90°, spaced by gaps of 10 mm and 5 mm in A and B patterns, respectively. The interlocking system was achieved by printing both patterns in the top surface of the bottom carbon layer and in the bottom surface of its adjacent carbon layer, interspersed by 5 mm and 2.5 mm in A and B paterns, respectively. A schematic representation of the both patterns is presented in Figure 77.

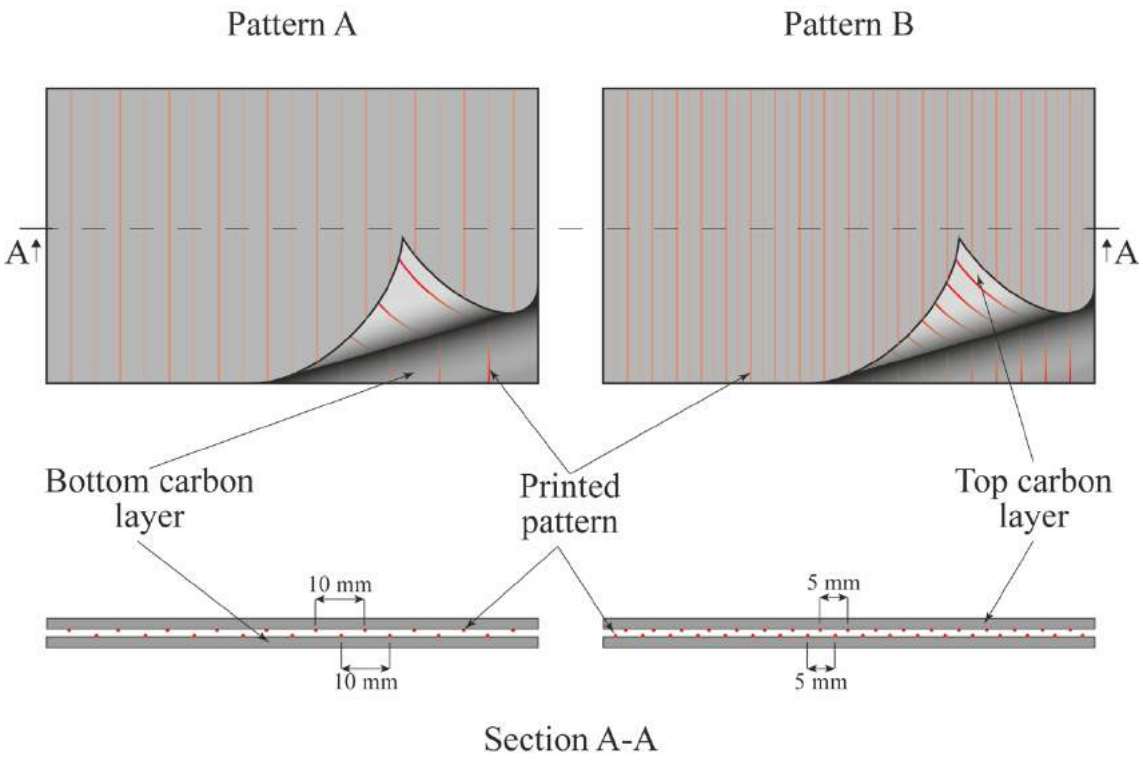

Figure 77: Schematic representation of Patterns A (at left) and B (at right).

Both patterns were directly printed over the UDCF tissues in a Prusa i3 MK3 commercial 3D printing machine. To minimise the impact of 3D printed patterns on laminate's morphology, thickness and weight, a 0.25 mm nozzle was used to perform all prints. UDCF fabrics with desired orientation and dimensions (220 x 220 mm) were previously cut in a laser cutting machine shown in Figure 12 a) (section 3.2.1, Chapter 3) and then carefully placed and attached to the removal printing support (so-called "printing bed" or just "bed") using a paper tape. The printing process parameters for both materials, PLA and TPU, are presented in Table 22.

Table 22: 3D printing process parameters

Nozzle diameter	Printing speed	Nozzle/bed distance	Temperature	
			Nozzle	Bed
mm	mm/s	mm	°C	°C
0.25	15	1 mm	215	60

Figure 78 presents a photography of an ongoing pattern 3D printing process over the UDCF dry fabric.

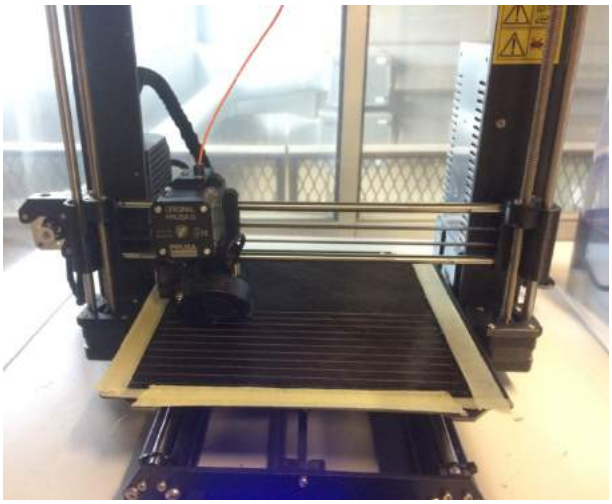

Figure 78: Photography of an ongoing pattern 3D printing process.

Figure 79 also presents the final 3D printed patterns over the UDCF dry fabric.

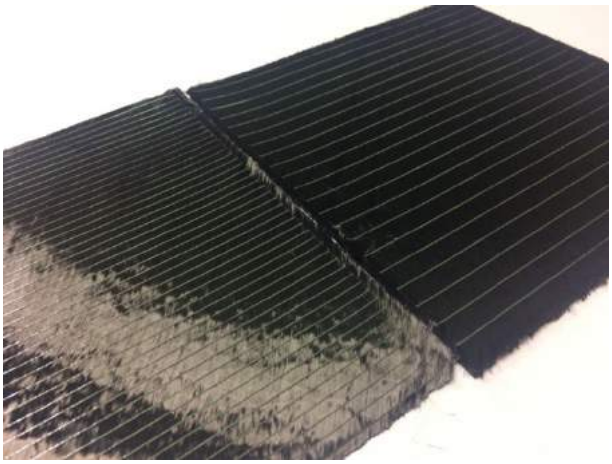

Figure 79: Final 3D printed patterns (Pattern A at right and Pattern B at left) over an UDCF fabric.

Due to the printing area available on Prusa i3 MK3 printing machine, two 220 × 220 (mm) laminates of each configuration were manufactured in order to ensure a sufficient number of specimens to conduct all characterisation experiments.

Finally, before resin infusion, all printed and no printed UDCF fabrics were carefully stacked up manually by the selected order and orientation in the vacuum bag infusion mould.

7.3 Characterisation and testing campaign

In this section will be introduced the main techniques used to characterise laminates and their components.

7.3.1 Materials characterisation

Prior to 3D printing, five samples of PLA and TPU filaments directly picked from the filament roll, were experimentally tested in order to assess their density, by using immersion method according to the procedure described in section 4.1.1 (Chapter 4).

After being printed over the UDCF fabrics, PLA and TPU patterns were observed under scanning electron microscope (SEM) in order to evaluate their adhesion to dry carbon fibres. Two samples of each pattern were cut directly from the printed fabrics and covered by a thin layer of gold–palladium before examination in order to prevent electrostatic charges in the material.

7.3.2 Laminates characterisation

Laminates' thickness was assessed using a caliper rule. All impact specimens were measured in four different locations in order to ensure a reliable average thickness.

The morphologic analysis of laminates and patterns was conducted under SEM in order to investigate laminates and printed filaments (patterns) cross-sections, patterns position and voids content. Four samples of each laminate were cut, carefully polished and covered by a thin layer of gold–palladium prior to inspection.

Before laminates' volume fraction determination, five laminates' samples were used to assess their respective specific mass by immersion method, using the same procedure described and equation 11 (section 4.1.1, Chapter 4).

To assess printed patterns areal weight, five prints of each pattern, namely, pattern A and B of PLA and TPU, were made directly over the printing support (bed), carefully removed and weight in a digital balance having a 1×10^{-4} g accuracy. Laminates' areal weight was determined following the same procedure and using the whole three specimens prepared to preform low velocity impact tests. A detailed description of areal weight procedure may be consulted in section 6.4.1 (Chapter 6).

Laminates' UDCF fabrics, resin and printed patterns volume fractions were estimated following the same procedure and calculations described in the previous section 6.4.2 (Chapter 6). All variables with the index "v" (e.g. W_v) in equations 32 to 40, should be interpreted as referent to PLA or TPU printed patterns.

7.3.3 Quasi-static mechanical tests

7.3.3.1 Three-point bending (3-PB) tests

Three-point-bending tests performed in according with procedure described in section 3.4.2 (Chapter 3), were carried out in order to assess laminates flexural properties. Five 170 x13 (mm) specimens of each laminate, with the 0° plies oriented perpendicularly to loading nose, were tested under the same conditions of that ones already described in section 5.3.2.2 (chapter 5) for the tests made on the bioinspired Bouligand-like layups.

Finally, laminates failure mode was analysed and compared to each other using a digital magnifier Leica DMS1000 showed in Figure 15 (section 3.4.2, Chapter 3).

7.3.3.2 Interlaminar shear strength (ILSS) tests

Laminates' interlaminar shear strength performance were evaluated by short-beam shear tests, in accordance with the procedure described previously in section 3.4.3 (Chapter 3). All experiments were performed using the same equipment, five similar 40 × 20 (mm) specimens and under exatly the same conditions already described before for the tests made on the bioinspired Bouligand-like laminates in section 5.3.2.3 (chapter 5).

Finally, the failure mode of each laminate was also analysed and compared to each other using a digital magnifier Leica DMS1000 showed in Figure 15 (section 3.4.2, Chapter 3).

7.3.4 Low velocity impact (LVI) tests

Low velocity impact (LVI) tests were performed by using the equipment and procedure described in section 3.4.4 (Chapter 3). In order to ensure an effective damage in specimens, an impact energy level of 40 J was imposed by using a 5.045 kg impactor placed at 0.810 m above the specimen impact surface, prior to test started.

As mentioned before, due to the small printing area available in the 3D printing machine, two 220 x 220 (mm) 3D printing reinforced laminated composite plates were produced for each configuration. Therefore, considering the LVI specimens' dimension requirement (150 x 100 (mm)) and laminates manufacturing time consuming, for each configuration, two impact specimens were cut from one plate and the other one from the other plate, ensuring a total of three specimens for each condition. On the other hand, four specimens from the reference no-printed laminates were also tested.

Back-face impact external damages were carefully visually inspected, and their extension measured by a caliper rule.

Ultra-sounds were used to assess specimens' internal damages. All inspections of 3D printed reinforced laminates were carried out using a Prisma phased array from Sonatest, equipped by a 5 MHz scanner. In order to ensure a reliable analysis, the scanner was accoupled to an automated home-made XY arm. Specimens' inspection was then performed inside a water tank to avoid scanner/specimen surface friction and improve acoustic signal. A photography of the experimental apparatus is presented in Figure 80.

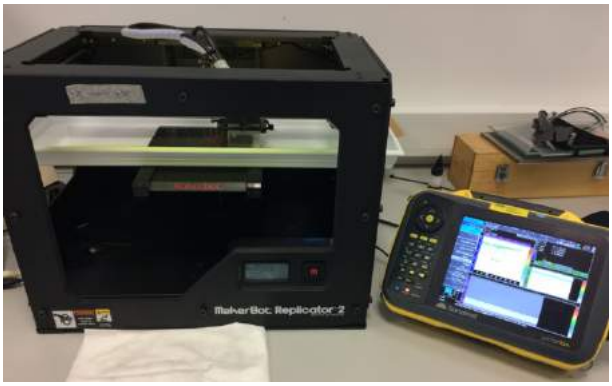

Figure 80: Ongoing ultra-sounds inspection with Prisma phased array accoupled to the automated home-made XY arm.

Phased array data was analysed on UTstudio software, from Sonatest, which allowed to assess length (a) and width (a) damage extent across specimens' thickness. A representative image of phased array data visualised on UTstudio software may be seen in Figure 81.

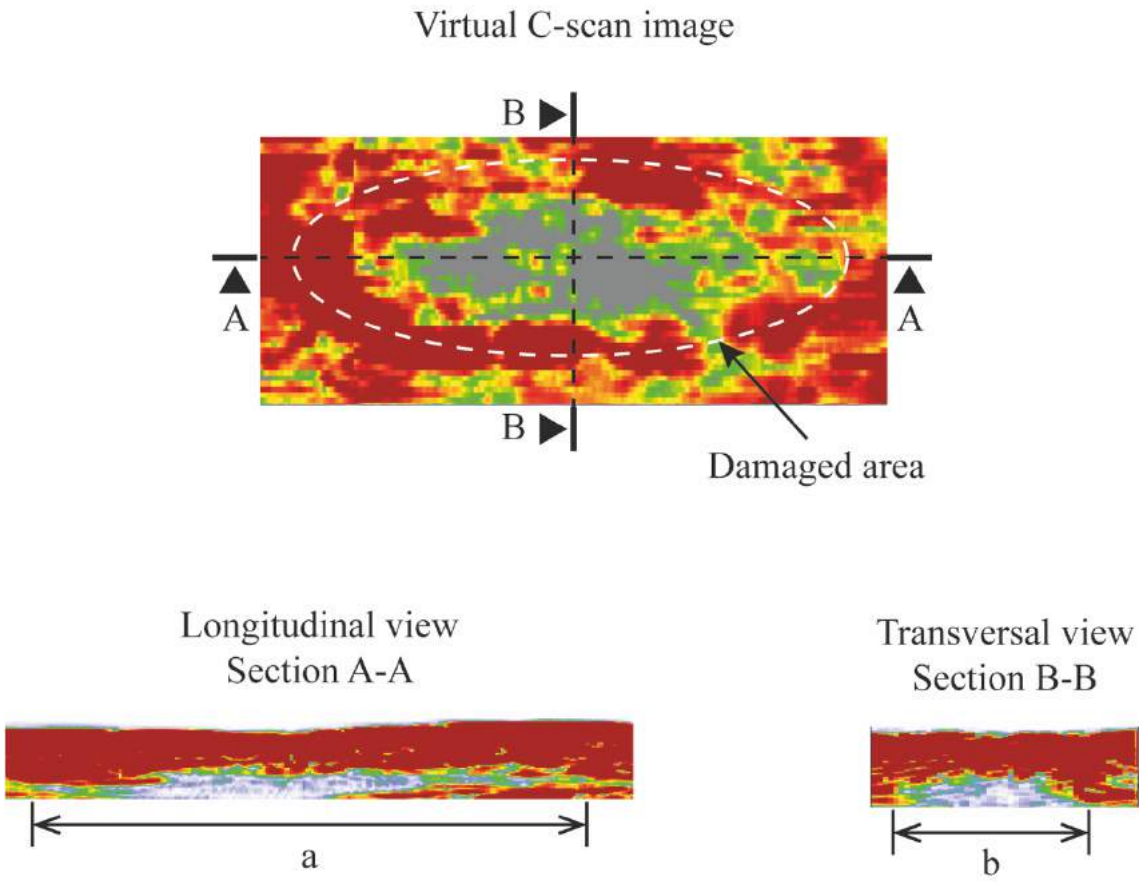

Figure 81: Representative image of Phased array data visualised on UTstudio software.

The image on top of figure represents a virtual C-scan view computed by the software. As may be seen, its definition is poor due to the acoustic sign overlapping. The longitudinal and transversal cross section views (bottom left and right on the figure, respectively) allow better defined any damage length (a) and width (b).

Considering the virtual C-scan image, it is perceptible an elliptical damage shape, but its limits cannot be precisely identified. Therefore, using the damage length and width projections over the virtual C-scan image it was possible to obtain a better approximation of the damaged area by calculating the ellipse area. The white ellipse depicted on C-scan image represents an approximation of the damaged area on a specimen using the previous procedure. Using this procedure, the elipse damage area was calculated in the specimens by using the following equation 41:

$$Damage\ area = \left(\frac{a}{2}\right) \times \left(\frac{b}{2}\right) \times \pi \tag{41}$$

where *a* and *b* are the lengths of major and minor elipse axes.

The 3D printing reinforced laminates damaged area calculated from equation 41 were than compared to damaged area of no-printed reference previously assessed by C-scan in the work presented in Chapter 5, impacted at the same impact energy level (40 J).

7.4 Results

In this section, obtained results and observations will be concisely presented.

7.4.1 Materials characterisation

Prior to laminates manufacturing, five samples of each one of their components, namely, UDCF Dynanotex HS 24/150 DLN2), Biresin CR83 epoxy resin and, PLA and TPU printing filaments were used to determine their density by immersion method. Table 23 presents the experimental results obtained from PLA and TPU printing filaments, whereas, UDCF tissues and epoxy resin specific mass may be consulted in Table 2 (in section 4.2, Chapter 4).

The specific mass experimentally determined were in good agreement with values given by the provider in filament material datasheets, where is referred that PLA has a specific mass of 1.24 g/cm^3 and TPU 1.12 g/cm^3.

Table 23: PLA and TPU printing filaments specific mass.

Material	Specific mass g/cm^3
PLA	1.253 ± 0.005
TPU	1.140 ± 0.005

Figure 82 a) and b) present a SEM micro-photography a PLA and a TPU filament printed directly over dry carbon fibre tissues.

The SEM visualisations of 3D printed patterns revealed a poor and almost non-existent adhesion between the PLA printed filaments and dry carbon fibres, as may be observed in Figure 82 a). On the other hand, Figure 82 b) shows that TPU printed filaments seem to develop a more effective adhesion to carbon fibres. A closer observation magnified 1500 times in the top right hand of Figure 82 b), shows a well-defined bonding between both materials.

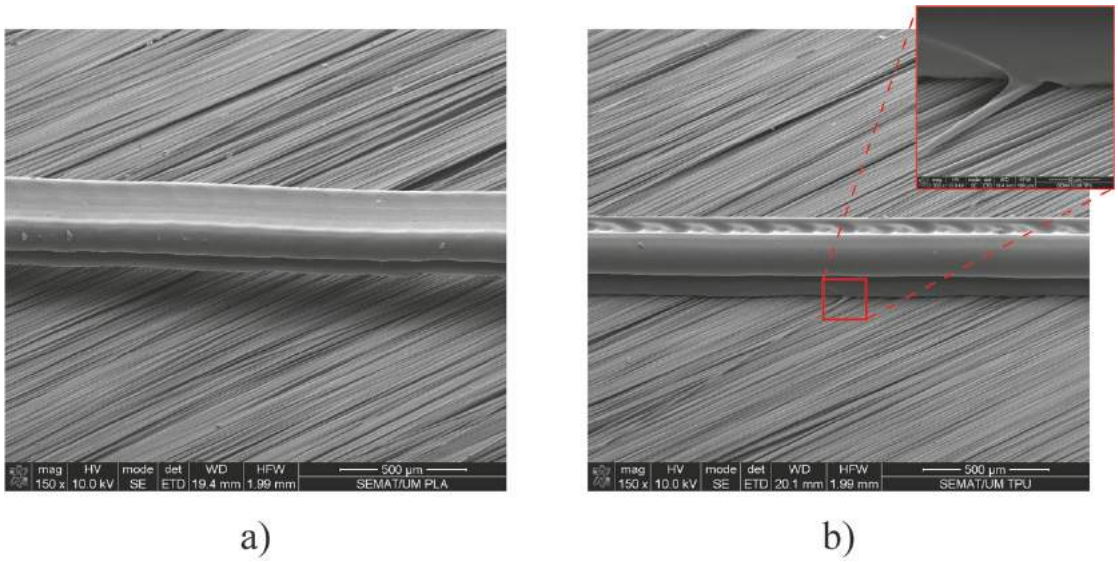

Figure 82: Photographs of a) PLA and b) TPU filament printed over dry carbon fibre tissues (magnified ×150).

From both observations it is also possible to see the non-uniform filament perimeter. Apparently, both filaments are composed by a doble layer of materials. Moreover, TPU filaments present a soft grooved top surface (Figure 82 b)) which could result from the printing nozzle movement and intrinsic high viscosity of the material.

7.4.2 Laminates characterisation

Concerning laminates characterisation, a set of experiments and observations were carried out to determine their components volume fraction, thickness, morphology and voids content.

As it was been mentioned above, laminates' compounds volume faction was determined according to the procedure described in section 6.4.2 (Chapter 6), which requires the 3D printed patterns areal weight to make the calculation. Therefore, five prints of each pattern (pattern A and B of PLA and TPU) were directly printed over the removing printing bed using the same 3D printing parameters used to print them over dry carbon fibres. After carefully removed them from the printing bed, all printed patterns were weight using the digital balance and their areal weight was estimated using equation 22 presented in section 6.4.1 (Chapter 6).

Table 24 summarises the experimentally obtained PLA and TPU printed patterns areal weights.

Table 24: PLA and TPU printed patterns average (± stander deviation) areal weight.

Printed material	Pattern	Areal weight
		g/m²
PLA	A	8.39 ± 0.35
	B	16.36 ± 0.62
TPU	A	6.50 ± 0.24
	B	12.61 ± 0.26

The areal weight of UDCF tissues (Dynanotex HS 24/150 DLN2) was previously experimentally determined in section 6.5.1 (Chapter 6) and, the experimental result may be seem in Table 14 of the same section.

In order to compute the UDCF fabrics and printing patterns volume fractions, it was necessary assess laminates' density. Five samples of each configuration were randomly picked from each laminate plate and their specific mass was determined using immersion method described in section 4.1.1 (Chapter 4). The experimental values determined for laminates thickness and specific mass as well as UDCF tissues and printed patterns volume fractions are presented in Table 25.

Table 25: Laminates thickness, specific mass and volume fractions of the UDCF and printed patterns.

Printed material	Printed pattern	Thickness	Specific mass	Volume fraction	
				UDCF	Printing
		mm	g/cm³	%	%
No printed pattern		3.83 ± 0.05	1.48 ± 0.01	62.0	-
PLA	A	4.16 ± 0.03	1.44 ± 0.01	57.3	1.0
	B	4.35 ± 0.02	1.43 ± 0.00	54.6	1.9
TPU	A	4.11 ± 0.04	1.44 ± 0.01	58.0	0.9
	B	4.63 ± 0.09	1.41 ± 0.00	51.6	1.5

As expected, 3D printing reinforced laminates have demonstrated a lower UDCF volume fraction when compared to the reference (no printed one). This is especially due to the increment on thickness, also observed, owing to the 3D printed patterns incorporation on the selected interfaces (Table 25). Should be noted that this incrementation on thickness were more notorious when pattern B was used as interlocking system, reaching plus 14 % for PLA and 21 % for TPU, when compared to the reference laminate, whereas, for laminates reinforced with pattern A, thickness incrementation achieved 9 % and 8 %, when PLA and TPU were used, respectively.

Besides the higher resin volume fraction resulting from the higher thickness of 3D printed reinforced laminates, the thermoplastic interlaminar interlock structures also contributed to reduce the laminates density, as may be observer in Table 25. However, this time, no correlation may be established between the pattern nor material used. With the exception of the laminate printed with TPU pattern B, which has shown density reduction of 5 % when compared to the reference (no printed) one, all the other new printed laminates have demonstrated a similar reduction of about 3 %.

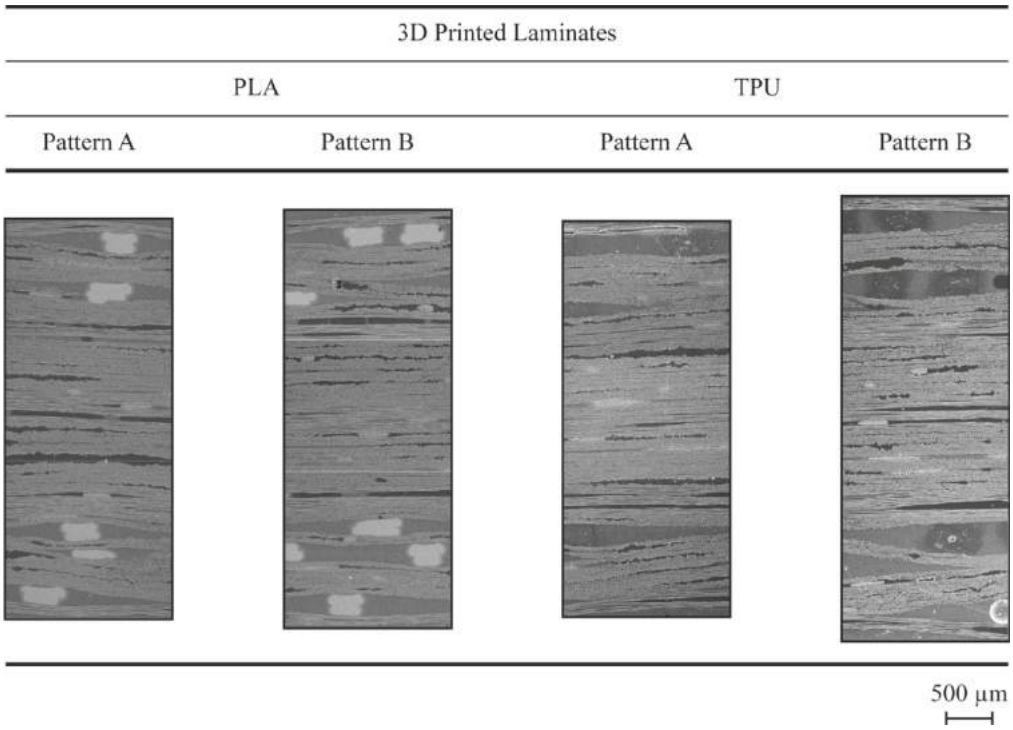

Figure 83: SEM observation of 3D printed interlocked laminates stratigraphy.

Figure 83 shows a stratigraphic image of each 3D printed interlocked laminate. From those images it is possible to observe the printed patterns, white spots when PLA was used and dark grey from the TPU printed structures. Independently on the printed material or pattern, the inclusion of these interlaminar interlock structures led to the formation of resin pockets close to their printed filaments, clearly identified on images as lighter grey uniform regions. Moreover, the higher number of filaments in configurations where pattern B were used, has led to large resin pockets surrounding them.

For a better understanding, in Figure 84 a) and b) show and indicate the different components of PLA and TPU printed laminates. Besides printed filaments and resin pockets, weft threads and the adhesive resin used to produce UDCF tissues, may be also identified in the photographs. As it was been observed in previous chapters (Chapter 5 and Chapter 6), those elements represent a significant volume and may play an important role on composites failure mode.

In Figure 84 a) and b) it is also possible to observe that the inclusion of 3D printed patterns in interlaminar regions have introduce waviness on their adjacent UDCF layers.

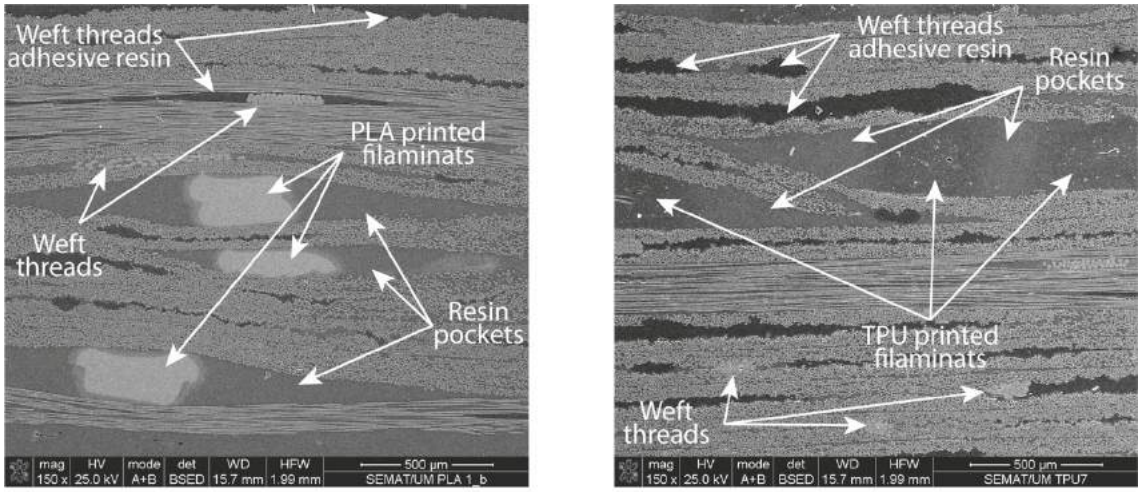

Figure 84: Different components of a) PLA and b) TPU reinforced laminates.

From SEM observations it was also possible to evaluate voids content into each configuration. Figure 85 presents a micro-photography of each 3D printing interlocked laminate where small voids are highlighted by a red ellipse. After several observations it was concluded that the presence of voids was almost insignificant and, when existent, they were usually located in resin pockets, indicating that they essentially resulted from air bubbles trapped during the vacuum bag infusion process.

Despite PLA filaments being well visible in SEM micro-photographs, it is not easy to define TPU filaments boundaries. Moreover, both filaments present a non uniform cross section that sometimes seems to present different geometry, even for filaments of the same material. Therefore, it was not possible to measure their dimensions with accuracy and it is only possible to state that PLA printed filaments cross-section presented width and height dimensions between 300 - 400 μm and 100 – 200 μm, while TPU filaments cross-sections had width and height dimensions between 350 - 450 μm and 150 – 250 μm, respectively.

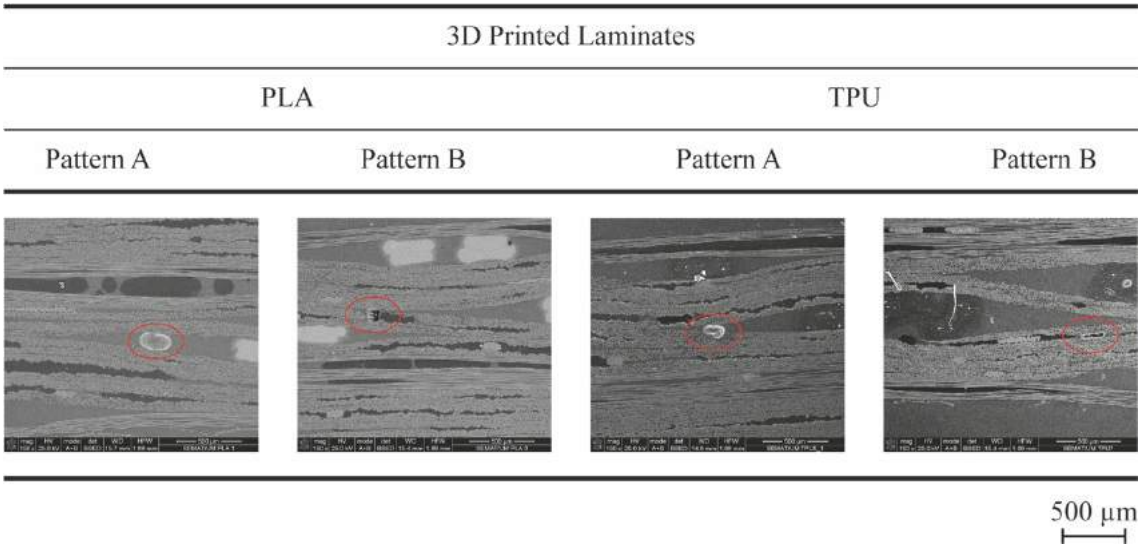

Figure 85 SEM images of voids inside 3D printing interlocked laminates (magnified ×150).

Another interesting observation was the presence of tinny air bubbles inside TPU printed filaments, as may be seen in Figure 86. This may be result of the overlapped printing of the characteristic TPU grooved top surface filaments, observed in Figure 82 b) (see section 7.4.1).

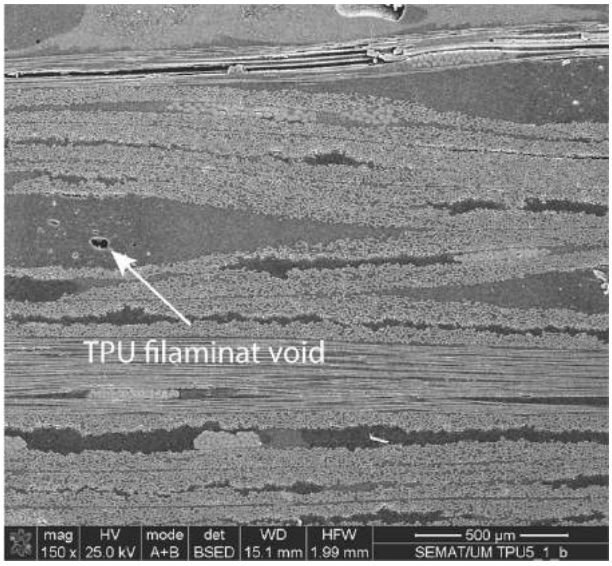

Figure 86: SEM image of tinny air bubbles inside TPU printed filaments (magnified ×150).

7.4.3 Quasi static mechanical test results: 3-PB and ILSS

Three-point bending (3-PB) and interlaminar shear strength (ILSS) tests were conducted on reference and 3D printed interlocked laminates in order to evaluate and compare their mechanical performance and failure mode.

Table 26 presents the results obtained from those two experimental tests, namely, 3-PB flexural modulus ($E_{flex.}$) and maximum stresses ($\sigma_{out.surf.}$), and ILSS interlaminar shear strength (τ_{13}) of each laminate.

Table 26: 3-PB flexural modulus ($E_{flex.}$) and maximum stresses ($\sigma_{out.surf.}$) and ILSS maximum shear strength (τ_{13}).

Printed material	Printed pattern	3-PB		ILSS
		$E_{flex.}$ GPa	$\sigma_{out.surf.}$ MPa	τ_{13} MPa
No print		38.2 ± 1.3	461.6 ± 25.3	18.8 ± 0.9
PLA	A	34.4 ± 1.2	467.6 ± 18.8	23.0 ± 1.2
	B	31.3 ± 0.5	470.4 ± 24.7	23.5 ± 0.7
TPU	A	34.1 ± 1.0	416.9 ± 23.7	22.8 ± 1.1
	B	30.8 ± 1.2	403.3 ± 31.3	21.3 ± 0.8

7.4.3.1 3-PB tests

3-PB results presented in Table 26, namely, maximum bending strength ($\sigma_{out.surf.}$) and flexural modulus ($E_{flex.}$), are graphically depicted in Figure 87 a) and b), respectively.

From Figure 87 a)'s chart may be concluded that, independently on the pattern, laminates printed with PLA were able to withstand roughly the same load than the reference laminate. On the other hand, TPU printed layups have shown lower load bearing capability when compared to any other laminates, and the TPU pattern B laminate seems to have slightly lower bending strength than any other laminate.

Considering Figure 87 b), all 3D printing interlocked laminates revealed a lower flexural elastic modulus ($E_{flex.}$), comparatively to the reference one (no printed). However, may be also observed from chart that laminates printed with the pattern A have shown slightly higher bending stiffness than their peers where pattern B was printed. Finally, PLA printed laminates seem to have slightly lower negative impact on E_{flex} than those laminates using TPU as printing material.

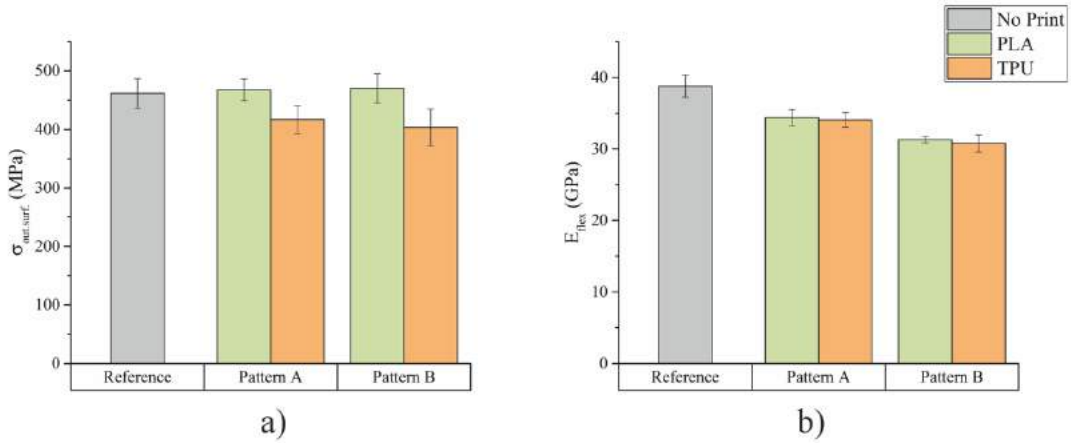

Figure 87: 3-PB results of a) maximum stress and b) flexural modulus for reference and 3D printing reinforced laminates.

Figure 88 presents images of the typical failure modes observed on the 3D printing interlocked laminates.

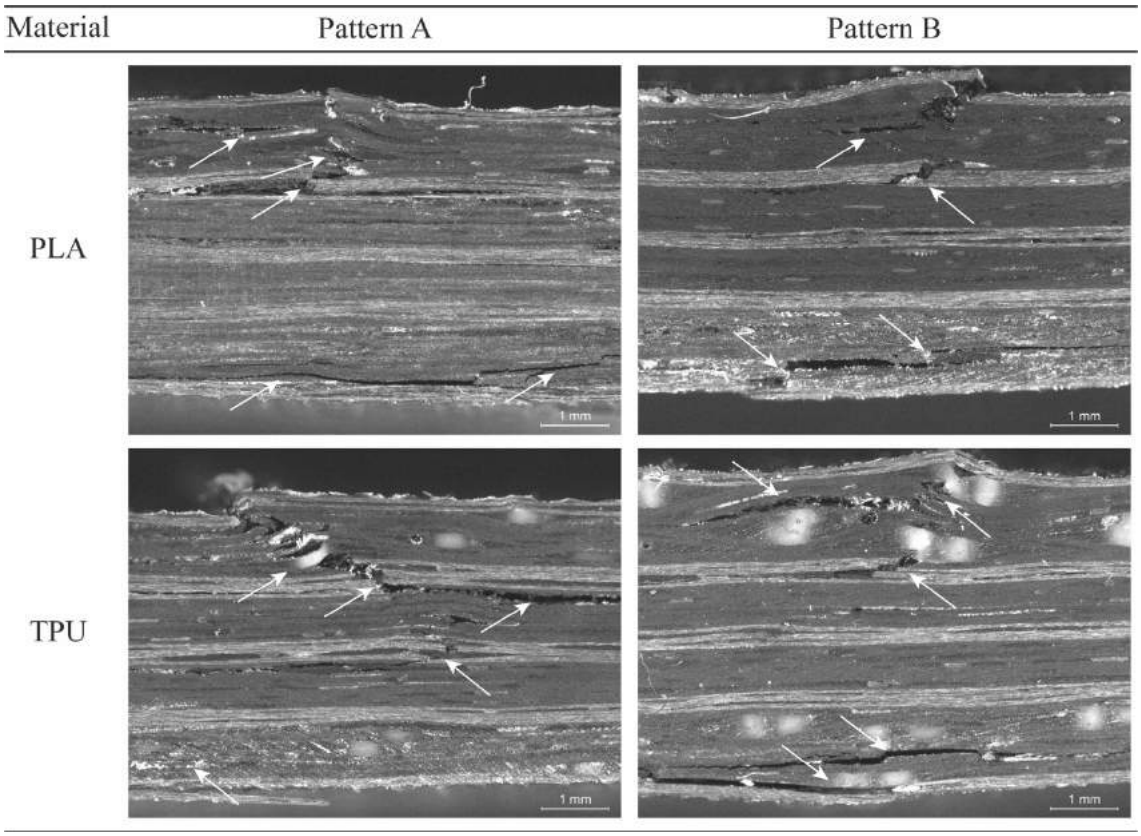

Figure 88: Failure mode of 3D printing reinforced laminates after 3-PB tests.

From 3-PB failure mode images of 3D printing interlocked laminates, may be seen that all configurations tend to fail catastrophically on their compression side (top surface on every images). On the other hand, on tensile side (bottom surface on every images), both PLA printing and TPU pattern B structures, have developed translaminar damages accompanied be several extensive delaminations. Contrarily, only a small delamination was observed on TPU pattern printed laminates.

7.4.3.2 ILSS test

Figure 89 depicts graphically the maximum shear stresses (τ_{13}) obtained in ILSS tests made on the reference and 3D printing interlocked laminates.

From the chart it is clear that 3D printing interlocked laminates presented higher global resistance to delamination than the reference layup. Considering only 3D printing interlocked layups, may be observed that, independently of the printed pattern, PLA printed laminates seemed to withstand higher shear stresses (τ_{13}) than TPU printed configurations. However, both materials, PLA and TPU, have demonstrated an antagonic behaviour according to the printing pattern used. The performance of PLA pattern B laminate seems to be slightly better than when the same material was used with pattern A and, contrarily, TPU printed laminates demonstrated higher interlaminar shear strenght when pattern A was used.

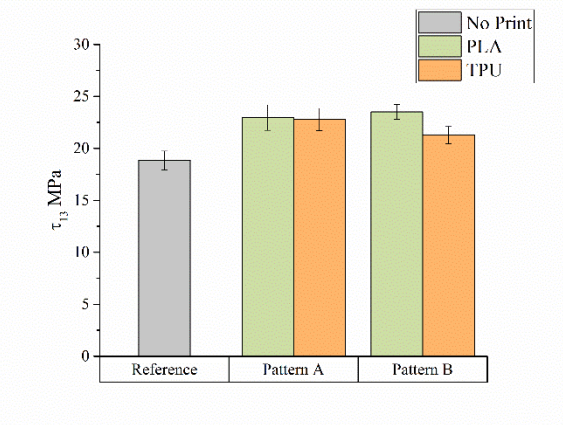

Figure 89: ILSS maximum interlaminar shear strength (τ_{13}) obtained on reference and 3D printing reinforced laminates.

Figure 90 shows typical images of ILSS failure modes of each 3D printing rinterlocked layups.

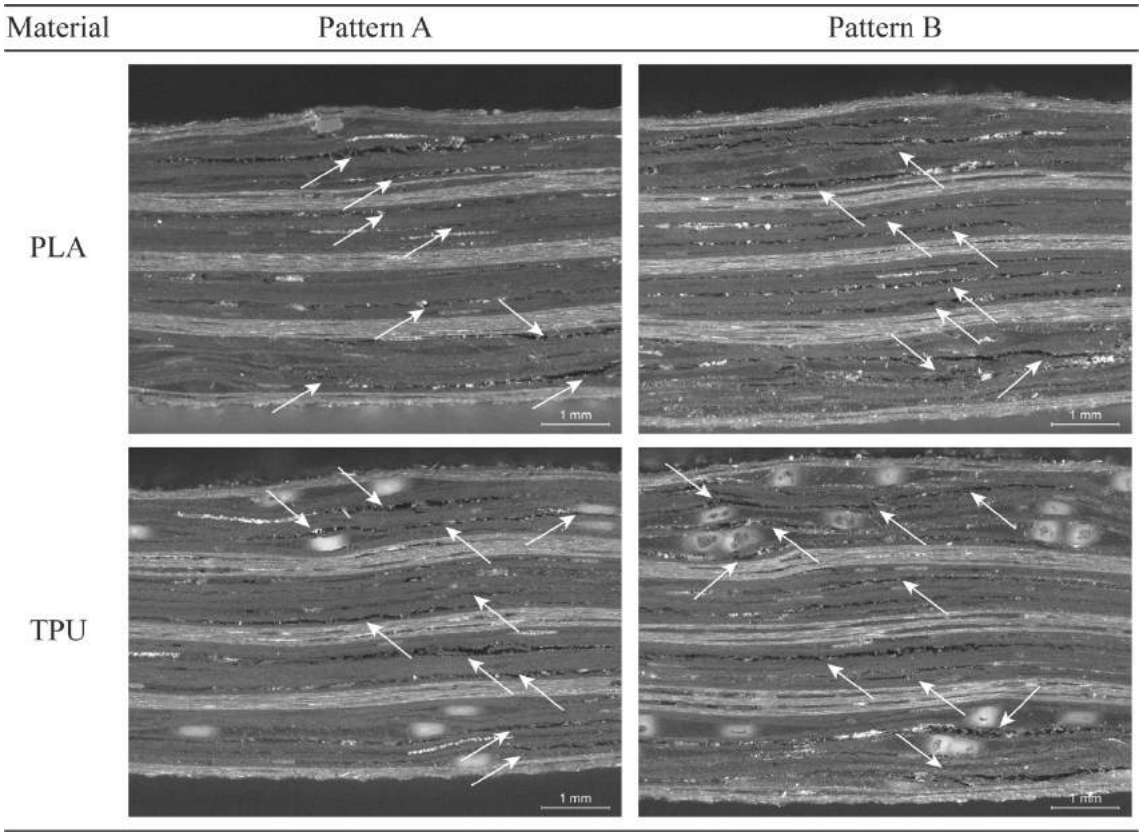

Figure 90: Failure mode of 3D printing reinforced laminates after short-beam shear tests.

The images above of ILSS failure mode show that no significant differences were found among the 3D printing interlocked laminates. All of them have developed several delaminations across their thicknesses but none delamination was found on the interfaces of 3D printing laminate.

7.4.4 Low Velocity Impact (LVI) tests results

All laminates were submitted to the low velocity impact (LVI) tests made at the 40 J impact energy level. As mentioned before, due to the small number of laminates available, the tests were performed on three specimens of each 3D printing locked laminates and on four of the reference layup.

Figure 91 presents the typical load vs displacement curves obtained from 40 J impact test made each laminate. The overlapping of the obtained curves, especially during the first elastic specimens responded (initial graph stage), confirm the good reliability of the LVI tests made. The first analysis of graphs indicates a clear higher impact load bearing capability of laminates printed with pattern B, independently on the printing material used.

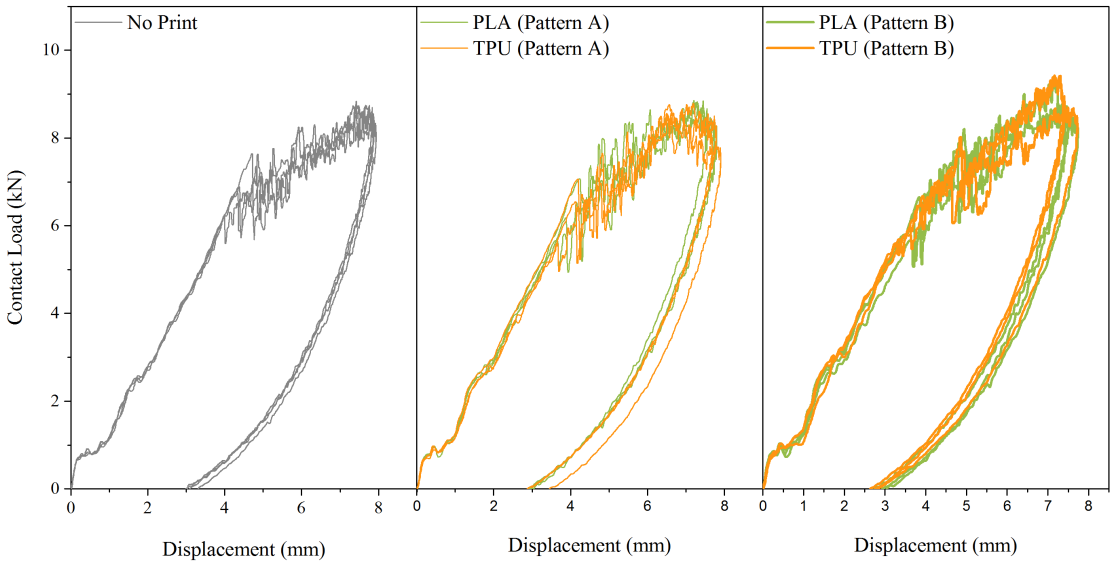

Figure 91: Load vs displacement curves of reference (no print) and 3D printing interlocked laminates categorised according both used printed patterns (A and B).

Table 27 summarises the results of the main indicators, used in this work, to evaluate the mechanical behavior of all tested laminates. As may be seen in table, the maximum impact energy (E_{max}) calculated form experimental data was shown to be slightly superior (40.5 J) than the theoretically established one (40 J).

Table 27: LVI tests results calculated from data obtained from the tests made on each laminate.

Imp. enegy	Printed material	Printed pattern	Peak Load	P_{cr}	E_{max}	E_{cr}	E_{abs}
			kN	kN	J	J	J
40	No printed one		8.71 ± 0.11	6.88 ± 0.51	40.47 ± 0.00	14.08 ± 1.79	27.73 ± 0.25
	PLA	A	8.77 ± 0.08	6.30 ± 0.59	40.46 ± 0.00	12.03 ± 0.76	27.74 ± 0.26
		B	9.00 ± 0.17	6.20 ± 0.41	40.45 ± 0.01	11.31 ± 0.98	27.89 ± 0.72
	TPU	A	8.66 ± 0.09	6.40 ± 0.60	40.46 ± 0.00	12.38 ± 1.81	28.49 ± 0.90
		B	9.23 ± 0.27	5.76 ± 0.16	40.45 ± 0.00	9.81 ± 0.49	27.10 ± 0.17

For better interpretation, experimental results of the peak and critical loads (P_{cr}), final absorbed (E_{abs}) and critical (E_{cr}) energies obtained from each tested structure are graphically depicted in Figure 92.

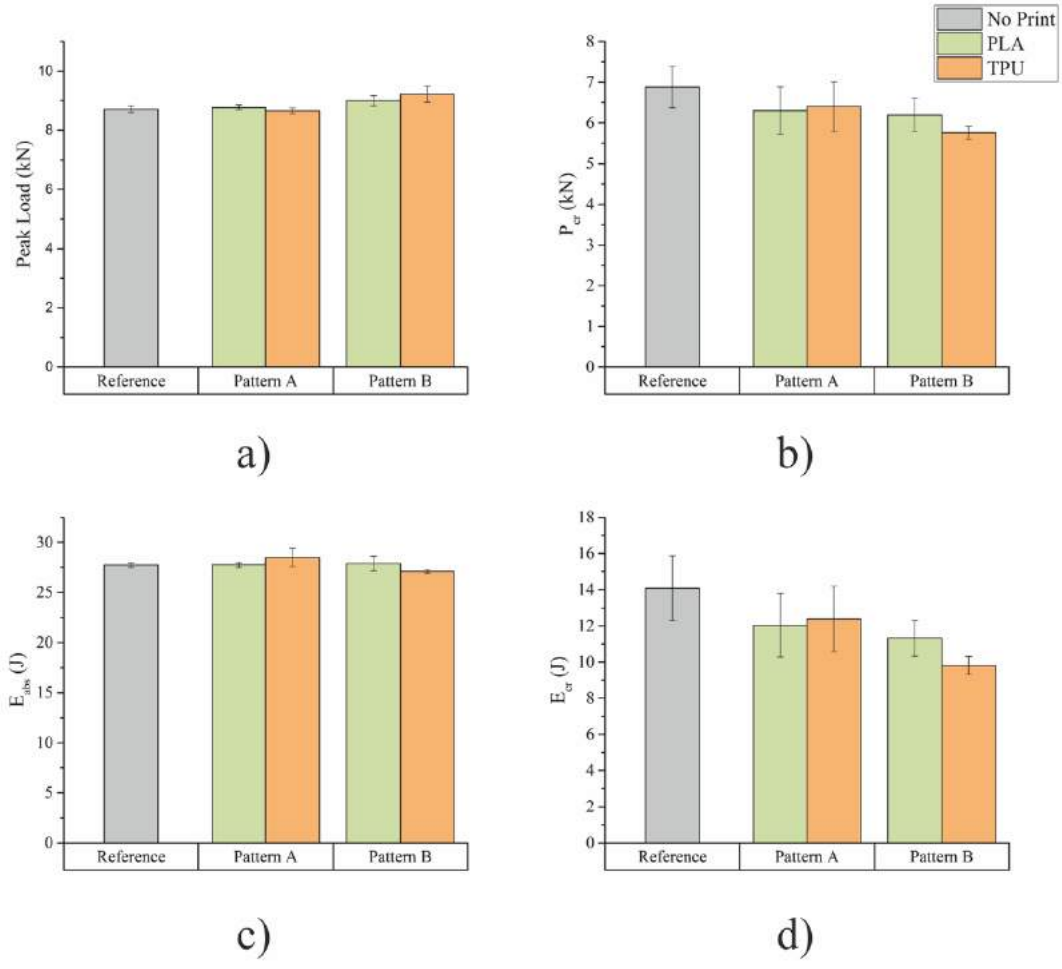

Figure 92: Graphical representation of a) peak load, b) critical load (P_{cr}), c) final absorbed energy (E_{abs}) and d) critical energy (E_{cr}) of each laminate.

The main remarks obtained from LVI experimental tests at the 40 J impact energy level on 3D printing interlocked laminates, when compared to the reference, are:

- 3D printing interlocked structures with pattern B have demonstrate slightly larger load bearing capability (peak load, Figure 92 a)) that all other layups. However, no significant and representative differences were found among laminates;
- All 3D printing interlocked structures showed to have lower load bearing capability before damage initiation (P_{cr}, Figure 92 b)). However, both pattern A interlocked structures demonstrated to have better performance, considering this property, than their peers where pattern B was printed. Moreover, when TPU was used as a printing material, pattern A structures revealed a superior performance than all other printing reinforced layups. Contrarily, regarding pattern B laminates, TPU printed structure has presented the lowest P_{cr} value;
- In terms of E_{abs}, no significant differences were found between reference and 3D printing interlocked laminates (Figure 92 c)). TPU reinforced layups have shown a slightly superior energy absorption, when was used to print pattern A. However, the same material has revealed a worse final energy absorption capability when pattern B was used;
- Similar to critical load (P_{cr}) case (Figure 92 b)), all 3D printing reinforced configurations have shown lower ability to dissipate energy before damage initiation (E_{cr}) (Figure 92 d)). Among 3D printing interlocked laminates and regarding E_{cr}, once again TPU printed layups have revealed the best and the worse performance for pattern A and B, respectively.

7.4.4.1 Visual inspections

A carefully visual inspection was made in all specimens submitted to impact to observe external damages and evaluate their back-face extent.

As expected, for impact at 40 J, all specimens exhibited damage on their back-faces. Figure 93 shows typical images of impact damage developed on reference and 3D printing reinforced structures' back-faces.

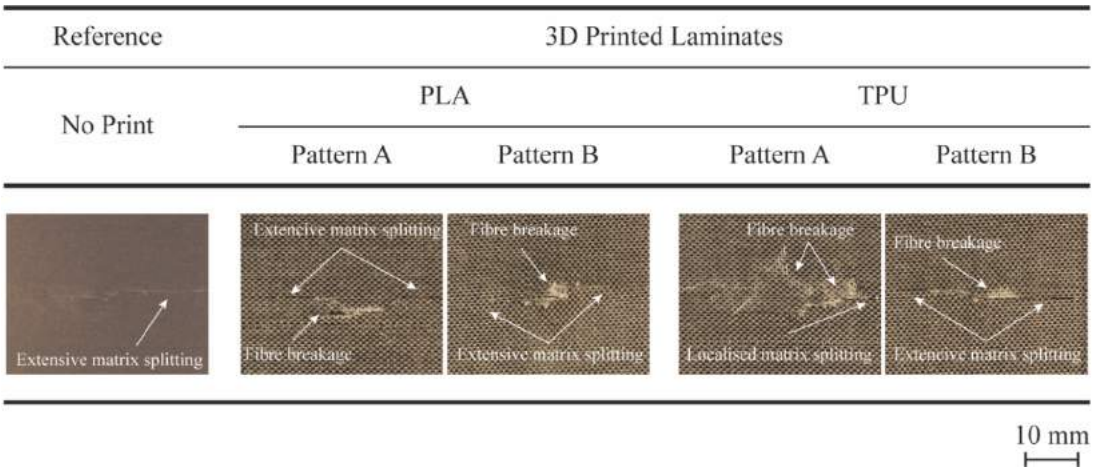

Figure 93: Back-face failure mode of reference and 3D printing reinforced laminates.

From the analysis made on back-face damages, it was possible to observe that most of specimens, reference and 3D printing interlocked laminates, have developed extensive matrix splitting, the exception was TPU pattern A laminate where only a localised matrix splitting were observed (Figure 93). On the other hand, contrary to the reference layup, all new 3D printing interlocked specimens presented fibre breakages on their back-faces.

Back-face damage extent, λ, were measured of all specimens. In Figure 94 are graphically depicted the values of back-face damage extent measured on reference and 3D printing reinforced impact specimens.

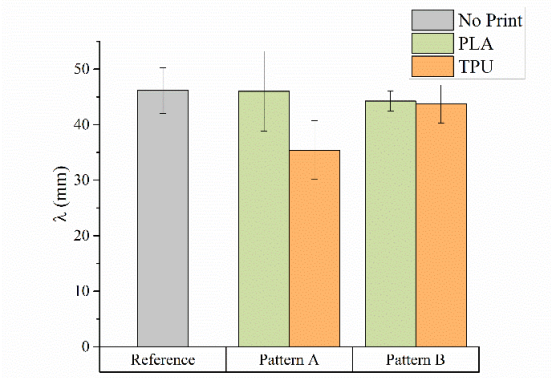

Figure 94: Back-face damage extent (λ) average of each laminate.

As may be seen on the chart, with the exception of PLA pattern A printed specimens, which revealed similar λ than reference laminate specimens, all the other 3D printing layups have developed smaller back-face damages. Moreover, according to the results, the most resistant laminate to extensive back-face damage formation was the TPU pattern A structure, which presented a reduction of 23 % in comparison to the reference layup. Both patterned B layups, printed with PLA and TPU, have shown a similar reduction of λ, presenting decreases of 4 % and 5 %, respectively.

7.4.4.2 Impact internal damage area

After impact at 40 J, all 3D printing specimens were inspected by phased array. Figure 95 presents the longitudinal and transversal cross-section of the typical damage found in each laminate visualised in phased array. As may be seen in those images, the high level of noise does not allow a precise definition of damage boundaries which led to some uncertainty in measurements.

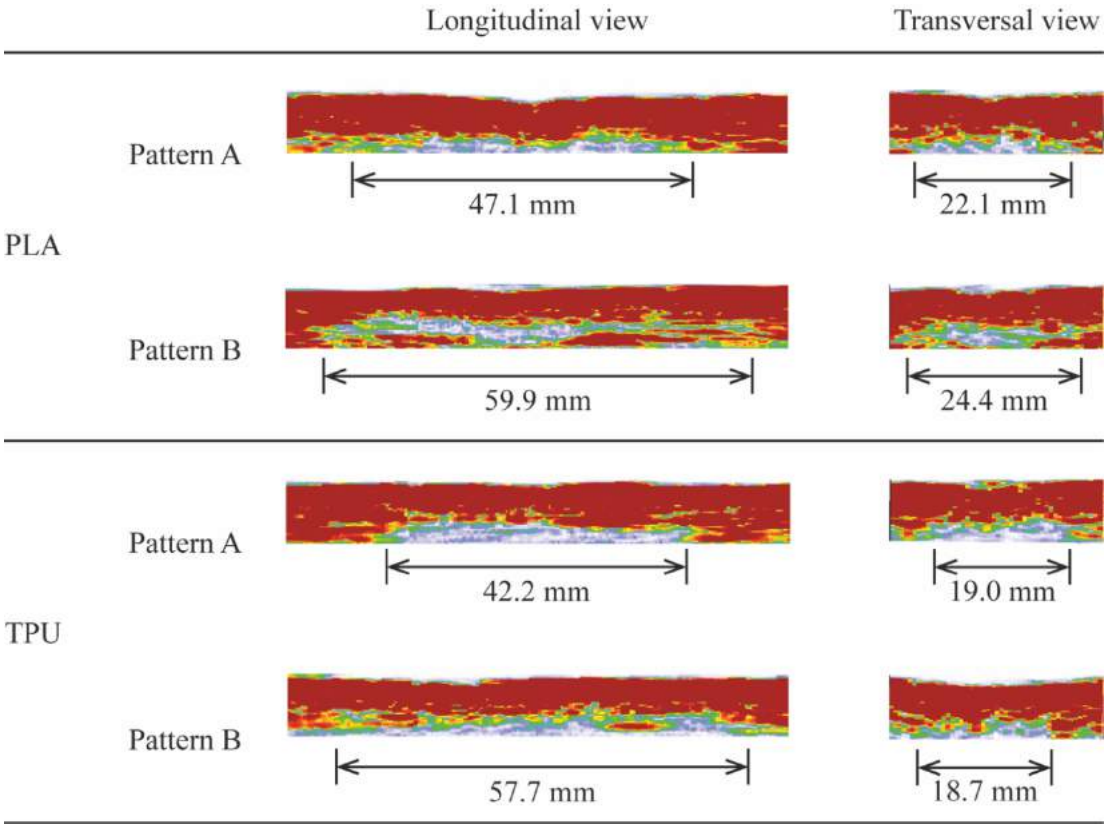

Figure 95: Phased array longitudinal and transversal cross section of a representative damage in each 3D printing reinforced laminate and its respective dimensions.

Table 28 presents the average damage length and width of each 3D printing structure, directly measured by using the UTstudio software, and their respective approximated area calculated by equation 41. The damage area of no printed reference layup was previously measured using C-scan in work presented in Chapter 5, and is presented in Table 28.

As may be seen from the results of Table 28, no significant variations on damage length and width were observed among the new 3D printing reinforced laminates. It is also possible to verify that, when compared to reference configuration and considering its damage area variation, 3D printing reinforced laminates did not present a substantial damage variation.

Table 28: Average damage length and width of 3D printing reinforced laminates, its respective approximated area and average damage area of the reference no printed laminate.

Laminate	Printed pattern	Damage		
		Length (a) mm	Width (b) mm	Area mm²
No print	-	-	-	946.36 ± 117.02†
PLA	A	54.67 ± 5.88	20.05 ± 2.50	880.31‡
	B	55.73 ± 6.76	24.38 ± 2.95	1067.04‡
TPU	A	51.60 ± 6,72	21.49 ± 1.80	871.05‡
	B	56.00 ± 1.63	20.45 ± 2.47	899.29‡

† C-scan measurement
‡ Equivalent damage area calculated using equation 41.

7.5 Discussion

In the previous section, laminates characterisation and mechanical test results were summarised and briefly presented. In this section a detailed discussion of those results will take place in order to understand the influence of 3D prints on laminates morphology and mechanical response.

7.5.1 3D printing over dry carbon fibres

With the purpose of creating an interlaminar interlocking mechanism to mitigate damage propagation in laminates composite materials, two different patterns were 3D printed over dry carbon fibres using two distinctive thermoplastic materials, namely, PLA and TPU.

After printing, the adhesion of those two materials were evaluated by SEM. Two typical micro-photographs of those observations were depicted in Figure 82 (section 7.4.1). Despite, apparently, there was no detachment of the filament from dry carbon fibres, during and after printing process, a massive debonding of PLA filaments was verified under SEM, as Figure 82 a) shows. A close insight over the contact zone between both materials (see Figure 96) revealed the presence of carbon fibre negatives on PLA filament surface that contacted the UDCF tissue, which may have perhaps been formed when the melt polymer first touched carbon fibres. This suggests that the apparent bonding between both parts, verified during printing process and PLA printed UDCF tissues handling, was mainly ensured by a weak mechanical linking and that no effective adhesion was achieved in the printing process. Figure 96 shows, pointed by white arrows, the carbon fibres negatives present on PLA filament surface.

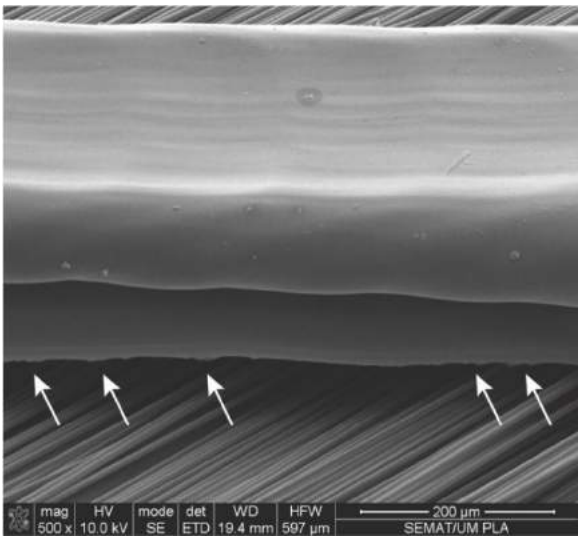

Figure 96: Weak mechanical bonding between PLA printed filament and dry carbon fibres (magnified × 500).

Contrary to PLA printed filaments, an effective adhesion was obtained between TPU and carbon fibres, as images depicted in Figure 82 b) and Figure 97 proves.

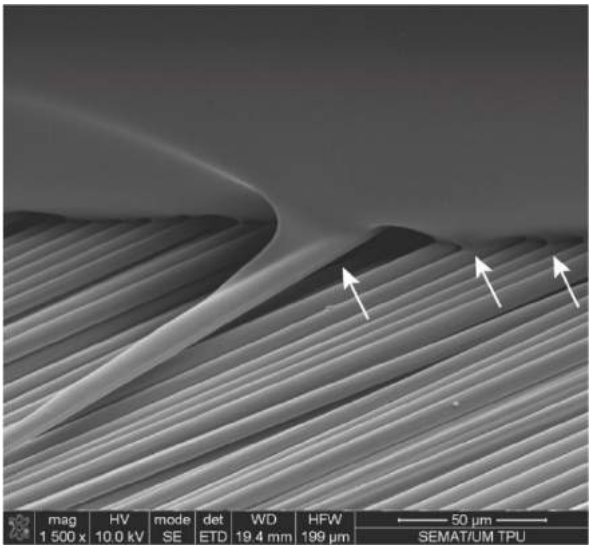

Figure 97: Effective adhesion between TPU printed filaments and carbon fibres (magnified × 500).

A deeply observation of the interface between TPU printed filaments and carbon fibres may be seen in the micro-photography presented in Figure 97. From this image it is possible to see that TPU printed filament partially or completely involves carbon fibres without signs of disruption on their interfaces. This indicates that a strong adhesion between both components was achieved.

Therefore, from those observations we conclude that the TPU was more efficient in ensuring an effective interlaminar interlocking system, since its adhesion to carbon fibres seems to be stronger than PLA.

7.5.2 3D printing reinforced laminates

As expected, the inclusion of 3D printed interlaminar interlocking mechanisms led to an increment on laminates thickness, when compared to reference (no printed). However, depending on the pattern or printing material, some variations were observed.

Figure 98 a)'s graphs present the comparison in terms of thickness between reference and 3D printing reinforced laminates. As may be seen, all printed laminates are thicker than the reference one but, between them, those where pattern B was used, revealed to be thicker than those printed with pattern A. Considering these latter ones (pattern A) no significant difference was observed when PLA or TPU were used as printing material: plus 9 % and 8 % thicker compared to reference, respectively. Contrarily, for pattern B laminates, a larger variation was observed between PLA and TPU printed structures: plus 14 % and 21 % thicker than the same reference laminate, respectively.

The larger thickness of pattern B laminates, comparatively to pattern A, may be explained by the smaller gap between printed filaments on the same interface. During the compression stage of vacuum bag infusion process, this small distance between filaments does not allow carbon fibres to bend and reorganise to fill efficiently the interlaminar region. Moreover, the presence of a higher number of printed filaments increase the probability of several filaments become aligned across laminate's thickness, leading to an increment of thickness. Therefore, the larger the amount of filaments, the smaller gap between them, and the higher probability of they are overlapped across laminates' thickness, which justify the higher thickness of TPU pattern B laminates, since those filaments have shown to be width than PLA ones.

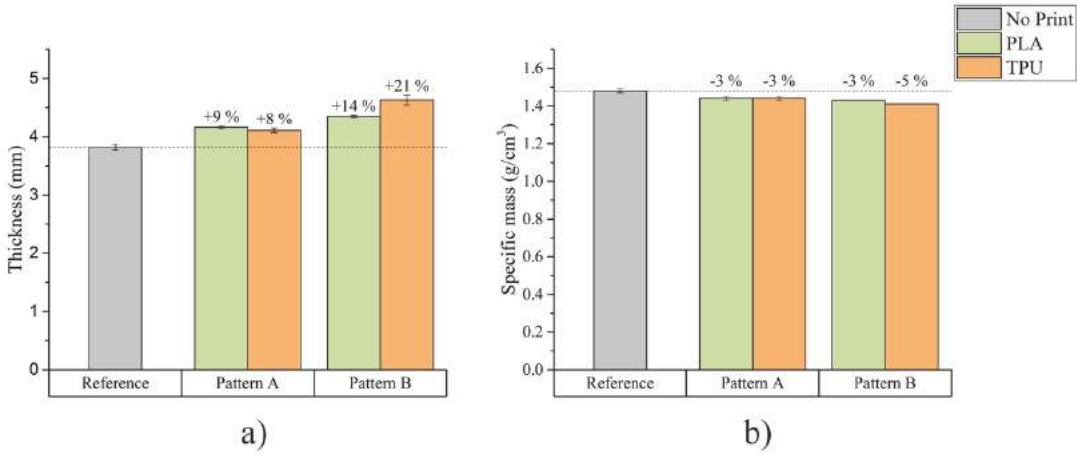

Figure 98: Comparison between reference and 3D printing reinforced laminates in terms of a) thickness and b) specific mass variation.

Despite make laminates thicker, the inclusion of 3D printed patterns has revealed to reduce their density when compared to reference configuration. Figure 98 b) presents the results obtained from the experimental specific mass measurements made in each laminate and compare them to each other.

The graph shows slight reductions in a range of 3 % to 5 % of the 3D printing modified laminates densities when compared to reference (no printed) one. Considering the same reference and printed pattern A laminates, no difference between PLA and TPU printed configurations was verified. In both cases density was reduced in 3 %, while for pattern B, the usage of TPU led to a lower laminate's density (less 5 %) than PLA reinforced configuration, which shows a reduction of 3 %, i.e. equal to that obtained in printed pattern A structures.

The main factor responsible for this reduction on density of 3D printing interlocked laminates is especially attributed to the usage of thermoplastic polymers to print the interlaminar interlocking systems and the consequent increment of resin volume fraction in these structures. Both PLA and TPU have much lower density than UDCF fabrics.

Figure 99 plots the matrix and carbon fibre fabric volume fractions in all laminates under study. As may be seen from the graph, the usage of 3D printed patterns led to an increment of, at least, 3 % of matrix volume fraction, comparatively to the reference no printed layup. It may be also observed that patterned B laminates also presented higher matrix volume fraction than patterned A ones. This is caused by the effect previously analysed from micro-photographs of laminates stratigraphy (Figure 83, section 7.4.2), where it was observed that extensive resin pockets were formed around pattern B printed filaments. Such phenomenon results from the small distance between filaments present in the same interface when parttern B is used, which unable carbon fibres to bend and properly fill the interlaminar region.

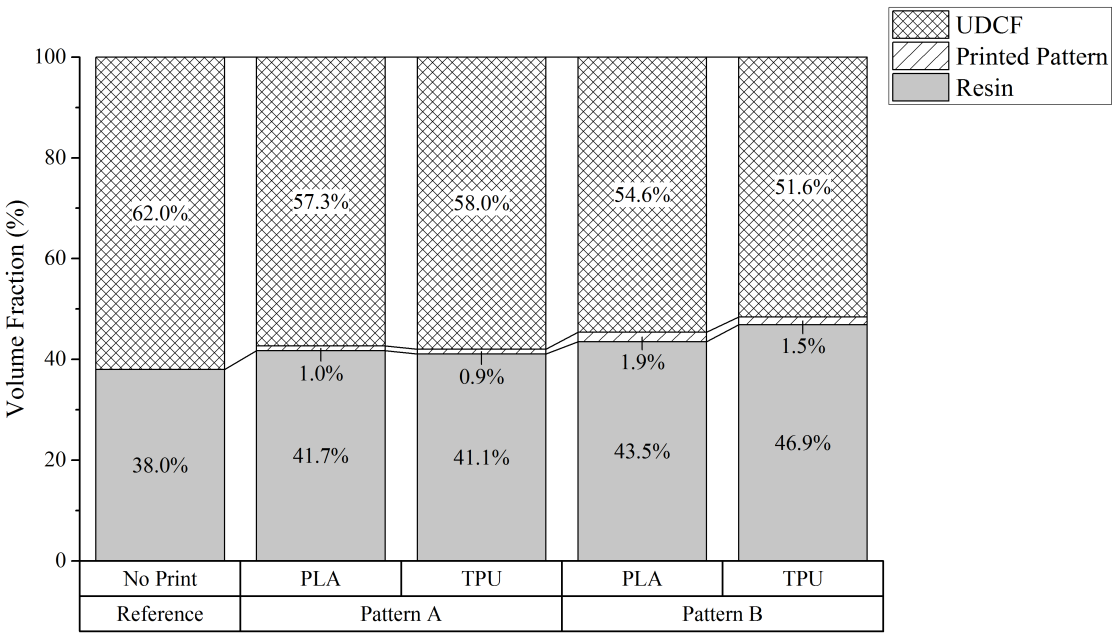

Figure 99: Matrix and UDCF volume fractions in the reference and printed patterns laminates

To summarise, it was observed that printed patterns play an important role on laminates thickness and density. It was concluded that, the smaller the gap between printed filament, the higher the probability of overlapping of them across laminates' thickness, which increases the overall thickness and, on the other hand, these much closer spacings lead to the formation of lager resin pockets, which result in the lower density of the laminates.

7.5.3 Quasi-static mechanical tests discussion

In previous section, it was concluded that printed patterns play an important role on laminates' resin volume fraction. Therefore, it seems relevant to have in mind this property in the discussion about the laminates quasi-static mechanical behaviour.

7.5.3.1 3-PB laminates performances

As it had been seen in Figure 87 a) (section 7.4.3.1), the laminates interlocked by PLA printed filaments have shown to withstand almost the same maximum bending stress as the reference layup. However, when TPU was used to print interlocking patterns, their mechanical behaviour drops up to 13 % (TPU pattern B). Thus, it is clear that printing material really affects the bending strength of laminates, while a small difference was observed from pattern A to pattern B. As it was concluded in the previous section (7.5.2), the usage of pattern A or B may lead to a difference in matrix volume fraction up to almost 6 %

(TPU pattern A to B), therefore, should be relevant analyse the influence of the matrix content in the bending strength of laminates using both printed patterns.

Experimental results of maximum outer surface stresses ($\sigma_{out.suf.}$) against resin volume fraction are presented in Figure 100 a). Once again, this figure revealed the strong dependence of laminate bending behaviour on the material used to print interlocking patterns.

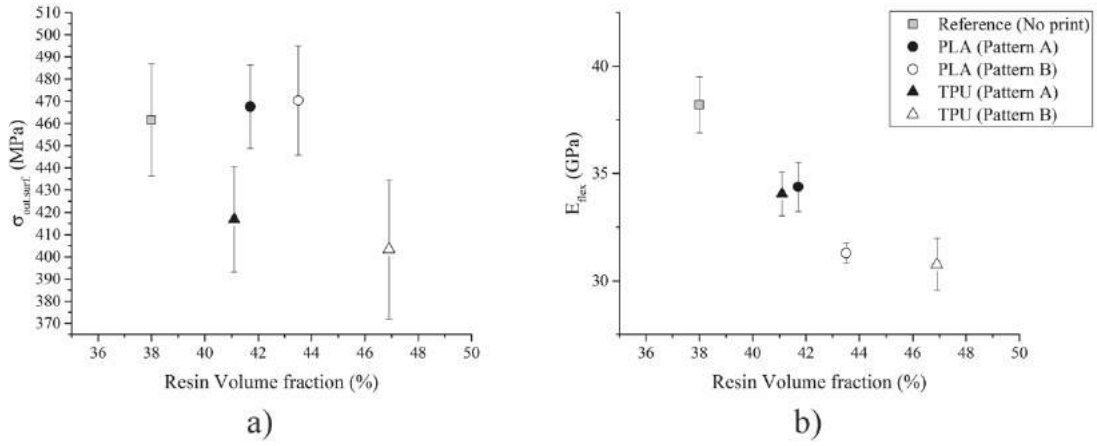

Figure 100: 3-PB results of a) maximum stress ($\sigma_{out.suf.}$) and b) flexural modulus ($E_{flex.}$) vs resin volume fraction of each configuration.

Independently of pattern, laminates printed with PLA have shown higher bending strength than the other layups and, especially, than those that used TPU. Moreover, resin volume fraction seems to play an antagonic effect on laminates bending strength, that also depending on the printing material. The bending strength ($\sigma_{out.suf.}$) of layups printed with PLA seem to slightly increase with the resin volume fraction increasing, whereas in structures using TPU printings, bending strength decreases when resin content increases. Complementary, both PLA and TPU printed laminates presented higher resin volume fraction when printing pattern B was used. Therefore, this suggests that laminates' responses do not depend on the resin volume fraction, but instead on the amount and printing material. While PLA seems to act as a reinforcement, TPU, perhapls due to its elastomeric nature, leads to a whose laminate's flexurial performance. This phenomenon seems to be intensified when the amount of each printing material is increased.

This conclusion is supported by failure modes photographs in Figure 88, where is clearly visible TPU filaments deformation on the compression side of the specimen (top side of photographs) surrounded by extensive catastrophic failure of UDCF layers. On the other hand, PLA reinforced laminates have shown more constrained failures without apparent PLA filaments deformation.

Figure 100 b) depicts the relationship between laminates' flexural modulus ($E_{flex.}$) and resin volume fraction. As expected, 3D printing reinforced laminates have shown lower flexural modulus than the

reference laminate, since the inclusion of those interlaminar interlocking systems led to an increment on resin volume fraction. Moreover, a strong dependency between both properties was observed, the higher the resin content on laminates, the lower the flexural modulus of those configurations. Should be also noticed that, for the same pattern, PLA reinforced laminates have presented higher flexural moduli than the TPU ones, which indicates that the printed material defomability has a significant contribution also in this composite bending property.

7.5.3.2 ILSS performance of laminates

As had been shown in Figure 89 (section 7.4.3.2), all new 3D printing reinforced laminates have shown higher global interlaminar shear stress resistance comparatively to the reference, when submitted to short-beam shear tests. From the results is possible to observe that PLA reinforced configurations have performed better than TPU ones, this phenomenon was especially verified when pattern B was printed on selected interfaces. As it was concluded in the previous section 7.5.3.1, in 3-PB tests discussion, the lower deformability of PLA seem to has some influence on ILSS results, on the other hand, the amount of printed filament seems to play an opposite role on this results. The increment on the amount of PLA has led to a better ILSS performance of the composite (PLA pattern B), however, when the same occurred for TPU, a worse global interlaminar shear resistance was verified (TPU pattern B).

As it was observed, the usage of pattern B to create an interlaminar interlocking mechanism, has led to an increment on laminates resin volume fraction. As it has been mentioned before in Chapter 5 and Chapter 6, several studies have reported a correlation between this laminate's characteristic and its interlaminar shear resistance [164][165][170].

Figure 101 presents the correlation between the interlaminar shear strength of the reference and 3D printing interlocked laminates and their resin volume fraction.

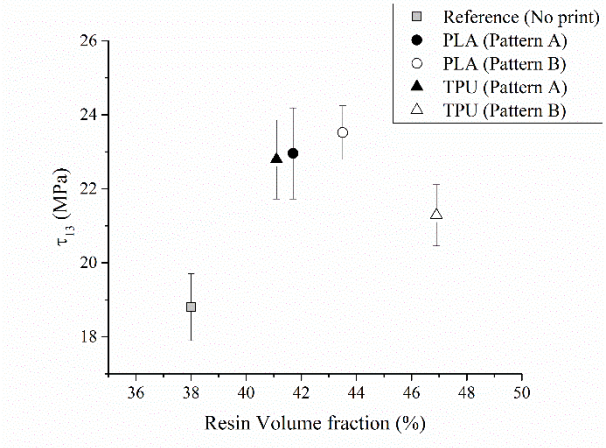

Figure 101: Correlation between laminates' interlaminar shear stress (τ_{13}) and resin volume fraction.

As may be seen, laminates' interlaminar shear strength (τ_{13}) increased as their resin volume fraction increase up to roughly 44 %, after this point a reduction of this mechanical property was observed. Should be also noticed that, among 3D printing interlocked layups, and as it was observed before, independently on their resin content, PLA reinforced configurations always have performed better than TPU ones. In fact, the worse performance was verified in laminates with printed TPU pattern B, while only a small difference was verified between laminates with PLA and TPU printed pattern A. On the other hand, observing ILSS failure mode of those new 3D printing reinforced laminates, no damages were found on reinforced interfaces of these configurations (see Figure 90, section 7.4.3.2). This suggests that, besides the formation of extensive resin pockets close to pattern B printed filaments, the elastomeric nature of TPU and its higher amount on this pattern, does not allow an effective carbon fibres compaction during vacuum bag infusion process, reducing interlaminar shear resistance of this configuration (TPU pattern B), as referred in literature [165]. Nevertheless, the small amount of TPU filaments on pattern A seems to do not affect severely this laminate characteristic, yielding a similar ILSS performance of PLA pattern A layup.

7.5.4 Laminates' thickness role on Low Velocity Impact (LVI) mechanical response

Laminates' thickness is a key factor on low velocity impact mechanical response [171]. Considering the increment on thickness resulting from the inclusion of 3D printed patterns on laminates when compared to the reference, the row results presented in section 7.4.4, Table 27 and Figure 92, may lead to a misinterpretation of their mechanical response. Therefore, and to reduce the thickness effect on data analysis, all LVI laminates' results were normalised to their own thickness. Figure 102 presents the results obtained from the LVI tests normalised to laminates' thicknesses.

As may be seen in Figure 102 a) to d), after normalised, reference configuration always has shown higher peak load, final absorbed energy and critical load and energy than 3D printing reinforced laminates, respectively.

Considering only 3D printing reinforced configurations, it is possible to observe that peak load and final absorbed energy (E_{abs}) (Figure 102 a) and c), respectively), seem to be insensitive to pattern or materials printed in laminates' interfaces. On the other hand, the critical load (P_{cr}) and energy (E_{cr}) (Figure 102 b) and d), respectively), revealed to be more susceptible to laminates' morphology. Independently on the printed material, pattern A laminates have always shown higher resistance to damage onset, in terms of load and energy, than patterned B configurations. However, and in spite of no significant differences had

been found in terms of P_{cr} and E_{cr} between PLA and TPU pattern A structures, the pattern B laminate printed with PLA has shown to slightly delaying those damage indicators to higher loads and energies, comparatively to its peer printed with TPU.

To summarise, it may conclude that the usage of 3D printing to interlocking carbon/epoxy composites have shown to have a negative impact in their LVI mechanical response. On the other hand, and only considering 3D printing reinforced laminates proposed in this work, no substantial changes were observed in terms LVI mechanical response among the different structures. Should be, however, noticed that the higher amount of TPU, in pattern B, has led to an early appearance of damage indicators, namely, critical load (P_{cr}) and energy (E_{cr}).

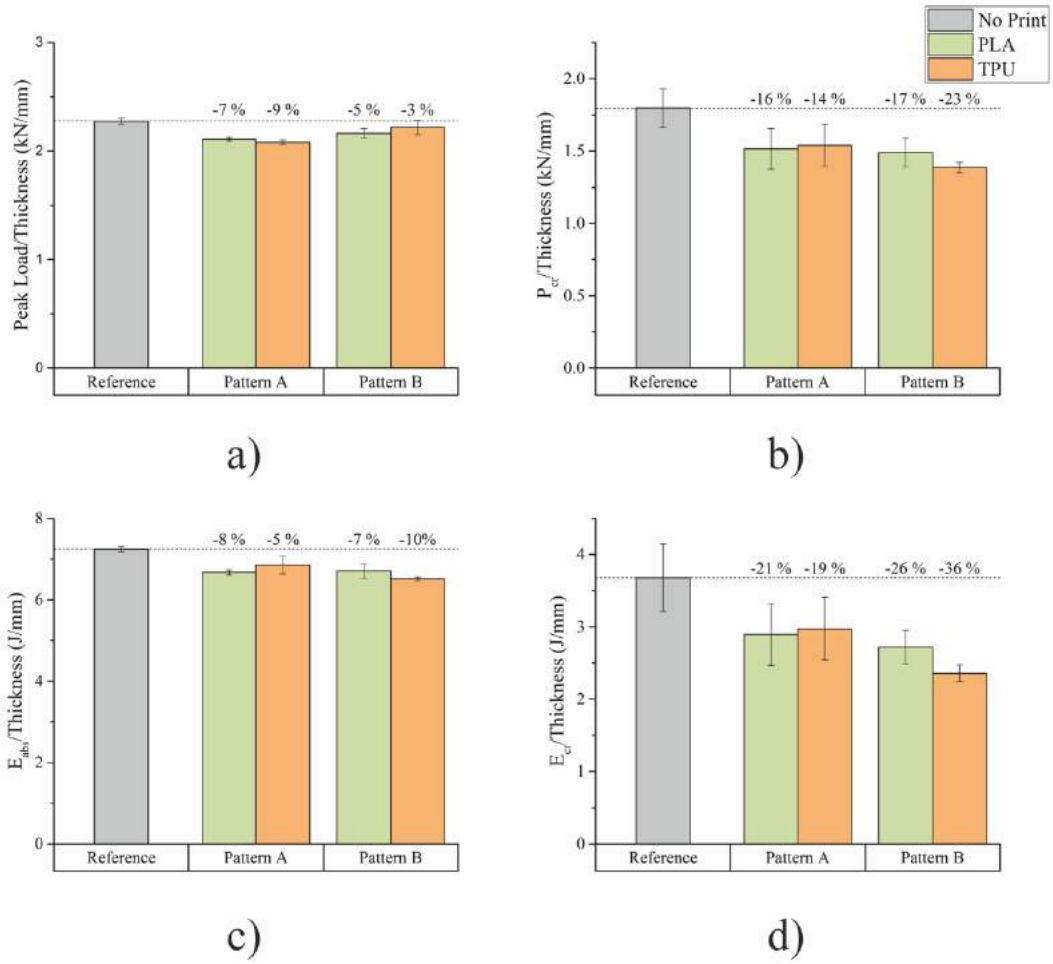

Figure 102: Graphical representation of a) peak load, b) critical load (P_{cr}), c) final absorbed energy (E_{abs}) and d) critical energy (E_{cr}) of each laminate normalised to its thickness.

7.5.5 Printed pattern role on low velocity impact (LVI) mechanical response

As it was observed in Figure 91 (section 7.4.4), for each 3D printing structure, all specimens have shown a similar mechanical response to LVI tests on contact load vs displacement graphs. However, a slightly

difference may be seen between pattern A to B laminates response immediately after critical load (P_{cr}). For a better analysis and to avoid the misunderstanding due to curves overlapping, Figure 103 presents contact load vs displacement graphs obtained for each specimen grouped by 3D printing structure. Black arrows on curves identify the critical load (P_{cr}) observed in each specimen.

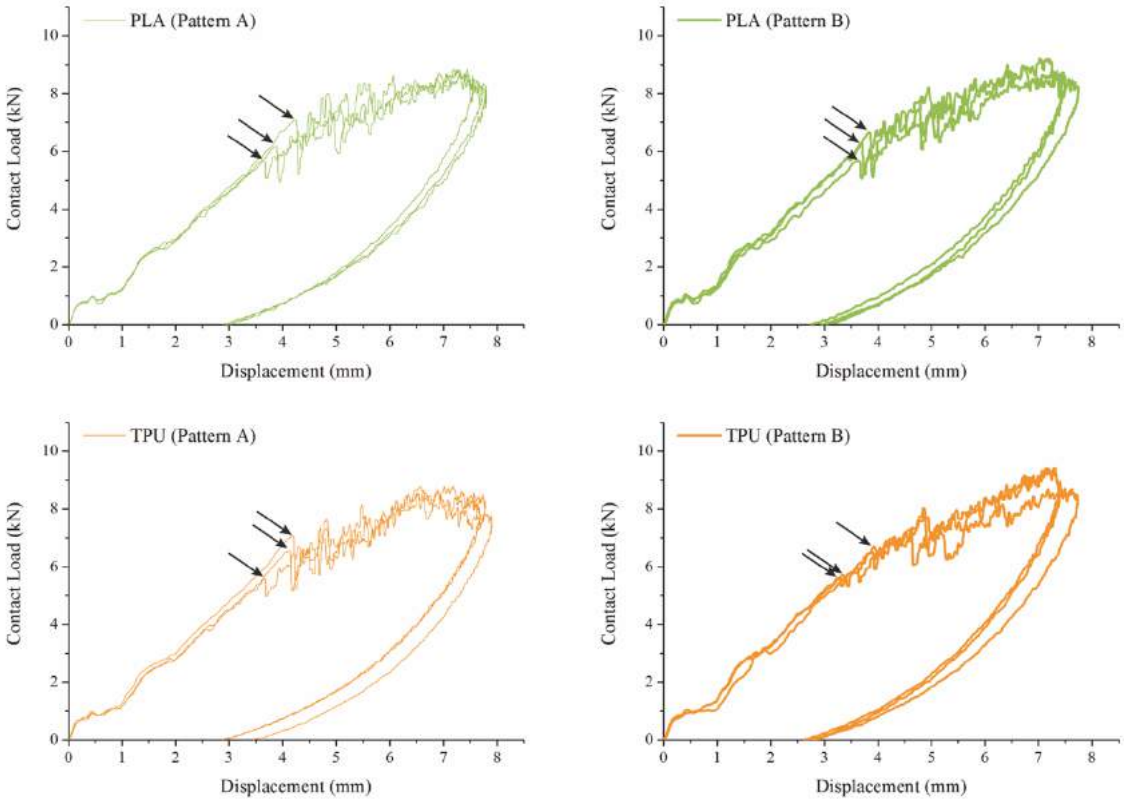

Figure 103: Contact load vs displacement curves of 3D printing interlocked laminates.

From pattern A curves (both graphs on left side) it is possible to see that, independently on printed material, PLA (top) or TPU (bottom), immediately after P_{cr}, all specimens have shown a severe load dropping, and consequent abrupt loss of their stiffness. On the contrary, in patterned B structures (both graphs on right side), after this critical point only have presented small load oscillations, roughly keeping their initial stiffness for a little longer.

This distinctive performance between both patterns seems to indicate that pattern A structures are more prone to develop early severe damages, as delaminations or fibre breakage, while pattern B laminates tend to first form subcritical damages, as matrix cracking, and only then more catastrophic damages, since their stiffness have shown to be kept longer after critical load.

Therefore, the larger amount of resin pockets formed around printed filaments observed into pattern B configurations (see Figure 83, section 7.4.2) seems to prioritise subcritical damage mechanisms, contrary to pattern A layups where the sudden load drop after the initial elastic response denounce the first formation of more severe damages.

7.5.6 Low velocity impact damage evaluation

The most direct method to evaluate and compare impact damage on composites is the measurement of back-face damage extent through visual inspection. Figure 104 compares the reference to the new 3D printing interlock laminates about their back-face damage extent (λ).

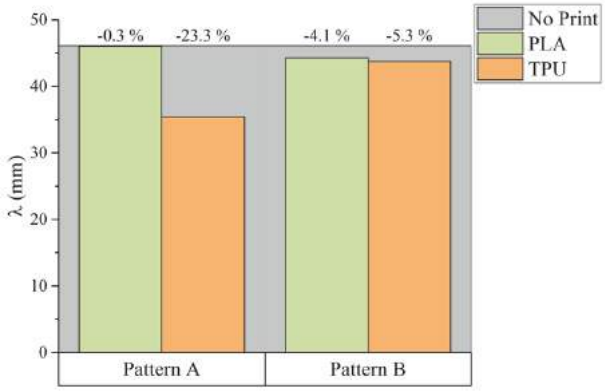

Figure 104: Comparison of 3D printing reinforced laminates back-face damage extent (λ).

As may be seen from Figure 104's graph, most of new laminates have developed less extensive back-face damages when compared to reference, the exception was PLA pattern A configuration that has shown almost similar damage in terms of extent. The results also reveal that independently on the printed material, pattern B configurations have developed identical damages. On the other hand, TPU pattern A laminate was the one whose has shown less propensity to form extensive back-face damages, reducing up to 23 % the damage extent in comparison to its peer printed with PLA and the no printed reference laminate.

Summarising, the larger amount of resin into the reinforced interfaces seems to uniformises the back-face bending behaviour of pattern B configuration leading to a similar damage extent, on the other hand, in pattern A configuration the influence of printing material looks to be higher, since the ductility of TPU appears to constrain back-face damage.

In order to compare internal damage area of 3D printing reinforced configurations to reference it was made an approximation using phased array damage length and width. Figure 105 presents a graphical comparison between reference and printed laminates internal damaged area after impact.

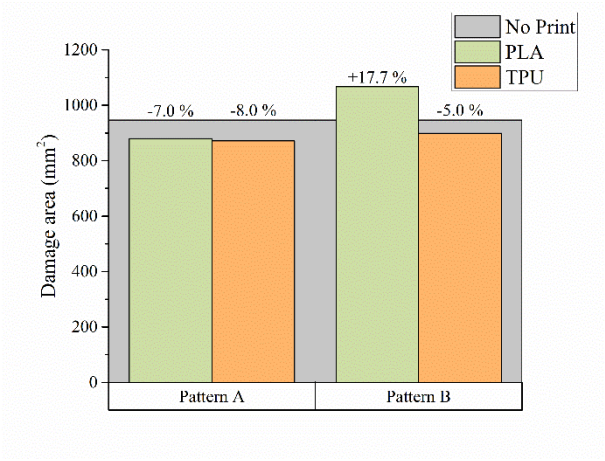

Figure 105: Comparison of 3D printing reinforced laminates damage area.

From the graph may be observed that only PLA pattern B structures seemed to have developed larger damages when compared to reference, while all the other laminates apparently were able to reduce impact damage in an identical way, from 5 % to 8 %. Nevertheless, among those new 3D printing reinforced configurations it is possible to observe that laminates printed with pattern A have shown a slightly reduction of damage area than TPU pattern B configuration. On the other hand, PLA printed laminates seem to develop larger damages than TPU for both patterns.

To summarise, for pattern A laminates, the influence of printed material on impact damage area seems to be almost insignificant, since no substantial differences were observed between PLA and TPU configurations. On the other side, in pattern B laminates the higher amount of resin on the printed interlaminar regions and the poor adhesion of PLA to carbon fibres seem to lead to extensive delaminations on this configuration, contrary to TPU reinforced one which has shown identical internal damage area than both pattern A laminates. Therefore, the elastomeric nature of TPU and its better adhesion to carbon fibres seem to confer higher damage tolerance to TPU pattern B configuration. Nevertheless, should be noticed that phased array damage evaluation may contain some measurement mistakes due to the high level of noise that may arise from the different materials phases inside laminates.

7.6 Conclusions

In this work a four novel 3D printing reinforced laminates were developed, produced and compared to a conventional carbon/epoxy aircraft reference. All laminates had the same carbon fibres stacking sequence and were manufactured by vacuum bag infusion. According to the results obtained from a FE model previously developed (Chapter 6), six interfaces were selected to be reinforced. Before impregnated, two patterns (A and B) were directly printed over dry carbon fibres on those interfaces using two different thermoplastic filaments, namely, a polylactic acid thermoplastic (PLA) and a polyether-

polyurethane elastomer (TPU), in order to create an interlocking interlaminar mechanism. After printing, the adhesion between printed filaments and carbon fibres was investigated under scanning electron microscope (SEM). Regarding laminates characterisation, their thickness, compounds volume fraction and morphology were assessed and visualised. Finally, laminates' mechanical performance was evaluated and compared under three-point bending (3-PB), interlaminar shear strength (ILSS) and 40 J low velocity impact (LVI) tests.

From SEM visualisation it was observed a poor adhesion between PLA printed filament to dry carbon fibres, when compared to TPU which has shown a strong bonding.

The introduction of interlaminar interlocking mechanisms into carbon/epoxy laminated composites lead to an increment on their thickness and resin volume fraction, which was particularly visible from laminates printed with pattern B where a thickness has increased at least 14 % and resin content about 5.5 %. This arises from the small distance between printed filaments of this pattern which does not allow carbon fibres to bend and properly fill the gap between them, leading to the formation of large resin pockets on them and increasing laminates' thickness.

Under 3-PB conditions, the higher content of resin on 3D printed interlocked laminates have led to a reduction of their flexural moduli when compared to the no printed reference. However, PLA interlocked laminates have shown higher load bearing capability than all other configuration. This may result from the elastomeric nature of TPU when compared to PLA.

Considering interlaminar shear strength of laminates, it was observed that laminates resin volume fraction plays an important role over this mechanical characteristic. Independently on the configuration, a correlation was verified between both factors. Laminates' ILSS strength seems to be increased with resin volume fractions up to approximately 44 %, however, after this point, a reduction of this mechanical property was observed.

Under 40 J of energy impact, after normalised to their thicknesses, all 3D printing reinforced laminates have shown lower mechanical behaviour when compared to no printed reference. However, all of them have shown similar or higher resistance to the development of external damages than the reference laminate. In fact, TPU pattern A structures has shown to be able to reduce back-face damage up to 23 % when compared to no printed laminate. In terms of internal damage, with the exception of PLA pattern B layup, all new 3D printing printed structures have developed smaller damages than reference. Nevertheless, another damage evaluation method must be applied to achieve more accurate results, since phased array data obtained in this work has shown to be quite difficult to be analysed due to the high level of noise, which perhaps result from the different material phases inside laminates.

Chapter 8
General Considerations About Damage Resistance Among Different Approaches

In last three chapters, it was presented and deeply discussed the three different approaches, according observations and results obtained from the laminates' morphologic analysis, mechanical response, damage resistance and, in some cases, tolerance. The present chapter aims to make an objective summary over the performance of those three approaches and their laminates regarding damage resistance. Therefore, all proposed structures will be compared to each other considering six damage resistance properties, namely, four characteristic low velocity impact mechanical responses (peak load, final absorbed energy (E_{abs}), critical load (P_{cr}) and energy (E_{cr})) and two typical damage measurements (back-face damage extent (λ) and internal damaged area) when submitted to 40 J of impact energy.

In order to perform a fair evaluation, peak load, E_{abs}, P_{cr} and E_{cr} will by normalised to their respective thickness in order to minimise its effect, while absolute measurements of back-face damage extent and internal damage area will be considered to compare different layups.

Finally, in order to facilitate the analysis regarding each characteristic, all graphs in this chapter are divided in three main section, green sector represents the Bouligand-like approach (Chapter 5), on the yellow sector the strategical interleaved veils (Chapter 6) and finally in orange 3D printing reinforced laminates (Chapter 7).

Figure 106 depicts a graph that presents peak load results of all laminates proposed in this thesis normalised to their respective thickness. As may be seen HL configuration from bioinspired Bouligand-like approach was the one whose presented larger load bearing capability under 40 J of impact energy.

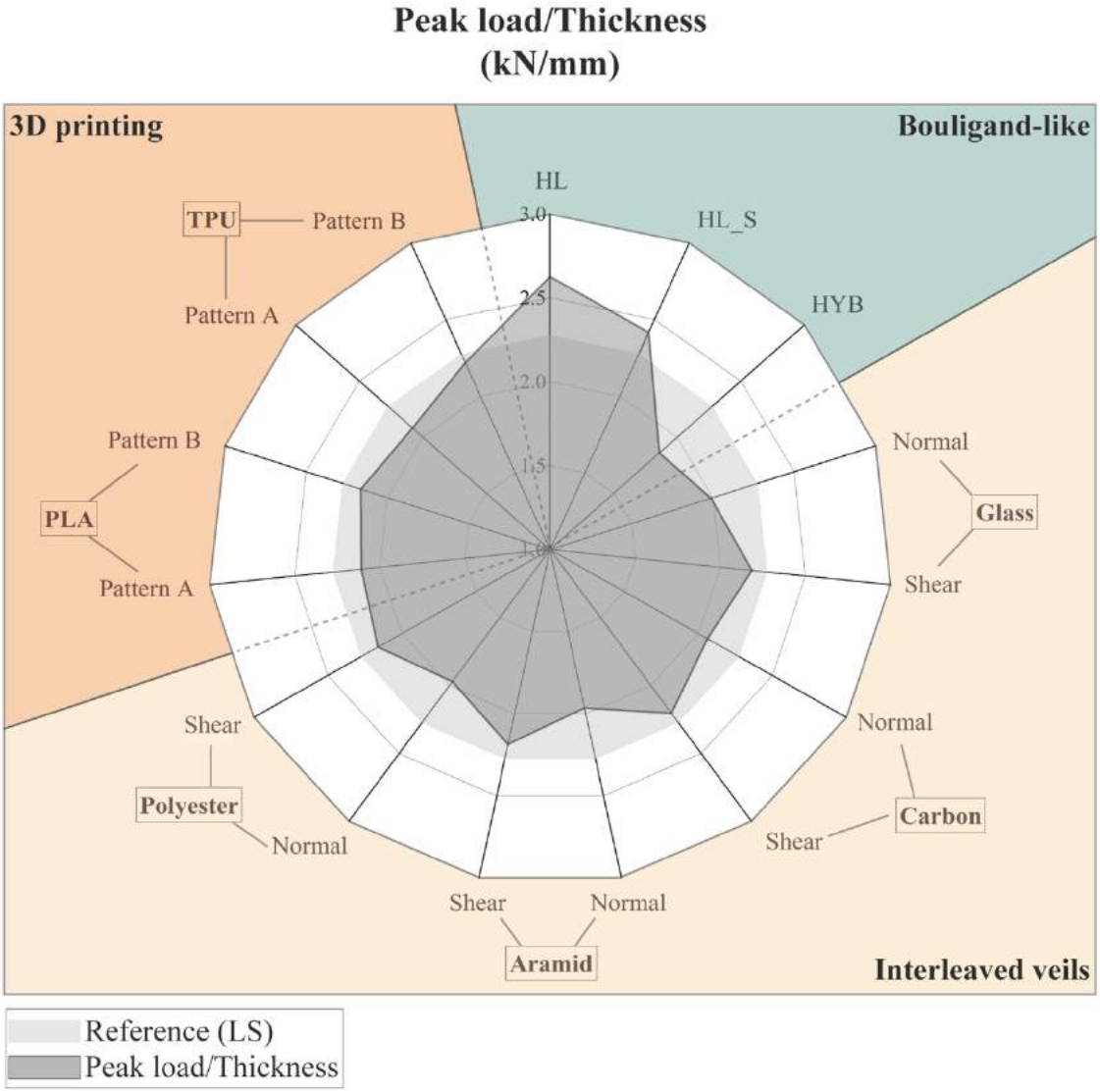

Figure 106: General comparison of normalised peak load of all laminates tested at 40 J impact energy.

Similarly, Figure 107's graph shows the final energy absorbed (E_{abs}) of each configuration normalised to their corresponding thickness. Once again, Bouligand-like HL laminate has demonstrated to be able to absorb more energy than all the other configuration proposed in this work.

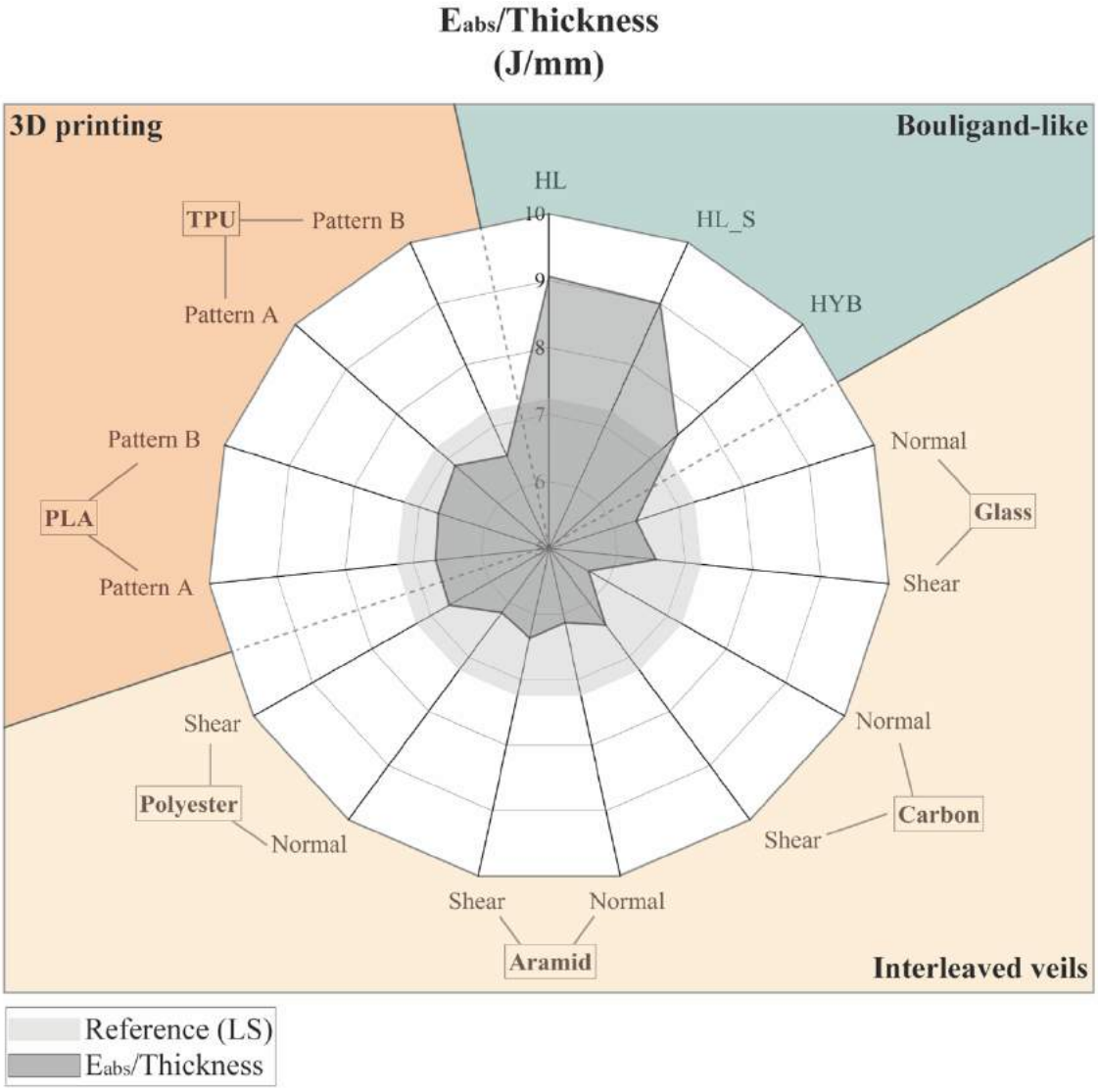

Figure 107: General comparison of normalised final absorbed energy (E_{abs}) of all laminates tested at 40 J impact energy.

Considering the critical load (P_{cr}), again, HL configuration, from bioinspired Bouligand-like approach, has revealed be capable to delay damage onset for higher loads when compared to all other layups. Figure 108 presents the comparison between Pcr observed in each laminate normalise to its thickness.

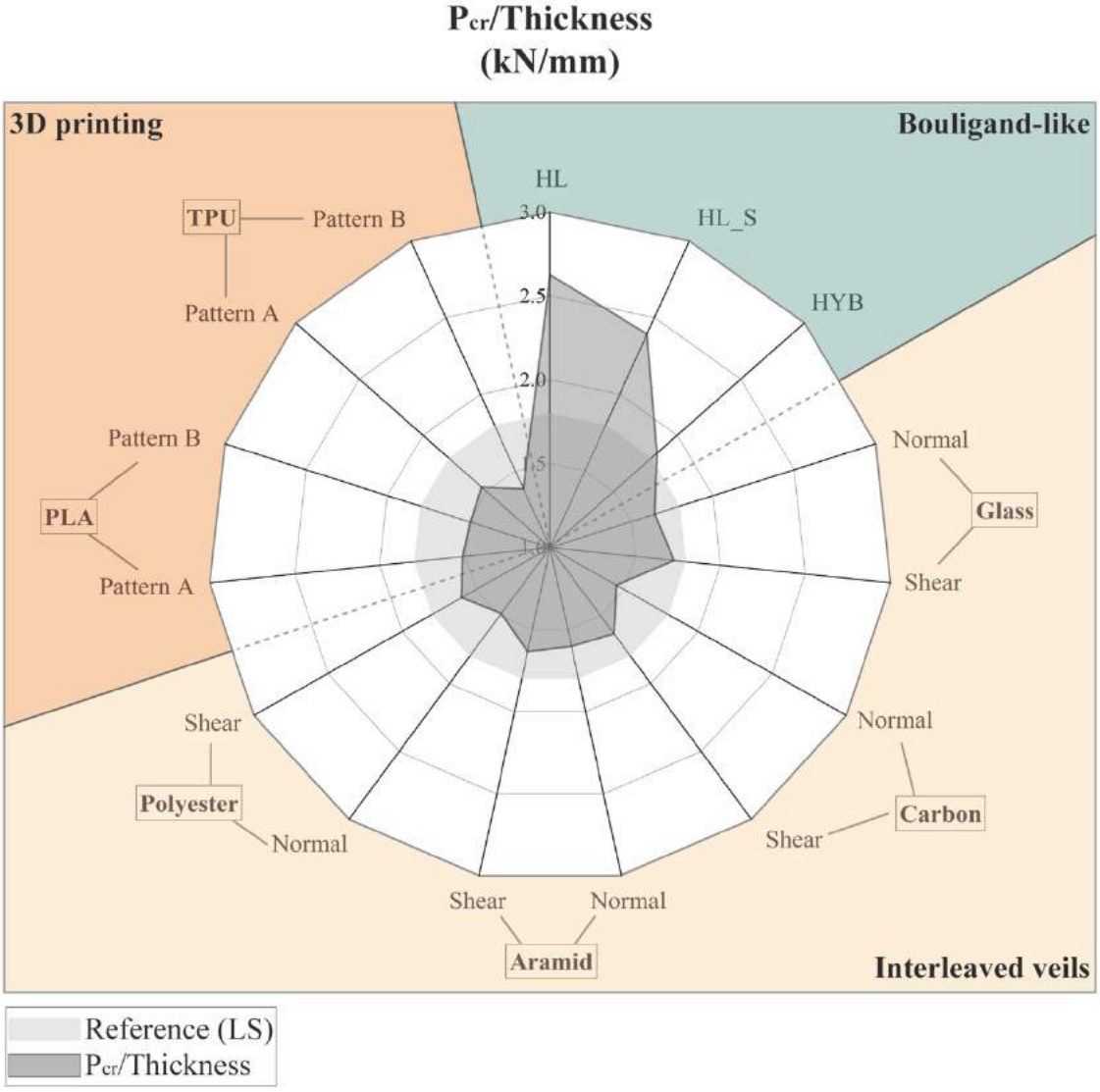

Figure 108: General comparison of normalised critical load (P_{cr}) of all laminates tested at 40 J impact energy.

Since critical energy (E_{cr}) is related to the previous critical load (P_{cr}), it is not surprising that the configuration which requires more energy to onset severe damage also will be HL laminate. Figure 109 presents graphically the comparison of this damage indicator obtain in all configurations, again, normalised to their thicknesses.

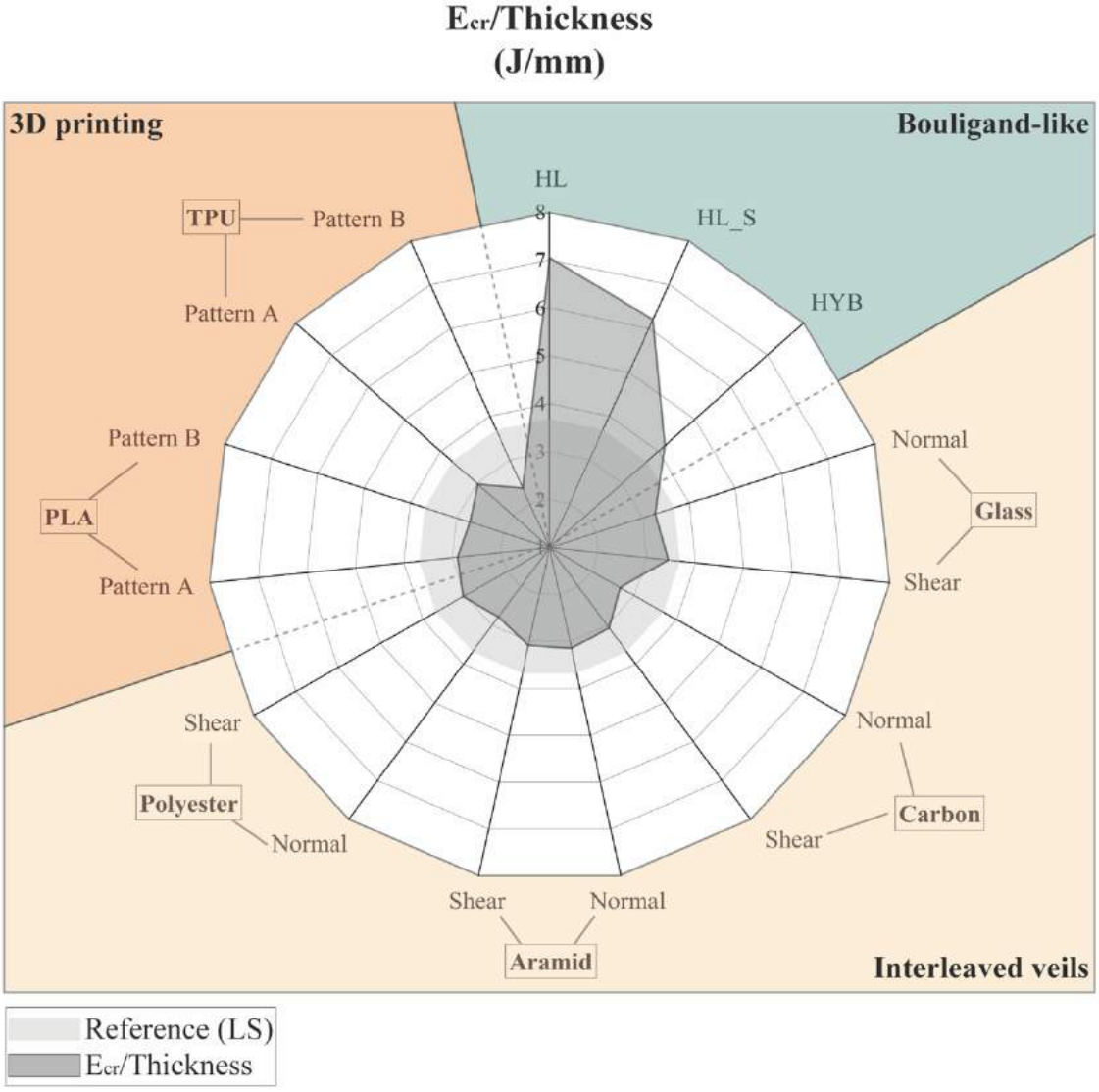

Figure 109: General comparison of normalised critical energy (E_{cr}) of all laminates tested at 40 J impact energy.

Back-face damage extent of each laminate, first visible indicator of damage severity, is graphically compared in Figure 110. According to the measurements performed, HL_S layup, once again, from bioinspired Bouligand-like approach was the one whose has revealed less extensive back-face damages.

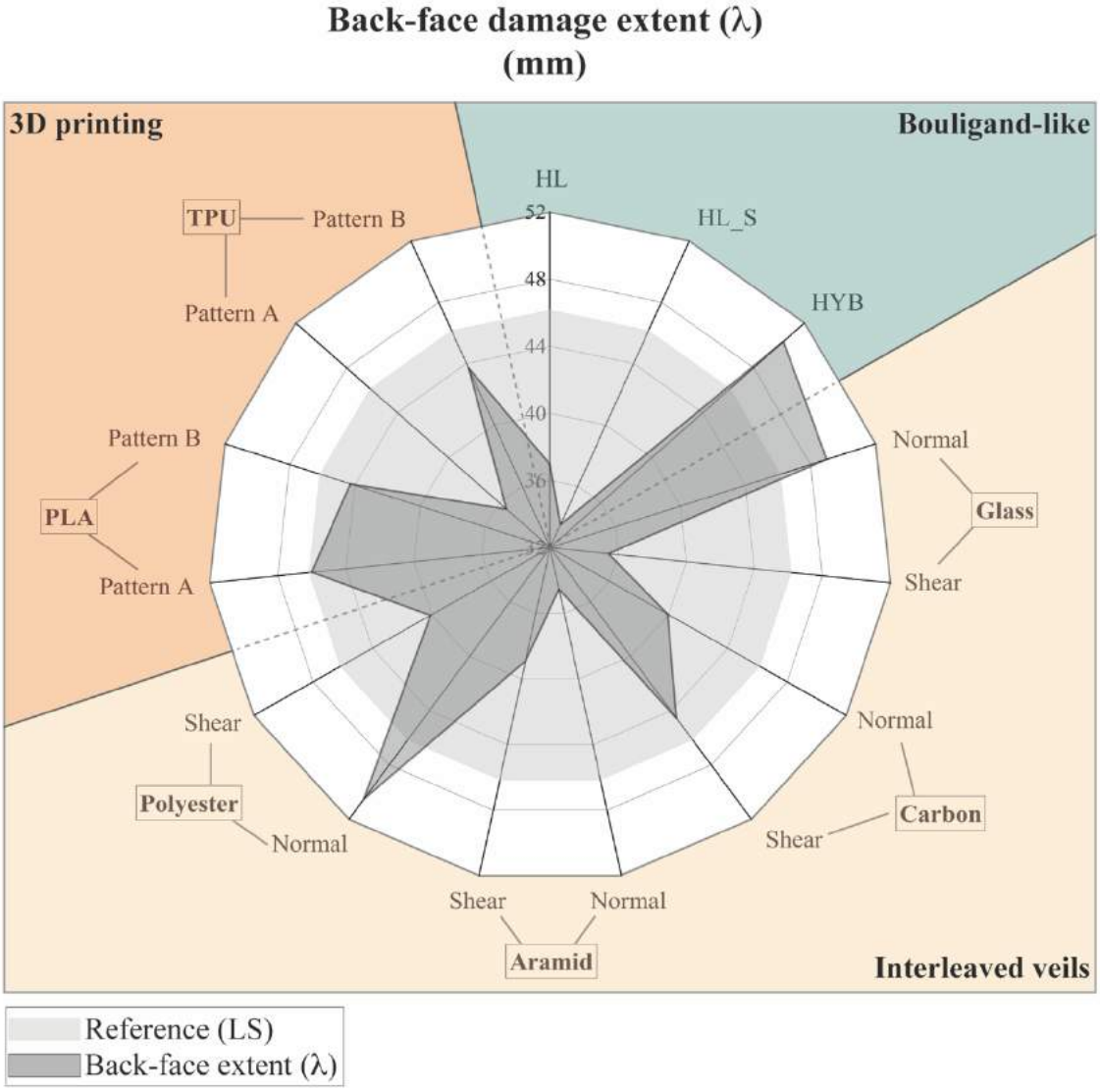

Figure 110: General comparison of back-face damage extent (λ) of all laminates tested at 40 J impact energy.

Finally, Figure 111 shows the comparison of internal damage area of each laminate. This time, interleaving shear stresses strategy has revealed to be more effective to avoid extensive impact damages, since the better configuration considering this property was laminates interleaved with aramid veils in most critical shear stresses interfaces.

Should be notice that, as explained above, 3D printing reinforced laminates damage area is an approximation, identified with a * sign after laminates' labels.

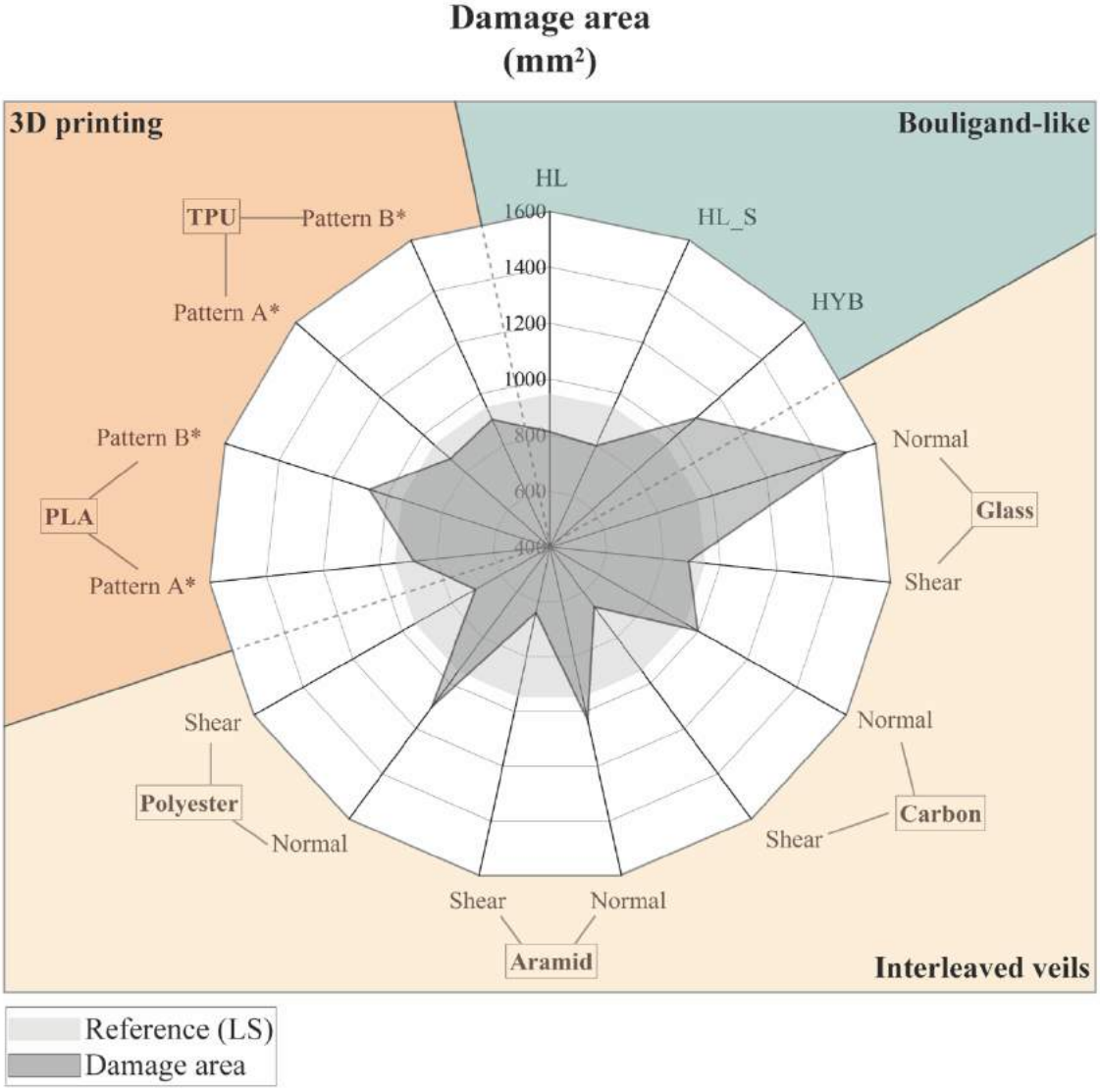

Figure 111: General comparison of internal damage area of all laminates tested at 40 J of impact energy.

Chapter 9
Final Considerations

This chapter aims to present the main conclusions of all work carried out along this thesis considering the objectives initially stablished toward the mitigation of low velocity impact damage in advanced composites. In order to meet those purposes, three distinctive main approaches were considered in this work, namely, Bioinspired Bouligand-like Architectures (**Chapter 5**), Strategical Thin Veils Interleaving (**Chapter 6**) and 3D Printed Interlaminar Interlocking Structures (**Chapter 7**).

Considering the first approach proposed, Bioinspired Bouligand-like Architectures (**Chapter 5**), and according to the experimental results and observation carried out, it may be conclude the following:

- Vacuum bag infusion has shown to be an appropriate processing technology to manufacture Bouligand-like carbon/epoxy composites, considering the almost inexistence of voids inside the final composite plate;
- Comparatively to the reference laminate (LS conventional aeronautic arrangement), under quasi-static loading condition, Bouligand-like configurations have shown identical tensile moduli, slightly superior flexural modulus (especially, HL and HL_S layups) and higher interlaminar shear resistance (ILSS);
- Bioinspired configurations failure mode under quasi-static tests (e.g. tensile, 3-PB and ILSS tests) have shown to be progressive and dominated by fibres orientation, while LS reference tends to fail catastrophically;
- Under low velocity impact conditions, especially HL and HL_S bioinspired configurations, have revealed higher peak load, critical load (P_{cr}) and energy (E_{cr}), superior energy absorption (especially at 40 J of impact energy and smaller external, and internal damages, comparatively to reference;
- Finally, the higher number of fibres aligned in loading direction yielded higher residual strength, after impact tests, to the reference laminates than to the bioinspired ones.

In **Chapter 6**, two strategies were developed to interleave thin veils into a conventional carbon/epoxy aircraft laminate. From the experimental results it may be conclude the following:

- The manufacturing of laminates strategically interleaved with thin veils by vacuum bag infusion has revealed to lead to the formation of several void spots inside the composite plate;
- The inclusion of thin veils into the most critical normal and shear stresses' interfaces lead to an increment of laminates' thickness and resin volume fraction;

- Under quasi-static loading conditions, the inclusion of thin veils into laminates has revealed a reduce the flexural modulus. However, and despite the presence of voids inside interleaved laminates, they presented higher global interlaminar shear strength, especially layups interleaved in the most critical shear stress interfaces, than the no-interleaved laminate of reference. Moreover, both mechanical properties have shown to be related to the resin volume fraction variation among the different laminates;
- Under low velocity impact, all interleaved laminates have revealed identical mechanical response than the non-interleaved reference. However, independently on the veils used, critical shear stresses' interleaving strategy has demonstrated better mechanical response when compared to normal stresses' strategy;
- Regarding impact damage, independently on veil used, most of interleaved laminates have developed smaller external and internal damages than the layup of reference. Concerning these aspects, shear stresses' strategy has performed better than normal stresses' one, confirming the key role of interleaving strategy, more than veils' material;
- The inclusion of thin veils into laminates did not affect residual strength after impact, since no significant different responses were observed among non- and interleaved structures.

Finally, in **Chapter 7**, the use of additive manufacturing (3D printing) to create interlaminar interlocking mechanisms was explored in order to constrain possible delaminations formed during low velocity impacts in advanced composite laminates. Therefore, and according to experimental results it may conclude that:

- Contrary to PLA, a good adhesion to the carbon fibres was achieved when TPU patterns were directly printed over the dry fabrics;
- Vacuum bag infusion process has shown to be an effective manufacturing technology to impregnate those novel composite structures;
- Print interlocking structures into laminates' interfaces have led to an incremented of thickness and resin volume fraction of the final composite plate. Moreover, from SEM images it was concluded that smaller gaps between printed filaments results in extensive resin pockets into 3D printing reinforced interfaces and thicker composites;
- Under quasi-static loading conditions, 3D printing modified laminates have revealed lower flexural moduli and higher interlaminar shear strength. Once again, both mechanical properties have shown to be related to laminates' resin volume fraction. The higher the resin content, the lower the flexural modulus and the higher the resistance to interlaminar shear stresses;

- When compared to no printed reference laminate, all 3D printing modified configurations have revealed lower mechanical properties.
- Similar or small back face damage extents were observed on those new 3D printing modified layups, when compared to the same reference. In terms of internal damage area, both patterned A structures have formed identical damaged areas. However, TPU has performed better when was used to print pattern B, contrary to PLA which even has formed larger internal damages area then reference configuration.

Overall, in this thesis was experimentally confirmed that the usage of bioinspired Bouligand-like carbon/epoxy laminates may delay impact damage for higher values of load and energy and, on the other hand, the strategical interleaving of thin veils into the most critical shear stresses' laminate interfaces is an effective method to reduce impact damages. Finally, the usage of arising technologies to create interlaminar interlocking mechanisms apparently may reduce low velocity impact damage of advanced composites. However, more deeply studies should be carried out to explore the potential of this last solution.

9.1 Future work

Considering all observations, results and conclusions presented in this thesis, some proposals of future work may be suggested:

- Regarding the observed potential of Bouligand-like laminates to delay impact damage and the effectiveness of interleaving strategies to reduce the same, should be considered the hypothesis of combine both approaches to design new advanced composites with superior damage resistance;
- Despite the apparent better results obtain from vacuum bag infused Bouligand-like laminates when compared to those manufactured using prepreg material systems, a deeper study is imperative in order to evaluate the role of manufacturing technology on advanced composites impact response;
- Similarly, considering the high potential revealed from strategic interleaving method, an extra enforce should be done to evaluate other parameters such alternative interleaving strategies, manufacturing processes and even other structures as nano-veils;
- Finally, considering the huge potential of additive manufacturing to create uncountable different number of patterns using equal number of materials, a deeper study should be conducted

regarding printing parameters and pattern geometries in order to evaluate the real potential of this arising technology.

REFERENCES

[1] M. F. S. F. Moura, A. B. Morais, and A. G. Magalhães, *Materiais Compósitos - Materiais, Fabrico e Comportamento Mecânico*, 1 ª. Porto: Publindústria, 2005.

[2] M. Balasubramanian, *Composite Materials and Processing*, First., vol. 1. CRC Press, 2013.

[3] F. A. Administration, "Aviation Maintenance Technician Handbook - Airframe," *Aviat. Maint. Tech. Handb. - Airframe*, vol. 1, p. 588, 2012.

[4] G. Gardiner, "Aerocomposites: The move to multifunctionality : CompositesWorld," 2015. [Online]. Available: http://www.compositesworld.com/articles/aerocomposites-the-move-to-multifunctionality. [Accessed: 14-Jul-2017].

[5] F. C. Campbell, *Manufacturing Processes For Advanced Composites*. Elsevier Advanced Technology, 2004.

[6] Autar K. Kaw, *Mechanics of Composite Materials*, 2nd ed., vol. 29, no. Taylor & Francis, Inc., 2006.

[7] R. M. JONES, *Mechanics of composite materials*, 2nd ed., no. 2. Taylor and Francis, Inc., 1999.

[8] F. Gnädinger, P. Middendorf, and B. Fox, "Interfacial shear strength studies of experimental carbon fibres, novel thermosetting polyurethane and epoxy matrices and bespoke sizing agents," *Compos. Sci. Technol.*, vol. 133, pp. 104–110, 2016.

[9] Y. J. Ma, J. L. Wang, and X. P. Cai, "The effect of electrolyte on surface composite and microstructure of carbon fiber by electrochemical treatment," *Int. J. Electrochem. Sci.*, vol. 8, no. 2, pp. 2806–2815, 2013.

[10] R. Mezzenga, L. Boogh, and J. A. E. Månson, "A review of dendritic hyperbranched polymer as modifiers in epoxy composites," *Compos. Sci. Technol.*, vol. 61, no. 5, pp. 787–795, 2001.

[11] H. Masaki, O. Shojiro, C. G. Gustafson, and T. Keisuke, "Effect of matrix resin on delamination fatigue crack growth in CFRP laminates," *Eng. Fract. Mech.*, vol. 49, no. 1, pp. 35–47, 1994.

[12] A. P. Mouritz, K. H. Leong, and I. Herszberg, "A review of the effect of stitching on the in-plane mechanical properties of fibre-reinforced polymer composites," *Compos. Part A Appl. Sci. Manuf.*, vol. 28, no. 12, pp. 979–991, 1997.

[13] L. Tong, A. P. Mouritz, and M. K. Bannister, *3D Fibre Reinforced Polymer Composites*. Elsevier Science Ltd, 2002.

[14] M. Kuwata, "Mechanisms of interlaminar fracture toughness using non-woven veils as interleaf materials," Queen Mary, University of London, 2010.

[15] A. Zucchelli, M. L. Focarete, C. Gualandi, and S. Ramakrishna, "Electrospun nanofibers for enhancing structural performance of composite materials," *Polym. Adv. Technol.*, vol. 22, no. 3, pp. 339–349, 2011.

[16] N. H. Nash, T. M. Young, and W. F. Stanley, "An investigation of the damage tolerance of carbon / Benzoxazine composites with a thermoplastic toughening interlayer," *Compos. Struct.*, vol. 147, pp. 25–32, 2016.

[17] N. H. Nash, T. M. Young, P. T. McGrail, and W. F. Stanley, "Inclusion of a thermoplastic phase to improve impact and post-impact performances of carbon fibre reinforced thermosetting composites - A review," *Mater. Des.*, vol. 85, pp. 582–597, 2015.

[18] K. Kong, O. Kwon, and H. W. Park, "Enhanced mechanical and thermal properties of hybrid SnO2-

woven carbon fiber composites using the facile controlled growth method," *Compos. Sci. Technol.*, vol. 133, pp. 60–69, 2016.

[19] B. X. Yang, K. P. Pramoda, G. Q. Xu, and S. H. Goh, "Mechanical reinforcement of polyethylene using polyethylene-grafted multiwalled carbon nanotubes," *Adv. Funct. Mater.*, vol. 17, no. 13, pp. 2062–2069, 2007.

[20] H. Y. Choi and F. Chang, "A Model for Predicting Damage in Graphite/Epoxy Laminated Composites Resulting from Low-Velocity Point Impact," *J. Compos. Mater.*, vol. 26, pp. 2134–2169, 1992.

[21] V. Tita, J. de Carvalho, and D. Vandepitte, "Failure analysis of low velocity impact on thin composite laminates: Experimental and numerical approaches," *Compos. Struct.*, vol. 83, no. 4, pp. 413–428, 2008.

[22] M. O. W. Richardson and M. J. Wisheart, "Review of low-velocity impact properties of composite materials," *Compos. Part A Appl. Sci. Manuf.*, vol. 27, no. 12 PART A, pp. 1123–1131, 1996.

[23] E. V González, P. Maimí, P. P. Camanho, C. S. Lopes, and N. Blanco, "Effects of ply clustering in laminated composite plates under low-velocity impact loading," vol. 71, pp. 805–817, 2011.

[24] A. Mouritz, P. Chang, and M. Isa, "Z-pin composites: aerospace structural design considerations," *J. Aerosp. Eng.*, vol. 24, no. 4, pp. 425–432, 2010.

[25] A. P. Mouritz and B. N. Cox, "A mechanistic approach to the properties of stitched laminates," *Compos. Part A Appl. Sci. Manuf.*, vol. 31, no. 1, pp. 1–27, 2000.

[26] Q. Cheng, Z. Fang, Y. Xu, and X.-S. Yi, "Improvement of the Impact Damage Resistance of BMI/Graphite Laminates by the Ex-situ Method," *High Perform. Polym.*, vol. 18, no. 6, pp. 907–917, 2006.

[27] S. M. García-rodríguez, J. Costa, V. Singery, I. Boada, and J. A. Mayugo, "The effect interleaving has on thin-ply non-crimp fabric laminate impact response : X-ray tomography investigation," *Compos. Part A J.*, vol. 107, no. January, pp. 409–420, 2018.

[28] K. N. Shivakumar, R. Panduranga, and M. Sharpe, "Interleaved Polymer Matrix Composites - A Review," *54th AIAA/ASME/ASCE/AHS/ASC Struct. Struct. Dyn. Mater. Conf.*, pp. 1–13, 2013.

[29] Y. Bouligand, "Twisted fibrous arrangements in biological materials and cholesteric mesophases," *Tissue Cell*, vol. 4, no. 2, pp. 189–217, 1972.

[30] J. L. Liu, H. P. Lee, and V. B. C. Tan, "Failure mechanisms in bioinspired helicoidal laminates," *Compos. Sci. Technol.*, vol. 157, pp. 99–106, 2018.

[31] J. L. Liu, H. P. Lee, S. H. R. Kong, and V. B. C. Tan, "Improving laminates through non-uniform inter-ply angles," *Compos. Part A Appl. Sci. Manuf.*, vol. 127, no. July, p. 105625, 2019.

[32] L. Mencattelli and S. T. Pinho, "Realising bio-inspired impact damage-tolerant thin-ply CFRP Bouligand structures via promoting diffused sub-critical helicoidal damage," *Compos. Sci. Technol.*, vol. 182, no. June, p. 107684, 2019.

[33] L. Mencattelli and S. T. Pinho, "Ultra-thin-ply CFRP Bouligand bio-inspired structures with enhanced load-bearing capacity, delayed catastrophic failure and high energy dissipation capability," *Compos. Part A Appl. Sci. Manuf.*, vol. 129, no. July 2019, p. 105655, 2020.

[34] L. Mencattelli and S. T. Pinho, "Herringbone-Bouligand CFRP structures: A new tailorable damage-tolerant solution for damage containment and reduced delaminations," *Compos. Sci. Technol.*, p. 108047, 2020.

[35] F. L. Neto and L. C. Pardini, *Compósitos Estruturais*, 1◦. Blucher, 2006.

[36] J. P. Nunes, J. F. Silva, J. C. Velosa, C. A. Bernardo, and A. T. Marques, "New thermoplastic matrix composites for demanding applications," *Plast. Rubber Compos.*, vol. 38, no. 2–4, pp. 167–172, 2009.

[37] P. J. Novo, J. F. Silva, J. P. Nunes, and a T. Marques, "Advances in Thermoplastic Pultruded Composites," no. July, pp. 19–24, 2015.

[38] R. F. Silva, J. F. Silva, J. P. Nunes, C. A. Bernardo, and A. T. Marques, "New Powder Coating Equipment to Produce Continuous Fibre Thermoplastic Matrix Towpregs," *Adv. Mater. Forum Iv*, vol. 587–588, pp. 246–250, 2008.

[39] S. V Hoa, *Principles of the manufacturing of composite materials*. 2009.

[40] P. K. Mallick, *Fiber- Reinforced Composites*. 2007.

[41] T. Starr, *Pultrusion for Engineers*. Woodhead Publishing Limited, 2000.

[42] R. Chaudhari, P. Rosenberg, M. Karcher, S. Schmidhuber, P. Elsner, and F. Henning, "High-pressure RTM process variants for manfuacturing of carbon fiber reinforced composites," *ICCM Int. Conf. Compos. Mater.*, vol. 2013-July, pp. 1560–1568, 2013.

[43] A. Vita, V. Castorani, M. Germani, and M. Marconi, "Comparative life cycle assessment of low-pressure RTM, compression RTM and high-pressure RTM manufacturing processes to produce CFRP car hoods," *Procedia CIRP*, vol. 80, pp. 352–357, 2019.

[44] J. Summerscales and T. J. Searle, "Low-pressure (vacuum infusion) techniques for moulding large composite structures," *Proc. Inst. Mech. Eng. Part L J. Mater. Des. Appl.*, vol. 219, no. 1, pp. 45–58, 2005.

[45] D. Modi, N. Correia, M. Johnson, A. Long, C. Rudd, and F. Robitaille, "Active control of the vacuum infusion process," *Compos. Part A Appl. Sci. Manuf.*, vol. 38, no. 5, pp. 1271–1287, 2007.

[46] B. Yenilmez, M. Senan, and E. Murat Sozer, "Variation of part thickness and compaction pressure in vacuum infusion process," *Compos. Sci. Technol.*, vol. 69, no. 11–12, pp. 1710–1719, 2009.

[47] N. C. Correia, F. Robitaille, A. C. Long, C. D. Rudd, P. Šimáček, and S. G. Advani, "Analysis of the vacuum infusion moulding process: I. Analytical formulation," *Compos. Part A Appl. Sci. Manuf.*, vol. 36, no. 12, pp. 1645–1656, 2005.

[48] D. Modi, M. Johnson, A. Long, and C. Rudd, "Analysis of pressure profile and flow progression in the vacuum infusion process," *Spec. Issue 12th Eur. Conf. Compos. Mater. ECCM 2006*, vol. 69, no. 9, pp. 1458–1464, 2008.

[49] Q. Bénard, M. Fois, and M. Grisel, "Peel ply surface treatment for composite assemblies: Chemistry and morphology effects," *Compos. Part A Appl. Sci. Manuf.*, vol. 36, no. 11, pp. 1562–1568, 2005.

[50] M. Kanerva and O. Saarela, "The peel ply surface treatment for adhesive bonding of composites: A review," *Int. J. Adhes. Adhes.*, vol. 43, pp. 60–69, 2013.

[51] J. A. Woods, A. E. Modin, R. D. Hawkins, and D. J. Hanks, "CONTROLLED ATMOSPHERIC PRESSURE RESIN INFUSION PROCESS," 2008.

[52] C. Niggemann, Young Seok Song, J. W. Gillespie, and D. Heider, "Experimental Investigation of the Controlled Atmospheric Pressure Resin Infusion (CAPRI) Process," *J. Compos. Mater.*, vol. 42, no. 11, pp. 1049–1061, 2008.

[53] L. W. Davies, R. J. Day, D. Bond, A. Nesbitt, J. Ellis, and E. Gardon, "Effect of cure cycle heat

transfer rates on the physical and mechanical properties of an epoxy matrix composite," *Compos. Sci. Technol.*, vol. 67, no. 9, pp. 1892–1899, 2007.

[54] R. Caspe, V. Coenen, a Nesbitt, and an Wilkinson, "Through-Thickness Melding of Advanced Cfrp for Aerospace Applications," *Iccm-Central.Org*, vol. 9, no. July, 2008.

[55] J. Zhang, Q. Guo, and B. L. Fox, "Study on thermoplastic-modified multifunctional epoxies: Influence of heating rate on cure behaviour and phase separation," *Compos. Sci. Technol.*, vol. 69, no. 7–8, pp. 1172–1179, 2009.

[56] V. Antonucci *et al.*, "Resin flow monitoring in resin film infusion process," *J. Mater. Process. Technol.*, vol. 143–144, no. 1, pp. 687–692, 2003.

[57] J. K. Kim, D. B. MacKay, and Y. W. Mai, "Drop-weight impact damage tolerance of CFRP with rubber-modified epoxy matrix," *Composites*, vol. 24, no. 6, pp. 485–494, 1993.

[58] J. Brandt, K. Drechslef, and F. Arendtsb, "Mechanical performance of composites based on various three-dimentional woven-fibre preforms," *Compos. Sci. Technol.*, vol. 3538, no. 95, pp. 381–386, 1996.

[59] R. Seltzer, C. González, R. Muñoz, J. Llorca, and T. Blanco-Varela, "X-ray microtomography analysis of the damage micromechanisms in 3D woven composites under low-velocity impact," *Compos. Part A Appl. Sci. Manuf.*, vol. 45, pp. 49–60, 2013.

[60] B. K. Behera and B. P. Dash, "Mechanical behavior of 3D woven composites," *Mater. Des. J.*, pp. 261–271, 2015.

[61] A. P. Mouritz and B. N. Cox, "A mechanistic interpretation of the comparative in-plane mechanical properties of 3D woven, stitched and pinned composites," *Compos. Part A Appl. Sci. Manuf.*, vol. 41, no. 6, pp. 709–728, 2010.

[62] H. Gu and Z. Zhili, "Tensile behavior of 3D woven composites by using different fabric structures," *Mater. Des.*, vol. 23, no. 7, pp. 671–674, 2002.

[63] A. P. Mouritz, "Review of z-pinned composite laminates," *Compos. Part A Appl. Sci. Manuf.*, vol. 38, no. 12, pp. 2383–2397, 2007.

[64] D. D. R. Cartié, G. Dell'Anno, E. Poulin, and I. K. Partridge, "3D reinforcement of stiffener-to-skin T-joints by Z-pinning and tufting," *Eng. Fract. Mech.*, vol. 73, no. 16, pp. 2532–2540, 2006.

[65] X. Zhang, L. Hounslow, and M. Grassi, "Improvement of low-velocity impact and compression-after-impact performance by z-fibre pinning," *Compos. Sci. Technol.*, vol. 66, no. 15, pp. 2785–2794, 2006.

[66] I. K. Partridge and D. D. R. Cartié, "Delamination resistant laminates by Z-Fiber® pinning: Part I manufacture and fracture performance," *Compos. Part A Appl. Sci. Manuf.*, vol. 36, no. 1, pp. 55–64, 2005.

[67] D. D. R. Cartié, A. J. Brunner, and I. K. Partridge, "Effects of mesostructure on crack growth control characteristics in z-pinned laminates," *Eur. Struct. Integr. Soc.*, vol. 32, no. C, pp. 503–514, 2003.

[68] R. B. Ladani *et al.*, "Multi-scale toughening of fibre composites using carbon nanofibres and z-pins," *Compos. Sci. Technol.*, vol. 131, pp. 98–109, 2016.

[69] I. K. Partridge and S. R. Hallett, "Use of microfasteners to produce damage tolerant composite structures.," *Philos. Trans. A. Math. Phys. Eng. Sci.*, vol. 374, no. 2071, pp. 2383–2397, 2016.

[70] M. D. Isa, S. Feih, and A. P. Mouritz, "Compression fatigue properties of z-pinned quasi-isotropic

carbon / epoxy laminate with barely visible impact damage," *Compos. Struct.*, vol. 93, no. 9, pp. 2269–2276, 2011.

[71] A. P. Mouritz, "Composites : Part A Delamination properties of z-pinned composites in hot – wet environment," *Compos. Part A*, vol. 52, pp. 134–142, 2013.

[72] L. Francesconi and F. Aymerich, "Effect of Z-pinning on the impact resistance of composite laminates with different layups," vol. 114, no. May, pp. 136–148, 2018.

[73] M. D. K. Wood, X. Sun, L. Tong, A. Katzos, A. R. Rispler, and Y. W. Mai, "The effect of stitch distribution on Mode I delamination toughness of stitched laminated composites - experimental results and FEA simulation," *Compos. Sci. Technol.*, vol. 67, no. 6, pp. 1058–1072, 2007.

[74] S. Solaimurugan and R. Velmurugan, "Influence of in-plane fibre orientation on mode I interlaminar fracture toughness of stitched glass/polyester composites," *Compos. Sci. Technol.*, vol. 68, no. 7–8, pp. 1742–1752, 2008.

[75] L. K. Jain, K. A. Dransfield, and Y.-W. Mai, "On the effects of stitching in CFRPs—II. Mode II delamination toughness," *Compos. Sci. Technol.*, vol. 58, no. 6, pp. 829–837, 1998.

[76] K. T. Tan, N. Watanabe, Y. Iwahori, and T. Ishikawa, "Understanding effectiveness of stitching in suppression of impact damage: An empirical delamination reduction trend for stitched composites," *Compos. Part A Appl. Sci. Manuf.*, vol. 43, no. 6, pp. 823–832, 2012.

[77] K. Dransfield, C. Baillie, and Y. W. Mai, "Improving the delamination resistance of CFRP by stitching-a review," *Compos. Sci. Technol.*, vol. 50, no. 3, pp. 305–317, 1994.

[78] J.-K. Kim and Y.-W. Mai, *Engineered Interfaces in Fiber Reinforced Composites*. United States: Elsevier Science & Technology, 1998.

[79] L. Francesconi and F. Aymerich, "Effect of stitching on the flexure after impact behavior of thin laminated composites," *J. Mech. Eng. Sci.*, vol. 0, no. 0, pp. 1–15, 2017.

[80] L. Boogh, B. Pettersson, and J. A. E. Månson, "Dendritic hyperbranched polymers as toughening agents for epoxy resins," *Polymer (Guildf).*, vol. 40, no. 9, pp. 2249–2261, 1999.

[81] D. Ratna, "Toughened FRP composites reinforced with glass and carbon fiber," *Compos. Part A Appl. Sci. Manuf.*, vol. 39, no. 3, pp. 462–469, 2008.

[82] J. M. Scott and D. C. Phillips, "Carbon fibre composites with rubber toughened matrices," *J. Mater. Sci.*, vol. 10, no. 4, pp. 551–562, 1975.

[83] J. Kim, C. Baillie, J. Poh, and Y. W. Mai, "Fracture toughness of CFRP with modified epoxy resin matrices," *Compos. Sci. Technol.*, vol. 43, no. 3, pp. 283–297, 1992.

[84] Y. X. He *et al.*, "Micro-crack behavior of carbon fiber reinforced thermoplastic modified epoxy composites for cryogenic applications," *Compos. Part B Eng.*, vol. 44, no. 1, pp. 533–539, 2013.

[85] G. Di Pasquale, O. Motto, A. Rocca, J. T. Carter, P. T. McGrail, and D. Acierno, "New high-performance thermoplastic toughened epoxy thermosets," *Polymer (Guildf).*, vol. 38, no. 17, pp. 4345–4348, 1997.

[86] J. Verrey, Y. Winkler, V. Michaud, and J. A. E. Månson, "Interlaminar fracture toughness improvement in composites with hyperbranched polymer modified resin," *Compos. Sci. Technol.*, vol. 65, no. 10, pp. 1527–1536, 2005.

[87] M. DeCarli, K. Kozielski, W. Tian, and R. Varley, "Toughening of a carbon fibre reinforced epoxy anhydride composite using an epoxy terminated hyperbranched modifier," *Compos. Sci. Technol.*, vol. 65, no. 14, pp. 2156–2166, 2005.

[88] S. Denneulin, P. Viot, F. Leonardi, and J. L. Lataillade, "The influence of acrylate triblock copolymer embedded in matrix on composite structures' responses to low-velocity impacts," *Compos. Struct.*, vol. 94, no. 4, pp. 1471–1481, 2012.

[89] D. R. Paul and L. M. Robeson, "Polymer nanotechnology: Nanocomposites," *Polymer (Guildf).*, vol. 49, no. 15, pp. 3187–3204, 2008.

[90] T. Mahrholz, J. Stängle, and M. Sinapius, "Quantitation of the reinforcement effect of silica nanoparticles in epoxy resins used in liquid composite moulding processes," *Compos. Part A Appl. Sci. Manuf.*, vol. 40, no. 3, pp. 235–243, 2009.

[91] E. F. Reia Da Costa, A. A. Skordos, I. K. Partridge, and A. Rezai, "RTM processing and electrical performance of carbon nanotube modified epoxy/fibre composites," *Compos. Part A Appl. Sci. Manuf.*, vol. 43, no. 4, pp. 593–602, 2012.

[92] F. H. Gojny, M. H. G. Wichmann, B. Fiedler, W. Bauhofer, and K. Schulte, "Influence of nano-modification on the mechanical and electrical properties of conventional fibre-reinforced composites," *Compos. Part A Appl. Sci. Manuf.*, vol. 36, no. 11, pp. 1525–1535, 2005.

[93] A. Godara *et al.*, "Influence of carbon nanotube reinforcement on the processing and the mechanical behaviour of carbon fiber/epoxy composites," *Carbon N. Y.*, vol. 47, no. 12, pp. 2914–2923, 2009.

[94] B. Ashrafi *et al.*, "Enhancement of mechanical performance of epoxy/carbon fiber laminate composites using single-walled carbon nanotubes," *Compos. Sci. Technol.*, vol. 71, no. 13, pp. 1569–1578, 2011.

[95] C. U. Pittman, W. Jiang, G.-R. He, and S. D. Gardner, "Oxygen plasma and isobutylene plasma treatments of carbon fibers: Determination of surface functionality and effects on composite properties," *Carbon N. Y.*, vol. 36, no. 1–2, pp. 25–37, 1998.

[96] R. Guzman de Villoria, P. Hallander, L. Ydrefors, P. Nordin, and B. L. Wardle, "In-plane strength enhancement of laminated composites via aligned carbon nanotube interlaminar reinforcement," *Compos. Sci. Technol.*, vol. 133, pp. 33–39, 2016.

[97] Q. An, A. N. Rider, and E. T. Thostenson, "Hierarchical composite structures prepared by electrophoretic deposition of carbon nanotubes onto glass fibers.," *ACS Appl. Mater. Interfaces*, vol. 5, no. 6, pp. 2022–32, 2013.

[98] Q. An, A. N. Rider, and E. T. Thostenson, "Electrophoretic deposition of carbon nanotubes onto carbon-fiber fabric for production of carbon/epoxy composites with improved mechanical properties," *Carbon N. Y.*, vol. 50, no. 11, pp. 4130–4143, 2012.

[99] H. Xu, X. Tong, Y. Zhang, Q. Li, and W. Lu, "Mechanical and electrical properties of laminated composites containing continuous carbon nanotube film interleaves," *Compos. Sci. Technol.*, vol. 127, pp. 113–118, 2016.

[100] V. P. Veedu *et al.*, "Multifunctional composites using reinforced laminae with carbon-nanotube forests," *Nat. Mater.*, vol. 5, no. 6, pp. 457–462, 2006.

[101] E. T. Thostenson, W. Z. Li, D. Z. Wang, Z. F. Ren, and T. W. Chou, "Carbon nanotube/carbon fiber hybrid multiscale composites," *J. Appl. Phys.*, vol. 91, no. 9, pp. 6034–6037, 2002.

[102] R. J. Sager *et al.*, "Effect of carbon nanotubes on the interfacial shear strength of T650 carbon fiber in an epoxy matrix," *Compos. Sci. Technol.*, vol. 69, no. 7–8, pp. 898–904, 2009.

[103] K. L. Kepple, G. P. Sanborn, P. A. Lacasse, K. M. Gruenberg, and W. J. Ready, "Improved fracture toughness of carbon fiber composite functionalized with multi walled carbon nanotubes," *Carbon*

N. Y., vol. 46, no. 15, pp. 2026–2033, 2008.

[104] E. J. Garcia, B. L. Wardle, A. J. Hart, and N. Yamamoto, "Fabrication and multifunctional properties of a hybrid laminate with aligned carbon nanotubes grown In Situ," vol. 68, pp. 2034–2041, 2008.

[105] S. S. Wicks, R. G. De Villoria, and B. L. Wardle, "Interlaminar and intralaminar reinforcement of composite laminates with aligned carbon nanotubes," *Compos. Sci. Technol.*, vol. 70, no. 1, pp. 20–28, 2010.

[106] S. S. Wicks, W. Wang, M. R. Williams, and B. L. Wardle, "Multi-scale interlaminar fracture mechanisms in woven composite laminates reinforced with aligned carbon nanotubes," *Compos. Sci. Technol.*, vol. 100, pp. 128–135, 2014.

[107] F. Ozdil and L. a. Carlsson, "Mode I Interlaminar Fracture of Interleaved Graphite/Epoxy," *J. Compos. Mater.*, vol. 26, no. 3, pp. 432–459, 1992.

[108] S. Singh and I. K. Partridge, "Mixed-mode fracture in an interleaved carbon-fibre/epoxy composite," *Compos. Sci. Technol.*, vol. 55, no. 4, pp. 319–327, 1995.

[109] S. F. Chen and B. Z. Jang, "Fracture Behaviour of Interleaved Fiber-Resin Composites," vol. 41, pp. 77–97, 1991.

[110] M. Yasaee, I. P. Bond, R. S. Trask, and E. S. Greenhalgh, "Damage control using discrete thermoplastic film inserts," *Compos. Part A Appl. Sci. Manuf.*, vol. 43, no. 6, pp. 978–989, 2012.

[111] X. Xu, Z. Zhou, Y. Hei, B. Zhang, J. Bao, and X. Chen, "Improving compression-after-impact performance of carbon–fiber composites by CNTs/thermoplastic hybrid film interlayer," *Compos. Sci. Technol.*, vol. 95, pp. 75–81, 2014.

[112] L. Liu, L. Shen, and Y. Zhou, "Improving the interlaminar fracture toughness of carbon/epoxy laminates by directly incorporating with porous carbon nanotube buckypaper," *J. Reinf. Plast. Compos.*, vol. 35, no. 2, pp. 165–176, 2016.

[113] S. U. Khan and J. K. Kim, "Improved interlaminar shear properties of multiscale carbon fiber composites with bucky paper interleaves made from carbon nanofibers," *Carbon N. Y.*, vol. 50, no. 14, pp. 5265–5277, 2012.

[114] E. J. Garcia, B. L. Wardle, and A. John Hart, "Joining prepreg composite interfaces with aligned carbon nanotubes," *Compos. Part A Appl. Sci. Manuf.*, vol. 39, no. 6, pp. 1065–1070, 2008.

[115] R. Guzman de Villoria, L. Ydrefors, P. Hallander, K. Ishiguro, P. Nordin, and B. Wardle, "Aligned Carbon Nanotube Reinforcement of Aerospace Carbon Fiber Composites: Substructural Strength Evaluation for Aerostructure Applications," *53rd AIAA/ASME/ASCE/AHS/ASC Struct. Struct. Dyn. Mater. Conf. AIAA/ASME/AHS Adapt. Struct. Conf. AIAA*, no. April, pp. 1–7, 2012.

[116] J. J. Stahl, A. E. Bogdanovich, and P. D. Bradford, "Carbon nanotube shear-pressed sheet interleaves for Mode i interlaminar fracture toughness enhancement," *Compos. Part A Appl. Sci. Manuf.*, vol. 80, pp. 127–137, 2016.

[117] S. H. Lee and H. Noguchi, "Shear characteristics of hybrid composites with non-woven carbon tissue," *JSME International Journal*, vol. 44, no. 4. pp. 535–541, 2001.

[118] L. Seung-Hwan, H. Noguchi, Y. Kim, and S. Cheong, "Effect of Interleaved Non-Woven Carbon Tissue on Interlaminar Fracture Toughness of Laminated Composites : Part II – Mode I," *J. Compos. Mater.*, vol. 36, no. 18, p. 2169, 2002.

[119] M. Kuwata and P. J. Hogg, "Interlaminar toughness of interleaved CFRP using non-woven veils: Part 1. Mode-I testing," *Compos. Part A Appl. Sci. Manuf.*, vol. 42, no. 10, pp. 1551–1559, 2011.

[120] M. Kuwata and P. J. Hogg, "Interlaminar toughness of interleaved CFRP using non-woven veils: Part 2. Mode-II testing," *Compos. Part A Appl. Sci. Manuf.*, vol. 42, no. 10, pp. 1560–1570, 2011.

[121] V. A. Ramirez, P. J. Hogg, and W. W. Sampson, "The influence of the nonwoven veil architectures on interlaminar fracture toughness of interleaved composites," *Compos. Sci. Technol.*, vol. 110, pp. 103–110, 2015.

[122] L. Walker, M. Sohn, and X. Hu, "Improving impact resistance of carbon- ® bre composites through interlaminar reinforcement," *Compos. Part A*, vol. 33, pp. 893–902, 2002.

[123] P. J. Hogg, "Toughening of thermosetting composites with thermoplastic fibres," *Mater. Sci. Eng. A*, vol. 412, pp. 97–103, 2005.

[124] B. Beylergil, M. Tanoglo, and E. Aktas, "Effect of polyamide-6,6 (PA 66) nonwoven veils on the mechanical performance of carbon fiber/epoxy composites," *Compos. Struct.*, vol. 194, no. February, pp. 21–35, 2018.

[125] G. W. Beckermann and K. L. Pickering, "Mode i and Mode II interlaminar fracture toughness of composite laminates interleaved with electrospun nanofibre veils," *Compos. Part A Appl. Sci. Manuf.*, vol. 72, pp. 11–21, 2015.

[126] S. van der Heijden *et al.*, "Interlaminar toughening of resin transfer moulded glass fibre epoxy laminates by polycaprolactone electrospun nanofibres," *Compos. Sci. Technol.*, vol. 104, pp. 66–73, 2014.

[127] P. Akangah, S. Lingaiah, and K. Shivakumar, "Effect of Nylon-66 nano-fiber interleaving on impact damage resistance of epoxy/carbon fiber composite laminates," *Compos. Struct.*, vol. 92, no. 6, pp. 1432–1439, 2010.

[128] M. Goodarz, S. H. Bahrami, M. Sadighi, and S. Saber-Samandari, "Low-velocity impact performance of nanofiber-interlayered aramid/epoxy nanocomposites," *Compos. Part B Eng.*, vol. 173, no. May, p. 106975, 2019.

[129] F. Sarasini *et al.*, "Effect of electrospun nanofibres and MWCNTs on the low velocity impact response of carbon fibre laminates," *Compos. Struct.*, vol. 234, no. December 2019, p. 111776, 2020.

[130] M. S. Islam and P. Prabhakar, "Interlaminar strengthening of multidirectional laminates using polymer additive manufacturing," *Mater. Des.*, vol. 133, pp. 332–339, 2017.

[131] G. Szebényi, T. Czigány, B. Magyar, and J. Karger-Kocsis, "3D printing-assisted interphase engineering of polymer composites: Concept and feasibility," *Express Polym. Lett.*, vol. 11, no. 7, pp. 525–530, 2017.

[132] V. Damodaran, A. G. Castellanos, M. Milostan, and P. Prabhakar, "Improving the Mode-II interlaminar fracture toughness of polymeric matrix composites through additive manufacturing," *Mater. Des.*, vol. 157, pp. 60–73, 2018.

[133] J. H. E. Cartwright and A. G. Checa, "The dynamics of nacre self-assembly," *J. R. Soc. Interface*, vol. 4, no. 14, pp. 491–504, 2007.

[134] F. Barthelat, J. E. Rim, and H. D. Espinosa, "A Review on the Structure and Mechanical Properties of Mollusk Shells – Perspectives on Synthetic Biomimetic Materials," in *Applied Scanning Probe Methods XIII*, 2009, pp. 17–44.

[135] J. Y. Rho, L. Kuhn-Spearing, and P. Zioupos, "Mechanical properties and the hierarchical structure of bone," *Med. Eng. Phys.*, vol. 20, no. 2, pp. 92–102, 1998.

[136] F. Libonati and L. Vergani, "Cortical Bone as a Biomimetic Model for the Design of New Composites," *Procedia Struct. Integr.*, vol. 2, pp. 1319–1326, 2016.

[137] S. N. Patek and R. L. Caldwell, "Extreme impact and cavitation forces of a biological hammer: Strike forces of the peacock mantis shrimp Odontodactylus scyllarus," *J. Exp. Biol.*, vol. 208, no. 19, pp. 3655–3664, 2005.

[138] L. Cheng, L. Wang, and A. M. Karlsson, "Image analyses of two crustacean exoskeletons and implications of the exoskeletal microstructure on the mechanical behavior," *J. Mater. Res.*, vol. 23, no. 11, pp. 2854–2872, 2008.

[139] N. A. Yaraghi *et al.*, "A Sinusoidally Architected Helicoidal Biocomposite," *Adv. Mater.*, vol. 28, no. 32, pp. 6835–6844, 2016.

[140] R. Yang, A. Zaheri, W. Gao, C. Hayashi, and H. D. Espinosa, "AFM Identification of Beetle Exocuticle: Bouligand Structure and Nanofiber Anisotropic Elastic Properties," *Adv. Funct. Mater.*, vol. 27, no. 6, 2017.

[141] E. A. Zimmermann *et al.*, "Mechanical adaptability of the Bouligand-type structure in natural dermal armour," *Nat. Commun.*, vol. 4, pp. 1–7, 2013.

[142] J. C. Weaver *et al.*, "The stomatopod dactyl club: A formidable damage-tolerant biological hammer," *Science (80-.).*, vol. 336, no. 6086, pp. 1275–1280, 2012.

[143] Prilfish, "Mantis Shrimp - Odontodactylus scyllarus," *Thailand Andaman Sea February 2008*, 2008. [Online]. Available: www.flickr.com. [Accessed: 13-Feb-2020].

[144] T. Apichattrabrut and K. Ravi-Chandar, "Helicoidal Composites," *Mech. Adv. Mater. Struct.*, vol. 13, no. 1, pp. 61–76, 2006.

[145] L. Cheng, A. Thomas, J. L. Glancey, and A. M. Karlsson, "Mechanical behavior of bio-inspired laminated composites Helicoidal structure," *Compos. Part A*, vol. 42, no. 2, pp. 211–220, 2011.

[146] L. K. Grunenfelder *et al.*, "Bio-inspired impact-resistant composites," *Acta Biomater.*, vol. 10, no. 9, pp. 3997–4008, 2014.

[147] J. S. Shang, N. H. H. Ngern, and V. B. C. Tan, "Crustacean-inspired helicoidal laminates," *Compos. Sci. Technol.*, vol. 128, pp. 222–232, 2016.

[148] F. Pinto, O. Iervolino, G. Scarselli, D. Ginzburg, and M. Meo, "Bioinspired twisted composites based on Bouligand structures," in *Bioinspiration, Biomimetics, and Bioreplication 2016*, 2016, vol. 9797.

[149] D. Ginzburg, F. Pinto, O. Iervolino, and M. Meo, "Damage tolerance of bio-inspired helicoidal composites under low velocity impact," *Compos. Struct.*, vol. 161, pp. 187–203, 2017.

[150] J. L. Liu, H. P. Lee, and V. B. C. Tan, "Effects of inter-ply angles on the failure mechanisms in bioinspired helicoidal laminates," *Compos. Sci. Technol.*, vol. 165, no. July, pp. 282–289, 2018.

[151] J. L. Liu, H. P. Lee, K. S. Lai, and V. B. C. Tan, "Bio-Inspired Laminates of Different Material Systems," *J. Appl. Mech.*, vol. 87, no. 3, pp. 1–7, 2020.

[152] M. R. Abir, T. E. Tay, and H. P. Lee, "On the improved ballistic performance of bio-inspired composites," *Compos. Part A Appl. Sci. Manuf.*, vol. 123, no. March, pp. 59–70, 2019.

[153] N. Suksangpanya, N. A. Yaraghi, R. B. Pipes, D. Kisailus, and P. Zavattieri, "Crack twisting and toughening strategies in Bouligand architectures," *Int. J. Solids Struct.*, vol. 150, pp. 83–106, 2018.

[154] E. E. Theotokoglou and E. P. Sideridis, "Study of unidirectional fiber reinforced epoxy composites

in short-beam bending test," *J. Reinf. Plast. Compos.*, vol. 36, no. 24, pp. 1781–1789, 2017.

[155] K. N. Shivakumar, W. Elber, and W. Illg, "Prediction of low-velocity impact damage in thin circular laminates," *AIAA J.*, vol. 23, no. 3, pp. 442–449, 1985.

[156] P. O. Sjoblom, J. T. Hartness, and T. M. Cordell, "On Low-Velocity Impact Testing of Composite Materials," *J. Compos. Mater.*, vol. 22, no. 1, pp. 30–52, 1988.

[157] W. J. Cantwell and J. Morton, "The impact resistance of composite materials - a review," *Composites*, vol. 22, no. 5, pp. 347–362, 1991.

[158] S. Gholizadeh, "A review of non-destructive testing methods of composite materials," *Procedia Struct. Integr.*, vol. 1, pp. 50–57, 2016.

[159] V. Munoz, M. Perrin, M. L. Pastor, H. Welemane, A. Cantarel, and M. Karama, "Determination of the elastic properties in CFRP composites: Comparison of different approaches based on tensile tests and ultrasonic characterization," *Adv. Aircr. Spacecr. Sci.*, vol. 2, no. 3, pp. 249–261, 2015.

[160] A. T. Nettles, "Some examples of the relation between processing and damage tolerance," *Int. SAMPE Tech. Conf.*, 2012.

[161] H. Conway, B. Bancroft, D. Chebot, M. Devoe, and C. Gouldstone, "Impact resistance and residual strength of carbon fiber epoxy laminates with vertically-aligned carbon nanotube interfacial reinforcement," *Int. SAMPE Tech. Conf.*, pp. 1642–1651, 2017.

[162] Y. Cao, Z. Cao, Y. Zhao, D. Zuo, and T. E. Tay, "Damage progression and failure of single-lap thin-ply laminated composite bolted joints under quasi-static loading," *Int. J. Mech. Sci.*, vol. 170, no. December, p. 105360, 2020.

[163] N. Suksangpanya, N. A. Yaraghi, D. Kisailus, and P. Zavattieri, "Twisting cracks in Bouligand structures," *J. Mech. Behav. Biomed. Mater.*, vol. 76, no. March, pp. 38–57, 2017.

[164] G. Mishra, S. R. Mohapatra, P. R. Behera, B. Dash, U. K. Mohanty, and B. C. Ray, "Environmental stability of GFRP laminated composites: An emphasis on mechanical behaviour," *Aircr. Eng. Aerosp. Technol.*, vol. 82, no. 4, pp. 258–266, 2010.

[165] A. Mehndiratta, "Analyzing Variation in ILSS of Fiber Reinforced Polymer Laminates with respect to Pressure variation in autoclave," *MOJ Polym. Sci.*, vol. 1, no. 3, pp. 127–129, 2017.

[166] L. Reis and M. De Freitas, "Damage growth analysis of low velocity impacted composite panels," *Compos. Struct.*, vol. 38, no. 1–4, pp. 509–515, 1997.

[167] S. M. Lee and P. Zahuta, "Instrumented Impact and Static Indentation of Composites," *J. Compos. Mater.*, vol. 25, no. 2, pp. 204–222, 1991.

[168] A. Wagih, P. Maimí, N. Blanco, and J. Costa, "A quasi-static indentation test to elucidate the sequence of damage events in low velocity impacts on composite laminates," *Compos. Part A Appl. Sci. Manuf.*, vol. 82, pp. 180–189, 2016.

[169] M. Mehdikhani, L. Gorbatikh, I. Verpoest, and S. V. Lomov, "Voids in fiber-reinforced polymer composites: A review on their formation, characteristics, and effects on mechanical performance," *J. Compos. Mater.*, vol. 53, no. 12, pp. 1579–1669, 2019.

[170] A. Esnaola, I. Tena, J. Aurrekoetxea, I. Gallego, and I. Ulacia, "Effect of fibre volume fraction on energy absorption capabilities of E-glass/polyester automotive crash structures," *Compos. Part B Eng.*, vol. 85, pp. 1–7, 2016.

[171] G. Belingardi and R. Vadori, "Influence of the laminate thickness in low velocity impact behavior of composite material plate," *Compos. Struct.*, vol. 61, no. 1–2, pp. 27–38, 2003.

[172] M. Herráez *et al.*, "Computational micromechanics evaluation of the effect of fibre shape on the transverse strength of unidirectional composites: An approach to virtual materials design," *Compos. Part A Appl. Sci. Manuf.*, vol. 91, pp. 484–492, 2016.

[173] J. Mohan, A. Ivanković, and N. Murphy, "Mode i fracture toughness of co-cured and secondary bonded composite joints," *Int. J. Adhes. Adhes.*, vol. 51, pp. 13–22, 2014.

[174] A. K. Pathak, M. Borah, A. Gupta, T. Yokozeki, and S. R. Dhakate, "Improved mechanical properties of carbon fiber/graphene oxide-epoxy hybrid composites," *Compos. Sci. Technol.*, vol. 135, pp. 28–38, 2016.

[175] M. A. Meyers, A. Y. M. Lin, P. Y. Chen, and J. Muyco, "Mechanical strength of abalone nacre: Role of the soft organic layer," *J. Mech. Behav. Biomed. Mater.*, vol. 1, no. 1, pp. 76–85, 2008.

[176] H. D. Espinosa, J. E. Rim, F. Barthelat, and M. J. Buehler, "Merger of structure and material in nacre and bone - Perspectives on de novo biomimetic materials," *Prog. Mater. Sci.*, vol. 54, no. 8, pp. 1059–1100, 2009.

[177] A. Y. M. Lin and M. A. Meyers, "Interfacial shear strength in abalone nacre," *J. Mech. Behav. Biomed. Mater.*, vol. 2, no. 6, pp. 607–612, 2009.

APPENDIX A

List of Material datasheets:

- Epoxy resin CR83 neat resin and CH83-6 hardener – Sika®;
- Unidirectional carbon cibre tissue Dynanotex HS 24/150 DLN2 – G. ANGELONI s.r.l.;
- Unidirectional carbon cibre tissue Dynanotex HS 15/50 SLN2 – G. ANGELONI s.r.l.;
- 24K 1600 dtex carbon fibres – Grafil;
- 15K 1000 dtex carbon fibres – Grafil;
- Glass fibre veil – ACP Composites;
- Carbon fibre veil – ACP Composites;
- Aramid fibre veil – ACP Composites;
- Polyester fibre veil – ACP Composites;
- Polylactic acid thermoplastic (PLA) printing filament – BQ;
- Thermoplastic polyether-polyurethane elastomer (TPU) printing filament – Recreus Industries s.l.;
- Two-parts adhesive EA 9394 AERO – Loctite®.

Tooling & Composites

Product Data Sheet
Version 04 / 2016

Biresin® CR83
Composite resin system

Product Description

Biresin® CR83 is an epoxy resin system with extremely low viscosity designed specifically for the infusion process for the production of high performance fibre reinforced composites parts and moulds. The system has thermal properties up to 80°C. Biresin® CR83 epoxy resin has a low tendency to crystallise.

Application Areas

Biresin® CR83 is especially suited to the infusion and injection processes due to its low viscosity range. It can be used in the marine and general industrial composite areas. Due to its good wetting properties it is particularly suited for use with carbon fibre reinforcement.

Features / Advantages

- 3 hardeners (B) give a wide range of processing times
- The reactivity can be adapted by mixing the hardeners
- Fast infusion and good wet-out of fabrics and non-wovens due to low viscosity and good wetting characteristics even at low temperatures
- All systems Germanischer Lloyd approved, Certificate No. WP 1420017 HH (attached)
- Glass transition temperatures up to 80°C dependent on curing conditions
- Carbon fibres are wet out well by all of the resin systems
- Biresin® CR83 resin (A) has a low tendency to crystallise

Physical Data		Resin (A)	Hardener (B)		
Individual Components		**Biresin® CR83**	**Biresin® CH83-2**	**Biresin® CH83-6**	**Biresin® CH83-10**
Mixing ratio, parts by	**weight**	100	30		
Mixing ratio, parts by	**volume**	100	36		
Colour		translucent	colourless to yellowish		
Viscosity, 25°C	mPa.s	~610	<10	<10	< 10
Density, 25°C	g/ml	1.14	0.95	0.94	0.95
			Mixture		
Potlife, 100 g / RT, approx. values	min		60	180	300
Mixed viscosity, 25°C, approx. values	mPa.s		155	170	155

Processing

- The material and processing temperatures should be in the range 18 - 35°C.
- The mixing ratio must be followed accurately to obtain best results. Deviating from the correct mix ratio will lead to lower performance.
- The final mechanical and thermal values are dependent on the applied postcuring cycles.
- It is recommended to clean brushes or tools immediately after use with Sika Reinigungsmittel 5.
- Additional information is available in “Processing Instructions for Composite Resins”.

Development of Exotherm of Biresin® CR83-Resin (A)-Hardener (B)-Mixtures, 100g / RT, insulated

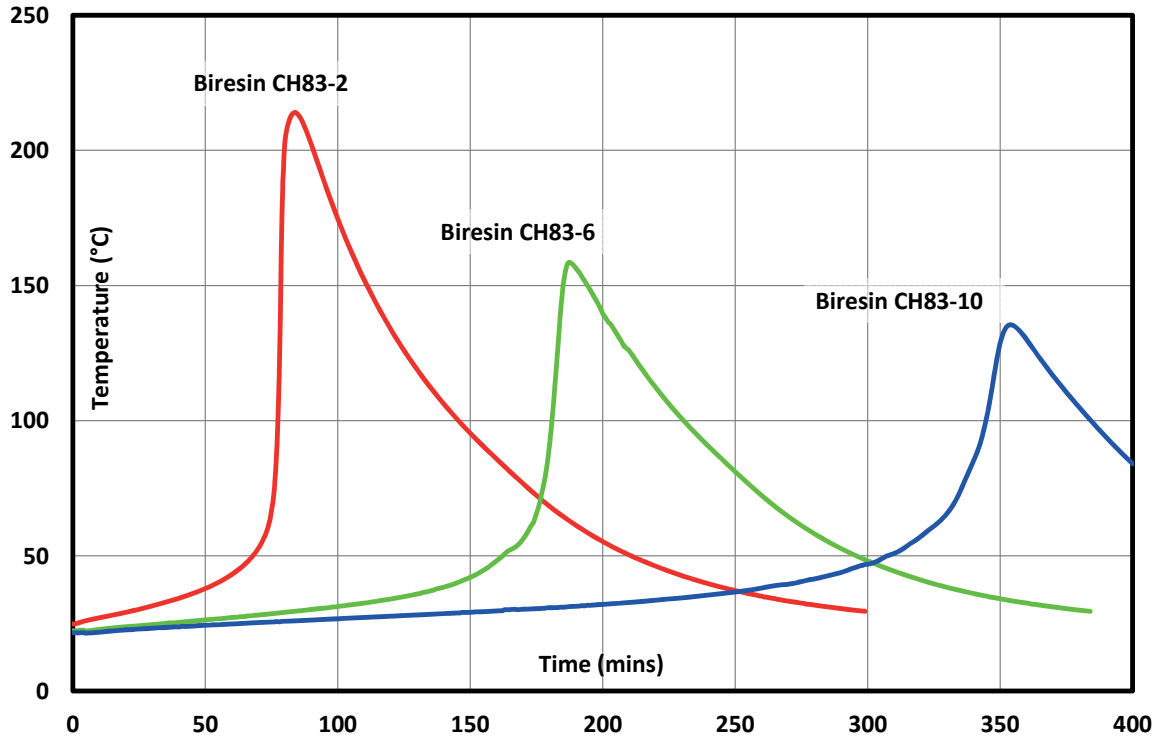

Development of Viscosity of Biresin® CR83 (A)-Resin-Hardener (B)-Mixtures, 25°C

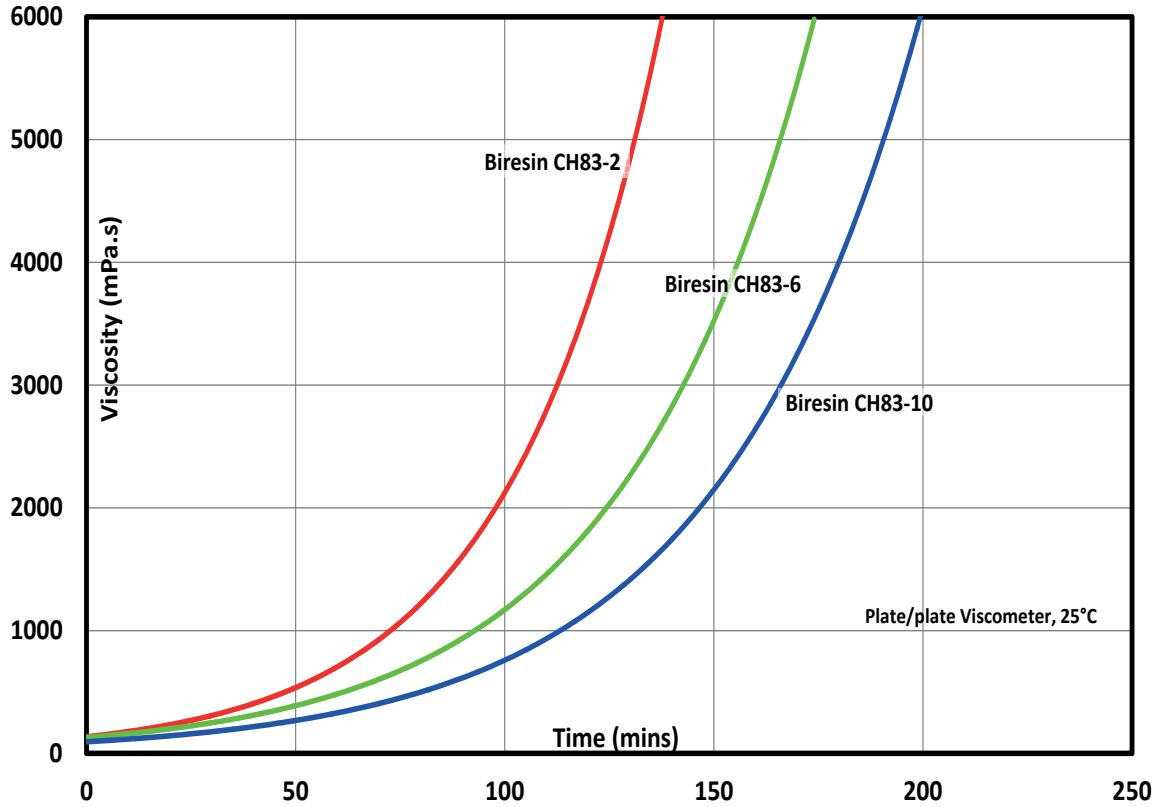

Typical Mechanical Properties of Fully Cured Neat Resin					
Biresin® CR83 resin (A)	with hardener (B) **Biresin®**		**CH83-2**	**CH83-6**	**CH83-10**
Tensile strength	ISO 527	MPa	84	91	86
Tensile E-Modulus	ISO 527	MPa	2,960	3,200	3,100
Elongation at break	ISO 527	%	6.7	8.4	7.9
Flexural strength	ISO 178	MPa	129	134	131
Flexural E-Modulus	ISO 178	MPa	3,125	3,360	3,340
Compressive strength	ISO 604	N/mm^2	107	111	109
Density	ISO 1183	g/cm^3	1.15	1.15	1.15
Shore-hardness	ISO 868		D 85	D 85	D 85
Impact resistance	ISO 179	kJ/m^2	93	84	83

Typical Thermal Properties of Fully Cured Neat Resin					
Biresin® CR83 resin (A)	with hardener (B) **Biresin®**		**CH83-2**	**CH83-6**	**CH83-10**
Heat distortion temperature	ISO 75B	°C	79	79	78
Glass transition temperature	ISO 11357	°C	84	80	81

Glass Transition Temperature vs. Cure Cycle

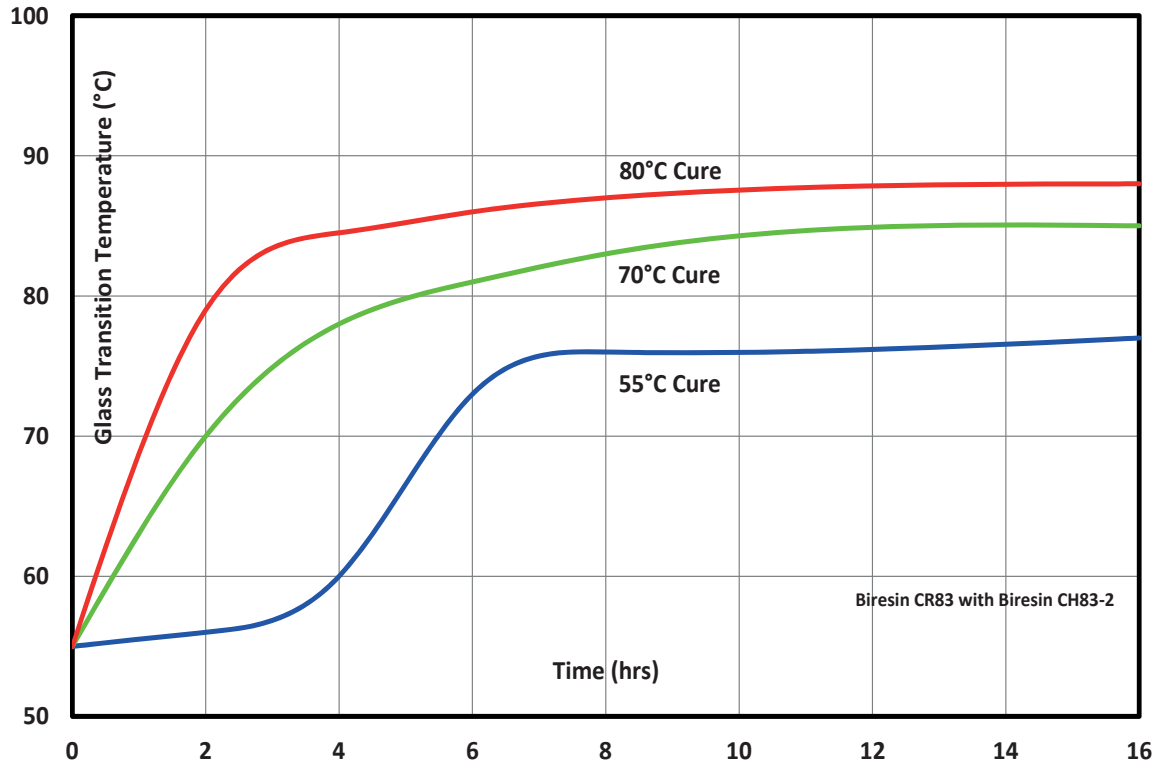

When curing a composite part, the whole of the part (including the very middle of the laminate) needs to see the cure temperature.

Packaging (net weight, kg)

Biresin® CR83 resin (A)	1,000	200		10
Biresin® CH83-2 hardener (B)		180	20	3.0
Biresin® CH83-6 hardener (B)		180	20	3.0
Biresin® CH83-10 hardener (B)		180	20	3.0

Storage

- Minimum shelf life of Biresin® CR83 resin (A) is 24 month and of Biresin® CH83-2, CH83-6 and CH83-10 hardeners (B) is 12 month under room conditions (18 - 25°C), when stored in original unopened containers.
- The tendency to of crystallise with this system is very low. However, if crystallisation of the resin (A) component appears, it can be easily removed by warming up the resin for a sufficient time to at least 60°C.
- Containers must be closed tightly immediately after use. The residual material needs to be used up as soon as possible.

Health and Safety Information

For information and advice on the safe handling, storage and disposal of chemical products, users shall refer to the most recent Safety Data Sheet (SDS) containing physical, ecological, toxicological and other safety related data.

Disposal considerations

Product Recommendations: Must be disposed of in a special waste disposal unit in accordance with the corresponding regulations.
Packaging Recommendations: Completely emptied packagings can be given for recycling. Packaging that cannot be cleaned should be disposed of as product waste.

Value Bases

All technical data stated in this Product Data Sheet are based on laboratory tests. Actual measured data may vary due to circumstances beyond our control.

Legal Notice

Further information available at:

Sika Deutschland GmbH
Subsidiary Bad Urach
Stuttgarter Str. 139
D - 72574 Bad Urach
Germany

Tel: +49 (0) 7125 940 492
Fax: +49 (0) 7125 940 401
Email: tooling@de.sika.com
Internet: www.sika.com

FABRIC DATA SHEET

G.Angeloni reference **HS 24/150 DLN2**

PROPERTIES		Nominal	Tolerance	Normative
Mass per unit area	g/m^2	**153**	± 5%	ISO 4605
Weave		**UNIDIRECTIONAL**		ISO 2113
Standard Width	mm	1000	± 3,5%	
Laminate thickness	mm	0,130	± 3,5%	(**)
Other informations		Polyester fiber net		

CONSTRUCTION		Description			Nominal mass	Tolerance
Fibre	Layer 1	Grafil 24K 1600 dtex	g/m^2	**70**	93%	± 3%
			%	49		
	Layer 2	Grafil 24K 1600 dtex	g/m^2	**70**		
			%	49		
	Layer 3	Polyester fiber net	g/m^2	**3**		
			%	2		
	Layer 4		g/m^2			
			%			
Adhesive		Resins compatible			7%	± 3%

(**) Theorical thickness for an epoxy laminate with 40% of reinforcement in volume.

Note : Technical information furnished is based on laboratory findings and believed to be correct. No warranties of any kind are made except that the materials supplied are of standard quality. All risk and liabilities arising from handling, storage and use of products, as well as compliance with applicable legal restrictions,rests with the user.

G.Angeloni srl
via Abate Tommaso , 72/A5 - 30020 Quarto d'Altino (VE) - ITALY
Tel. +39 0422 823801 - 780580 Fax +39 0422 782782
E-Mail : info@g-angeloni.com

G. ANGELONI
Since 1927

Dynano tex

UNIDIRECTIONAL DATA SHEET

G.Angeloni
reference

HS 15/45 SLN2

PROPERTIES		Nominal	Tolerance	Normative
Mass per unit area	g/m^2	**48**	± 6%	ISO 4605
Weave		Pure UNIDIRECTIONAL		ISO 2113
Standard Width	mm	1000	± 3,5%	
Laminate thickness	mm	0,055	± 3,5%	(**)
Other informations		Single Layer		

CONSTRUCTION		Description			Nominal Mass	Tolerance
Quality of Fiber	Layer 1	Grafil 15K 1000 dtex	g/m^2	**45**	90%	± 4%
			%	95		
	Layer 2	Polyester fibre net	g/m^2	**2,5**		
			%	5		
	Layer 3		g/m^2			
			%			
	Layer 4		g/m^2			
			%			
Adhesive		Resins compatible			10%	± 5%

(**) Theorical thickness for an epoxy laminate with 40% of reinforcement in volume.

Note : Technical information furnished is based on laboratory findings and believed to be correct. No warranties of any kind are made except that the materials supplied are of standard quality. All risk and liabilities arising from handling, storage and use of products, as well as compliance with applicable legal restrictions,rests with the user.

G.Angeloni srl
via Abate Tommaso , 72/A5 - 30020 Quarto d'Altino (VE) - ITALY
Tel. +39 0422 823801 - 780580 Fax +39 0422 782782
www.g.angeloni.com

MITSUBISHI RAYON
CARBON FIBER & COMPOSITES

GRAFIL 34-700

Grafil 34-700 carbon fiber is a continuous, high strength, PAN based fiber. It is available in 12K and 24K filament count tows. They can be supplied in either round tow or flat tow formats. The flat tow (designated by 'WD') is the ideal fiber to use in applications where spreading is required, e.g., tape production. The round tow is used in applications where spreading is not necessarily required, e.g., braiding and weaving.

Typical Fiber Properties

Tow Tensile	Strength	700 4830	ksi MPa	SRM 16
	Modulus	34 234	msi GPa	
Typical Density		0.065 1.80	$lb.in^3$ g/cm^3	SRM 15
Typical Yield	12K	620 800	yds/lb mg/m	SRM 13
	24K	310 1600	yds/lb mg/m	SRM 13

Typical Mechanical Properties

Tensile Properties	0º	Strength	373 2572	ksi MPa	ASTM D3039 / 0º8ply
		Modulus	19.9 137	msi GPa	ASTM D3039 / 0º8ply
	90º	Strength	11.l7 81	ksi MPa	ASTM D3039 / 0º16ply
		Modulus	1.34 9.2	msi GPa	ASTM D3039 / 0º16ply
Compressive Properties	0º	Strength	198 1365	ksi MPa	ASTM D3410 / 0º16ply
		Modulus	18.5 127	msi GPa	ASTM D3410 / 0º16ply
	90º	Strength	28.5 196	ksi MPa	ASTM D3410 / 0º20ply
		Modulus	1.49 10.2	msi GPa	ASTM D3410 / 0º20ply
Flexural Properties	0º	Strength	253 1745	ksi MPa	ASTM D790 / 0º16ply, L/D=32, Vf=61%
		Modulus	19.1 132	msi GPa	ASTM D790 / 0º16ply, L/D=32, Vf=61%
	90º	Strength	14.9 102	ksi MPa	ASTM D790 / 0º16ply, L/D=16, Vf=61%
		Modulus	1.28 8.8	msi GPa	ASTM D790 / 0º16ply, L/D=16, Vf=61%
ILSS	Strength		14.1 97	ksi GPa	ASTM D2344 / 0º16ply, L/D=4, Vf=59%

- 250F Epoxy Prepregs
- Resin: Mitsubishi Rayon #340 resin system
- Tensile and compressive properties are normalized to 60% fiber volume

5900 88th St
Sacramento, CA 95828
USA
Tel: 916-386-1733
Fax: 916-383-7688
Web: www.mrcfac.com

03/2010
ISO 9001:2008
FM 56416

6, Orchard Court
Binley Business Park
Harry Weston Road
Binley, Coventry CV3 2TQ UK
Tel: +44 (0) 2476 447272
Fax: +44 (0) 2476 449565

PYROFIL™ TR50S 15K

Typical Fiber Properties

Tow Tensile	Strength	710 4,900	ksi MPa	JISR 7601
	Modulus	35 240	msi GPa	
Typical Density		0.066 1.82	$lb.in^3$ g/cm^3	JISR 7601
Typical Yield	15K	496 1,000	yds/lb mg/m	JISR 7601

5900 88th Street
Sacramento, CA
95828, USA
Tel: 916.386.1733
Fax: 916.383.7668
Web: www.grafil.com

ISO 9001:2008
FM 56416

03/2010

6, Orchard Court
Binley Business Park
Harry Weston Road
Binley, Coventry CV3 2TQ UK
Tel: +44 (0) 2476 447272
Fax: +44 (0) 2476 449565

Fiberglass Tissue

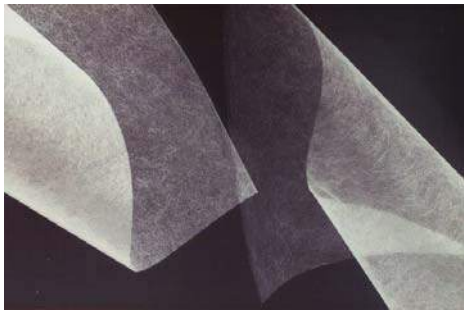

Fiberglass Tissue is a lightweight, advanced, non-woven fiberglass veil incorporating 100% E-Glass fibers, approximately 1" in length, bonded together in a random fiber matrix. The non-woven construction allows a resin-rich surface that increases chemical stability and reduces the risk of micro-cracks forming in the composite surface. It has excellent formability and drape and wets out evenly. Fiberglass Tissue can be used to provide a smooth covering for composite structures or to add stiffness with minimal weight gain and thickness.

Physical Properties

Weight	.3 oz/yd^2	.5 oz/yd^2	1 oz/yd^2
Thickness	.003"	.005"	.0075"
Fiber Type	E-CR Fiberglass	E-CR Fiberglass	E-CR Fiberglass
Material Grade	8000130	8000100	8000111
Binder	Polyester	Polyester	Polyester

Technical Properties

Average Tensile (MD)	2.0 lb/in	5.0 lb/in	10.0 lb/in
Average Tensile (CD)	2.0 lb/in	5.0 lb/in	10.0 lb/in
Elongation (MD)	0.50 %	-	1.50 %
Elongation (CD)	0.50 %	-	1.50 %

MD-Machine Direction. CD-Cross Direction.

78 Lindbergh Ave I Livermore, CA 94551
1-800-811-2009 I P. 925-443-5900 I F. 925-443-5901

Carbon Fiber Tissue

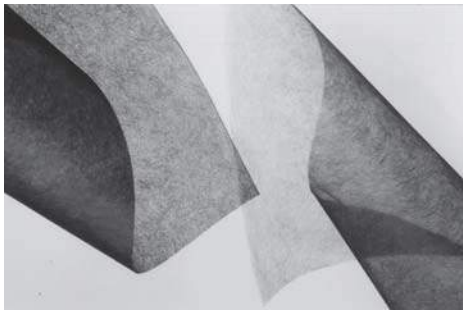

Carbon Tissue is a lightweight, advanced non-woven carbon fiber veil incorporating 100% carbon fibers, approximately 1" in length, bonded together in a random fiber matrix. The non-woven construction allows a resin-rich surface that increases chemical stability and reduces the risk of micro-cracks forming in the composite surface. It has excellent formability, drape and wets out evenly. Carbon Tissue can be used to provide a smooth covering for composite structures or to add stiffness with minimal weight gain and thickness. It is compatible is compatible with polyester, vinyl-ester and epoxy resins.

Physical Properties			
Weight	.2 oz/yd^2	.3 oz/yd^2	.5 oz/yd^2
Thickness	.0021"	.0025"	.0055"
Fiber Type	PAN Carbon Fiber	PAN Carbon Fiber	PAN Carbon Fiber
Material Grade	8000015i	8000018	800020i
Binder	Polyester	Polyester	Polyester

Technical Properties			
Average Tensile (MD)	3.0 lb/in	5.2 lb/in	7.0 lb/in
Average Tensile (CD)	3.0 lb/in	3.0 lb/in	7.0 lb/in
Air Permeability	1,220 ft^3/ft^2/min	940 ft^3/ft^2/min	840 ft^3/ft^2/min
Elongation (MD)	0.90%	0.50%	0.60%
Elongation (CD)	1.4%	1.2%	1.1%
Mullen Burst	2.8 psi	6.0 psi	10.5 psi

MD-Machine Direction. CD-Cross Direction

78 Lindbergh Ave I Livermore, CA 94551
1-800-811-2009 I P. 925-443-5900 I F. 925-443-5901

Aramid Tissue

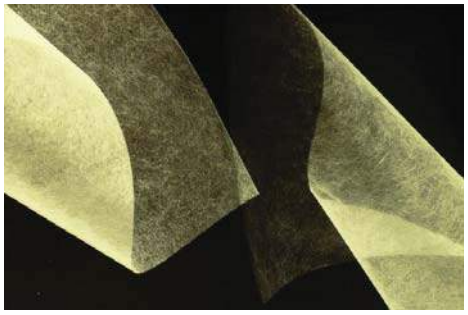

Aramid Tissue is a advanced non-woven aramid fiber veil incorporating 100% KEVLAR® fibers, approximately 1" in length, bonded together in a random fiber matrix. The non-woven construction allows a resin-rich surface that increases chemical stability and reduces the risk of micro-cracks forming in the composite surface. This lightweight material offers excellent formability, drape and wets out evenly. Aramid Tissue can be used to increase impact resistance and toughness. It is compatible with polyester, vinyl-ester and epoxy resins and is suitable for use in wet layup, vacuum bagging and resin infusion manufacturing.

Physical Properties

Product	.25oz	.4oz
Weight	.25 oz/yd^2	.4 oz/yd^2
Thickness	.0025"	.0052"
Fiber Type	KEVLAR® 29	KEVLAR® 29
Material Grade	8000056	8000054
Binder	Polyester	Polyester

Technical Properties

Product	.25oz	.4oz
Average Tensile (MD)	3.0 lb/in	6.3 lb/in
Average Tensile (CD)	3.0 lb/in	6.3 lb/in
Elongation (MD)	4.5%	2.0%
Elongation (CD)	4.5%	2.0%

KEVLAR® is a registered trademark of E.I. du Pont de Nemours and Company and is used with permission. MD-Machine Direction. CD-Cross Direction.

78 Lindbergh Ave I Livermore, CA 94551
1-800-811-2009 I P. 925-443-5900 I F. 925-443-5901

Aero-Veil

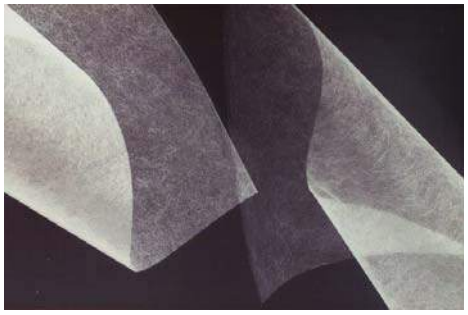

Aero-Veil is a lightweight non-woven fabric of synthetic fibers specifically designed to improve the aesthetic qualities of wet layup laminates. It can be used to provide a smooth covering for composite structures or to reinforce a surface coat with minimal weight gain and thickness. Aero-Veil has excellent formability, drape and wets out evenly. It is suitable for in applications up to 485°F (250°C).

Physical Properties	
Weight	.0047"
Thickness	.5 oz./yd^2
Fiber Type	Polyester

Technical Properties	
Tensile Strength (MD)	10.7 lbs
Tensile Strength (CD)	7.4 lbs
Tear Strength (MD)	4.2 lbs
Tear Strength (CD)	5.1 lbs
Mullen Burst Strength	11 psi
Air Permeability	1080 ft^3/min/ft^2
Softening/Melt Point	347°F to 482°F

MD-Machine Direction. CD-Cross Direction.

78 Lindbergh Ave I Livermore, CA 94551
1-800-811-2009 I P. 925-443-5900 I F. 925-443-5901

PLA filament: technical datasheet

PROPERTY	VALUE	UNITS	TEST METHOD
General properties			
Specific gravity	1.24	g/cm^3	ASTM D792
Mechanical properties			
Flexural elastic modulus	3600	MPa	ISO 178
Flexural Strength	108	MPa	ISO 178
Hardness, Sh D	85	Sh D	ASTM D2240
Thermal properties			
Heat distortion temperature HDT B (0,45MPa)	56	°C	ISO 75/2B
Melting temperature	145-160	°C	ASTM D3418
Glass Transition Temperature	56-64	°C	ASTM D3418

In addition to the described properties, we have performed tensile tests on tensile specimen printed with our PLA and on injection moulded tensile specimen in order to ascertain the mechanical properties of the final printed object. The following table contains the results:

Mechanical properties	Injection moulded tensile specimen	Printed tensile specimen[a]	Printed tensile specimen[b]	Units	Test method
Tensile strength at break	52	50	39	MPa	ISO 527
Tensile elongation at break	5	9	4	%	ISO 527
Tensile modulus	1320	1230	1120	MPa	ISO 527

[a] Stretch-direction is parallel to the layers.
[b] Stretch-direction is perpendicular to the layers.

Tensile specimen	Layer height (mm)	Shell thickness (mm)	Bottom/top thickness (mm)	Fill density (%)	Print design
Tensile specimen print-direction is parallel to the layers	0.2	2	0.2	100	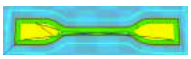
Tensile specimen print-direction is perpendicular to the layers	0.3	1	0.3	100	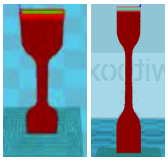

Filaflex®Original 82A

Filaflex is a Thermoplastic Polyether-Polyurethane elastomer with additives that allow high printability in FDM printers, Filaflex® has a remarkable hydrolysis resistance, high resistance to bacteria and low temperature flexibility properties in printed parts.

Property	Unit	Value	Test method according to
Hardness	Shore A	82	DIN ISO 7619-1 (3s)
Density	g/cm³	**1.12**	DIN EN ISO 1183-1-A
Tensile strength	MPa	45	DIN 53504-S2
Elongation at break	%	600	DIN 53504-S2
Stress at 20% elongation	MPa	**2.5**	DIN 53504-S2
Stress at 100% elongation	MPa	6	DIN 53504-S2
Stress at 300% elongation	MPa	10	DIN 53504-S2
Tear strength	N/mm	70	DIN ISO 34-1Bb
Abrasion loss	mm³	25	DIN ISO 4649-A
Compression set 23°C / 72 hours	%	25	DIN ISO 815
Compression set 70°C / 24 hours	%	45	DIN ISO 815
Tensile strength after storage in water at 80°C for 42 days	MPa	32	DIN 53504-S2
Tensile strength after storage in water at 80°C for 42 days	MPa	32	DIN 53504-S2
Elongation at break after storage in Water at 80°C for 42 days	%	600	DIN 53504-S2
Notched impact strength (Charpy) at +23°C	kJ/m²	**kB**	DIN EN ISO 179-1
Notched impact strength (Charpy) at -30°C	kJ/m²	**kB**	DIN EN ISO 179-1

3D PRINTING PARAMETERS	VALUE
Printing Temperatures	215-250°C
Printing Speed	20-60 mm/s
Hot-Bed temperature	0 °C
Optimal layer height	0,2mm
Minimal Nozzle diameter	0,4mm or higher recommended)
Rectraction parameters	3,5-6,5 mm (speed 20-160 mm/s)

FILAFLEX ® ORIGINAL MSDS

1. PRODUCT AND COMPANY IDENTIFICATION

1.1 TRADE NAME: FilaFlex®

1.2 COMPANY DETAILS:

RECREUS INDUSTRIES S.L.

C/EL ENVELOPE, 13-14,

POL. INDUS. FINCA LACY.

03600 ELDA, (Alicante), SPAIN

Tel: 0034 865 777966 info@recreus.com www.recreus.com

2. HAZARDS IDENTIFICATION

Classification of the substance or mixture

This product is not classified as dangerous for health or the environment according to EC norm 1272/2008/CE (CLP) .

Label elements:

This product does't need dangerous label according to EC norm 1272/2008/CE (CPL)

3. COMPOSITION/INFORMATION ON INGREDIENTS

Polymer. Thermoplastic polyurethane. Polyurethane polymer from methylenediphenyl diisocyanate, glycols, polyether polyol and additives.

REGULATORY COMPLIANCE INFORMATION FOR FOOD CONTACT APPLICATION

1) EUROPEAN REGULATION N. 10/2011, 14 January 2011:

The starting monomers and the additives used, are included in the Union List of authorized substances, as in annex 1 of regulation n. 10/2011, as updated with regulation 175/2015.

2) FDA STATUS:

The starting monomers and the additives used, are included in FDA CFR21.

DISCLAIMER:

Is under responsibility of the 3d printer parts manufacturer or end user the compliance of the plastic object, for the specific use, with the overall migration limit, the specific migration limit and other restrictions.

Do not hesitate to contact our technical service for explanations, advising and for any other need.

4. FIRST AIDS

1. General instruction: Change clothes impregnated with the product.
2. In case of inhalation: Supply fresh air. In case of disturbances, consult a doctor.

3. After inhalation of decomposition products, breathe fresh air, rest, seek medical help.
4. In case of skin contact: Wash with soap and water. Visit your doctor if irritation continues skin.

5. After contact with molten product, cool rapidly with cold water. No skin separating the solidified product. Call a doctor immediately.

6. In case of eye contact: Rinse opened eye for several minutes under running water. If symptoms persist, consult a doctor. Remove contact lenses, if present and easy. Continue rinsing.

7. If swallowed: Rinse mouth and drink plenty of water. Do not induce vomiting. Consult doctor in case of persistent symptoms**.**

5. FIRE-FIGHTING MEASURES

5.1 Suitable extinguishing media: Water, Foam, Dry chemical

5.2 Burning releases carbon monoxide, carbon dioxide, oxides of nitrogen and traces of hydrogen cyanide. In the event of fire and/or explosion do not breathe f**u**me.

5.3 Firemen must wear self-contained b**r**eathing apparatus.

5.4 Do not allow contaminated extinguishing water to enter the soil, ground**-** water or surface waters.

6. Measures in case of accidental release

6.1 Personal precautions

- Protective equipment and emergency procedures
- Avoid dust formation.
- Do not breathe dust.
- Keep away from sources of ignition.
- Avoid eye contact.
- Danger of slipping on spilled product or pouring.

6.2 Environmental cautions:

Do not discharge into drains / surface water / ground water.

6.3 Methods and Materials for containment and cleaning up

Allow to solidify, pick up mechanically. Dispose of the material collected according to regulations.

7.HANDLING AND STORAGE

Handling

Adequate ventilation and if necessary, effective exhaust must be provided at the workplace of fused deposition modeling process.

Provided good ventilation and/or local exhaust systems are used, the Workplace Exposure Limit(s) stated in Chapter 8 should not be exceeded. Dust must be removed by effective exhaust ventilation.

Storage

Keep container tightly closed and dry. Storage temperature: < 40 °C

8.Exposure controls / personal protection

Ventilation:

During fused deposition modeling operations, use with ventilation adequate to reduce levels of air contaminants below that which may cause personal injury or illness. Local exhaust ventilation that removes air contaminants from the breathing zone is prefer ed. General, mechanical, or dilution ventilation may be suitable.

Respiratory protection:
In case of dust formation use respiratory equipment with filter type particle filter P1 according to EN 143.

Hand protection:
Suitable materials for safety gloves; EN 374-3: polyvinyl chloride - PVC (>= 0.5 mm)
Contaminated and/or damaged gloves must be changed.

Eye protection:
Wear eye/face protection.

Skin and body protection:
Wear suitable protective clothing.

Further protective measures:
Do not breathe dust/vapor. Grease skin.

9. Physical and chemical properties:

Appearance:	Various colors
Odor:	Odorless
Odour Threshold:	NA
PH:	NA
Boiling Point (° C):	NA
Melting point (° C):	220-240
Softening point (° C):	105
Evaporation Rate:	NA
Properties Flammable / Explosive:	NA
Vapor pressure / vapor density:	NA
Relative density:	1.13
Solubility:	NA
Octanol / water partition:	NA
Auto-ignition temperature:	NA
Decomposition temperature:	NA
Viscosity:	NA
Other properties:	NA

10.Stability and reactivity

Reactivity: Non-applicable

Chemical stability

Thermal decomposition / conditions to be avoided:

- No decomposition with storage and proper handling.
- Avoid impact, friction, heat, sparks, and electrostatic charges.

Possibility of dangerous reactions: Non-applicable.

Conditions to be avoided: No further relevant information.

Incompatible materials: Strong oxidants.

Strong decomposition products

- Irritant gases / vapours.
- Toxic gases / vapours.
- Smoke.
- Carbon monoxide (CO) and carbon dioxide (CO_2) emissions

11.TOXICOLOGICAL INFORMATION

Acute toxicity LD50 oral rat: > 5000 mg/kg

Acute toxicity LD50 subcutaneous, rat: > 5000 mg/kg

Primary skin irritation, rabbit: non-irritant

Primary mucosae irritation, rabbit: non-irritant

Skin sensitisation according to Magnusson/Kligmann (maximizing test):
No sensitisation established on guinea-pigs

Additional information: According to our experience and information the product has no harmful effects on health if properly handled.

12. ECOLOGICAL INFORMATION

Ecotoxicity

It is not expected to be very toxic, but if ingested by birds or aquatic life, can cause adverse mechanical effects

Mobility

Bioconcentration is not expected because of the high molecular weight (MW > 1000). In the terrestrial environment, material is expected to remain in the soil. In the aquatic environment material will sink and remain in the sediment.

Persistence and degradability

This solid water-insoluble polymeric are expected to be inert in the environment. Surface degradation is expected with exposure to sunlight. Appreciable biodegradation is not expected.

Additional ecological information

General instructions: CPA 1 (auto classification): not dangerous for water.

13. DISPOSAL CONSIDERATIONS

Dispose in accordance with applicable international, national and local laws, ordinances and statutes. For disposal within the EC, the appropriate code according to the European Waste Catalogue (EWC) should be used.

After containers have been emptied as thoroughly as possible (e.g. by pouring, scraping or draining until "drip-dry"), they can besent to an appropriate collection point set the framework of the existing take-back scheme of the chemical industry. Containers must be recycled in compliance with national legislation and environmental regulations.

The product is suitable for mechanical recycling. After appropriate treat**m**ent it can be remelted and reprocessed into new moulded articles. Mechanical recycling is only possible if the material has been selectively retrieved and ca efully segregated according to type.

14. TRANSPORT INFORMATION

Not regulated.

15. Regulatory information

Not regulated.

16. Other information

The data is based on the current state of knowledge, but it is not a guarantee of the product features and it is not legally valid in a contractual relationship.

Technical Process Bulletin

LOCTITE EA 9394 AERO
Epoxy Paste Adhesive
(KNOWN AS Hysol EA 9394)

INTRODUCTION
LOCTITE EA 9394 AERO is a two-part structural paste adhesive, which cures at room temperature and possesses excellent strength to 350°F/177°C and higher. Its thixotropic nature and excellent high temperature compressive strength also make it ideal for potting, filling and liquid shim applications. LOCTITE EA 9394 AERO is qualified to MMM-A-132 Rev A, Type I, Class 3.

The mechanical properties in this data sheet are also valid for LOCTITE EA 9394S AERO. LOCTITE EA 9394S AERO is only available in Semkits and differs from LOCTITE EA 9394 AERO as it has 1 part less thixotrope in the Part B to aid packaging. All other mechanical and handling properties similar.

FEATURES
- Room Temperature Cure
- Good Gap Filling Capabilities
- 350°F/177°C Performance
- Potting Material
- Room Temperature Storage
- Outstanding Mechanical Properties
- Long Pot Life
- Low Toxicity

Uncured Properties

	Part A	Part B	Mixed
Color	Gray	Black	Gray
Viscosity, 77°F	4000-8000 Poise	200-700 Poise	1600 Poise
Brookfield, HBT	Spdl 7 @ 20 rpm	Spdl 4 @ 20 rpm	Spdl 5 @ 20 rpm
Viscosity, 25°C	400-800 Pa·S	20-70 Pa·S	160 Pa·S
Brookfield, HBT	Spdl 7 @ 2.09 rad/sec	Spdl 4 @ 2.09 rad/sec	Spdl 5 @ 2.09 rad/sec
Density (g/ml)	1.50	1.00	1.36
Shelf Life			
@ <77°F/25°C	1 year	1 year	

This material will normally be shipped at ambient conditions, which will not alter our standard warranty, provided that the material is placed into its intended storage upon receipt. Premium shipment is available upon request.

LOCTITE EA 9394 AERO
Epoxy Paste Adhesive
(KNOWN AS Hysol EA 9394)

Handling
Mixing - This product requires mixing two components together just prior to application to the parts to be bonded. Complete mixing is necessary. The temperature of the separate components prior to mixing is not critical, but should be close to room temperature (77°F/25°C).

Mix Ratio	Part A	Part B
By Weight	100	17

Note: Volume measurement is not recommended for structural applications unless special precautions are taken to assure proper ratios.

Pot Life (450 gram mass) 90 minutes @ 75°F/25°C
Method - ASTM D 2471 in water bath**.**

Application
Mixing - Combine Part A and Part B in the correct ratio and mix thoroughly. THIS IS IMPORTANT! Heat buildup during or after mixing is normal. Do not mix quantities greater than 450 grams as dangerous heat buildup can occur causing uncontrolled decomposition of the mixed adhesive. TOXIC FUMES CAN OCCUR, RESULTING IN PERSONAL INJURY. Mixing smaller quantities will minimize the heat buildup.

Applying - Bonding surfaces should be clean, dry and properly prepared. For optimum surface preparation consult the LOCTITE Surface Preparation Guide. The bonded parts should be held in contact until the adhesive is set. Handling strength for this adhesive will occur in 24 hours @ 77°F/25°C, after which the support tooling or pressure used during cure may be removed. Since full bond strength has not yet been attained, load application should be small at this time.

Dual Cartridge Application
We recommend that you do not precondition the kits, dispense adhesive at ambient temperature. If pre-heating is required for the cartridge kits, do not exceed 90°F for a maximum time of four hours.

- Do not assemble the static mixer onto the cartridge while conditioning.
- Do not place the assembled cartridges upright in the oven.
- Seat kit into the cartridge sleeve/tray and ensure proper placement against the gun plungers. **Misalignment during triggering of the plungers can result in kit damage.**
- Burp the adhesive at **low pressure** prior to dispensing through the static mixer.
    - Allows for both Piston, A & B sides to be equally level during initial dispensing, thus preventing an adhesive backflow.
    - It's possible that the Piston-B Side may be unleveled with the Piston-A side due to the heating & positioning of the cartridge. The Part B resin viscosity is much lower than the Part A resin viscosity 200 ml kit failures will occur if the inlet pressure is set too high while triggering the plungers.
- Start the plungers at **low pressure (20 psi)** then increase to the desired pressure
- Over heating of the cartridge in an oven and then applying high pressure can result in **kit damage and/or resin blowback.**

- Do not allow the adhesive to sit in the static mixer unattended for more than 90 minutes.
    - The material is curing within the static mixer and when pressure is re-applied back onto the plungers, back pressure will occur and potentially result in cartridge failure.

Failure to follow the recommended procedures stated in this TDS will void the Warranty of the Adhesive.

Note: Special precautions are recommended to minimize carbonate formation in large assemblies subject to extended open times in humid environments. A special memo is available upon request from Henkel providing users with suggestions for minimizing carbonate formation.

Curing - LOCTITE EA 9394 AERO may be cured for 3 to 5 days @ 77°F/25°C to achieve normal performance. Accelerated cures up to 200°F/93°C (for small masses only) may be used as an alternative. For example, 1 hour @ 150°F/66°C will give complete cure**.**

Cleanup - It is important to remove excess adhesive from the work area and application equipment before it hardens. Denatured alcohol and many common industrial solvents are suitable for removing uncured adhesive. Consult your supplier's information pertaining to the safe and proper use of solvents.

Bond Strength Performance

Tensile Lap Shear Strength - tested per ASTM D1002 after curing for 5 days @ 77°F/25°C. Adherends are 2024-T3 bare aluminum treated with phosphoric acid anodized per ASTM D3933.

	Typical Results	
Test Temperature, °F/°C	psi	MPa
-67/-55	3,300	22.7
77/ 25	4,200	28.9
180/82	3,000	20.7
200/93	2,900	20.0
250/121	2,300	15.8
300/149	1,600	11.0
350/177	1,200	8.3
400/204	600	4.1

After Exposure to/Test Temperature	Typical Results psi	MPa
Room Temperature Control (no exposure)	4,300	29.6
77°F/25°C Water - 7 days @77°F/25°C	4,100	28.2
Isopropyl Alcohol - 7 days @77°F/25°C	4,000	27.6
Hydraulic Oil - 7 days @77°F/25°C	4,100	28.2
JP-4 Fuel - 7 days @ 77°F/25°C	4,200	28.9

Peel Strength

T-Peel strength tested per ASTM D1876 after curing for 5 days @ 77°F/25°C. Adherends are 2024-T3 AlClad aluminum treated with phosphoric acid anodized per ASTM D3933.

Test Temperature, °F/°C	Typical Results Lb/in	N/2 mm
77/25	5	22

Bell Peel strength tested per ASTM D3167 after curing for 7 days @ 77°F/25°C. Adherends are 2024-T3 AlClad aluminum treated with phosphoric acid anodized per ASTM D3933.

Test Temperature, °F/°C	Typical Results Lb/in	N/25mm
77/25	20	89

Service Temperature

Service temperature is defined as that temperature at which this adhesive still retains 1000 psi/6.9 MPa) using test method ASTM D1002 and is 350°F/177°C.

Bulk Resin Properties

Tensile Properties - tested using 0.125 inch/ 3.18 mm castings per ASTM D638.

Tensile Strength @ 77°F/25°C	6,675 psi	46.0 MPa
Tensile Modulus @ 77°F/25°C	615 ksi	4,237 MPa
Shear Modulus, dry @ 77°F/25°C	212 ksi	1,461 MPa
Shear Modulus, wet @ 77°F/25°C	149 ksi	1,027 MPa
Elongation at Break @77°F/25°C	1.66%	
Shore D Hardness, @ 77°F/25°C	88	
Tg dry	172°F	78°C
Tg wet	154°F	68°C

LOCTITE EA 9394 AERO
Epoxy Paste Adhesive
(KNOWN AS Hysol EA 9394)

Compressive Properties - tested with rectangular specimens 0.5 in/12.7 mm width by 1.0 in/25.4 mm length by 0.5 in/12.7 mm height per ASTM D695.

Compressive Strength, °F/°C	psi	MPa
77/25	10,000	68.9

Electrical Properties - tested per ASTM D149, D150.

	0.1 KHz	1.0 KHz	10.0 KHz
Dielectric Constant	7.72	7.51	7.20
Dissipation Factor	.017	.022	.033
Thermal Conductivity	7.92×10^{-4} cal/sec-cm-°C		[0.331 W/(m•K)]
Volume Resistivity	4.05×10^{13} ohm-cm		[4.05×10^{11} ohm]
Surface Resistivity	4.60×10^{13} ohm		
Coefficient of Thermal Expansion	55.6µm/m°C @ 40°C		
	80.6µm/m°C @ 100°C		

Handling Precautions
Do not handle or use until the Material Safety Data Sheet has been read and understood.
For industrial use only.

DISPOSAL INFORMATION
Dispose of spent remover and paint residue per local, state and regional regulations. Refer to HENKEL TECHNOLOGIES MATERIAL SAFETY DATA SHEET for additional disposal information.

PRECAUTIONARY INFORMATION
General:
As with most epoxy based systems, use this product with adequate ventilation. Do not get in eyes or on skin. Avoid breathing the vapors. Wash thoroughly with soap and water after handling. Empty containers retain product residue and vapors so obey all precautions when handling empty containers.

LOCTITE EA 9394 AERO
Epoxy Paste Adhesive
(KNOWN AS Hysol EA 9394)

PART A
CAUTION! This material may cause eye and skin irritation or allergic dermatitis. It contains epoxy resins.

PART B
WARNING! This material causes eye and skin irritation or allergic dermatitis. It contains amines.

Before using this product refer to container label and HENKEL TECHNOLOGIES MATERIAL SAFETY DATA SHEET for additional precautionary, handling and first aid information.

Note
The data contained herein are furnished for information only and are believed to be reliable. We cannot assume responsibility for the results obtained by others over whose methods we have no control. It is the user's responsibility to determine suitability for the user's purpose of any production methods mentioned herein and to adopt such precautions as may be advisable for the protection of property and of persons against any hazards that may be involved in the handling and use thereof. In light of the foregoing, **Henkel Corporation specifically disclaims all warranties expressed or implied, including warranties of merchantability or fitness for a particular purpose, arising from sale or use of Henkel Corporation's products. Henkel Corporation specifically disclaims any liability for consequential or incidental damages of any kind, including lost profits.** The discussion herein of various processes or compositions is not to be interpreted as representation that they are free from domination of patents owned by others or as a license under any Henkel Corporation patents that may cover such processes or compositions. We recommend that each prospective user test his proposed application before repetitive use, using this data as a guide. This product may be covered by one or more United States or foreign patents or patent applications.

Rev. 9/2013

Henkel Corporation Aerospace | 2850 Willow Pass Road | Bay Point, CA 94565
PHONE: +1.925.458.8000 | FAX: +1.925.458.8030| www.henkel.com/aerospace